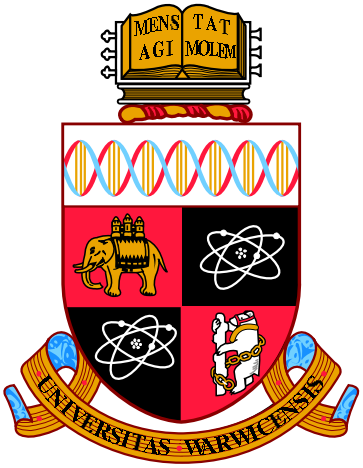

Measurement of the neutral D meson mixing parameters in $D^0 \to K_S\pi^+\pi^-$ decays

by

Tomáš Pilař

Thesis

Submitted to the University of Warwick

for the degree of

Doctor of Philosophy

Department of Physics

June 2014

THE UNIVERSITY OF WARWICK

Contents

List of Figures

List of Tables

Acknowledgments

I'd like to mention and thank everyone who was instrumental in helping me to reach this point. Most immediately I want to thank my primary supervisor Tim Gershon for his advice and guidance, leading me into and out of the analysis discussed in this thesis and not the least for the thorough proof-reading of it. Big thanks also to Paul Harrison who started me on the path of Particle Physics, advised and lead me through my undergraduate and postgraduate studies at Warwick and Michal Kreps for his many insights helpful for the analysis. I want to thank my colleague analysts Nick Torr, and Jordi Garra Ticó who worked with me on the combined analysis (of which this thesis is a part) and Mat Charles who was many times a surrogate supervisor to me. Thanks go to John Back, Dan and Dan, Rafael, David, Charlotte, Matt Williams, Mark, Anton and the rest of the Warwick LHCb office, both old and new as well as the members of T2K office many of which helped keep me sane at many times. Thanks go especially to Matt Reid, colleague and year-mate, who was also incidentally my first and last flat mate - those seasons of SG-1 with Leffe Royale and kebab in St. Genis we'll never get back. Extra special thanks go to Tom Latham for his patience with my questions, who taught me more about physics and programming than I knew in the first place.

I wish to acknowledge the hard work done by the LHCb collaboration for building and commissioning the detector, for operating the immense apparatus necessary to collect the data we analyse and I am grateful for all the help lent by everyone throughout my studies. It's been the brightest and the most amazing community I have been a part of.

There are no words to describe the debt I owe my parents Zdeněk Pilař and Júlia Pilařová, siblings Kristína, Erika and Zdeněk and my entire family for supporting me throughout my life to this point and especially for supporting my studies overseas for the last not-quite-decade. It is to them that I dedicate my thesis. Last but not least, this work wouldn't be possible without the constant support of my better half Valentina.

Declarations

This thesis is submitted to the University of Warwick in support of my application for the degree of Doctor of Philosophy. It has been composed by myself and has not been submitted in any previous application for any degree. All of the work presented were carried out by the author in the collaboration with Mat Charles, Nick Torr and Jordi Garra Ticó except for where indicated by citing the original source.

Abstract

A model-independent measurement of the charm mixing parameters x_D and y_D in the $D^0 \to K_S\pi^+\pi^-$ decay mode is presented. The method uses ratios of yields in symmetric bins of the Dalitz plot and is binned in decay time. This is an alternative approach that does not require the knowledge of the phase-space model of the decay. It also preserves good sensitivity to x_D and to the relative sign between x_D and y_D. Charm mixing parameters are an important step to measuring CP violation in charm mixing. The measured values of the mixing parameters are $x_D = (1.89 \pm 0.43 \pm 0.21 \pm 0.51)\%$ and $y_D = (-2.59 \pm 1.36 \pm 1.13 \pm 3.12)\%$ where the uncertainties are statistical, systematic, and due to input parameters respectively.

Introduction

In particle physics, the oscillation of neutral particles into anti-particles and vice versa (also known as "mixing") has been long known to occur in nature and has been observed in K mesons and B mesons some time ago. The minute scope of mixing in D mesons predicted by the Standard Model makes the observation of mixing in the charm sector more difficult.

A related, and arguably more important, phenomenon is the violation of the Charge-Parity combined symmetry which is necessary for Baryogenesis[a] - a necessary component for the explanation the origin of matter in the Universe. The scientific consensus is that the Standard Model does not contain enough CP violating effects to satisfy this condition and thus the search for CP violation is an excellent probe of new physics.

The most precise measurement of charm oscillations, as of early 2014, has been released by LHCb [2] which confirmed mixing in D mesons, excluding the no-mixing hypothesis with a very high statistical significance (more than 10σ confidence level). However, this observation is thanks to a very good precision of the measurement of the y_D mixing parameter, while the x_D mixing parameter is still consistent with zero[b].

The LHCb experiment is uniquely equipped to measure the charm mixing parameters and to search for CP violation in the charm sector thanks to a very large charm cross-section and extremely good vertex resolution close to the primary interaction point. This allows for a very good time resolution necessary for measurements such as this.

This analysis is performed on the 2011 dataset collected at LHCb. There are continuations of this analysis being performed on the 2012 dataset which improves the effective yields by almost an order of magnitude. While this analysis is unlikely

[a] CP violation is one of the three Sakharov conditions required for Baryogenesis [1].

[b] The dimensionless mixing parameters x_D and y_D are the standard parametrisation of meson mixing, for detailed treatment, see chapter 1

to be sensitive to CP violation, the continuations with the entire Run 1 dataset from LHCb are in fact quite likely to be sufficiently sensitive to improve the world averages.

The channel chosen in this thesis has useful properties that make it a good candidate for a complementary study to the more canonical mixing measurements. Thanks to the knowledge of strong phase in the decay, the mixing parameters are recovered directly, rather than rotated and more importantly, the relative sign between x_D and y_D can be obtained. Currently there have been several results from this channel published by charm factories (BaBar, Belle, CLEO) mostly on fitting the amplitude model to the Dalitz plot of the decay. The measurements of x_D and y_D collated by the Heavy Flavour World Averaging Group can be seen in fig. 1 [3]. Recently a paper was published by the Belle Collaboration with the most precise measurement of mixing parameters in the $D^0 \to K_S\pi^+\pi^-$ yet (not included in Figure 1) with $x_D = 0.56 \pm 0.19$ and $y_D = 0.30 \pm 0.15$ (see Table 1) [4].

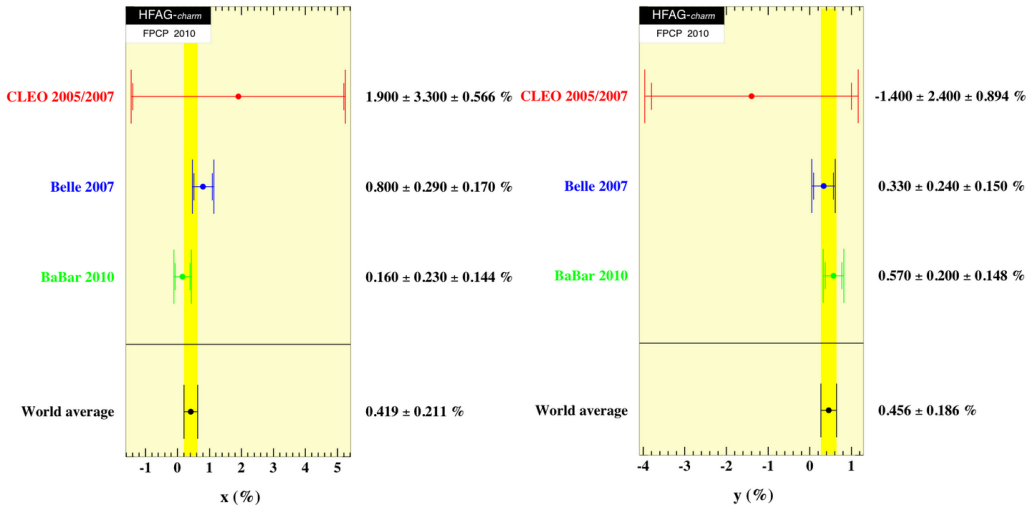

(a) Measurements of x_D (b) Measurements of y_D

Figure 1: World average of charm mixing parameters in the $D^0 \to K_S\pi^+\pi^-$ channel. Adapted from [3].

This thesis discusses a model independent way of measuring the mixing parameters (which was pioneered by several analyses originally intending to measure the γ unitary angle using the $B \to DK$, $D \to K_Shh$ decays) which has several advantages over other methods. It's model-independent, therefore isn't subject to model related systematic uncertainties (but is subject to systematic uncertainties due to strong phase input parameters), is not subject to time-biases and it sacrifices

Fit type	Parameter	Fit result
No CPV	$x(\%)$	$0.56 \pm 0.19^{+0.03+0.06}_{-0.09-0.09}$
	$y(\%)$	$0.30 \pm 0.15^{+0.04+0.03}_{-0.05-0.06}$
CPV	$x(\%)$	$0.56 \pm 0.19^{+0.04+0.06}_{-0.08-0.08}$
	$y(\%)$	$0.30 \pm 0.15^{+0.04+0.03}_{-0.05-0.07}$
	$\lvert q/p \rvert$	$0.90^{+0.16+0.05+0.06}_{-0.15-0.04-0.05}$
	$\arg(q/p)(^\circ)$	$-6 \pm 11 \pm 3^{+3}_{-4}$

Table 1: Measurement of charm mixing parameters in the $D^0 \to K_S\pi^+\pi^-$ channel using a full amplitude fit by the Belle Collaboration published in early 2014 [4].

sensitivity to y_D in favour of x_D.

Given that the analysis described in this thesis was performed in collaboration with several colleagues, it is salient to enumerate contributions of my colleagues to the work in this thesis:

- Trigger definitions and selection development.
- Swimming formalism and development.
- Monte Carlo Sample 5 as described in section 3.2
- Decay Tree Fitter constraints

Chapter 1

Theory

1.1 Standard Model

The Standard Model (SM) is a non-Abelian quantum field gauge theory that forms the basis of particle physics [5]. It was formed throughout the second half of the 20^{th} century and describes what we believe are fundamental particles and four of the five fundamental interactions. It should be noted that the Higgs interaction is still being explored and the gravitational interaction is not included in the Standard Model.

The Standard Model contains fundamental fermions (spin $1/2$ particles) and bosons (spin 1 particles). The fundamental fermions can be seen in Table 1.1 and consist of six quarks and six leptons arranged into three generations. The first generation of fermions (up, down, electron and electron neutrino) composes ordinary matter while higher generations are only observed in high-energy phenomenona such as cosmic rays and particle accelerators. The successive generations of fundamental fermions differ only in flavour and mass, with third generation being the heaviest (see Figure 1.1). Every fermion also has an antimatter counterpart with same mass and opposite quantum numbers (such as electromagnetic charge).

The fundamental bosons that mediate interactions are listed in Table 1.2. The photon is the carrier of the electromagnetic force described by quantum electrodynamics, the W and Z bosons carry the weak force which is described by the unification of EM and weak force theories into electro-weak theory. The gluons carry the strong force which is described by quantum chromodynamics. The name originates from the use of colour to denote the strong charge. The QCD theory is a SU(3) symmetric theory, with red, green and blue being the charge values (the sum

Generation of matter	Fermion	Electric Charge	Mass(MeV/c^2)
I	Up	$+2/3$	2.5 ± 0.8
	Down	$-1/3$	5.0 ± 0.9
	Electron	-1	$0.5119989\ldots$
	Electron Neutrino	0	$< 2 \times 10^{-6}$
II	Charm	$+2/3$	1290 ± 110
	Strange	$-1/3$	100 ± 30
	Muon	-1	$105.658367\ldots$
	Muon Neutrino	0	< 0.19
III	Truth	$+2/3$	172900 ± 900
	Beauty	$-1/3$	4190 ± 180
	Tau	-1	1776.82 ± 0.16
	Tau Neutrino	0	< 18.2

Table 1.1: The fundamental fermions in the Standard model. Masses are taken from the Particle Data Group [6].

of red, blue and green is white or zero), which gives rise to eight distinct gluons. The last force is mediated by the Higgs boson and is called the Higgs interaction after the proponent of the theory. This interaction is responsible for the mass of all fundamental particles.

The fundamental quarks can never be observed outside of hadrons, such as meson and baryons - this principle is called colour confinement. It arises from the fact that the magnitude of strong interaction is so large that the release of energy by breaking the interaction is sufficient for quark-pair creation [8]. Mesons are combinations of a quark and an anti-quark while baryons are combinations of three quarks. In each case, the total colour of the resulting particle is zero.

There is a large number of hadrons known to current science. In fact the large number of what were originally considered elementary particles drove physicists to create categories for these, i.e. the "Eight-fold" Way - somewhat similar to Mendeleev's Periodic Table[a], and to theorise that hadrons might constitute various combinations of fewer, more-fundamental particles. We currently speak of light-unflavoured, strange, charmed, bottom hadrons to indicate the presence of strange, charm and beauty quarks or to indicate the absence of these. There are no known hadrons containing the truth quark because of its short lifetime and currently there

[a]The Eight-fold Way proposed independently by Gell-Mann and Ne'eman organised the known mesons and baryons of spin $1/2$ into two octets and spin $3/2$ baryons into a decuplet [9]. A missing particle Ω^- was predicted and was discovered two years later [10].

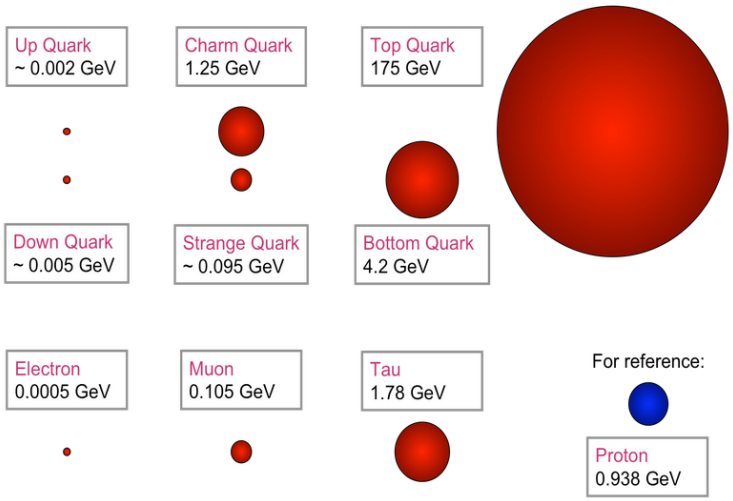

Figure 1.1: Relative fundamental fermion masses. Adapted from [7] .

Interaction	Boson	Electric Charge	Mass(GeV/c^2)
Electromagnetic	Photon	0	massless
Weak	$W^{\pm}$	± 1	80.399 ± 0.023
	Z	0	91.1876 ± 0.0021
Strong	Gluon	0	massless
Higgs	Higgs	0	125.9 ± 0.4

Table 1.2: The fundamental bosons in the Standard Model. The masses are taken from the Particle Data Group [6].

are several searches for $t\bar{t}$ resonances underway at major experiments [11] [12].

1.1.1 Lagrangian

As a quantum field theory, the Standard Model is constructed by first identifying desirable symmetries of the system and then constructing the most general Lagrangian density $\mathcal{L}$ such that the fields composing the Lagrangian density obey the given symmetries. The symmetries required are the global Poincaré symmetry (rotational, translational and special relativity reference frame invariance) and internal gauge symmetry.

Using a perturbative approach, the Lagrangian can be decomposed into terms for free fields and terms for the coupling between fermionic and bosonic

fields due to various interactions. We assume that, in the absence of interactions, the free fields are described purely by kinetic free terms

$$\mathcal{L} = \mathcal{L}_{EW} + \mathcal{L}_{QCD} + \mathcal{L}_{H} + \mathcal{L}_{YU} \tag{1.1}$$

where $\mathcal{L}_{EW}$ describes the Dirac fermion term, Electro-Weak boson field terms and their Electro-Weak coupling term, $\mathcal{L}_{QCD}$ describes Dirac spinors (quarks) and the interaction with gluons, $\mathcal{L}_{H}$ describes the Higgs Field and $\mathcal{L}_{YU}$ is the Yukawa interaction between fermions and the Higgs field which allows for fermion mass.

1.1.2 Higgs Field

The Higgs mechanism in the Standard Model generates fermionic and bosonic mass. Trying to implement simple mass terms arising from the Dirac or Schrödinger equations are not satisfactory:

- Dirac mass terms arising from the basic Dirac Lagrangian are invariant under electroweak symmetry
- Schrödinger Lagrangian is not Lorentz invariant
- Bosonic mass term depends on the choice of gauge.

The simplest renormalizable solution is adding a scalar field

$$\phi = \frac{1}{\sqrt{2}} \begin{pmatrix} \phi^{+} \\ \phi^{0} \end{pmatrix} \tag{1.2}$$

with a Lagrangian

$$\mathcal{L}_{H} = \left[\left(\partial_{\mu} - igW_{\mu}^{a} t^{a} - ig' Y_{\Phi} B_{\mu} \right) \phi \right]^{2} + \mu^{2} \phi^{\dagger} \phi - \lambda \left(\phi^{\dagger} \phi \right)^{2} \tag{1.3}$$

where $v = \sqrt{-\mu^2/\lambda} \approx 246\ GeV$ is the vacuum expectation value and $m_H = \sqrt{-2\mu} \approx 125\ GeV$ is the mass of the Higgs boson [13]. The term

$$\mu^{2} \phi^{\dagger} \phi - \lambda \left(\phi^{\dagger} \phi \right)^{2} \tag{1.4}$$

describes the Higgs Potential in the shape of a "Mexican hat" in the complex plane of ϕ (see Figure 1.2) which is minimised at a circle of points with constant $|\phi|$ rather than $\phi = 0$ [14].

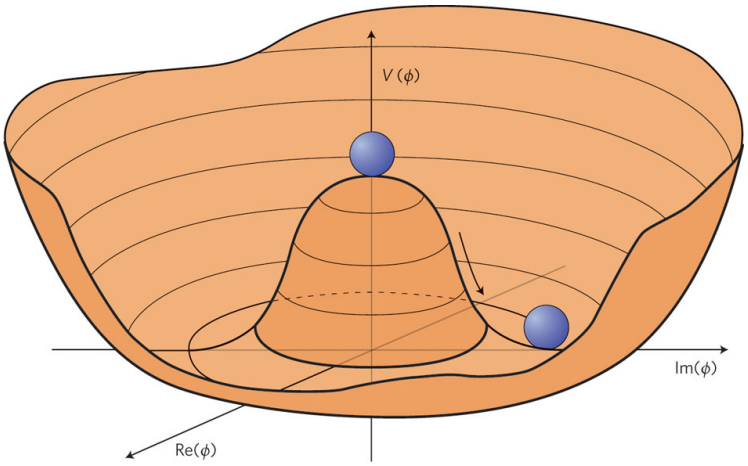

Figure 1.2: Illustration of the Higgs potential in complex plane [15].

The Higgs field permeates the universe and its vacuum expectation value means that the vacuum is no longer empty. The potential spontaneously breaks three out of four degrees of freedom in the electroweak SU(2) $\times$ U(1) group which couple to the weak bosons (W^-, W^+, Z^0) introducing mass. The last degree of freedom becomes a massive boson - the Higgs boson [13].

1.1.3 CKM Matrix and Quark Mixing

The weak force can violate quark flavour, i.e. up-type quarks can transform to down type quarks and vice versa, mediated by the charged weak bosons W^+ and W^-. This arises from the Yukawa couplings that provide mass to fermions. The Yukawa Lagrangian (for first generation of matter) can be written as

$$\mathcal{L}_{YU} = -y_e \bar{E}_L \Phi e_R + y_d \bar{Q}_L \Phi d_R + y_u \bar{Q}_L \Phi u_R + h.c. \tag{1.5}$$

where the left hand chiral fermionic fields are doublets

$$E_L \equiv \begin{pmatrix} \nu_e \\ e^- \end{pmatrix}, Q_L = \begin{pmatrix} u \\ d \end{pmatrix}$$

while the right handed fields are singlets

$$(e^-)_R, (u)_R, (d)_R$$

This construction implies that the charged weak bosons interact with only the left handed chiral fields. Each Yukawa term is invariant under both $SU(2)$ and $U(1)_Y$

transformations. The Yukawa coupling gives fermions their mass through the interaction with the Higgs field with $m_f \propto y_f$ which changes the free parameters of the SM from fermion masses to strengths of Yukawa couplings.

Generalising this to three generations introduces interactions between the different generations of quarks which means y_d and y_u are now 3×3 complex matrices (by construction we allow the generations to mix), but the couplings can be diagonalised by choosing a new basis for the quark fields

$$y_d \to U_d^{L\dagger} y_d U_d^R \tag{1.6}$$

and similarly for y_u. The U^L and U^R transform the quark fields

$$\begin{aligned} d_R^i &\to (U_d^R)^{ij} d_R^j \qquad & d_L^i &\to (U_d^L)^{ij} d_L^j \\ u_R^i &\to (U_u^R)^{ij} u_R^j \qquad & u_L^i &\to (U_u^L)^{ij} u_L^j \end{aligned} \tag{1.7}$$

This transformation cancels in all kinematical terms of the Lagrangian and in all interactions apart from W^+ and W^- interaction terms where the W boson current reads

$$J^{+\mu} = \frac{1}{\sqrt{2}} \bar{u}_L^i \gamma^\mu d_L^i \to \frac{1}{\sqrt{2}} \bar{u}_L^i \gamma^\mu (U_u^{L\dagger} U_d^L)^{ij} d_L^j \tag{1.8}$$

Where $V \equiv (U_u^{L\dagger} U_d^L)^{ij}$ does not cancel and is a 3×3 matrix. The matrix has to be unitary, each quark field can absorb one complex phase and the overall global phase is immaterial due to phase invariance of the Lagrangian. These constraints reduce the number of free parameters of V to four which can be chosen to be three Euler angles and one complex phase. The resulting matrix V (eq. 1.9) is called the Cabibbo-Kobayashi-Masakawa (CKM) mixing matrix [16] and the mixing angles determine the probability of a given quark flavour being changed in an interaction (see Figure 1.3). It can be written as

$$\begin{aligned} V &= \begin{pmatrix} V_{ud} & V_{us} & V_{ub} \\ V_{cd} & V_{cs} & V_{cb} \\ V_{td} & V_{ts} & V_{tb} \end{pmatrix} \\ &= \begin{pmatrix} c_{12}c_{13} & s_{12}c_{13} & s_{13}e^{-i\delta} \\ -s_{12}c_{13} - c_{12}s_{23}s_{13}e^{-i\delta} & c_{12}c_{13} - s_{12}s_{23}s_{13}e^{-i\delta} & s_{23}c_{13} \\ s_{12}c_{13} - c_{12}s_{23}s_{13}e^{-i\delta} & -c_{12}s_{13} - s_{12}c_{23}s_{13}e^{-i\delta} & c_{23}c_{13} \end{pmatrix} \end{aligned} \tag{1.9}$$

where $c_{13} \equiv \cos\theta_{13}$, $s_{12} \equiv \sin\theta_{12}$ etc. for the three rotation angles $\theta_{12}, \theta_{13}, \theta_{23}$ and δ being the complex phase that allows for CP violation in the weak interactions

(which is the only hitherto confirmed source of CP violation)[b].

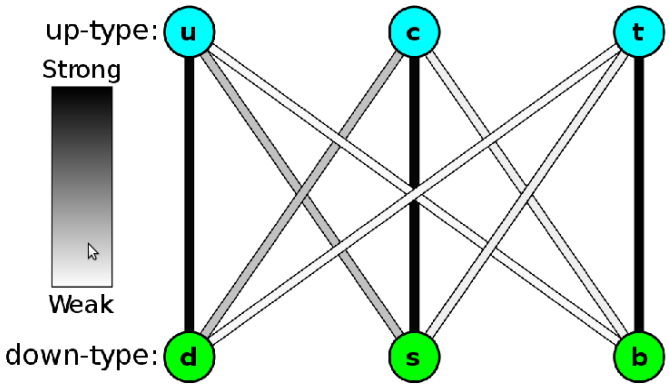

Figure 1.3: Transitions between quark flavours as described by the CKM matrix.

The CKM matrix can be parametrised using the Wolfenstein parametrisation [17] which is more convenient for expressing the apparent hierarchy among flavour-changing weak interactions shown in Figure 1.3 as

$$V = \begin{pmatrix} 1-\lambda^2/2 & \lambda & A\lambda^3(\rho - i\eta) \\ -\lambda & 1-\lambda^2/2 & A\lambda^2 \\ A\lambda^3(1-\rho-i\eta) & -A\lambda^2 & 1 \end{pmatrix} \tag{1.10}$$

with $\lambda = s_{12}, A\lambda^2 = s_{23}$ and $A\lambda^3(\rho - i\eta) = s_{13}e^{-i\delta}$ which is correct up to $\mathcal{O}(\lambda^3)$.

The unitarity of the CKM matrix can be expressed as

$$\sum_k V_{ik}V_{jk}^* = 0 \tag{1.11}$$

for all like-charged quarks $i, j,\ i \neq j$ which, given that each term describes a complex number, is an equation for a triangle (called a unitarity triangle) such as one shown in Figure 1.4. This particular triangle is popular[c] because of its importance in B physics, especially B meson mixing since it describes the relationship between b and d quarks which compose neutral B mesons and because $V_{ud}V_{ub}^* \sim V_{cd}V_{cb}^* \sim V_{td}V_{tb}^* \sim \mathcal{O}(\lambda^3)$ leading to a triangle with comparable sides. Given that the angles of this triangles represent degrees of freedom of the CKM

[b]The symmetry of the combined CP (charge conjugation and parity) operation and breaking thereof is discussed in section 1.3 of this chapter.

[c]This triangle is often referred to as The Unitarity Triangle

matrix, measuring the angles of the triangle in Figure 1.4 is a good way of obtaining information about the CKM matrix.

In comparison, if one were to construct a unitarity triangle corresponding to charm physics, one would obtain

$$V_{cd}V_{ud}^* + V_{cs}V_{us}^* + V_{cb}V_{ub}^* = 1 \tag{1.12}$$

where $V_{cd}V_{ud}^* \sim -V_{cs}V_{us}^* \sim \mathcal{O}(\lambda)$ and $V_{cb}V_{ub}^* \sim \mathcal{O}(\lambda^5)$ which would represent a very acute triangle with one side much much shorter than the other two. Thus this would not be an ideal choice for extracting information about the CKM matrix.

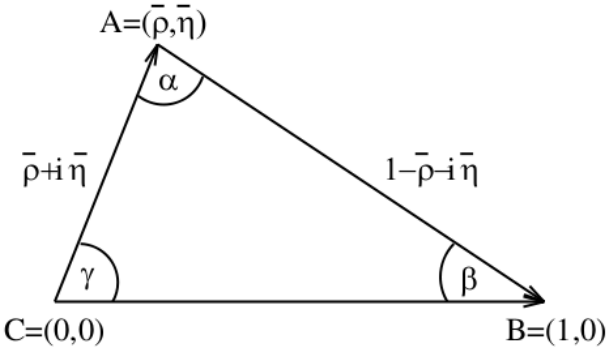

Figure 1.4: The CKM Unitarity triangle that describes the unitarity condition 1.11 for $i = d,\ j = b$. Here $\bar{\rho} \approx \rho\left(1 - \frac{\lambda^2}{2}\right), \bar{\eta} \approx \eta\left(1 - \frac{\lambda^2}{2}\right)$. Adopted from [17].

1.1.4 Beyond SM

While the Standard Model is one of the most successful theories in the history of physics, verified by the comparison of post-dictions and predictions to experimental measurements to an unparallelled degree, it fails to explain several important phenomena observed in the universe or address several concerns of theoretical physics, some of which are listed below.

- Existence of matter dominated universe (see §1.3).
- Neutrino mass and oscillations.
- The arbitrary number of generations of matter.
- The presence of dark matter and compatibility with the Standard Model of Astrophysics.

- Quantum Gravity.
- Hierarchy due to Higgs mechanism[d].
- Strong CP problem (see §1.3)
- Large number of free parameters fixed by experiments rather than theory.

This is a strong indication that there is either a more fundamental theory, or at least some yet unproven extension of the Standard Model explaining these phenomena. There are many candidate theories and extensions that attempt to do so, such as supersymmetry and string theory.

1.2 Neutral Meson Mixing

Given that flavour is not conserved in weak interactions, a meson may "transform" into an anti-meson provided the rest of the quantum numbers apart from flavour are identical between the two particles. This is true for neutral mesons and the process is known as "oscillation" or "mixing"[e].

Phenomenologically, the meson mixing can occur via "long range" or via "short range" processes. Long range involves re-scattering of intermediate particles such as K or π (see Figure 1.5). These processes are hard to model theoretically and due to the fact that they are the dominant contribution to charm mixing in SM the theoretical predictions for charm mixing have large uncertainties [19].

The short range process is a "box"-diagram involving an exchange of W bosons and virtual quarks. Specifically for charm, this diagram contributes $\mathcal{O}(10^{-5})$ to mixing but could be enhanced by new physics. Similarly, any observation of CPV in charm mixing at the current experimental levels would be immediate evidence of new physics.

[d]The Hierarchy problem is a question that asks why the weak force is 10^{32} times stronger than gravity since both involve empirical constants of nature (Fermi's constant for weak force and Newton's gravitational constant). If one were to use the Standard Model to calculate radiative corrections to the Fermi's constant, it would appear much closer in scale to the Newton's constant. Equivalently this can be posited as quadratic radiative corrections to the Higgs mass $\delta_H^2 \approx -\frac{|\lambda_f|^2}{8\pi^2}[\Gamma_{UV} + \dots]$, where λ_f is the Yukawa coupling of a given fermion, diverge if the scale Λ_{UV} is chosen to be the Planck scale [18]. These depend on the mass of the fermion due to the Yukawa coupling so the most massive fermions will contribute the most to the corrections. The worry is that in future extensions of the SM that allow the calculation of the Higgs mass, these corrections will have to be fine-tuned out and the Higgs mass would be unstable. And no-one likes fine-tuning.

[e]Note that neutral meson mixing and quark mixing are different concepts.

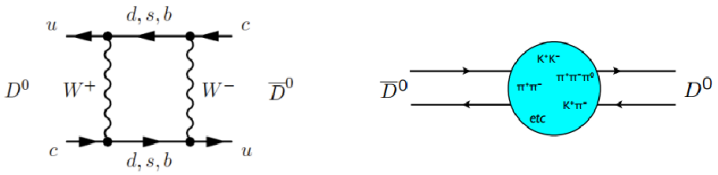

Figure 1.5: Diagrams illustrating mixing mechanisms - short range on the left and long range on the right. Short range is a single weak interaction described by a Feynman diagram, long range shows lots of complicated processes involving light meson pairs and triplets.

The formalism of neutral meson mixing in the Standard Model can be described starting from the difference between Hamiltonian eigenstates ($|D_1\rangle$, $|D_2\rangle$) corresponding to physical propagating states of neutral mesons and the flavour eigenstates ($|D^0\rangle$,$|\bar{D}^0\rangle$) which represent the pure quark content which enters weak interactions. We can use the flavour eigenstates to form a basis

$$\left|D^0\right\rangle = \begin{pmatrix} 1 \\ 0 \end{pmatrix}, \qquad \left|\bar{D}^0\right\rangle = \begin{pmatrix} 0 \\ 1 \end{pmatrix}. \tag{1.13}$$

Then we can express the Hamiltonian eigenstates as the linear combination of the flavour eigenstates. The Schrödinger equation describing the time evolution of a meson in the flavour basis becomes

$$i\frac{d}{dt}\begin{pmatrix} a \\ b \end{pmatrix} = \mathcal{H}\begin{pmatrix} a \\ b \end{pmatrix} \equiv \left(M_{ij} - \frac{i}{2}\Gamma_{ij}\right)\begin{pmatrix} a \\ b \end{pmatrix}, \tag{1.14}$$

where the mass matrix M_{ij} and the decay width matrix Γ_{ij} are Hermitian but $\mathcal{H}$ is not Hermitian and is called the *effective Hamiltonian*. The CPT invariance[f] requires that $\mathcal{H}_{11} = \mathcal{H}_{22}$. The off-diagonal elements of the effective Hamiltonian describe the absorptive (M_{12}) and dispersive (Γ_{12}) elements of meson mixing. The eigenstates of the effective Hamiltonian are given by

$$\begin{pmatrix} M_{11} - \frac{i}{2}\Gamma_{11} & M_{12} - \frac{i}{2}\Gamma_{12} \\ M_{12}^{\star} - \frac{i}{2}\Gamma_{12}^{\star} & M_{11} - \frac{i}{2}\Gamma_{11} \end{pmatrix}\begin{pmatrix} p \\ q \end{pmatrix} = \lambda_{1,2}\begin{pmatrix} p \\ q \end{pmatrix}, \tag{1.15}$$

and the eigenvalues $\lambda_{1,2} \equiv m_{1,2} - \frac{i}{2}\Gamma_{1,2}$. Taking a ratio of elements of the eigenvec-

[f]It is assumed that CPT (charge conjugation, parity and time reversal) is conserved as per the CPT theorem which predicts that every Lorentz invariant quantum field theory (such as SM) with a Hermitian Hamiltonian (eigenvalues of Hamiltonian are real) must observe CPT symmetry [20].

tors one can find

$$\pm \frac{q}{p} = \pm \sqrt{\frac{M_{12}^{\star} - \frac{i}{2}\Gamma_{12}^{\star}}{M_{12} - \frac{i}{2}\Gamma_{12}}} \tag{1.16}$$

with $|p|^2 + |q|^2 = 1$. Mass eigenstates can then be expressed as

$$|D_{1,2}\rangle = p\left|D^0\right\rangle \pm q\left|\bar{D}^0\right\rangle. \tag{1.17}$$

We define for convenience the dimensionless quantities

$$\Gamma = \frac{\Gamma_1 + \Gamma_2}{2}, \qquad x = \frac{m_1 - m_2}{\Gamma}, \qquad y = \frac{\Gamma_1 - \Gamma_2}{2\Gamma}, \tag{1.18}$$

where m_i, Γ_i are the mass and the width of the i-th eigenstate and Γ is the average width of the two eigenstates. These are called the *mixing parameters*[g]. The time evolution of a Hamiltonian eigenstate is given by[h]

$$|D_{1,2}(t)\rangle = e^{-\frac{\Gamma t}{2}} h_{1,2}(t)\,|D_{1,2}\rangle\,, \tag{1.19}$$

with

$$h_{1,2}(t) = e^{\mp \frac{(y+ix)\Gamma t}{2}}. \tag{1.20}$$

1.2.1 Methods to extract mixing parameters

There are several methods of measuring the mixing parameters, each with its own advantages and disadvantages. Given that the mixing parameters represent a perturbation from the default unmixed state, one generally has to measure a deviation compared to the null state, such as measuring the perturbation of an exponential of the decay probability due to mixing. This might introduce uncertainty based on the knowledge of the null state.

When the mixing parameters are large, such as in strange and beauty mixing, the effect can be observed directly as an asymmetry between the number of decayed mesons and anti-mesons to semileptonic modes in a clean production environment. Alternatively, and more precisely, one can measure the time dependent oscillation of the asymmetry of the mixed and unmixed decay rate of neutral mesons in flavour specific modes (see Figure 1.6 and 1.7). This requires extremely

[g] The mixing parameter x_D (subscript D denotes the neutral charm meson D^0) represents the normalised difference between the masses of the two physical eigenstates. The parameter y_D represents the normalised difference between the decay widths of the two physical eigenstates.

[h] For a detailed derivation please see [6].

good resolution of the B decay vertex and good momentum resolution as well as an efficient tagging mechanism with the disadvantage that the fit is sensitive to x only. The B_d^0 mixing extraction neglects y_B which is assumed to be small compared to x_B ($< 1\%$, see 1.3.1) as the effect of such small magnitude of y_B on the decay rate would be almost indistinguishable from time resolution effects.

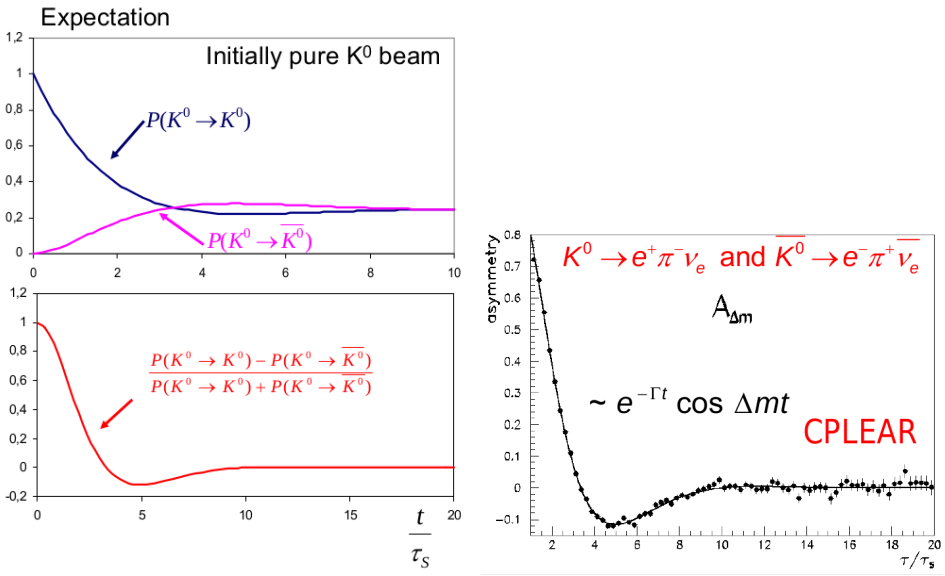

Figure 1.6: Mixing in the strange sector, illustration of the asymmetry of decay rates (left) and measurement by CPLEAR (right). Adopted from [21].

Extracting mixing parameters in the charm sector uses different methods. Due to the small size of the mixing parameters one requires an extremely good tag compared to beauty mixing. The commonly used decay of $D^*(2010)^+ \to D^0\pi^+$ has a mistag rate of $\sim 0.1\%$.

Using semileptonic decays where the final state is only accessible via mixing, one can extract the rate of mixing (defined as $R_M \equiv \frac{(x^2+y^2)}{2}$) directly from the decay rate

$$r\left(t\right) \approx \frac{e^{-t}}{4}(x^2 + y^2) \tag{1.21}$$

assuming no CP violation. This is not very sensitive to mixing parameters due to the fact that the mixing parameters appear in quadratic.

Alternatively one can use decays to hadronic non-CP eigenstates (such as $K^+\pi^-$ where the unmixed decay is doubly-Cabibbo-suppressed (DCS) and the mixed decay is Cabibbo-favoured (CF) leading to a ratio of decay rates, in absence

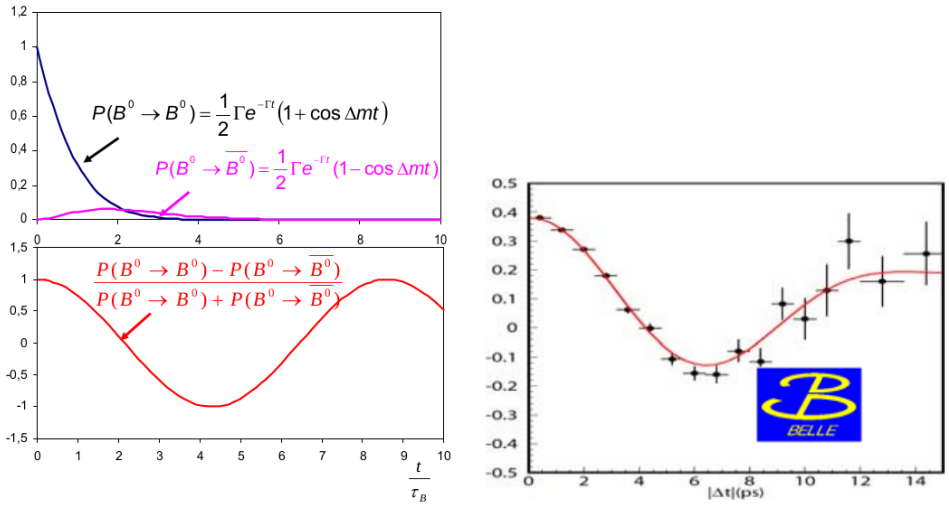

Figure 1.7: Mixing in the beauty sector, illustration of the asymmetry of decay rates (left) and measurement by BELLE (right). Adopted from [22].

of CP violation

$$\frac{r(t)_{WS}}{r(t)_{RS}} \approx \left(R_D + \sqrt{(R_D)}y't + \frac{1}{2}R_M t^2\right) \tag{1.22}$$

with WS and RS denoting the so-called "wrong sign" decay (DCS decay) and "right sign" decay (CF decay) of the mother particle with R_D denoting the ratio of suppressed to favoured decay rates [2]. Here the parameters are transformed by the strong phase difference between the decay amplitudes

$$\begin{aligned} x' &\equiv x\cos\delta_{K\pi} + y\sin\delta_{K\pi} \\ y' &\equiv x\cos\delta_{K\pi} - y\sin\delta_{K\pi} \end{aligned} \tag{1.23}$$

giving

$$x'^2 + y'^2 = x^2 + y^2 \tag{1.24}$$

and the fit parameters become R_D, y' and x'^2. One can integrate $r(t)$ to get the time-integrated rate

$$R = R_D + \sqrt{R_D}y' + R_M \tag{1.25}$$

which is more readily available experimentally but generally carries less statistical power because of poor independent knowledge of R_D[i]. It should be noted that this method of extracting mixing parameters requires knowledge of the relative strong

[i] One can extract R_D from the time-dependent fit to the WS/RS ratio as the intercept of the x-axis.

phase $\delta_{K\pi}$ between the CF and DCS decays[j], it does not provide information about the relative sign of x and y and generally is less sensitive to x due to a quadratic relationship[k].

Should one choose to use three-body (or more) decays to extract mixing parameters (such as $D^0 \to K^+\pi^-\pi^0$) the mixing equations apply separately across the phase-space with the relative strong phase varying with position in phase-space. This can be mitigated by binning the phase-space such that the relative strong phase is approximately constant in each bin and extracting the values of the relative strong phase with a separate analysis of quantum correlated decays, such as a $\psi(3770) \to D^0\bar{D^0}$. However R_D will still vary with phase-space.

Decays to CP eigenstates such as K^+K^- can be used in comparison with decays to $K^-\pi^+$ to extract the y_{CP} parameter

$$y_{CP} = \frac{\Gamma(D^0 \to \pi^+\pi^-)}{\Gamma(D^0 \to K^-\pi^+)} - 1 = \frac{\Gamma(D^0 \to K^+K^-)}{\Gamma(D^0 \to K^-\pi^+)} - 1 \tag{1.26}$$

$$y_{CP} = \frac{1}{2}\left(\left|\frac{q}{p}\right| + \left|\frac{p}{q}\right|\right) y\cos\phi - \frac{1}{2}\left(\left|\frac{q}{p}\right| - \left|\frac{p}{q}\right|\right) x\sin\phi \tag{1.27}$$

$$y_{CP} \approx y\cos\phi - A_M x\sin\phi \tag{1.28}$$

with ϕ being the complex argument of $\frac{q}{p}$. The y_{CP} parameter measures mixing and CP violation in mixing (specifically in difference of decay widths). By taking the ratio of decay rates, one can cancel lifetime bias (assuming any such bias is common to both decay modes). In the limit of CP conservation, $y_{CP} = y$ and thus with good independent knowledge of y, this allows to probe CP violation in charm mixing.

Should one use decays to a three-body self-conjugate final state, such as $K_S h^+h^-$ in this analysis, the mixing equations will hold at every point of Dalitz space. Furthermore, one can compare the expected number of events in symmetric parts of the Dalitz plot as indicated in chapter 6 to extract mixing information without knowledge of the Dalitz plot distribution.

It is also possible to use coherent $D^0\bar{D^0}$ production at e^+e^- collisions to determine x, y and R_D simultaneously using decays of $\psi(3770)$ decaying into quantum correlated $D^0\bar{D^0}$ pairs. Thanks to this correlation, the time-integrated rates

[j]The relative strong phase information can be obtained from quantum correlated decays of $\psi(3770) \to D^0\bar{D^0}$ readily produced at charm factories.

[k]Having defined R_M as $R_M \equiv \frac{x^2+y^2}{2}$ the equation 1.25 depends on y' and x^2 and consequently can measure y' to much better precision than x

of decay are sensitive to interference due to amplitude from indistinguishable final states. This interference is dominated by individual decay amplitudes but has a contribution due to mixing. These can be either single-tagged or double-tagged (for example using semileptonic decays).

1.2.2 $D^0 \to K_S h^+ h^-$ decay channel

The decay channel $D^0 \to K_S h^+ h^-$ offers both advantages and disadvantages when extracting mixing and CPV parameters. The decay has a three-body final state which means the phase-space can be described by a Dalitz plot (see appendix A) and the decay amplitude is phase-space dependent. This offers more information for fitting, but makes the analysis more complicated by introducing a decay model that has to be accounted for.

As a three body decay, the triggering at LHCb is more complicated than a two-body decay such as $D^0 \to h^+ h^-$ leading to a considerably reduced dataset in comparison.

The model-dependent full-amplitude fit allows for the extraction of the phase-space dependent relative strong phase between the amplitudes ($\delta_{K_S\pi^+\pi^-}$) which is useful for some mixing extraction methods outlined earlier. Furthermore, this means that the mixing parameters are accessed directly (not rotated by the strong phase). This allows for several important measurements such as the relative sign of x and y and comparison of y and y_{CP}. A good measurement of x is also important since the current world average has x consistent with null hypothesis within $\sim 2\sigma$ (see 1.3.2) and this channel provides access to non-rotated x with good precision.

As an alternative to a full-amplitude fit, one can perform a fit binned in phase-space if one has access to strong-phase information measured by a different analysis. This fit can be time-dependent, time-binned or time-integrated. This thesis uses a time-binned, phase-space binned fit as described in chapter 6.

1.3 CP Violation

After P symmetry was proven to be broken [1] it was proposed that laws of physics were invariant under the combined CP (that is charge-conjugation and parity) operation. However we now recognize this is not the case.

We recognise three different types of violation of this symmetry:

1. CP violation in decay.
2. CP violation in mixing.
3. CP violation in the interference between decay and mixing.

The first is the difference between the decay rates of a particle and antiparticle to a specific set of CP conjugate final states or a single self-conjugate final state. The second is the difference in the rate of oscillation of a meson to anti-meson compared to the reverse. The measurement of CPV parameters in mixing generally depends on the measurement of the mixing parameters themselves. The third kind of CP violation can be observed in the interference between direct decays and decays after the mother meson has mixed. One example of a potential occurence of this kind of CP violation is the measuremnt of mixing parameters using the interference of Cabibbo-favoured mixed decays and doubly-Cabibbo-suppressed unmixed decays in the "Wrong-sign" to "Right-sign" ratio fit (see eq. 1.22).

The importance of CP violation searches can be motivated by one of the shortcomings of the Standard Model. There is far more matter observed in the known universe than antimatter. This can be explained by several hypotheses[m] such as the Electroweak Baryogenesis [25]. In general, Baryogenesis requires three Sakharov Conditions to occur [1], one of which is presence of CP violating processes in Nature. Currently theorists agree that the quark sector of the Standard

[1] In the famous $\theta - \tau$ puzzle, the two particles were thought to be different even though they had the same mass and lifetime and were otherwise indistinguishable except they decayed into 2 π and 3π respectively. This breaks parity symmetry which was assumed to hold. When it was proven in 1956 that parity could be violated [23] in weak decays it became obvious the θ and τ are the same particle.

[m] Such as: Leptogenesis [24] which adds right-handed neutrinos and gives them mass via the See-Saw mechanism and proposes that the matter-antimatter asymmetry is due to a lepton asymmetry generated by the otherwise sterile right-handed heavy neutrinos - this theory was popular in the last decade because of its relative simplicity and emerging measurements of neutrino mass and oscillations; Electro-weak Baryogenesis [25] which postulates that the asymmetry was produced by CP violating processes in the electro-weak sector; GUT (Grand Unified Theory) Baryogenesis [26] which assumes that the baryon asymmetry is due to decays of various GUT bosons.

model does not contain enough CP violating processes to satisfy the Sakharov conditions[n].

Another unanswered question in the Standard Model is the absence of CP violation in the strong interactions. The general version of QCD Lagrangian

$$\mathcal{L} = -\frac{1}{4}F_{\mu\nu}F^{\mu\nu} - \frac{n_f g^2 \theta}{32\pi^2}F_{\mu\nu}\tilde{F}^{\mu\nu} + \bar{\phi}(i\gamma^\mu D_\mu - me^{i\alpha\gamma_5}) \tag{1.29}$$

violates CP for non-zero angle θ and chiral mass phase α. The experimental lower boundary from neutron electric dipole measurements are extremely small (currently $|d_n| < 2.9 \times 10^{-26} ecm$ [27]) which implies that these parameters take vanishing value ($\theta < 10^{-10} rad$ [27]) in Nature. This is either an example of "fine tuning" or alternatively could be explained by the existence of theoretical (and hitherto unobserved) "axions" to cancel CP violation in QCD processes [28].

1.3.1 Mixing and CP Violation in beauty and strange sector

The meson mixing in strange sector is historically the first instance of meson mixing observed [29]. The Hamiltonian eigenstates are very closely aligned with CP eigenstates which means that the major modes of decay of K_1 and K_2 will be 3π and 2π respectively. The fact that the mass of K_1 is just a little larger than the combination of three pions means that the decay is a factor 600 slower compared to $K_2 \to 2\pi$ because of the restricted phase-space. Quantitatively the mixing parameters are: $x_K = 0.942 \pm 0.007$ and $y_K \approx -1$ [6] ($y_K \equiv \frac{\Gamma_{K_L} - \Gamma_{K_S}}{\Gamma_{K_L} + \Gamma_{K_S}}$). The natural labelling of the Hamiltonian eigenstates thusly becomes K_S for "K-short" and K_L for "K-long" because the decay time is a clear experimental difference.

The mixing in the beauty sector has been well established for a few decades now [30]. The mixing parameter y_B for B^0 mesons is assumed to be zero or insignificant[o] i.e. there is no difference in decay times for the two Hamiltonian eigenstates. The mass difference is however significant with $x_B = 0.775 \pm 0.007$ [3] leading to the labelling of the eigenstates as B_H and B_L for the heavy and light eigenstate respectively.

[n] Given the quantity of matter in the universe and using the Cosmic Microwave Background one can estimate what fraction of matter remained post-annihilation.

[o] While M_{12} and thus x gets most contribution from the short range "box-diagram" mixing, Γ_{12} and therefore y gets most contribution from the long range mixing with exchange of mesonic self-conjugate states such as $\pi^+\pi^-$, K^+K^- and D^+D^- mesons. Hence magnitude of y is restricted by the the branching fractions of the mother meson to these states. While for D^0 and B_s^0 these are reasonably common, B_d^0 does not decay into these favourably [6].

In the beauty-strange sector, meson mixing for neutral B_s mesons has been observed only recently [31]. The current values of mixing parameters are $x_{B_s} = 26.82 \pm 0.23$ [3] and $y_{B_s} = 0.093 \pm 0.010$ [6][P] [32]. The large difference between x and y again lends itself for labelling the eigenstates "light" and "heavy".

The CP symmetry was proven to not hold in 1964 [33] when K_L was shown to decay into 2π which is a CP-forbidden state. This is an example of CP violation in mixing. The first observation of CPV in decay came in the kaon system in 1999 [34].

The CP symmetry violation has been observed in the beauty system as well in 2001 [35]. The current world average is $\sin 2\beta = 0.68 \pm 0.02$ (see Figure 1.8). In the limit of CP conservation $\sin 2\beta = 0$. This is another example of the interference between decay and mixing.

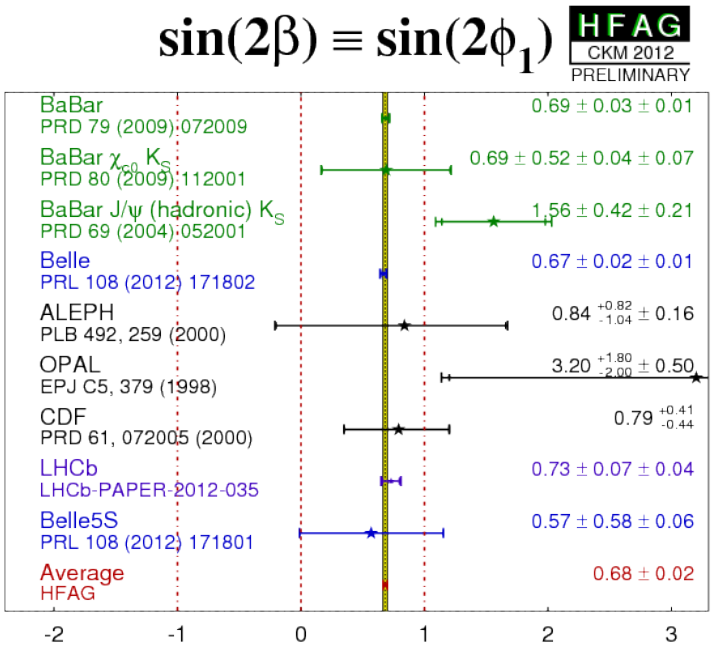

Figure 1.8: Preliminary world average fit of the CP violating parameter $\sin 2\beta$ for 2012. In the limit of CP conservation $\sin 2\beta = 0$. Adopted from [3].

[P]The quantity denoted $\Delta\Gamma_s/\Gamma_s$ in the PDG summary in fact corresponds to $\Delta\Gamma_s$ rather than $2y_{B_s}$ as the summary indicates.

1.3.2 Mixing and CP Violation in charm sector

The charm sector differs from both strange and beauty in the magnitude of the mixing amongst others. The current world average of mixing parameters for charm mesons are $x = (0.39 \pm 0.17)\%$ and $y = (0.67 \pm 0.17)\%$ [3] (see Figures 1.9 and 1.10), which establishes a significant difference in lifetimes but x is consistent with the null hypothesis. The minute scope of mixing in the charm sector explains why the observation of charm mixing came only recently, significantly later than in the beauty sector.

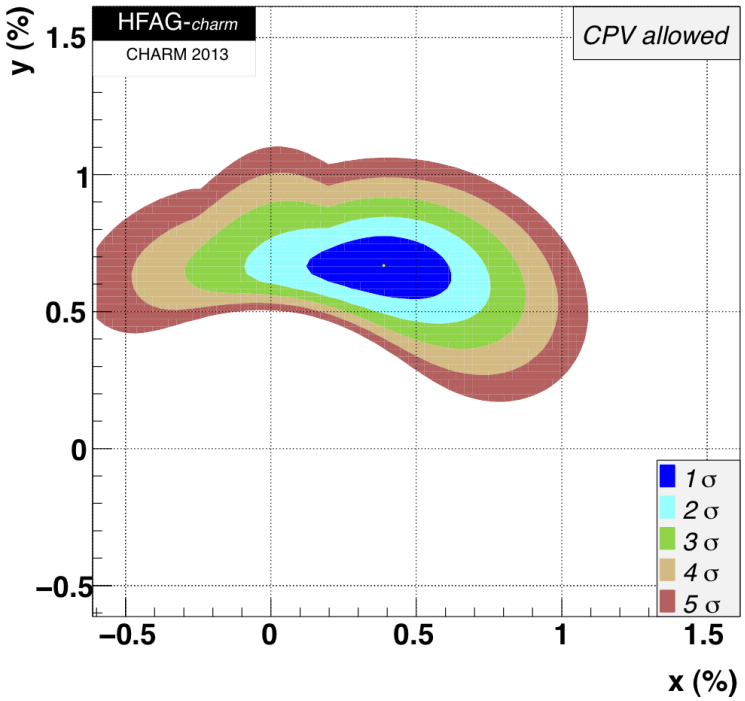

Figure 1.9: World average fit contours of x and y mixing parameters for charm mesons allowing for CP violation. Adopted from [3].

The current world averages of CP violation in the charm sector are very consistent with the null hypothesis, however there are promising avenues of exploration, such as the comparison of y_{CP} and y and one of the reasons why charm mixing is interesting that any CP violation in charm mixing would be a strong indication of new physics.

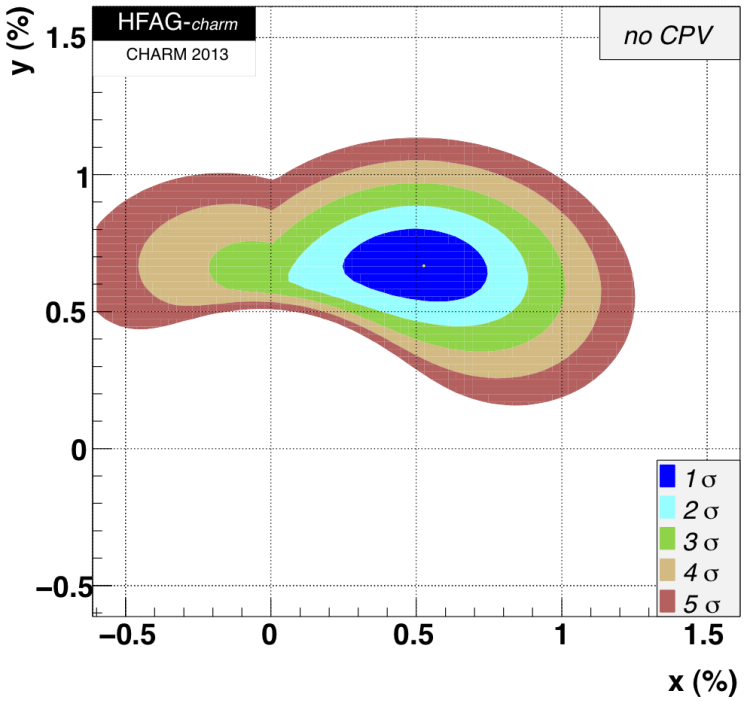

Figure 1.10: World average fit contours of x and y mixing parameters for charm mesons disallowing any CP violation. Adopted from [3].

Chapter 2

The LHCb Experiment

2.1 The LHC Ring

The Large Hadron Collider beauty (LHCb) experiment is one of the four main experiments located on the circumference and utilising the accelerator facilities of the Large Hadron Collider. The LHC is a two-ring accelerator located on the Swiss-French border near Geneva, Switzerland in the old LEP tunnel and its 26.7 km long circumference at a depth of 45-170 m crosses both countries. The collider uses older accelerators for injection purposes as seen in Figure 2.1. The acceleration process begins with the linear particle accelerator LINAC2 which produces protons at $50\ MeV$ which are injected into the Proton Synchrotron Booster (PBS) where the protons are accelerated to $1.4\ GeV$. Further on the Proton Synchrotron (PS) accelerates the beams to $26\ GeV$ and finally the the Super Proton Synchrotron reaches the energy of $450\ GeV$. At this point the protons can be injected into the two LHC rings which facilitate the final acceleration to collision energy. The collisions last for several hours until the proton bunches are depleted and the luminosity drops below an effectivity threshold at which point the beams are dumped, reinjected and reaccelerated. A single iteration of beam injection to beam dump is called a fill.

The LHC achieved collision energy $\sqrt{s} = 7\ TeV$ in 2010 and $\sqrt{s} = 8\ TeV$ in 2012 [36]. The design specifications intend the LHC to operate at centre-of-mass energy $\sqrt{s} = 14\,TeV$ and peak luminosity of $10^{34}\,cm^{-2}s^{-1}$ (2080 bunches per beam spaced $25\ ns$ apart) after a set of upgrades is performed [37]. The collider facilitates four main experiments (ATLAS, CMS, LHCb, ALICE) and is operated by the European Centre for Nuclear Research (CERN).

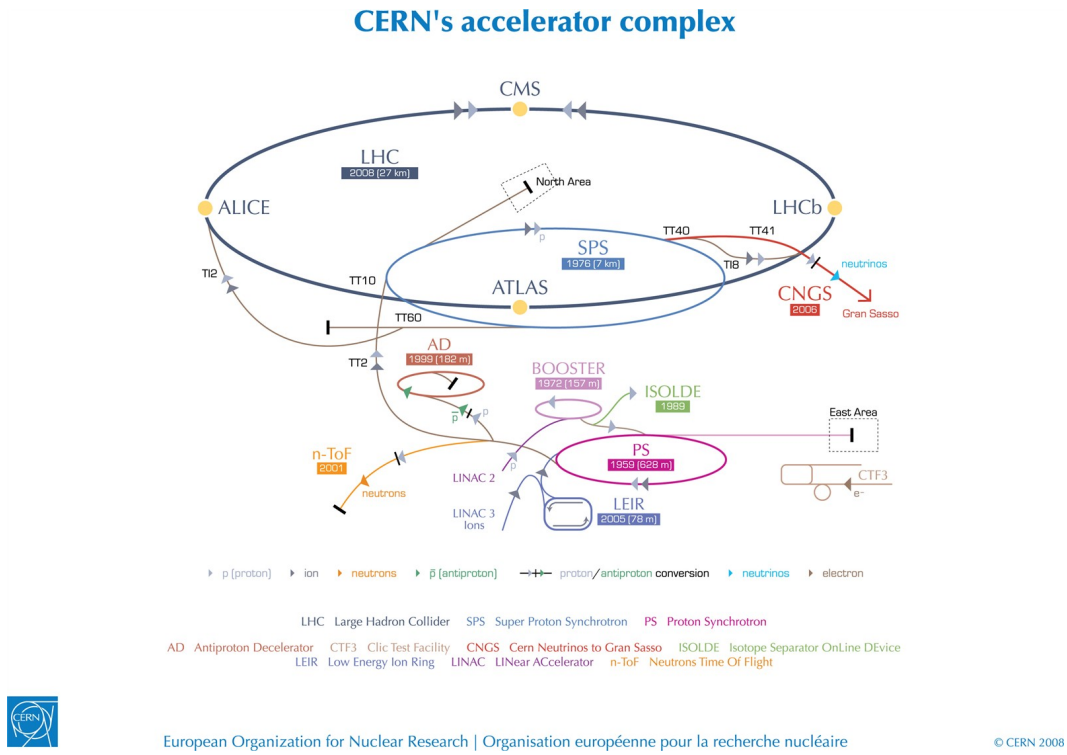

Figure 2.1: The scheme of the Large Hadron Collider complex with injection accelerators and experiments (the PBS is labelled BOOSTER in this scheme) [38].

The luminosity can be related to the beam parameters by

$$L = fn\frac{N_1 N_2}{A} \tag{2.1}$$

with f being the revolution frequency, n the number of proton bunches in a circulating beam, N being the number of protons in a bunch for respective beams and A is the cross-section area of the proton bunch. The luminosity recorded by LHCb through the first run can be seen in Figure 2.2.

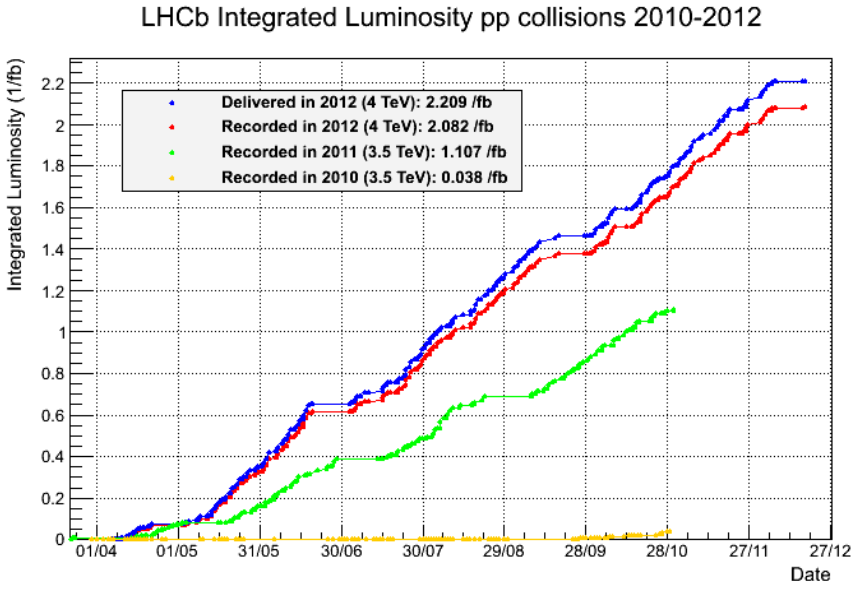

Figure 2.2: Integrated recorded LHCb luminosity throughout the first run of data-taking [39].

2.2 LHCb Detector

The LHCb detector is a forward arm spectrometer (see Figure 2.3) with an angular acceptance of $10 - 250 \ \ mrad$ in the vertical and $10 - 300 \ \ mrad$ in the horizontal plane (The horizontal plane is the bending plane of the magnet). The geometry uses a right handed coordinate system located at the Interaction Point with z-axis pointing downstream, y-axis pointing vertically upwards and the x-axis completing the Cartesian system. The primary aim of the LHCb experiment is to measure Standard Model parameters with high precision and look for evidence of new physics and CP violation by studying heavy flavour physics, particularly decays of hadrons produced in $b\bar{b}$ and $c\bar{c}$ pair-production.

The LHCb design is based on an expected luminosity of $2 \times 10^{32} \ cm^{-2}s^{-1}$ with 10^7 $b\bar{b}$ pairs and 10^{12} $c\bar{c}$ pairs produced annually [40]. This means that the average number of pp collisions per bunch crossing is ~ 1, compared to ~ 40 for ATLAS or CMS. This greatly reduces the complexity of event analysis. The lower luminosity is achieved by a controlled misalignment of beams such that the shared cross-section of the bunches is lower. The advantage of this approach is that the luminosity is kept constant throughout the fill since the effectivity threshold that triggers a refill is higher than the LHCb delivered luminosity, see Figure 2.4. The

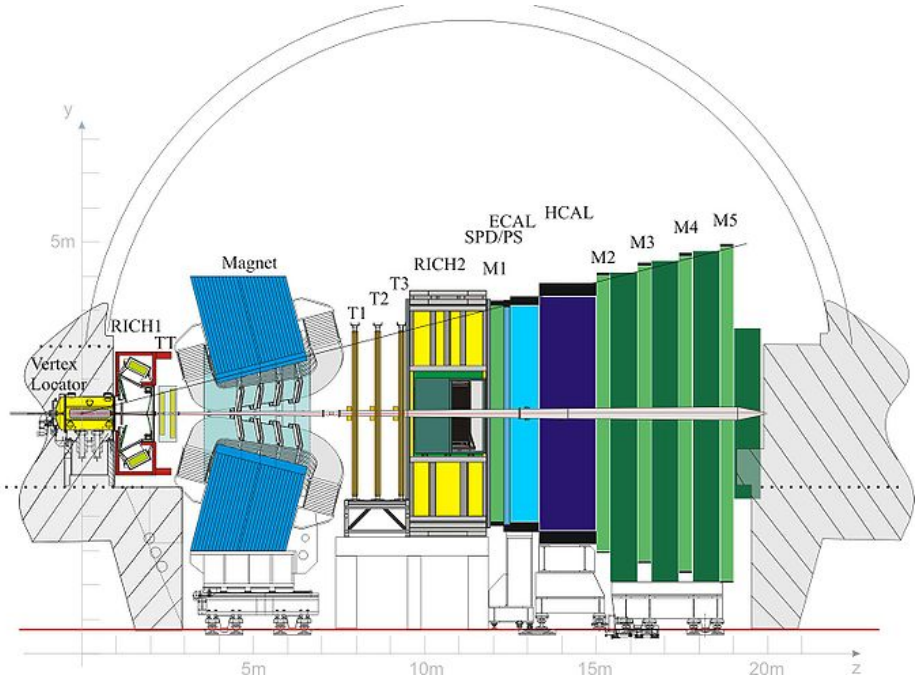

Figure 2.3: The geometry of the LHCb detector as viewed in the y-z plane cross-section. The individual sub-detectors are indicated.

2011 data-taking run has seen luminosity above the design specifications, consistently at $3 \times 10^{32}\ cm^{-2}s^{-1}$ [39].

The design of the detector was motivated by the chief area of physics it studies. The majority of the $b\bar{b}$ pairs are produced close to the beam-line as shown in Figure 2.5. The angular acceptance of $\sim 4\%$ of the 4π solid angle allows for detection of $\sim 40\%$ of $b\bar{b}$ produced. The Vertex Locator along with very good tracking provide excellent time resolution necessary for flavour physics. Particle identification using Cherenkov detectors allows for excellent $\pi - K$ separation which is vital in many channels.

The LHCb detector consists of (starting from the interaction point) Vertex Locator (VELO), Ring Imaging Cherenkov Detectors (RICH1 and RICH2), Tracker Turicensis (TT), Magnet, Inner Tracker (IT), Outer Tracker (OT), Scintillator Pad Detector (SPD), Pre-Shower Detector (PS), Electromagnetic Calorimeter (ECAL), Hadronic Calorimeter (HCAL) and Muon Chambers (M1 - M5). The Trigger and Software is described in this chapter as well.

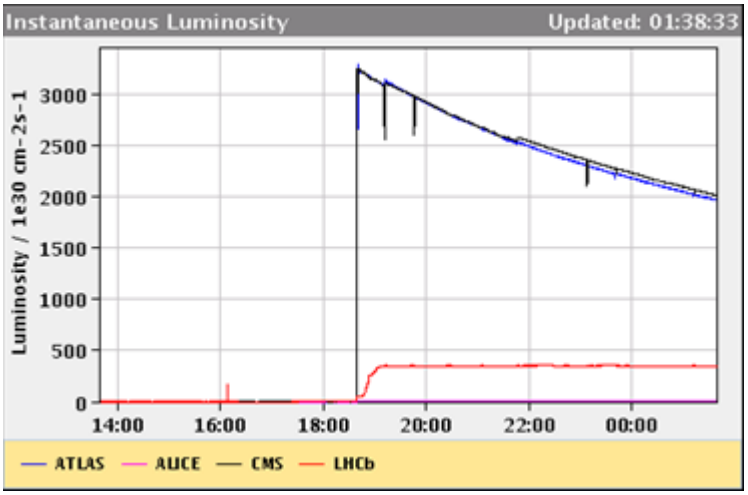

Figure 2.4: Instantaneous luminosity at ATLAS (blue), CMS (black) and LHCb (red). Shows that LHCb luminosity remains constant throughout the fill thanks to luminosity levelling. The turn on shape of the luminosity for LHCb is again due to the levelling. First the beams are completely misaligned and the levelling algorithm moves them closer together until the desired instantaneous luminosity is achieved. Adopted from [41]

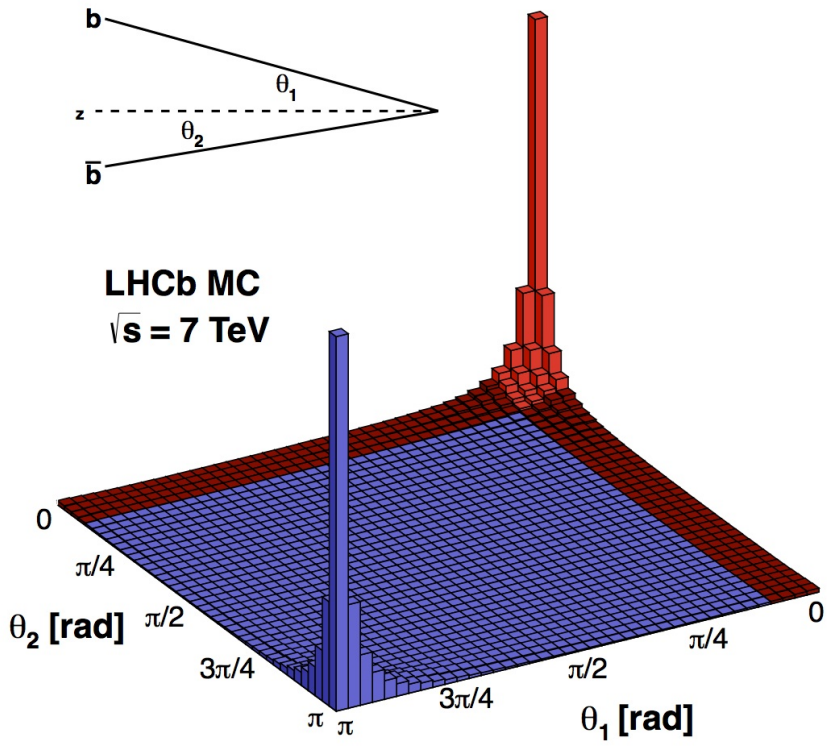

Figure 2.5: The angular distribution of $b\bar{b}$ pair production and LHCb acceptance in red. Adopted from [42]

2.3 Vertex Locator

The Vertex Locator (VELO) is a silicon strip detector that encloses the interaction point. When fully closed, the VELO is located $8.2\ mm$ from the interaction point. Due to the proximity to the beam line, the VELO is evacuated - it shares the beam-pipe vacuum. The fact that LHCb surrounds an injection point for the LHC required the VELO to be retracted out of position at $30\,mm$ while the injection takes place. The geometry takes advantage of the narrow phase-space characteristics of $b\bar{b}$ pair production and consists of 42 sensor modules with alternating semicircle-shaped radial (R) and azimuthal (ϕ) silicon micro-strip detectors consisting of 2048 readout channels each. There are also four R modules further upstream (VETO) to roughly determine the number of pp interactions in the event. The full length of the VELO is 600 mm.

The acceptance of the VELO is $2 < \eta < 5$ where η is the pseudo-rapidity and is defined as

$$\eta = \frac{1}{2} ln \left(\frac{|p| + p_z}{|p| - p_z} \right) \tag{2.2}$$

Furthermore, a track inside the angular acceptance has to cross at least 3 VELO sensors, this requires sensors to be spaced by $5\ cm$ or $3.5\ cm$ near the interaction point to account for the possibility of missing hits on one sensor. The full angular acceptance was ensured by overlapping sensors in the x-y plane when the VELO is closed, to this effect the two sides of the VELO are shifted with respect to each other by $1.5\ cm$ as shown on Figure 2.6.

2.3.1 RF foil

The Vertex Locator is shielded from the powerful RF field emitted by the beam by means of an aluminium corrugated foil that encloses the sensors in a Faraday cage. The foil rests $2\ mm$ from the sensors which are under potential difference of $400V$. The foil alignment is checked using beam-gas material interactions, which are used to map the VELO and the RF foil when in operation [44].

2.3.2 Sensors

The sensor modules are pairs of silicon micro-strip detectors, each containing both the R sensor from one side and the ϕ sensor from the other. The sensors have a thickness of $300\ \mu m$ and a radius of $42\ mm$ with 2048 readout channels. The

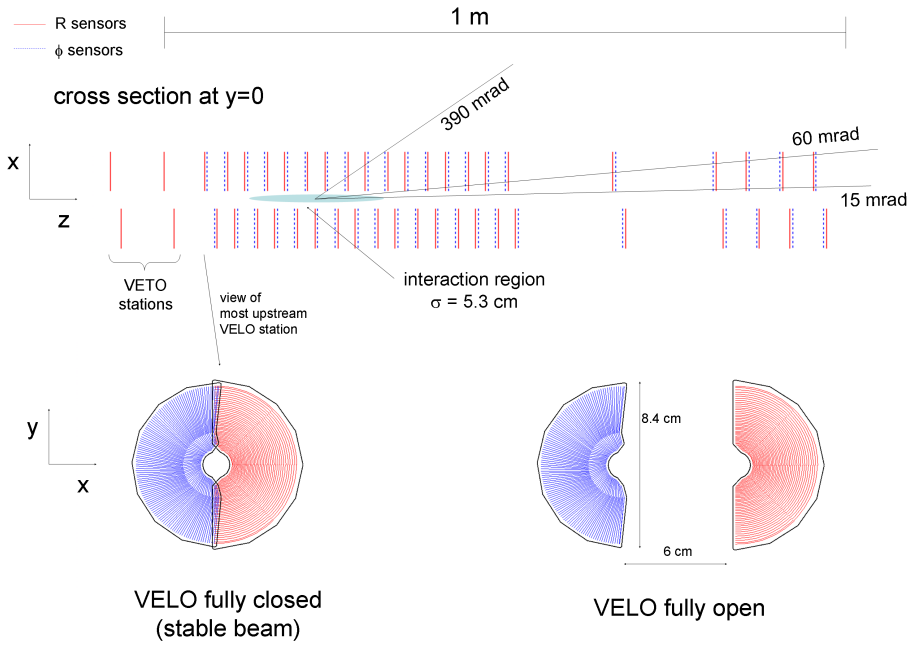

Figure 2.6: The positioning of VELO sensor modules with R (red) and ϕ sensors (blue). Shows both retracted and closed positions. Also shows 4 pile-up sensors downstream. [43]

R sensor is subdivided into 4 sectors and measures the transverse distance from the beam-line (where transverse means x and y coordinate added in quadrature). The ϕ sensor detects the azimuthal angle around the beam-line and is subdivided into inner and outer region to better deal with large occupancies and to prevent large differences between inner and outer channel widths. The ϕ sensors are skewed to improve pattern recognition with successive strips being skewed in different directions. Cylindrical polar geometry was preferred thanks to faster reconstruction of tracks and vertices compared to a Cartesian coordinate scheme. Together the sensors can provide complete 3 dimensional position for hits. The layout of the sensors can be seen in Figure 2.7.

2.3.3 VELO/Tracking Performance

The VELO uses analogue readout electronics which allows for resolution better than digital equivalent (resolution smaller than the individual strip size). The single-hit resolution is a comparison between the intercept of a reconstructed track

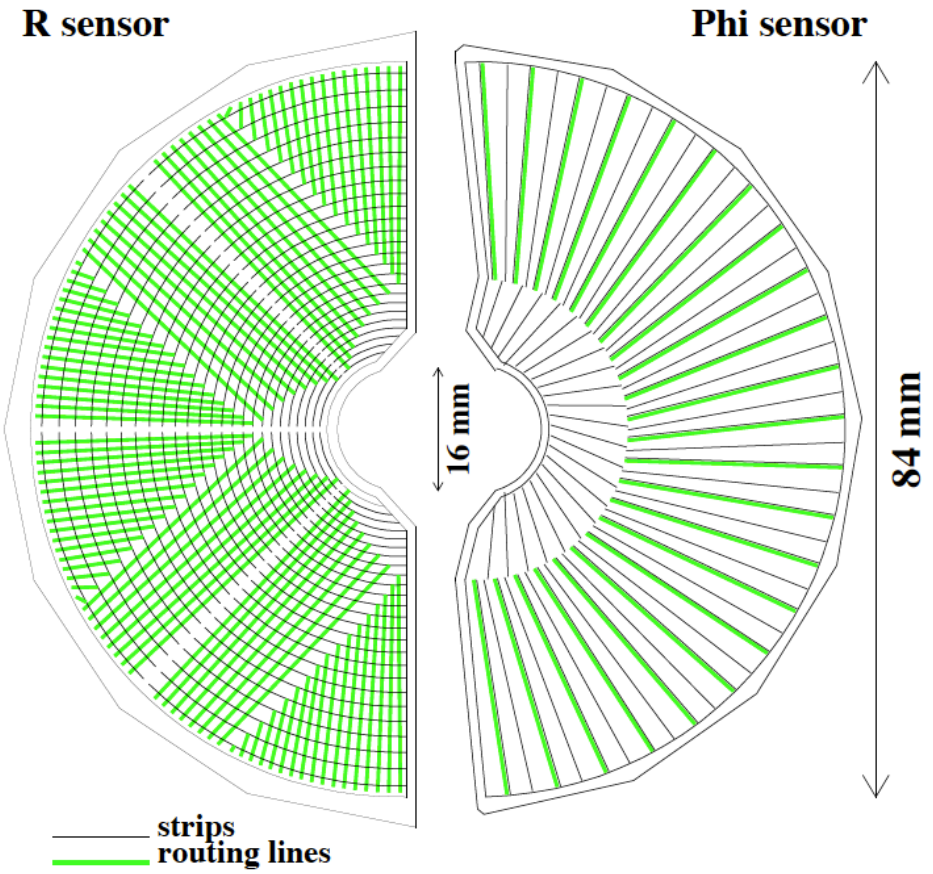

Figure 2.7: Scheme of R (Left) and ϕ (Right) sensors with readout channels [43].

with the sensor and the actual measurement the sensor provided. This resolution is of the order of $1 - 10\ \mu m$ depending on charge sharing between adjacent VELO clusters and on angle of incidence of the track on the sensor. The resolution for a typical 40-track Primary Vertex is $\sim\ 10\ \mu m$ in the x-y plane and $\sim\ 50\ \mu m$ in the z-axis. The distance of the track from the Primary Vertex is generally called the Impact Parameter (IP). Its resolution in LHCb is $\sim\ \ 20\ \mu m$ for a typical track with $p \sim 1 GeV/c$, see Figure 2.8.

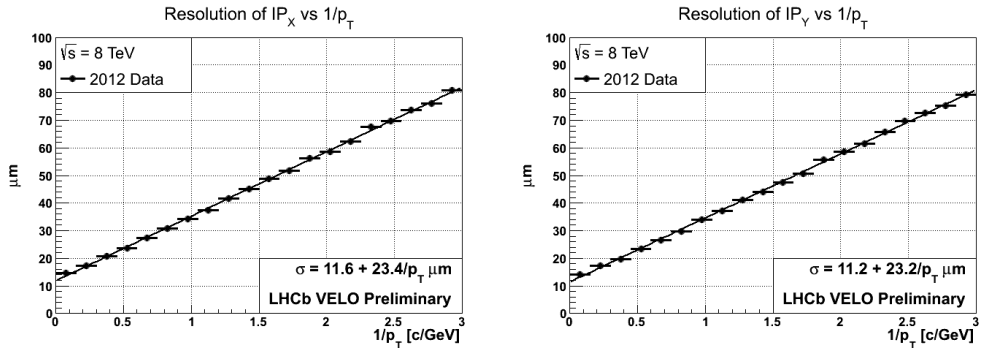

Figure 2.8: The Impact Parameter resolution of VELO depending on transverse momentum of the particle. Resolution in x axis (Left) and in y axis (Right) shown. [45]

2.4 Ring Imaging Cherenkov Detectors

The Ring Cherenkov Imagining Detectors (RICH) are a pair of Cherenkov detectors used for particle identification, especially $\pi - K$ separation. The scheme of these is shown in Figure 2.9. The principle of Cherenkov radiation is that particles travelling through a medium faster than the local speed of light emit a cone of light with incident angle governed by eq. 2.3 where n is the refraction index of the medium, c is the speed of light and v is the speed of the particle

$$\theta_c = \frac{c}{nv}. \tag{2.3}$$

The RICH 1 is located immediately downstream from the Vertex Locator. It consists of two chambers filled with an aerogel and the C_4F_{10} gas Cherenkov scintilation media[a] and a set of mirrors that reflect the scintillation light to Hybrid Photon Detectors (HPD) which are outside the LHCb acceptance and do not interfere with the detected particles. This design was motivated by tight material budget inside the LHCb acceptance cone and heavy supports needed to suspend the HPD arrays as well as heavy shielding from the nearby magnet. The lower angular acceptance of RICH 1 is $25\ mrad$ due to the beampipe, the higher acceptance is $300(250)\ mrad$ in the horizontal (vertical) plane and the momentum acceptance is $1 - 60\ MeV$.

The RICH 2 has a larger but similar design, filled with CF_4 and is located downstream from the magnet and the Inner Tracker. The angular acceptance of

[a]Desired properties are low speed of light in the medium (refractive index) to promote Cherenkov radiation and high interaction length to not cause the passing particles to decay.

RICH 2 is $15-100\ mrad$ in the horizontal and $15-120\ mrad$ in the vertical plane and the momentum acceptance is $\sim 15-100 MeV$. This is due to several limitations such as material budget requiring HPDs outside the acceptance, secondary mirrors to reduce z-length. The HPDs are also shielded from the nearby magnet [40].

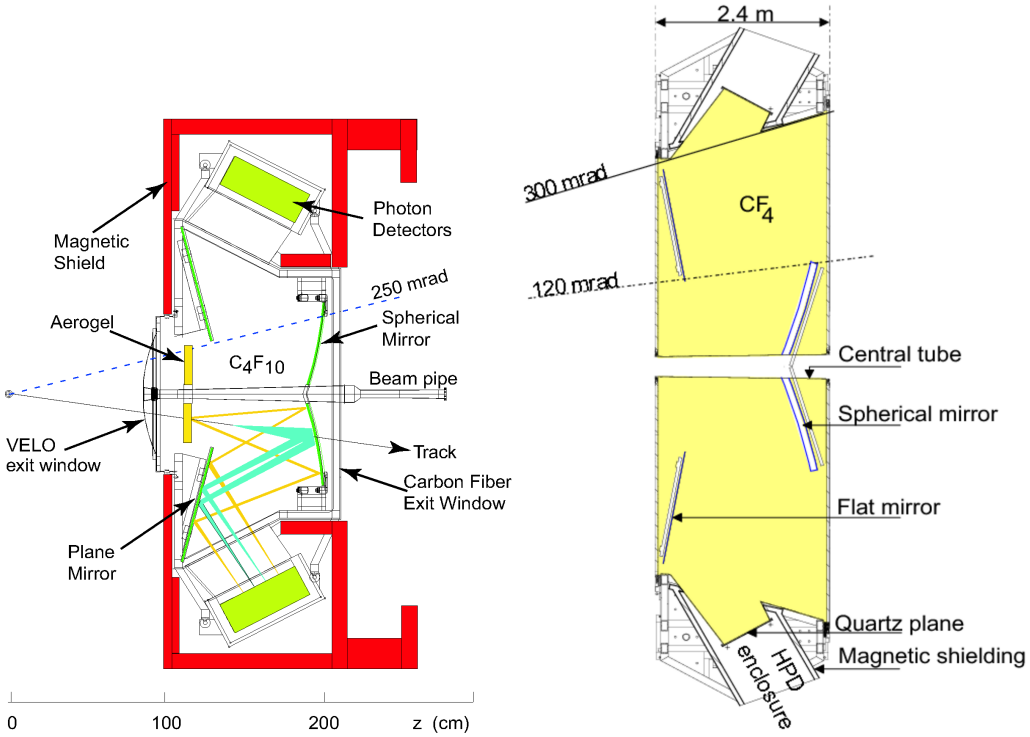

Figure 2.9: Scheme of RICH 1 in a y-axis direction (Left) and RICH 2 in x-axis direction (Right) [43].

The HPDs used in both detectors are vacuum photoelectron detectors using silicon strips and $20\ keV$ acceleration potential.

Together the RICH detectors provide particle identification when combined with momentum information measured by the tracking. The system also uses a neural network to provide a more comprehensive discriminator for particle identification. The kaon identification efficiency is $\sim 95\%$ with π mis-ID fraction of $\sim 10\%$ [43]. Figure 2.10 shows the dependence of Cherenkov angle on momentum for different types of particles.

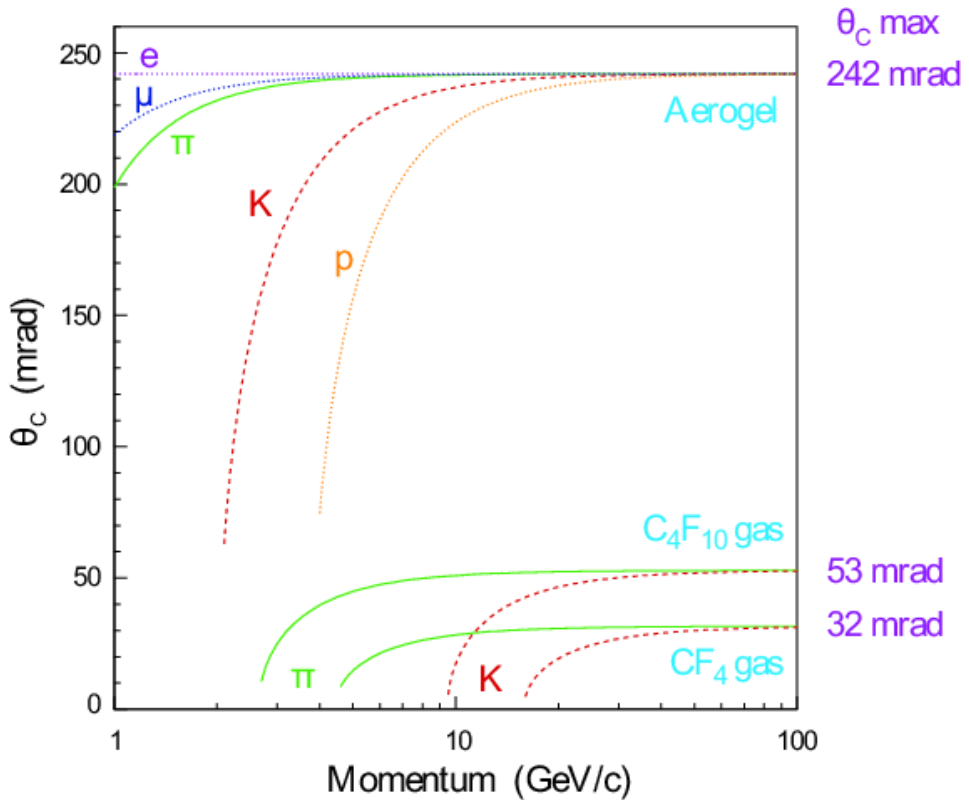

Figure 2.10: A plot of Cherenkov angle depending on the particle momentum for different long-lived particles. The plot shows Aerogel, CF_4 and C_4F_{10} gases as mediums [43].

2.5 Magnet

The LHCb uses a warm magnet shown in Figure 2.11 which provides a magnetic field for momentum measurement using the tracking stations in the angular acceptance of $250\ mrad$ vertically and $300\ mrad$ horizontally. The motivation for a warm magnet were economic and construction reasons [40]. The magnet consists of two coils aligned in the x-z plane and angled at $45°$ in the y-z plane producing B field mostly in the y direction making the horizontal plane the bending plane (see Figure 2.12). The coil has a nominal current of $5.85\ kA$ and can be switched so that the polarity of the magnet can be reversed (polarities are known as MagDown $B_y < 0$ and MagUp $B_y > 0$). The nominal path-integrated magnetic field is $4\ Tm$ [43].

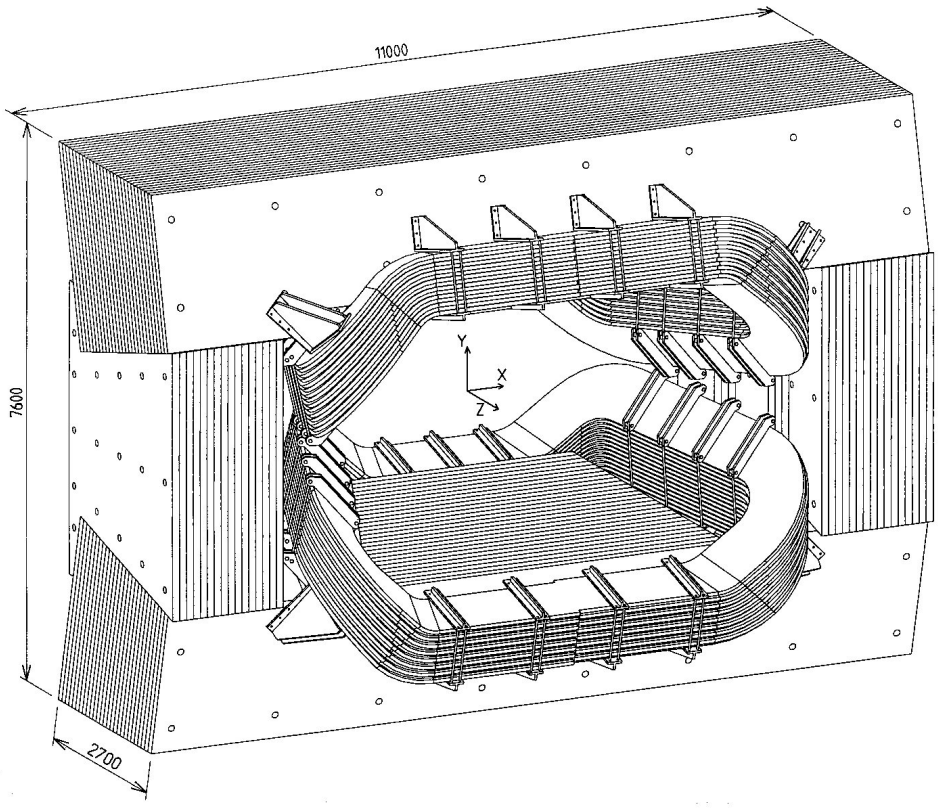

Figure 2.11: The LHCb magnet. Dimensions are in mm. [40]

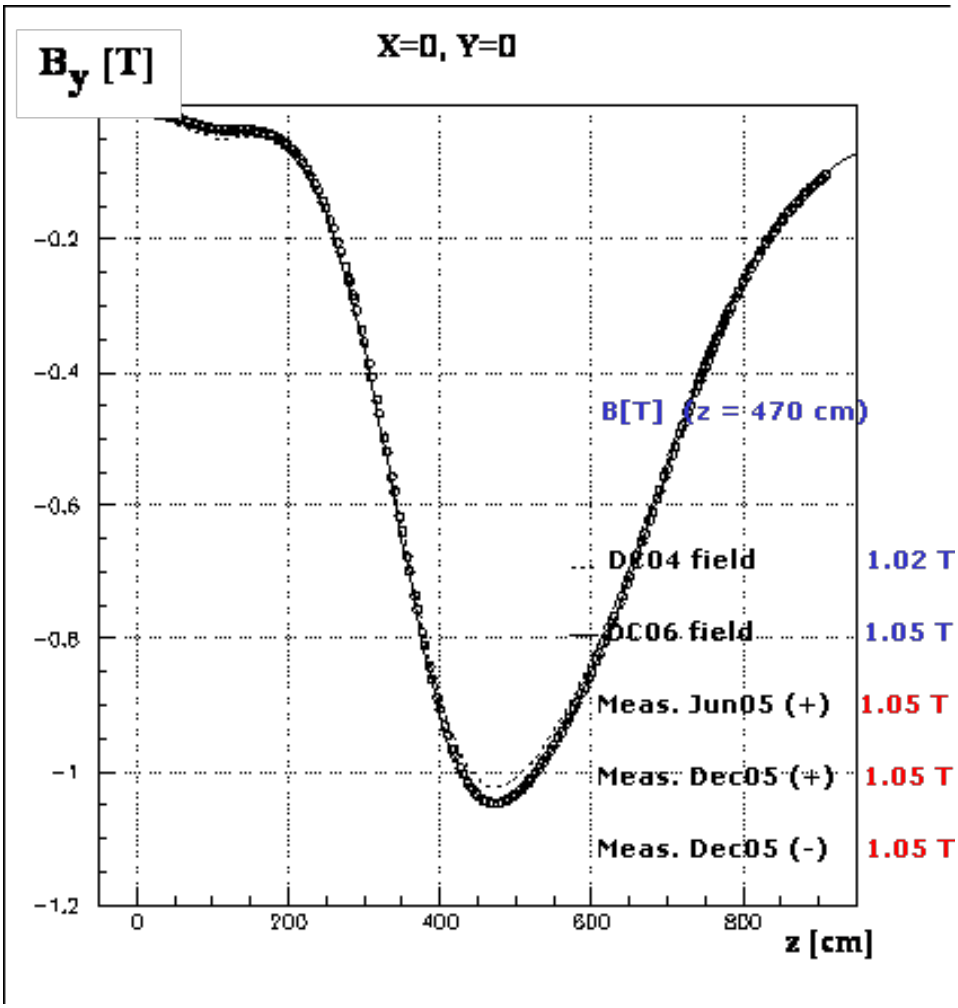

Figure 2.12: Magnetic field in T as a function of z-distance along the $x = y = 0$ axis ($x = y = z = 0$ is the Interaction Point) for MagDown polarity [43].

2.6 Tracking

The tracking in the LHCb experiment comprises of several sections: the VELO, the Silicon Tracker (ST) and the Outer Tracker (OT). The Silicon Tracker consists of the Tracker Turicensis (renamed after Trigger Tracker became a misnomer) which is located upstream from the Magnet and the Inner Tracker which comprises the inner part of the three tracking stations downstream from the Magnet. The locations of the individual tracking stations are shown in Figure 2.3.

2.6.1 Silicon Tracker

The Silicon Tracker has two main parts, Tracker Turicensis and the Inner Tracker. They both utilise silicon micro-strip technology with strip pitch of $200\ \mu m$ to detect particle hits. The TT is upstream from the Magnet and covers the entire LHCb acceptance with $150\,cm$ width and $130\,cm$ height. It consists of four planes of silicon strips separated by $30\ cm$ which are alternatingly skewed by a stereo angle $\pm 5^{\circ}$ as shown in Figure 2.13. The individual strips have a thickness of $500\ \mu m$, dimensions of $10 \times 10\ cm$ and carry 512 readout channels.

The IT is located in the centre of the three tracking stations downstream from the magnet and has four sets of seven sensors arranged around the beampipe in the region of high occupancy as seen in Figure 2.14. Each sensor carries 384 readout channels. Adjacent ST strips within the same detection plane are staggered in the z and x planes to help eliminate acceptance gaps.

2.6.2 Outer Tracker

The Outer tracker is located in the three tracking stations T1-T3 downstream from the Magnet, around the Inner Tracker. With the IT, the OT completes the tracking stations as shown in Figure 2.15. It consists of drift-time detectors in the form of straw tubes filled with a mixture of Argon (70%) and CO_2 (30%) to guarantee a fast drift time $t_d < 50\ ns$ and a good drift coordinate resolution of $200\ \mu m$. Each tracking stations consists of four layers of the OT arranged with a skew of $\pm 5^{\circ}$ in the third and fourth layer. The arrangement of straw tubes in a layer is shown in Figure 2.16. The signal is read out from the ends of the tubes.

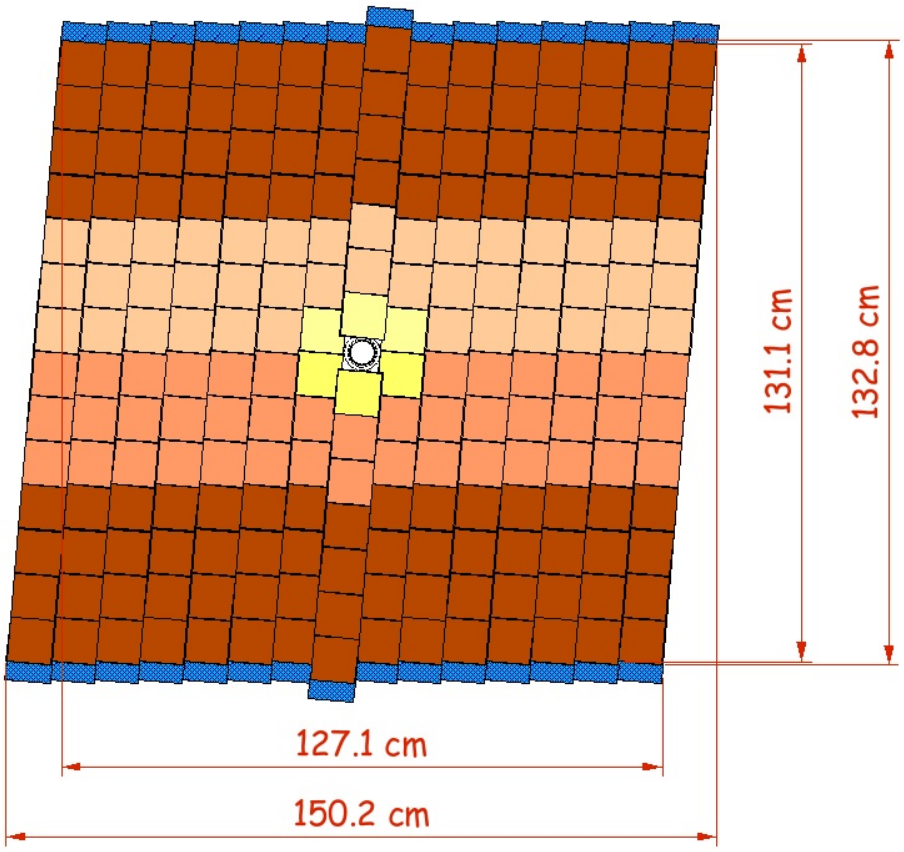

Figure 2.13: The Tracker Turicensis plane with a 5° skew. The three different colours (red, orange, yellow) indicate three sectors the TT is divided into (M,L,K) from the inside out [43].

2.6.3 LHCb Tracking

Track reconstruction starts with hits in the VELO which are used to build so called "VELO-seeds", track candidates. Additionally there are seeds from tracking stations, T-seeds. This is because the magnetic field is weak in these segments so tracks reconstruct as straight lines. VELO seeds or T-seeds can be promoted to a long track if the position and gradient of a VELO seed and a T-seed match. Alternatively an algorithm picks a VELO seed and an associated hit in a tracking station based on a rough extrapolation of the trajectory. The algorithm will search for more hits in the tracking stations and after a sufficient number has been found, the track is promoted to a long track. If a T-seed has hits in TT but cannot be extrapolated into a long track, it remains a Downstream track. Similarly if a VELO seed cannot be associated with hits in tracking stations past TT, the track remains an Upstream

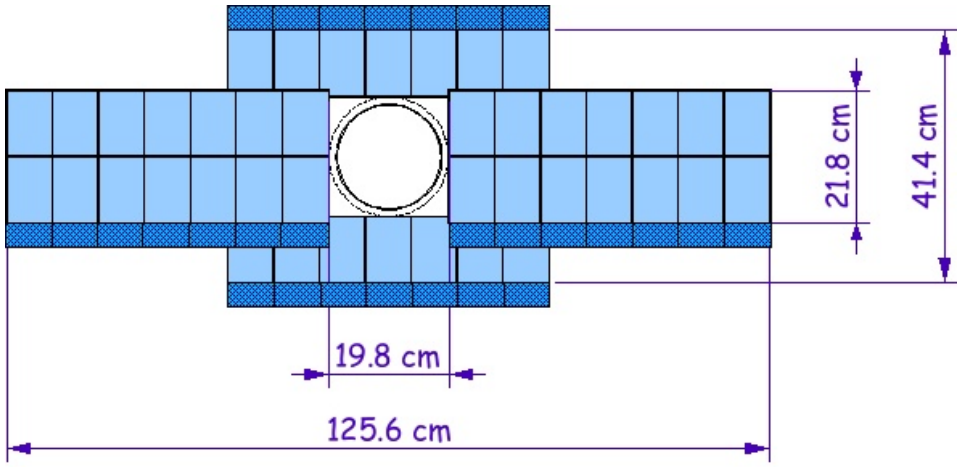

Figure 2.14: The Inner Tracker consisting of four sets of seven sensors arranged around the beam-pipe. Located in the centre of the three tracking stations T1-T3 [43].

track. Clone tracks are killed by comparing similar hits and then tracks are fitted using a Kalman filter that accesses the detector description to account for multiple scattering and energy loss due to material interaction. The χ^2 of the tracks is used to monitor the quality of the event reconstruction. The schema of the different track types can be seen in Figure 2.17.

2.6.4 Tracking performance

The best way to monitor the performance of the track reconstruction is by the efficiency of track finding and by the momentum resolution. Efficiency can be determined by a tag-and-probe technique with two-body decays such as $J/\psi \to \mu\mu$ where one daughter is well-reconstructed (tag) while the other is partially reconstructed (probe) and the efficiency expresses the probability of matching the probe to the tag. The 2011 average datataking efficiency was $\sim 96\%$ which is in line with the design specifications [39].

The momentum resolution is important for determining the mass of mother particles as well as for correct particle identification. The average long track momentum resolution for $20\,GeV$ tracks is $\sim 0.5\%$ while for a $150\,GeV$ track the resolution is $\sim 1\%$ [43].

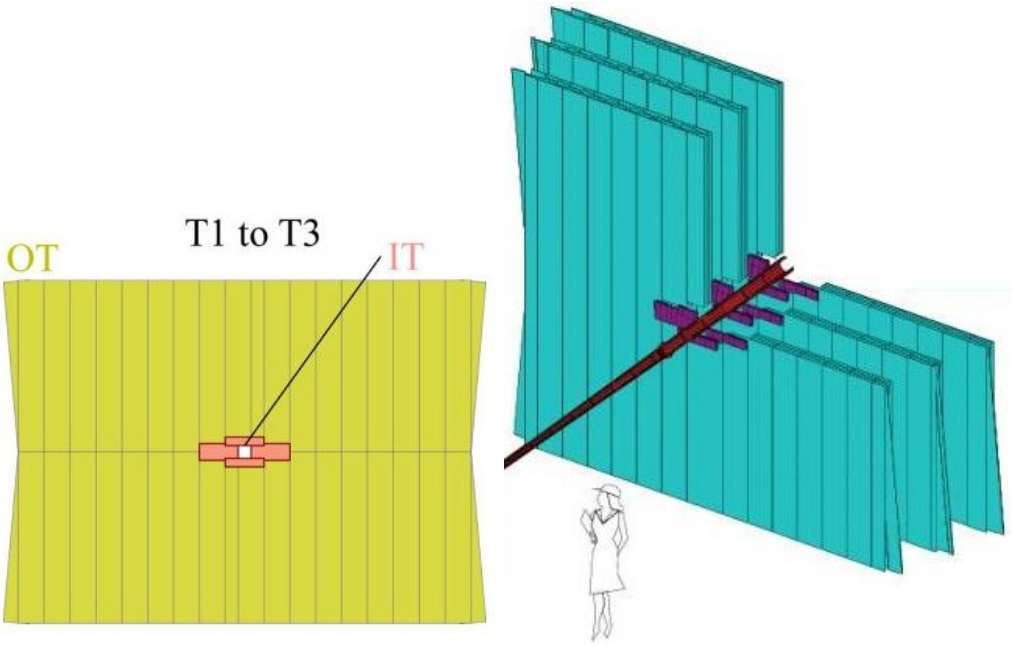

Figure 2.15: Arrangement of Inner Tracker and Outer Tracker in the Tracking Stations T1-T3 [43].

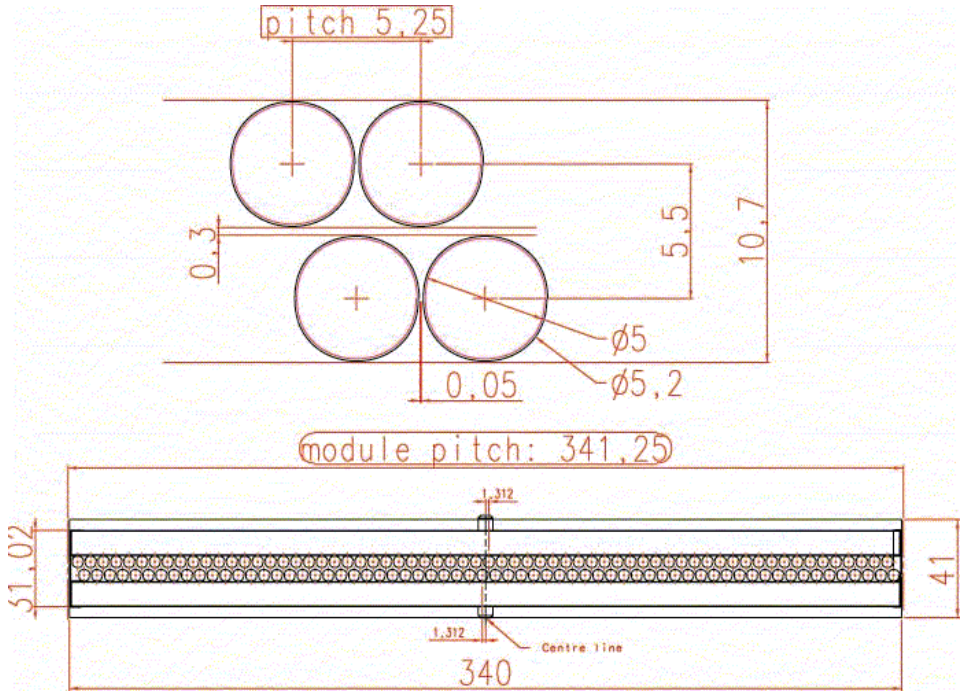

Figure 2.16: The Outer Tracker layer consisting of an arrangement of straw tubes. Measurements are in cm [40]

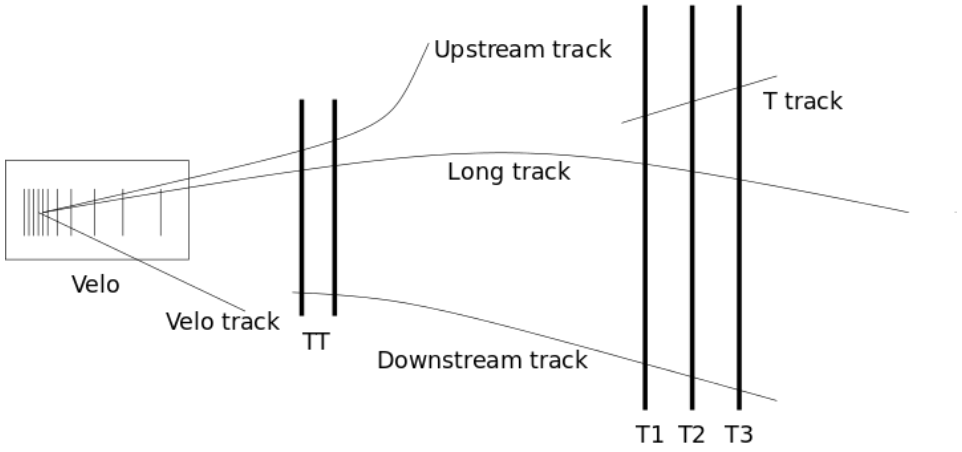

Figure 2.17: Different types of tracks observed in LHCb [43].

2.7 Calorimeters

The main purposes of the calorimeters are to differentiate between electrons, photons and hadrons, to provide a measurement of their energies (although, except for photons, the momentum resolution is generally better than the energy resolution), to help reconstruct neutral particles such as γ and π^0 as well as to provide fast triggering information, especially for electron triggers [40]. The Calorimeter covers the entire LHCb acceptance and consists of Scintillator Pad Detector (SPD), Pre-Shower Detector (PS), the Electromagnetic Calorimeter (ECAL) and the Hadronic Calorimeter (HCAL) and which can be seen in Figure 2.3.

The most immediate task of the Calorimeter is to identify electrons at the L0 trigger speed to veto 99% of the inelastic pp collisions and enrich the data with b events by a factor of 15. For this, the Calorimeter triggers on electrons and hadrons with high transverse energy E_T[b]. All components of the Calorimeter have variable cell granularities to account for higher occupancies near the beamline as seen in Figure 2.18. The ECAL is segmented into three regions with PS and SPD being segmented projectively, i.e. the size of the calorimeter elements scales with the distance from the interaction point. The HCAL has only two regions with much larger granularity compared to the ECAL because of the large size and energy of hadronic showers.

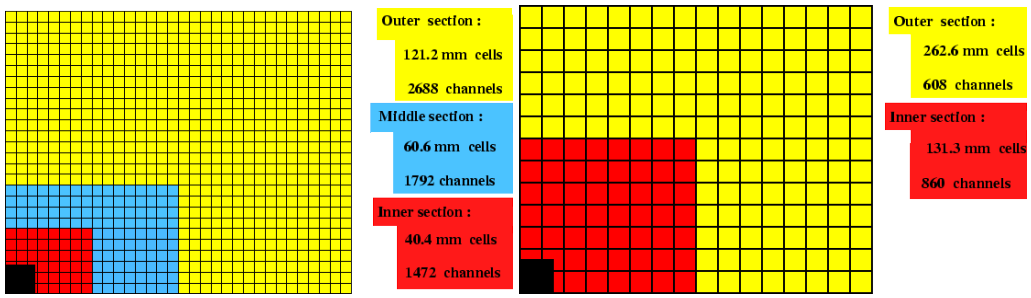

Figure 2.18: Calorimeter schemes indicating the sections with different granularities for ECAL and PS/SPD (Left) and for the HCAL (Right). One quadrant of the Calorimeter is shown, the rest are symmetric. The black region is the beampipe region not in the Calorimeter acceptance [43].

All Calorimeter sections use photo multiplier tubes (PMT) which collect scintillation photons from the showering particles using wavelength shifting fi-

[b]Transverse energy is defined as $E_T = \sqrt{E_x^2 + E_y^2}$. Due to the rough symmetry of the detector geometry and of the event production, we use transverse momentum p_T and transverse energy E_T rather than the x and y components.

bres. The PMT signal is then used in the trigger and for further online and offline analysis.

2.7.1 Scintillator Pad Detector and Pre-Shower Detector

The chief purpose of the SPD and the PS Detector is to separate photons from neutral hadrons such as π^0. The SPD and the PS are almost identical, $15\ mm$ thick, high-granularity scintillator pads with a $15\ mm$ thick lead (Pb) converter placed in between. They are also segmented in the same way as outlined earlier with SPD being projectively smaller than the PS which is smaller than the ECAL etc. The SPD registers hits from charged particles, which identifies projected energy deposits that did not originate from neutral particles (electron-pion separation) and also can be used as a veto due to high occupancy. The PS allows for separation of electromagnetic showers in the z-direction and helps discriminate between charged and neutral pions based on the combined shape of the shower in PS and ECAL. The electron identification efficiency is $\sim 95\%$ while the π^0 mis-ID rate is $< 5\%$ from the Calorimeter alone. This can be refined with inclusion of RICH information [43].

2.7.2 Electromagnetic Calorimeter

The ECAL is segmented into three sections due to varying occupancies depending on distance from the beamline. The calorimeter is composed of scintillator pads separated by layers of lead both to promote showering and act as an energy absorber. The lead layer is $2\ mm$ thick with the scintillator pads made of $4\ mm$ thick polystyrene. Each module contains 66 scintillator pads. The inner acceptance of the ECAL is $25\ mrad$, limited by the high radiation region around the beampipe. The relative energy resolution of the ECAL is $(8 - 10/\sqrt{E} \pm 0.9)\%$ where E is in GeV [43].

2.7.3 Hadron Calorimeter

The HCAL is similar to the ECAL in composition with modules made of polystyrene scintillator and iron (Fe) for absorber in an alternating fashion. The orientation of the scintillators is parallel to the particle flow as shown on 2.19. Each module is composed of iron plates $10\ mm$ thick with $3\ mm$ thick scintillator pads slotted in. The length of the HCAL module corresponds to 5.6 hadronic interaction lengths in steel and the robustness of the construction corresponds to the size of

the hadronic showers it has to contain. The relative energy resolution of the HCAL is $(69/\sqrt{E} \pm 9)\%$ with E in GeV [43].

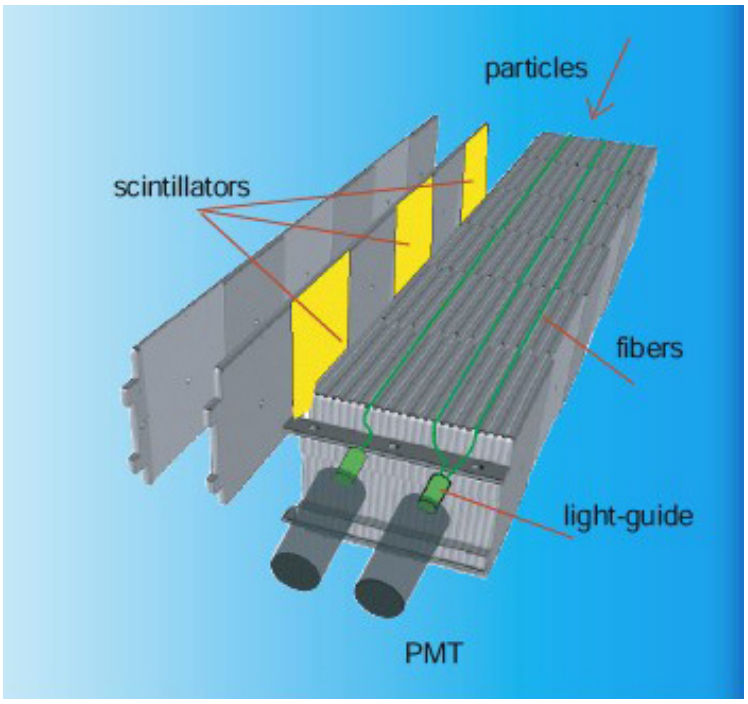

Figure 2.19: The implementation of a HCAL module shows the unusual orientation with respect to the particle flow. The absorber is iron and the scintillator is polystyrene [43].

2.8 Muon Chambers

The Muon Chambers (see Figure 2.20 are of great importance to a heavy flavour experiment because muons are present in many flavour hadron decays of interest. The presence of muons in a decay generally correlates with a much reduced background compared to hadronic decays making the events experimentally cleaner. A high-p_T muon trigger helps eliminate QCD background from the primary interaction and enriches the data with b and c events - that is to say events with b and c quarks have an increased probability of producing energetic muons than events with only light flavours. This means the muon chamber is used for triggering as well as offline analysis [43].

The Muon system at LHCb consists of five chambers M1-M5 where M1 is located upstream of the Calorimeter and the M2-M5 are downstream at the end of

the detector as shown in Figure 2.3. This separation results in an improved transverse momentum resolution important for the muon trigger. The angular acceptance of the muon Chambers is $16 - 258\ mrad$ in the vertical and $20 - 306\ mrad$ in the horizontal plane. The muon stations are separated by $80\ cm$ thick iron absorber sections to select highly penetrating muons and to get a measurement of the penetrating energy. Muons of momentum $\sim 5\ GeV/c$ will be able to reach the 5th muon station. The muon stations increase in size projectively to keep the angular acceptance. The M1-M3 stations have good x-resolution thanks to a high granularity of sensors to get a good measurement of the particle momentum, especially in the bending plane. They are divided into four regions according to radial distance from the beamline to account for varying occupancy. The M4-M5 stations are used mainly to help select highly penetrating muons. The muon stations use Multi-Wire Proportional Chambers (MWPC) except for central regions of M1 which uses triple Gas Electron Multiplier (GEM) due to the high occupancy and serious radiation damage in the region.

High efficiency for muon identification and low muon mis-ID rate[c] is essential for rare decays with muons (such as $B_s \to \mu^+\mu^-$). The muon identification extrapolates good tracks from the tracking system towards the muon stations. The track is identified as a muon if sufficient hits are found in a region around the extrapolated track. This region is parametrized using the track momentum and is different for the four regions of the muon chambers to optimize the efficiency and reduce the mistag rate. The efficiency of the muon system is studied using the $J/\psi \to \mu^+\mu^-$ decay while the mistag rate is determined using $\Lambda \to p\pi^-$ decays and two-body D^0 decays. The muon tag efficiency depends weakly on the momentum and transverse momentum and is $> 95\%$ for particles of $p_T > 1.0\ GeV$ and $p \sim 10\ GeV$ [43].

There are two reasons for hadron to muon mis-ID. A hadron track could be coincidental with muon hits in the muon chambers or the hadron can actually decay in flight into a muon which will most likely lead to the association of the muon hits with the hadron track. The mis-ID of protons is solely due to the first reason and is well below 1% for tracks of sufficient p_T and p. The kaon/pion misID occurs for both reasons and the mis-ID rate is $< 1\%$ for particles of $\sim 20\ GeV$. The muon identification efficiency and the hadron mis-ID depends on the momentum and transverse momentum and in fact drops with increasing p and p_T because the

[c]Mis-ID or mistag rate is the probability that a wrong particle is incorrectly identified/tagged (false positive rate). Compare with ID/tagging efficiency which is the probability that the corrent particle is tagged/identified correctly.

region of interest for matching muon hits to an extrapolated track narrows with increasing p and p_T.

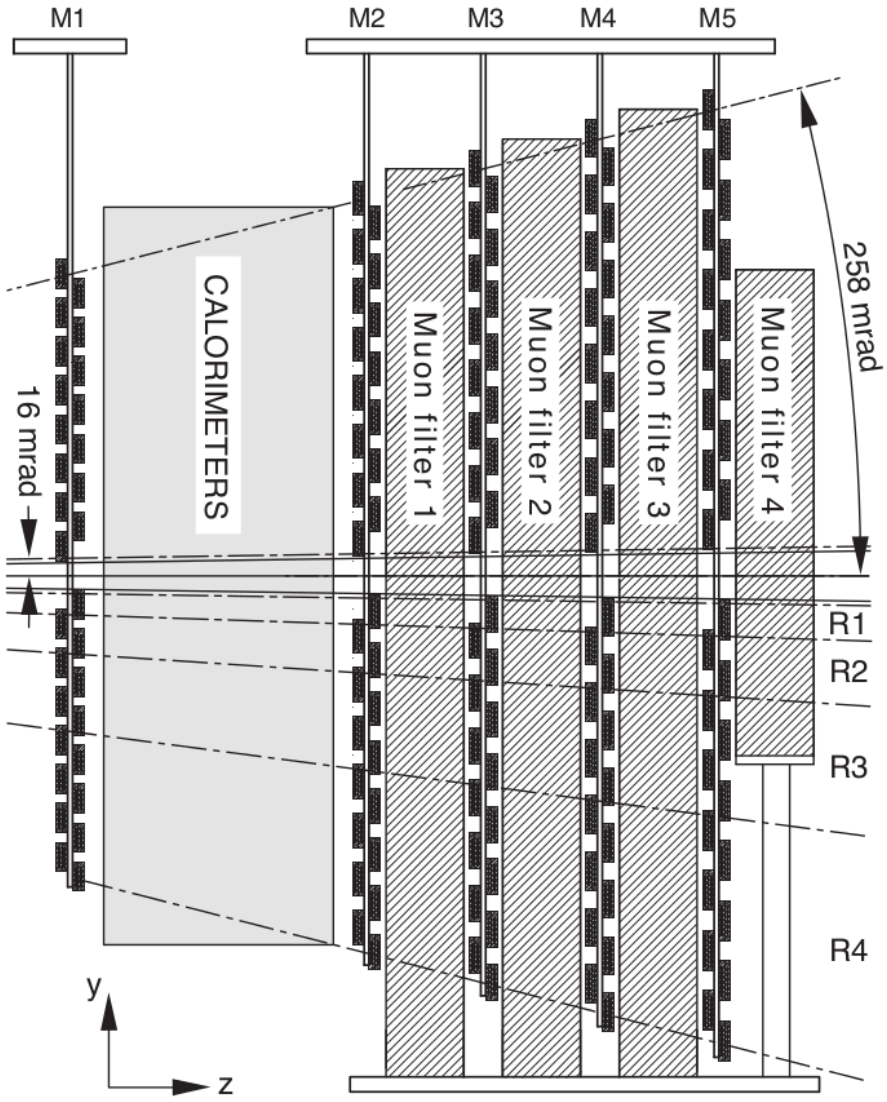

Figure 2.20: Side view of the Muon Chambers. [40]

2.9 LHCb Trigger

The design luminosity of $2 \times 10^{32} cm^{-2} s^{-1}$ (about a factor 40 less compared to ATLAS or CMS) results in about $10\,MHz$ rate of events with at least two charged tracks with enough hits in the VELO and Tracking to be reconstructed into long tracks [43]. The purpose of the trigger is to reduce this rate to $\sim 3\ kHz$ which is

written to tape for offline analysis while enriching the selected data with events of high interest (see Figure 2.21). Within this, $300\ Hz$ has been allocated to charm physics and the charm production at LHCb is factor ~ 10 larger than b production[d]. The trigger is separated into a custom-electronics hardware L0 trigger operating synchronously with collisions and a software High Level Trigger run on a processor farm. The original design also included a hardware L1 trigger which has since been absorbed into the other two.

Functionally there are three eventualities with a signal chain present (i.e. not pure combinatoric background) that can result in a trigger accepting the event:

- Trigger On Signal (TOS)
- Trigger Independent of Signal (TIS)
- Trigger On Both (TOB)

The TOS is the case where the signal chain in the event has been recognized by the trigger which fired.

In the TIS case, the signal chain is present but something else in the event caused the trigger to fire. This should result in data that is unbiased by trigger decisions provided that the cause of the trigger firing is independent of the signal chain.

The TOB case results from both the signal chain and some other part of the event causing the trigger to fire. The TOB events are notoriously difficult to analyse due to correlations and provided the number of TOB events is small, they are usually removed from the dataset and neglected.

2.9.1 L0

The L0 is an extremely fast trigger implemented on custom-built hardware aimed at fast rejection of uninteresting events. It reduces the rate of the events from the collision rate to less than $1.1\ MHz$[e]. The L0 is composed of the L0 Calorimeter trigger, the L0 Muon trigger and L0 Pileup. The Calorimeter and Muon L0 triggers select events with large transverse momentum and energy, which are common characteristics in many heavy flavour topologies. Specifically the Calorimeter

[d] This means that the charm trigger must be highly selective, and the offline selection for charm analyses is generally only marginally tighter than what is used in the trigger [46].

[e] This is the rate at which the full detector can be read out [43].

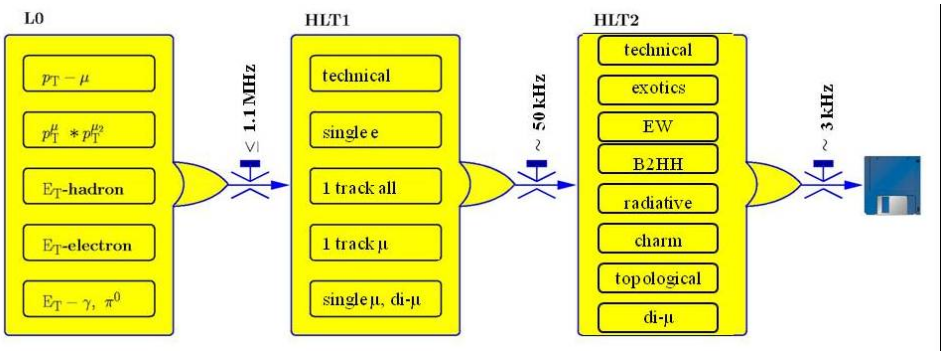

Figure 2.21: Diagram showing the trigger implementation at LHCb. Adapted from [43]

trigger combines information from all sections of the Calorimeter, the transverse energy (E_T) sum in HCAL is used to veto events with no visible interactions and the SPD count is used to determine track multiplicity. The Muon trigger selects one or two muon tracks with highest p_T in each quadrant. The Pileup estimates the overall number of pp interactions (the number of Primary Vertices) in the event. The L0 Decision Unit (L0DU) collates this information and combines it into a single L0 Decision. The time between the collision and an L0 Decision being accepted in the Front End (FE) electronics is $4\ \mu s$ including time of flight of particles, cable delay, and delays in FE electronics [43].

2.9.2 High Level Trigger

The High Level Trigger (HLT) is a C++ built application running on a filter farm of several thousand CPU nodes. Divided into two parts the HLT1 and HLT2 it reduces the event rate from $1.1\,MHz$ to $3\,kHz$. It is completely software based, with configuration facilitated by the use of Trigger Configuration Keys (TCK) which allows for modularity and for complete rerunning of the HLT offline. This is also used in a deferred trigger (implemented in 2012) which writes a portion of the events which are not immediately processed by the HLT to disk. These events are processed by the HLT during time between individual fills. The HLT is split into HLT1 which is used to confirm L0 decisions and partially reconstruct tracks and HLT2 which contains more complicated topological trigger conditions and dedicated settings for for individual analyses.

HLT1

The main feature of HLT1 is partial event reconstruction with full VELO track reconstruction. The VELO tracks are used to find vertices with at least 5 tracks originating from them and such vertices within $300\,mm$ around the bunch crossing point are considered primary vertices. Cuts are applied on the quality of VELO tracks and signal-like VELO tracks are associated with track hits. HLT1 also has a Muon trigger where VELO tracks are extrapolated to M3 and hits are searched for in a window of interest around the extrapolation. The track is then flagged as a muon if there is at least one extra hit in M2, M4 and M5. The track is then reconstructed using the VELO seed, the Tracking and potential Muon hits and the momentum and the Impact Parameter (IP) are determined. The HLT1 lines used in this analysis are discussed in section 3.3.

HLT2

With the output of HLT1 low enough to allow for offline track reconstruction, the HTL2 uses a loose selection on momentum and on the IP of a track before categorising tracks as individual particles and using them to create common resonances (for example $K^0_S \to \pi^+\pi^-$). These are used for the reconstruction of decays and an invariant mass cut is generally applied. The HLT2 lines used for this analysis are discussed in section 3.3.

2.10 Reconstruction Software

LHCb uses several software packages to process data. The simulated (MC[f]) and real data are treated, as far as possible, identically. This generally involves a sequential processing of events where MC is produced using simulation packages and then digitised into detector hits. From there the same packages are used for reconstruction, triggering and offline analysis of both real data and digitised MC.

2.10.1 Simulation

LHCb uses the PYTHIA [47] [48] physics generator to simulate initial pp collisions with appropriate settings. The MC produced for 2011 analyses

[f]MC stands for Monte Carlo, it is a simulation method named after the famous Monte Carlo Casino because the method uses repeated random sampling and resembles gambling and recording results in a real casino.

used PYTHIA 6.0 written using FORTRAN but LHCb is now moving towards PYTHIA 8.0 which is implemented in C++. The heavy flavour products of collisions generated by PYTHIA are decayed using the EVTGEN package [49] which is described in appendix C. This is all facilitated by the LHCb package GAUSS [50] [51]. The creation of detector hits and material interactions including multiple scattering is performed using GEANT4 [52]. A good description of the detector including geometry and material is essential for a good match between MC and real data. In fact in the MC sample used in this analysis there is still a $\sim 10\%$ IP resolution discrepancy between LHCb MC and data which is thought to originate partly from an imperfect detector geometry description such as the VELO RF foil shape [53]. The digitised hits are processed using the LHCb package BOOLE [54] that simulates the detector response to the generated detector interactions, including the readout electronics and the L0 trigger. At this point the Raw Data output is of the same format as real data and can be processed by the same methods.

2.10.2 High Level Trigger

The HLT is facilitated using the MOORE [55] package. It is implemented fully using software which provides several advantages over a hybrid or hardware implementation. The modular configuration using Trigger Configuration Keys (TCK) allows for changing the trigger settings fairly easily, the trigger can be re-run on real data or MC offline allowing for lifetime bias corrections (see appendix B).

2.10.3 Reconstruction

The Raw Data is reconstructed using the BRUNEL [56] package to determine or fit for physical quantities such as vertices, momenta, particle identification probabilities, energies etc. The output of Brunel is a Data Summary Table (DST) containing all information about the event in the form of particles, tracks, vertices, etc. and is used for offline analysis.

2.10.4 Stripping and Offline Selection - DaVinci

The offline analysis in LHCb uses the DAVINCI [57] package to preselect signal candidates from full data using a series of pre-configured selections called stripping with loose cuts to reduce the dataset to a manageable level. Each individual analysis will generally have their own stripping selection for the production

of their dataset and the stripping is performed centrally using the LHC Grid resources. The individual analyses will then use DaVinci to produce ROOT tuples and custom written tools to perform the analysis.

Chapter 3

Data Selection

3.1 Dataset Description

This analysis uses the 2011 LHCb dataset which has an integrated luminosity of $1fb^{-1}$. The D^0 candidates are reconstructed from $D^{\star\pm}$ decays where the $D^{\star\pm}$ originates from the primary vertex of the event. The good resolution of the primary vertex and the D^0 decay vertex provided by the VELO enables the LHCb to achieve a very good decay time resolution. This is one of the requirements for any probe into the charm mixing phenomenon[a]. The $D^{\star\pm}$ mother is required to decay into

$$\begin{aligned} D^{\star+} &\to D^0\pi_s^+ \\ D^{\star-} &\to \bar{D^0}\pi_s^- \end{aligned} \tag{3.1}$$

where the subscript $_s$ on the pion stands for "soft" due to the restricted phase-space of the decay limiting its momentum. The charge of the soft pion acts as a tag for the flavour of the produced D^0 meson.[b] The D^0 meson is then required to decay into

$$D^0 \to K_S\pi^+\pi^- \tag{3.2}$$

which is a self-conjugate three-body decay. This places extra importance on the tag of the D^0 as both meson and anti-meson decay into the same final state. On

[a] Given that charm mixing is expected to be $\mathcal{O}(1\%)$ this would mean a deviation from the mean D^0 decay time by $\mathcal{O}(10^{-15})$ s. Leveraging clever techniques enables the extraction of mixing with much poorer resolution than would be otherwise required for a direct measurement but the magnitude illustrates why fine decay time resolution is necessary.

[b] This is the common D^0 tag used in charm measurements, the nominal mistag rate in current experiments is $\sim 0.1\%$ [6], also see section 7.5.

the other hand, this simplifies the selection process as one treats both D^0 and $\bar{D}^0$ datasets simultaneously. The strange meson decays into two pions: $K_S \to \pi^+\pi^-$.

The $D^{\star\pm}$ production cross-section at LHCb is $677 \pm 74 \ \mu b$ [58] with the branching fraction of $D^{\star\pm} \to D^0\pi^\pm$ being $(67 \pm 0.5)\%$ [6] and the branching fraction for $D^0 \to K_S\pi^+\pi^-$ being $(2.83 \pm 0.20)\%$. This nominally yields $\sim 1.28 \times 10^{10}$ D^0 decays of interest produced in the 2011 run of the LHCb. The data is however selected in several stages to remove background. These include *trigger* which is run online during the detector operation before the data is saved to tape (see 2.9) and *stripping* which is run centrally on all LHCb data and which creates actual candidates from daughter tracks (see 2.10.4). The offline selection is undertaken using custom written C++ application with the use of ROOT libraries.

3.2 Monte Carlo description

The Monte Carlo simulation (MC) is produced centrally at LHCb to ensure the transparency and repeatability of data analyses. The MC is produced with conditions as close to real data as possible, see section 2.10.

Several different samples generatd using diferent models[c] are used at different points of the analysis. These are listed in table 3.1. All of the samples used were generated purely as signal, that is, every event generated contained the signal decay chain. However, as the sample is digitised and reconstructed, due to the reconstruction efficiency, some of the events were not reconstructed and because the trigger may misfire on combintoric events, some ghost events are thusly created

[c] A brief note on the models used:
The flat phase-space model is very useful in determining how phase-space is disturbed by various operations on the dataset, such as selection, but does not actually contain the phase-space information of the decay and thus cannot be used for more advanced purposes such as fit validation. For resonant MC, we used the BaBar 2010 model which is the newest model to date. The advantage of such MC is that it can be used to validate the fitter as it most closely approximates the phase-space of real data. In terms of production and amount of information simulated, we use simple toy, full toy and full simulation. Simple toy contains only yields generated in each bin separately using a given PDF. This is quick to do and can be generated by the fitter directly but potentially loses some information due to the binning of the PDF before the generation. The full toy generates full phase-space information along with the correct decay time according to the full amplitude model. This is much more precise than simple toy but much harder to perform and generally not done on the spot but produced centrally for the entire analysis. The full simulation is the most difficult to perform and is done centrally for the LHCb by the MC group. It contains the simulation of the whole detector. In terms of filtering, the techniques used were generation-level filtering which is easy to perform and requires very little added processing power but care must be taken such that the filtering does not remove events that would have been potentially accepted. Reconstruction-level filtering or "final"-filtering only saves those events which are signal and therefore achieves perfect density of events but the disadvantage is large amounts of additional processing power required.

and included in the final sample. No detector noise and random triggers are added arteficially to the sample.

Sample	number of events	post selection
1. Flat phase-space, gen-filtered	$5M$	$5.8k$
2. Resonant, mix., gen-filtered	$10M$	$11.6k$
3. Resonant, mix., final-filtered	$200k$	$25k$
4. Resonant, mix., simple-toy	$80M$	$80M$
5. Resonant, mix., full-toy	$100M$	$100M$

Table 3.1: List of Monte Carlo samples used in the analysis. "Gen-filtered" represents generation level filtering while "final-filtered" represents filtering done after full simulation of the event.

The Sample 1 is generated using a flat phase-space decay model for D^0 and has generator cuts applied (see appendix D) to boost statistics of the sample post selection. This sample was used to determine the effect of the selection process on the phase-space of the decay (see section 6.5).

The Sample 2 was generated using BaBar 2010 D^0 decay model [59] with mixing parameters set at $x_D = y_D = 1\%$. This sample was used to validate the fitters for the different methods. After selection was applied, it was determined that the retention rate was not high enough and more statistics were required.

The Sample 3 was produced with the same method as Sample 2 but additionally using filtering at the final stage of the selection guaranteeing that all the events in the sample pass the selection process. Due to some mis-implementation of the trigger, the sample retains only $\sim 12.5\%$ events after truth-matching is applied. This is due to $\sim 50\%$ contamination with downstream K_S candidates (see below) and due to a factor of ~ 4 reduction by trigger efficiency.

The Sample 4 is a toy sample generated in 16 CLEO bins (CLEO binning is a way of binning the phase-space to integrate out the strong phase, see sec. 6.2.1). The sample is a distribution of the D^0 decay time t selected independently in each CLEO bin i from the PDF described by eq 6.9. The central values of the yields in CLEO bins are chosen by forcing the yield divided by the time-integral of the eq. 6.9 to be constant across CLEO bins. The total yield is also representative of the dataset yield as extracted in chapter 4. This sample is used to validate the fitter as described in section 6.4.

The Sample 5 is a toy sample generated using the 2008 BaBar model [60] with full phase-space treatment. The events in the sample contain the D^0 position

in the phase-space and the D^0 decay time. It's also used to validate the fitter as described in section 6.4.

3.3 Trigger Configuration

The trigger configuration for this analysis consists of a set of trigger requirements designed specifically to select $K_S\pi^+\pi^-$ combinations. For HLT1 (see section 2.9.2) the D^0 candidate is required to have resulted in a TOS decision for the single track trigger line `Hlt1TrackAllL0`, the requirements of which are described in table 3.2. This selection is run on all events in LHCb that trigger L0 to validate the presence of a displaced hadron track [46].

Property	Cut
Track IP	> 0.1 mm
Number VELO hits per track	> 9
Number missed VELO hits per track	< 3
Number OT+ITx2 hits per track	> 16
Track IP_{χ^2}	> 16
Track p_T	> 1.7 GeV
Track p	> 10 GeV
Track χ^2/DoF	< 2.5

Table 3.2: List of conditions for the `Hlt1TrackAllL0` trigger line. This line is run on all L0 events to validate the L0 decision [46].

For HLT2, the D^0 candidate has have resulted in a TOS decision for the line `Hlt2CharmHadD02HHKs` which is described in table 3.3 and is specific for this analysis.

The K_S reconstruction can use candidates that decayed in the VELO (see section 2.3) which are called "LongLong" or "LL" (they result in two "long" tracks, see section 2.6) or it can use candidates that decay downstream from the VELO in which case they are called "DownDown" or "DD" (they leave two "down" tracks). The LL K_S candidates have better track resolution compared to the DD candidates owing to the VELO hits. Due to a misconfiguration of the trigger no DD candidates were saved in the 2011 run reducing the potential dataset.

The trigger configuration was fixed throughout the duration of the 2011 run but the changes to the trigger software require multiple processing runs when evaluating trigger efficiencies or when performing swimming [d]. Various improvements

[d] The swimming technique requires that all selection criteria that are potentially decay time bias-

Property	Cut
D^0 daughter π p_T	$>$ 1000.0 MeV
D^0 daughter π p	$>$ 1500.0 MeV
D^0 daughter π track χ^2/DoF	$<$ 5.0
D^0 decay vertex χ^2/DoF	$<$ 10.0
D^0 decay vertex displacement w.r.t PV	$>$ 2.0 mm
K_S daughter π p	$>$ 2000.0 MeV
K_S daughter π χ^2_{IP} w.r.t PV	$>$ 9.0
K_S daughter π track χ^2/DoF	$<$ 20.0
K_S mass window (w.r.t PDG value)	$\pm$ 50.0 MeV (before vertexing) $\pm$ 11.4 MeV (after vertexing)
K_S vertex displacement w.r.t PV	$<$ 650.0 mm
K_S vertex displacement χ^2 w.r.t PV	$>$ 100.0
K_S DIRA	$>$ 0.9999
D^0 decay vertex χ^2/DoF	$<$ 20.0
D^0 p_T	$>$ 2000.0 MeV
D^0 mass window (w.r.t PDG value)	$\pm$ 100.0 MeV
D^0 DIRA	$>$ 0.0
Number of tracks in an event	$<$ 120

Table 3.3: List of conditions for the `Hlt2CharmHadD02HHKs` trigger line that result in a TOS decision. This list only applies to LL K_S reconstruction.

to the High Level Trigger (see 2.9.2) in 2012, especially a specialised topological trigger and inclusion of K_S downstream tracks led to a significant increase in available yield from the 2012 data taking compared to the 2011 run. This analysis uses only the 2011 dataset (see chapter 4).

3.4 Stripping Selection

This analysis uses a single stripping line which is included in the stripping software run centrally on all LHCb data. All events from the charm trigger stream are required to pass the `StrippingDstarD2KShh` line described in table 3.4.

ing are rerun multiple times by the swimming algorithm which examines the resulting acceptance function. Due to the early development stages of the swimming framework, only rectangular cuts could be swum. With more development, in further analyses, using a multivariate selection while retaining swimming should be possible.

Given that the swimming technique requires rerunning of the trigger, should the trigger change, the swimming algorithm must be run separately on the old trigger and the new trigger, in other words the dataset needs to be partitioned and swimming rerun on all sections separately. This becomes tedious when the trigger undergoes numerous changes throughout the data taking. For a brief outline of the swimming technique see appendix B

Property	Cut
D^0 daughter π p	$>$ 1500 MeV
D^0 daughter π track χ^2/DoF	$<$ 4.0
D^0 daughter π (DLL$_e$ - DLL$_\pi$)	$<$ 10.0
D^0 daughter π (DLL$_p$ - DLL$_\pi$)	$<$ 15.0
D^0 daughter π (DLL$_K$ - DLL$_\pi$)	$<$ -1.0
K_S DIRA	$>$ 0.9997
K_S mass window (w.r.t PDG)	$\pm$ 11.4 MeV
K_S vertex displacement χ^2 w.r.t PV	$>$ 100.0
D^0 decay time	$>$ 0.3 ps
D^0 vertex χ^2/DoF	$<$ 13.0
D^0 DIRA	$>$ 0.0
D^0 p_T	$>$ 1500 MeV
D^0 mass window (w.r.t PDG)	$\pm$ 130.0 MeV (before vertexing) $\pm$ 110.0 MeV (after vertexing)
$D^{\star+}$ p_T	$>$ 2200 MeV
$D^{\star+}$ vertex χ^2/DoF	$<$ 20.0
π^+_{soft} (DLL$_e$ - DLL$_\pi$)	$<$ 5.0
Δm window	$>$ 0.0 MeV $<$ 15.0 MeV
Number of tracks in an event	$<$ 150

Table 3.4: Requirements for the `StrippingDstarD2KShh` line used in this analysis.

The stripping software reconstructs shortlived particles from longlived tracks in the same way as the trigger software. After the line reconstructs the candidates and filters them using a series of cuts it writes them to a dedicated output stream. Since the dataset only contains K_S LL candidates, the stripping too only reconstructs D^0 using K_S LL daughters. The number of events that pass the stripping selection in the 2011 dataset is $\sim 4.80 \times 10^5$. This indicates a combined efficiency of reconstruction, trigger and stripping of 3.75×10^{-5}.

Should an event contain multiple candidates, one of them is chosen at random (the first one in the event record). This is motivated by the implementation of swimming which was unable to select a different candidate apart from the first one in the event record. Future improvements to the swimming framework should allow for a minor improvement in the data quality by enabling a better choice of best candidate.

3.5 Offline Selection

The offline selection is performed using a custom C++ application written with the use of ROOT libraries. Due to the requirements of swimming (see section B) and the fact that the data purity is reasonably high before introducing a selection (see fig. 3.8) rectangular cuts were chosen as the method of background reduction. The cuts used are shown in table 3.5.

The signal mass windows are shown in table 3.6. The central values for the mass windows are slightly shifted from their PDG values, however the m_D window is wide enough for this to cause no effect in the final measurement, while for the Δm window it is in fact desirable to have an asymmetric window given the asymmetric distribution. The central values of the window cuts are not treated as constraints on the parameters for the PDF models of the Δm and m_D distributions.

The selection was optimised using a signal window signal purity criterion, investigating each cut independenently using the sPlot technique [e] to determine the distributions of each variable of interest for peaking and non-peaking components of the mass spectrum. The cut values were optimised manually using these distributions to minimize background and maximize retained signal.

Property	Cut
D^0 Ln(χ^2_{IP}) (w.r.t to PV)[f]	< 3.2
D^0 decay time	< 10.0 ps
D^0 flight distance (w.r.t PV)	> 2.0 mm
K_S flight distance (w.r.t D^0 end vertex)	> 10.0 mm
π_s PID (DLL_e - DLL_π)	< 2.0
π_s ghost probability	< 0.7
`DecayTreeFitter` DoF	> 0

Table 3.5: List of rectangular cuts used in the offline selection. This does not include mass windows which are listed in table 3.6

.

[e] The sPlot technique is a statistical method of predicting the distribution of property x for subclasses A and B of some sample if one has access to the distribution of some control variable y for the subclasses and the distribution of x for the entire sample. The mechanism works if x and y are independent and usually the mass of the D^0 meson and the difference in masses between the $D^{\star\pm}$ mother and the D^0 daughter are good control variables [61]

[f] Note that the D^0 log(χ^2_{IP}) cut is applied in the final selection (see chapter 5) only in the method described in this thesis and not in the additional methods in this anlysis.

Property Window	Cut
D^0 mass (w.r.t to $1865.9MeV$)	$<$ 21.9 MeV
Δm (w.r.t to to $145.75MeV$)	$<$ 1.75 MeV

Table 3.6: Signal window cuts on m_D and Δm used in the offline selection. The central values for the window cuts are indicated.

3.6 Kinematic Constraints

There are two kinematic constraints that are useful to improve the resolution of key variables used in the analysis. First, it's useful to constrain the mass of the D^0 mother to the world average value and use Dalitz coordinates under this constraint. Secondly, one can constrain the π_s to originate from the primary vertex[g]. The LHCb software package `DecayTreeFitter` [62] (DTF)[h] can be used to refit the signal decay tree in the event given constraints and extract key variables under these constraints. This refitting is not perfect and, especially in the case of secondary D^0 candidates or in the case of combinatorial background, the refit can fail. These events have to be accounted for and removed from the dataset, but they are primarily composed of non-signal events (see section 3.7 and section 5.4).

3.6.1 Constraining π_s to Primary Vertex

If one constrains the π_s to come from the primary vertex, one is also constraining the $D^{\star\pm}$ origin vertex to PV by the virtue of particle reconstruction. This has the effect of improving the resolution of the Δm spectrum considerably (see fig. 3.1) since the resolution of the PV is significantly better than the resolution of the $D^{\star\pm}$ vertex if one only uses the kinematic information of D^0 and π_s particles.

[g] On the determination of the primary vertex:
First seeds are formed by clustering tracks and merging clusters that are significantly close together. Seeds with low track multiplicity are vetoed. For each seed, the position of the PV is determined by minimizing the sum of impact parameter significances of all the associated tracks. This is done iteratively while discarding tracks with IP that is too large until all the tracks point to the PV position. Vertices with low resulting track multiplicity are discarded.

[h] This method was originally developed on BaBar. The canonical way of reconstructing a decay chain is from bottom up, where one fits decay vertices of the grand-daughters first, before fitting daughters and finally the mother. This has issues with propagating constraints and fitting information from top down, such as constraining the mass of the mother. Some particle decays cannot be reconstructed in the normal way at all since they depend on mother constraints too much such as $K_S \to \pi^0\pi^0$. The DTF was developed as a complementary way of fitting the decay chain, where it parametrises the chain in terms of decay lengths, vertex positions and momentum parameters and fits the whole parameter space at once, while taking constraints into account. To perform the fit more efficiently, a Kalman filter is used.

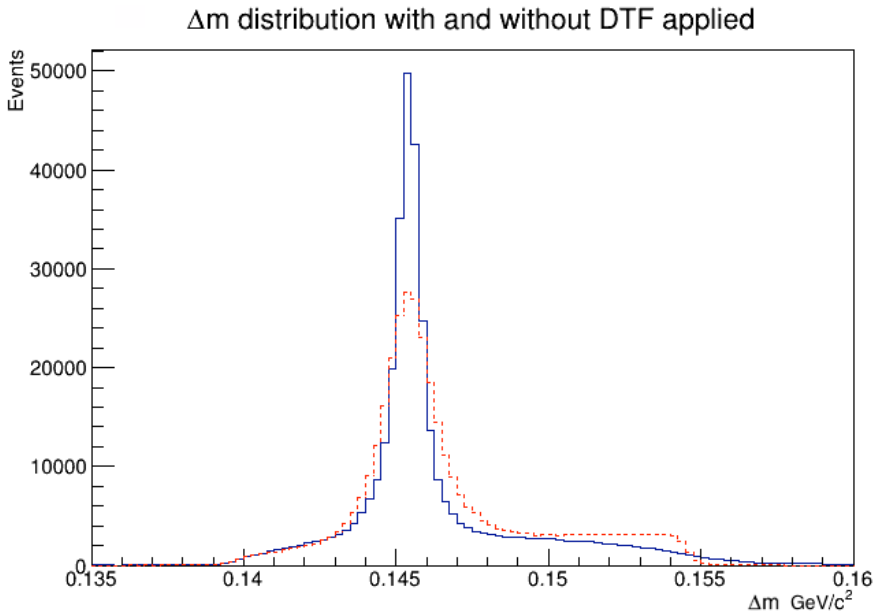

Figure 3.1: The distribution of Δm before (red) and after (blue) constraining the π_s to the PV. The `DecayTreeFitter` refit is forced to converge by requiring $\chi^2_{DTF}/\text{DoF} < 10$. An effect of earlier Δm window cut can be seen on the red plot at $\Delta m \sim 0.155\ MeV/c^2$. The data used is the full 2011 dataset.

3.6.2 Constraining D^0 mass

Constraining the D^0 mass to the PDG value is useful for constraining the Dalitz plot coordinates to lie within the kinematic boundary of the Dalitz plot. The resolution of the D^0 mass spectrum of the dataset causes the boundary of the Dalitz plot to be "fuzzy" (see fig. 3.2) which can cause problems for an amplitude fit with events in a kinematically forbidden region. At the same time the allowed region close to the boundary is artificially depleted which requires further corrections. Applying the DTF results in a sharp kinematic boundary (see fig. 3.3).

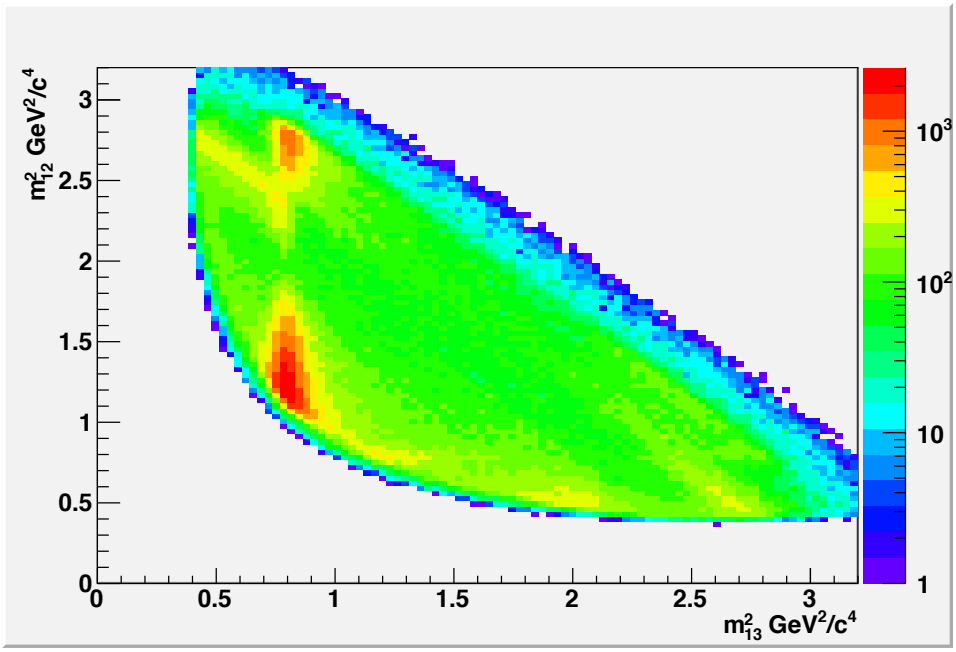

Figure 3.2: The distribution of candidates without m_D constraint in the phase-space forms a Dalitz plot with a "fuzzy" boundary. The data used is the full 2011 dataset.

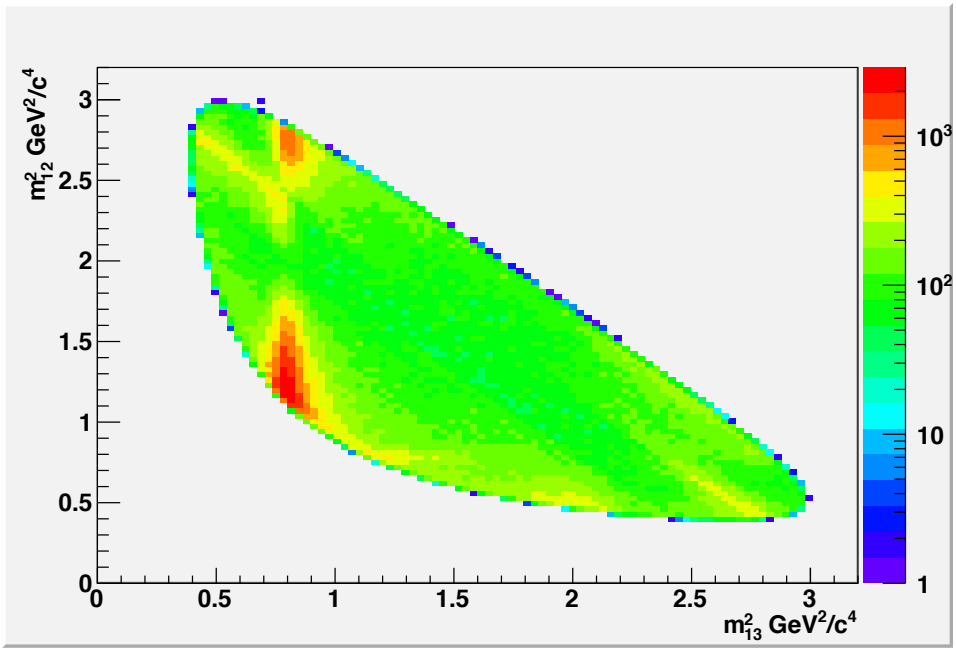

Figure 3.3: The distribution of candidates after `DecayTreeFitter` refitting with a m_D constraint and forcing the refit to converge by requiring $\chi^2_{DTF}/\text{DoF} < 10$. The phase-space forms a Dalitz plot with a clear, sharp boundary (any remaining "fuzziness" is due to rectangular binning. The data used is the full 2011 dataset.

3.7 DecayTreeFitter fit quality

The `DecayTreeFitter` does not converge perfectly for all events that pass the selection. The number of events where the fit fails can be seen in table 3.7. One can define quality-of-fit variables such as $\chi^2_{m_D}$ which is the χ^2 of the decay tree refit under the m_D constraint and similarly for the Δ_m constraint and divide them by their respective numbers of degrees of freedom for normalization. The resulting variables can be used to determine how well the `DecayTreeFitter` converged. The distribution of $\chi^2_{m_D}/\mathrm{DoF}_{\mathrm{m_D}}$ compared to the distribution of $\chi^2_{\Delta_m}/\mathrm{DoF}_{\Delta_\mathrm{m}}$ can be seen in fig. 3.4.

DTF constraint fit failure	Number of Events
D^0 mass	508
π_s to PV	499
D^0 mass and π_s to PV	62
Good convergence	189732

Table 3.7: Number of events that pass the offline selection, are in signal windows, and fail the `DecayTreeFitter` refit. The criterion for convergence is $\chi^2/\mathrm{DoF} < 10$.

Given that the majority of the events that fail the `DecayTreeFitter` are secondary and background events (see section 5.4) they can be cut from the dataset without the loss of signal.

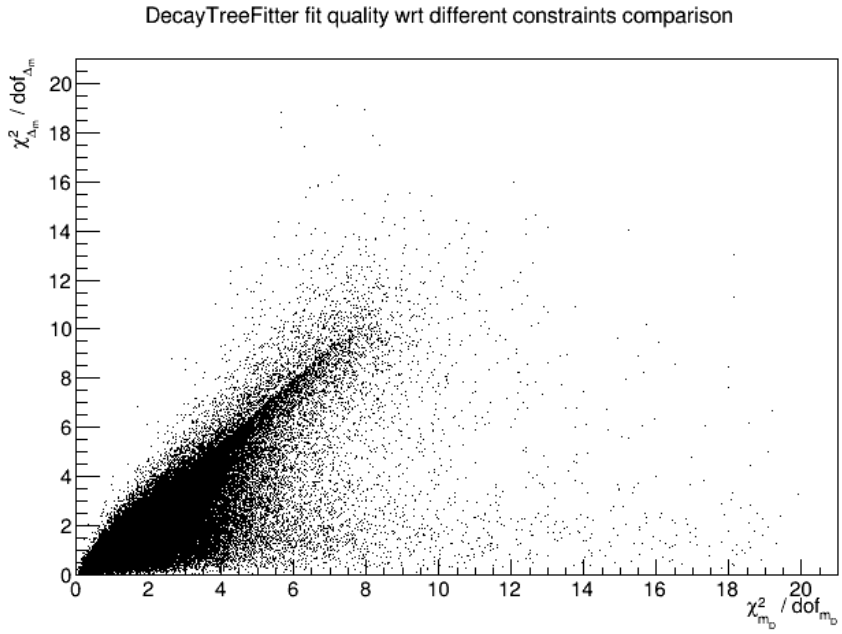

Figure 3.4: Fit quality scatter-plot for `DecayTreeFitter` refits with different constraints. The x-axis is the m_D constraint refit quality and the y-axis is the π_s refit quality. The good fit requirement is a square window $\chi^2_{DTF}/\text{DoF} < 10$ for both m_D and Δm. The data is the full 2011 dataset. There is a strong correlation between the two quality constraints.

3.8 Selection Efficiency

Using the method for extracting yields described in chapter 4 one can determine the efficiency of the offline selection by performing the extraction before and after the selection is applied. This determines not only the retention rate of the selection but also the purity and the purity increase due to selection. For the purposes of this analysis, a simple m_D fit was used to determine the peaking and non-peaking composition of the dataset for selection optimisation.

The number of events retained before and after applying the offline selection with their respective retention rates can be seen in table 3.8. The simple fits to the datasets before and after the offline selection is applied can be seen in fig 3.5. These fits are performed on the full 2011 LHCb dataset with no Δm signal window applied.

The discrepancy between the output of stripping and input to selection is due to a small preselection on m_D and Δm that is much wider than the signal window but is used to define the domain of the yield fits.

Event Category	No selection	Sel. w/ signal window	Retention rate
Peaking	278022	198579	0.714
Non-peaking	40303	7366	0.123
Purity	87.3%	96.4%	-

Table 3.8: Number of events in different categories retained at different stages of the offline selection. Data is the full 2011 LHCb dataset with constraints discussed in section 3.6.

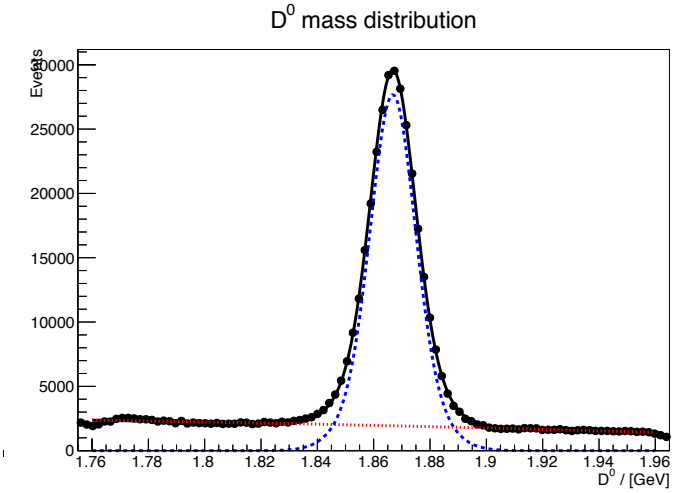

(a) Before selection

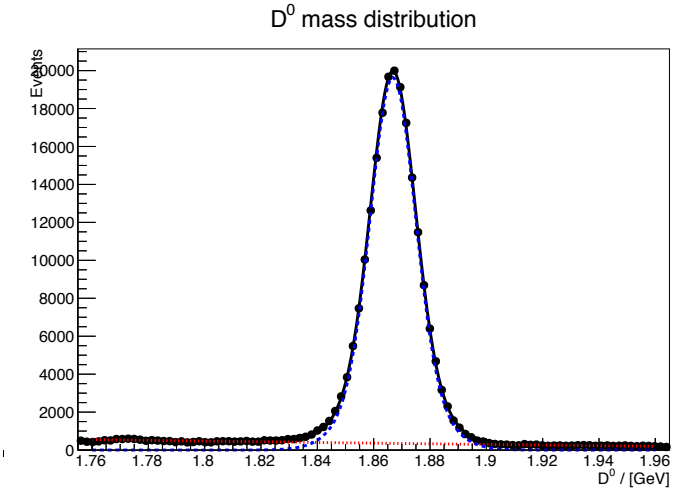

(b) After selection

Figure 3.5: Simple fits to m_D spectrum for selection optimisation, before applying the offline selection (a) and after applying the selection (b). The data is the full 2011 LHCb dataset. The yields and purities in the signal window are shown in table 3.8. Note the dataset has no Δm window applied.

Chapter 4

Yield Extraction

After applying the selection, the dataset is composed of several different categories with prompt and secondary subcategories where indicated. The yields of each of these are extracted using a fit to the D^0 candidate mass (m_D) and $D^* - D^0$ mass difference (Δm). The differentiation between subcategories of signal and mis-tagged events is done using the D^0 candidate impact parameter χ^2 distribution (χ^2_{IP}).

4.1 Signal and Background categorisation

We recognise four different categories of data in our sample as shown in Table 4.1.

Category	Component	Subcategory
1	Signal	a. Prompt b. Secondary
2	Misreconstructed π_{soft}	a. Prompt b. Secondary
3	Reflection background	
4	Combinatoric background	

Table 4.1: The categorisation of signal and background components of the dataset.

The signal sample consists of real D^0 with a real π_s. This means the sample exhibits a signal-like peak for both m_D and Δm. The prompt subcategory contains D^0 originating from D^* that were produced at the Primary Vertex. The secondary subcategory is produced in decays of other particles, such as B mesons and differs in the shape of the Δm peak which is wider than the prompt signal peak due to the

fact that `DecayTreeFitter` assumes that the D^0 meson originated at the PV, and weakly depends on the lifetime of the D^0 mother.

The misreconstructed π_s sample consists of real D^0 candidates that have a random soft pion assigned. This means the sample behaves as combinatoric background in the Δm spectrum but as signal in the D^0 mass spectrum[a]. The D^0 candidates in this category may come from both prompt and secondary origins. The sample lacks a reliable D^0 tag which means it has to be treated as background even though the D^0 candidates are correctly reconstructed.

The reflected background consists of D^0 candidates decaying into a different final state, such as $K^-\pi^+K_S$ where one of the daughters is misreconstructed from kaon to pion or vice versa. This yields a non-peaking m_D spectrum but a peaking Δm spectrum since the D^* mass reconstruction depends on the D^0 mass reconstruction[b].

The combinatoric background consists of both misreconstructed D^0 and π_s meaning that it peaks in neither m_D or Δm distributions.

4.2 Neglected background categories

During the characterisation of the background data, several categories were examined and determined to not contribute significantly to the final sample of the data, these are shown in Table 4.2. The potential backgrounds to investigate were obtained by the analysis of the possible decay products of D^0 while consulting previous charm analyses [2] as well as examining a minimum bias sample of Monte Carlo.

The most common way of eliminating a given background is a choice of selection cuts. The effect of these on the given background was determined using Monte Carlo samples generated to emulate given backgrounds[c].

All reflected backgrounds are suppressed by tight particle identification cuts. Singly reflected backgrounds (one particle is misidentified) peak under a tail

[a] The π_s is a D^0 sibling and does not enter the D^0 mass hypothesis in any way. It merely acts as the tag for the flavour of the D^0 meson. It also has a large impact on the Δm distribution since the Δm distribution effectively describes the leftover kinetic energy after the $D^{\star\pm}$ meson decays into the D^0 daughter and the π_s.

[b] Another view is to consider that in the D^* rest frame, the Δm is proportional to the opening angle between the D^* daughters and since a wrong mass hypothesis doesn't alter the opening angle, the Δm remains peaking.

[c] These samples are used as signal samples for other analyses which examine those decay channels, thus "Yesterday's signal has become Today's background noise."

of the m_D distribution, thus any significant contribution will destabilise the fit and coversely a goot fit to the tails of the Δm distribution provides evidence for the lack of singly reflected backgrounds. Doubly reflected backgrounds could peak under both m_D and Δm but requires two particles to be misindentified, one misindentified as a heavier particle and one as a lighter particle. This is a common background for decays containing $K\pi$ pairs which can be mutually misidentified and the resulting m_D distribution remains unchanged. For this analysis, tight cuts on K_S reconstruction limit the potential for it to be misidentified[d]. A potential decay to $K_S Ke$ was investigated for double reflection and it does not contribute to the final decay sample due to very low branching fraction and low π to e misidentification probability.

A possible peaking background from direct decays of $D^0 \to 4\pi$ could contaminate the final sample since it shares the final decay products with the signal chain. A tight cut on the K_S minimum flight distance however requires the origin vertex of two of the final pions to be significantly removed from the D^0 decay vertex, so any such reconstructed decays will not come from real D^0 mesons and thus will not peak in m_D.

Background	Behaviour
$D^0 \to K_S K\pi$	Peak in Δm and under a tail of m_D
$D^0 \to 4\pi$	Peak in Δm and in m_D if the decay chain matches
$D^+ \to K\pi\pi^0$	Peak in both m_D and Δm
$D^0 \to K_S Ke$	Peak in both m_D and Δm

Table 4.2: Background categories which were determined not to contribute to the final dataset.

Any residual contribution by these backgrounds reflects in the poorer quality of the fit which estimates yields and backgrounds and therefore is transparently included in the systematic error due to the uncertainty on the background estimation.

4.3 Characterisation of m_D signal and background distributions

The probability density functions (PDF) for individual components of the m_D distribution are summarised in Table 4.3 and shown in Figure 4.1. They are

[d] $\pi^0 \to ee$ was examined as a potential candidate but the particle identification cuts suppress this significantly

mostly chosen empirically to best represent the data.

Category 1 & 2	Double Gaussian, shared mean
Category 3 & 4	Quadratic Chebyshev polynomial

Table 4.3: The parametrisation of the m_D distribution components.

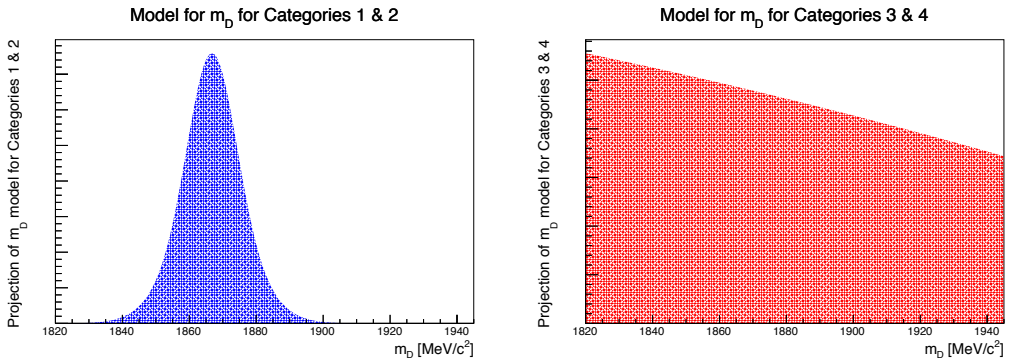

(a) Signal and Misreconstructed π_s (b) Reflected and Combinatoric Background

Figure 4.1: Illustrations of the PDF models used to fit the respective categories in the m_D spectrum.

The signal peak component for categories one and two is parametrised simply using a double Gaussian and the PDF is shared among category one and two components. A triple Gaussian was considered but the net gain in fit quality was negligible. Both prompt and secondary subcategories share the same PDF because the width increase of the distribution for the secondary component was not found significant enough to require a separate PDF.

Category three and four samples are non-peaking in the m_D distribution and are parametrised using quadratic Chebyshev polynomials[e] with no constraints on the parameters. The Chebyshev polynomials were chosen because the offset of the characteristic mass of the fit to 1860 MeV coupled with low yields of background caused minor instabilities with a standard polynomial formulation.

[e]Chebyshev polynomials form a basis spanning the set of all polynomial functions, which is different to the standard basis of ax^n. Thus all polynomial functions can be expressed as a linear combination of Chebyshev polynomials and in turn Chebyshev polynomial basis can be expressed in the standard ax^n basis. The motivation for this choice of basis for the polynomial PDF is purely practical, it was observed that this results in a more stable fit.

4.4 Characterisation of Δm distributions

The Δm distribution components are characterised using the PDFs shown in Table 4.4 with illustrations shown in fig 4.2. Again, the PDFs are chosen empirically to achieve best fit quality.

Category 1a	Triple Gaussian with a shared mean
Category 1b	Double Gaussian with a shared mean (independent of mean of 1a)
Category 2	Quadratic Chebyshev Polynomial (share parameters with 4)
Category 3	Double Gaussian with a shared mean (share parameters with 1b)
Category 4	Quadratic Chebyshev Polynomial (share parameters with 2)

Table 4.4: The characterisation of the Δm distribution components

The prompt signal component is characterised by a triple Gaussian, the secondary signal component is a double Gaussian with a separate mean from the prompt. The triple Gaussian for the prompt signal is necessary to achieve good fit quality for the signal peak, but the secondary component is wider and the fit contains less information which led to the choice of a double Gaussian for the secondary peak.

Category three component peaks in Δm distribution and is characterised by the same form as secondary signal given that the resolution is worse compared to the signal peak due to the wrong mass hypothesis for the D^0 daughters. The parameters are shared since the yields of the reflected background are small enough that a difference from the parametrisation of the secondary component is negligible.

The shape of the combinatoric and misreconstructed π_s background is approximated using a simple quadratic Chebyshev polynomial. While the common method of fitting charm Δm background is with a phase-space dependent model that mimics the background of two daughters incorrectly assumed to come from a common mother [63], it was found that in the case of low yields for combinatoric background the data can be well approximated using a simple Chebyshev polynomial which is computationally simpler. The model underestimates the background at the extreme lower edge of the phase-space but this effect is negligible.

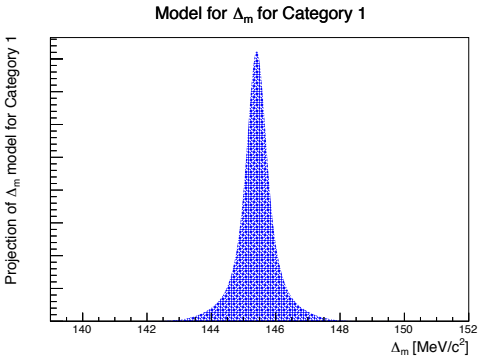

(a) Prompt Signal

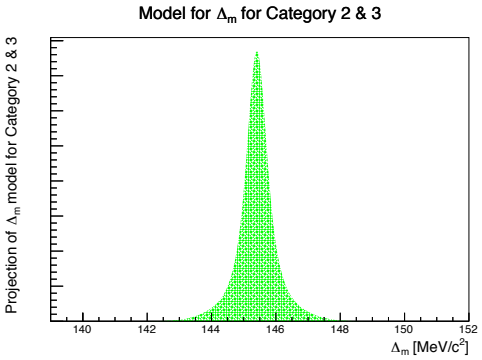

(b) Secondary Signal events and Reflected Background

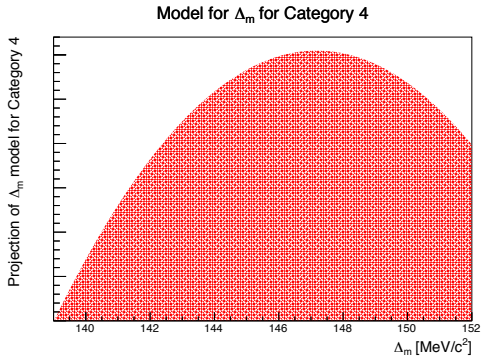

(c) Misreconstructed π_s Combinatoric Background

Figure 4.2: Illustrations of the PDF models used to fit the respective categories in the Δm spectrum.

4.5 Characterisation of $Ln(\chi^2_{IP})$ distribution

The $Ln(\chi^2_{IP})$ variable describes the fit quality of the event if one requires that the D^* originated in the Primary Vertex. This allows one to distinguish between prompt events and secondary events that originate in decays of other hadrons such as B^0 mesons. It's also a better choice of discriminator compared to the impact parameter because it accounts for the error on the measurement of the impact parameter as well as the magnitude. The PDFs fitted to the $Ln(\chi^2_{IP})$ distribution for different categories are described in Table 4.5 and illustrated in Figure 4.3.

The prompt signal component is characterised using a bifurcated Gaussian

Category 1a Category 2a	Double Gaussian with bifurcated Gaussian, mean invariant of decay time
Category 1b Category 2b	Double Gaussian with bifurcated Gaussian, mean depends on time
Category 3 Category 4	Bifurcated Gaussian, mean and sigma depend on time

Table 4.5: The characterisation of the $Ln(\chi^2_{IP})$ PDF components.

added to a double Gaussian[f]. The parameters of the prompt signal PDF do not depend on the D^0 decay time.

The secondary signal component shares the PDF with prompt signal, but the mean of the secondary PDF depends on the lifetime of D^0. This dependence is parametrised in Table 4.6. The widths of the bifurcated Gaussian are also multiplied by a scaling factor representing the fact that the secondary component is more poorly resolved than the prompt component.

Since category 2 events are real D^0 candidates, they share the $Ln(\chi^2_{IP})$ PDFs with category 1 events and are not distinguishable using the $Ln(\chi^2_{IP})$ distribution.

Category 3 and 4 events contain misreconstructed D^0 candidates and share the same $Ln(IP_{\chi^2})$ PDF. They are characterised using a bifurcated Gaussian with parameters depending on time as shown in Table 4.6.

Category 1b,2b mean	Quadratic polynomial
Category 4 mean	Quadratic polynomial
Category 4 left sigma	Linear polynomial
Category 4 right sigma	Linear polynomial

Table 4.6: The time dependence of the χ^2_{IP} PDF component parameters.

[f]The expected form of the distribution is well approximated by the bifurcated Gaussian. The double Gaussian has a physical significance as a resolution function. That is why a scaling factor is applied for the secondary component, it is expected the secondary component has poorer resolution on the impact parameter due to the fact that the tracks are further removed from the primary vertex.

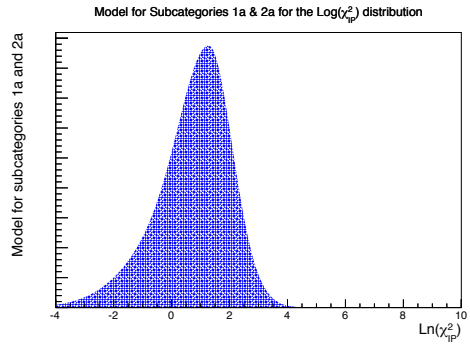

(a) Prompt Signal and Prompt Misreconstructed π_s

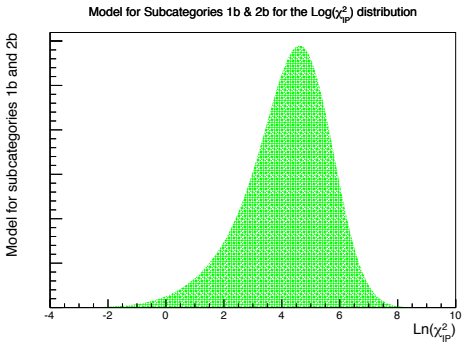

(b) Secondary Signal and Secondary Misreconstructed π_s

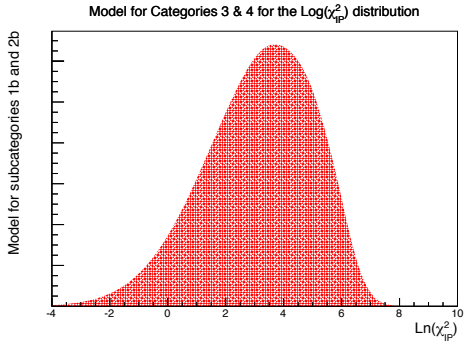

(c) Reflected and Combinatoric Background

Figure 4.3: Illustrations of the PDF models used to fit the respective categories in the $Ln(\chi^2_{IP})$ spectrum.

4.6 Fitting Strategy

The m_D and Δm PDFs are fitted using an unbinned maximum likelihood function to a 2D m_D- Δm distribution with an extended fit. The total PDF fitted is a sum of the components multiplied by their yields as shown in equation 4.1 with p_i representing the PDF of category i and n_i represents the yield of the corresponding category of events.

$$\begin{aligned} n_{tot} \cdot p^{\Delta m} \cdot p^{m_D} =& n_{1a} \cdot p_{1a}^{\Delta m} \cdot p_{1a}^{m_D} + n_{1b} \cdot p_{1b}^{\Delta m} \cdot p_{1b}^{m_D} + n_{2a} \cdot p_{2a}^{\Delta m} \cdot p_{2a}^{m_D} + \\ & n_{2b} \cdot p_{2b}^{\Delta m} \cdot p_{2b}^{m_D} + n_3 \cdot p_3^{\Delta m} \cdot p_3^{m_D} + n_4 \cdot p_4^{\Delta m} \cdot p_4^{m_D} \end{aligned} \tag{4.1}$$

The yields of n_{1b} and n_{2b} are determined using the $Ln(\chi^2_{IP})$ distribution and fixed in the fit. The n_{1b} yield is shown on figures 4.5 and 4.6 for illustration.

The $Ln(\chi^2_{IP})$ distribution is fitted using a separate unbinned maximum likelihood fit. To determine the form of the lifetime dependence of the parameters that do depend on lifetime, the distribution is binned in lifetime and the fit is simultaneous in all the bins of lifetime. Adaptive binning algorithm is performed to choose the binning scheme such that each bin contains at least 6000 events[g]. The extracted secondary yield integrated in the signal window is then used as an input in the m_D-Δm 2D fit and fixed to describe the secondary component of Category 1 and 2. Since the fit uses the same PDF for Category 1a and 2a and similarly the same PDF to describe 1b and 2b, the extracted number of secondary events is the sum of yields of categories 1b and 2b. Nevertheless, the 2D fit can distinguish between categories 1 and 2 and therefore can extract the correct proportions.

The fit is simultaneous in 15 bins of lifetime and has 8 global degrees of freedom and 3 degrees of freedom per decay time bin. This is 53 degrees of freedom in total. The shape of the $Ln(\chi^2_{IP})$ distribution for signal events is well known for previous charm analyses [2]. The shape of the distribution for the background events is extracted from mass sidebands. The fit was validated for quality by good covergence in each time bin and for stability by varying the adaptive binning target bin size. The errors on the estimation of the yields for secondary components are propagated to the systematic errors on the final fit, see chapter 7.

4.7 Extracted Yields

The resulting fit to $Ln(\chi^2_{IP})$ distribution can be seen in Figure 4.4. This is the sum of the simultaneous fits in time bins to give the impression of the overall distribution rather than a projection of a single total PDF.

The pull shown on the same figure is generally contained within the 2σ boundaries drawn horizontally on the plot. One can observe a structure in low $Ln(\chi^2_{IP})$ where the fit first underestimates and then overestimates the number of events. This effect is negligible due to the low number of events in the region and the location in the distribution - all events in that region are prompt. The second observable structure is at $2 < Ln(\chi^2_{IP}) < 5$ where all three components are present

[g]The algorithm is simple, the data is binned with an extremely fine binning such that on average there are fewer than 1 event per microbin. Then the algorithm aggregates the bins from start to finish and whenever the cumulative event counter overflows the specified number of events, the cumulative counter is reset and the lower microbin edge is used as a bin boundary. Last bin is forced to contain at least half of the specified number of events or else the last two bins are merged. Then the entire sample is rebinned using the binning thusly obtained.

with similar yields. This fluctuation is irreducible as the introduction of more complicated models for component PDFs destabilises the fit. Given that the fluctuation is generally contained within the 2σ boundary, the effect is neglected. The projections of the fit within individual bins are shown in appendix E and they show that the pulls of each individual fit are all within the 2σ boundaries. These structures and the fact that the plot is a composition of independent fits explains the relatively large value of the minimized χ^2/dof function

The projections of the simultaneous fits in each bin can be found in appendix E. The extracted number of prompt and secondary events can be seen in Table 4.7.

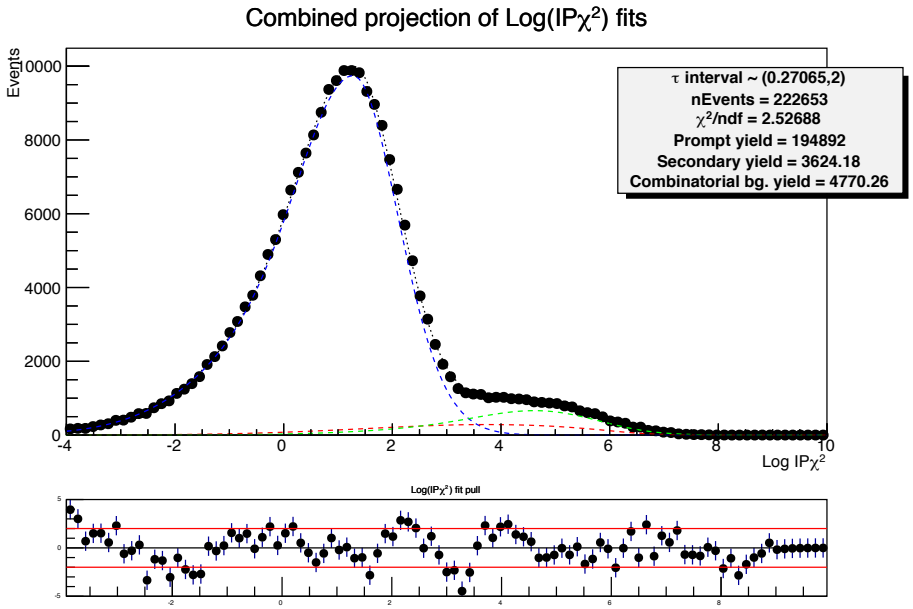

Figure 4.4: Fit to the $Ln(\chi^2_{IP})$ distribution. The prompt subcategory is blue, secondary subcategory is green while the background categories (3 and 4) are characterised by the red component. Note that this projection was created by combining simultaneous fits in bins of decay time that can be found in appendix E.

Category	Raw fit data	$Ln(\chi^2_{IP})$ signal window
1a + 2a	197253	194892
1b + 2b	10017	3624.2
3 + 4	15852	4770.3

Table 4.7: The yield of subcategories A and B as extracted from the fit to the $Ln(\chi^2_{IP})$ distribution. Note that the subcategory yields are combined in categories 1 and 2.

The m_D and Δm distributions of the full dataset described in section 3.1 is

fitted using the models introduced in sections 4.3 and 4.4. The results of the fit can be seen in figures 4.5 and 4.6.

One should note that since these are projections of the full 2D distributions on their respective axes, the standard m_D and Δm window cuts are not applied. The two dimensional fit allows for a good fit of category 2 and 3 which would be much more difficult with sequential 1D fits.

The yields are obtained by integrating the PDF in the signal window and multiplying by the appropriate fit fraction. The yields as obtained from the m_D and Δm distributions are shown in Table 4.8.

Category	Raw fit data	m_D and Δm signal window
1a	194566	185839
2a	31936	10340
1b+2b	3974.5	3540.4
3	2606.7	988.9
4	23212.5	2985.2
Purity	75.91%	91.23%

Table 4.8: The yield of different categories of events as extracted from fits to m_D and Δm distributions. Purity is defined as the ratio of Category 1 events over over the total yield.

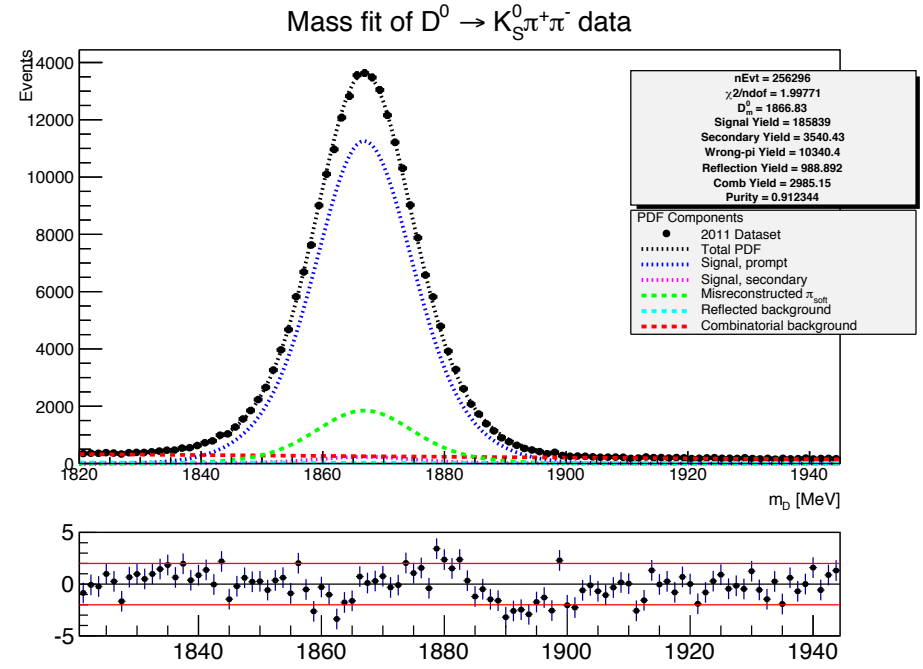

(a) m_D fit. Linear scale.

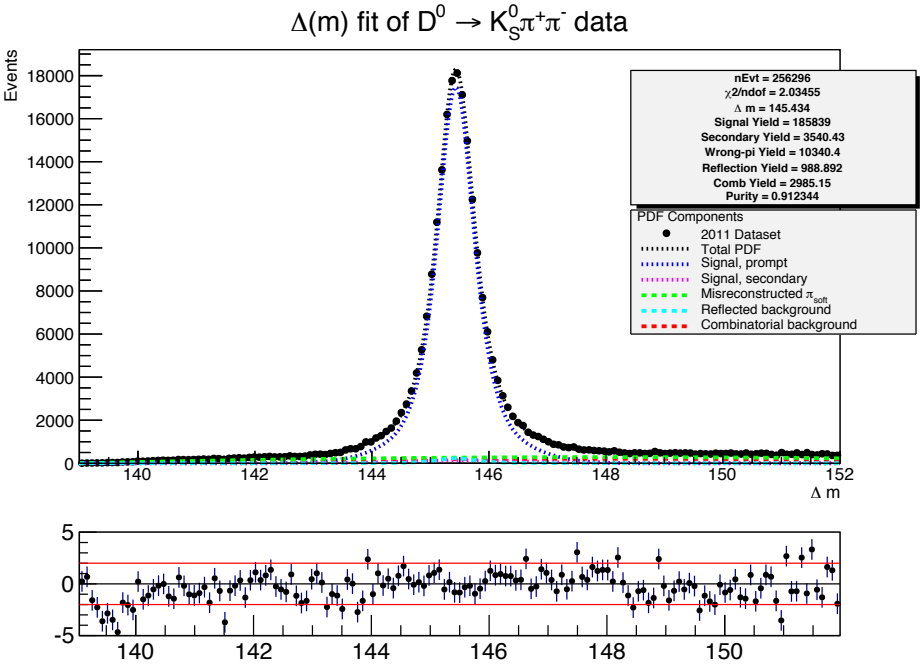

(b) Δm fit. Linear scale.

Figure 4.5: Projections of the 2D fit to the distributions of m_D (left) and Δm (right) with the full 2011 dataset. The yields are integrated in the signal window over Δm and m_D respectively. Categories 1,2,3 and 4 are represented by blue, green, cyan and red respectively.

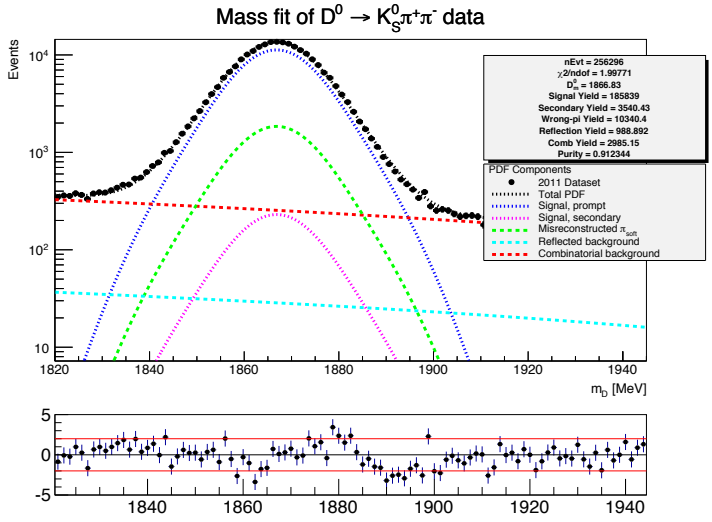

(a) m_D fit. Logarithmic scale.

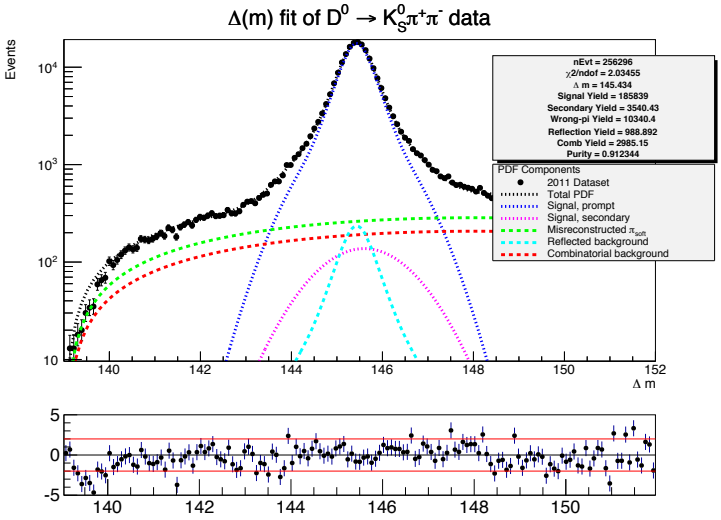

(b) Δm fit. Logarithmic scale.

Figure 4.6: Projections of the 2D fit to the distributions of m_D (left) and Δm (right) with the full 2011 dataset. The yields are integrated in the signal window over Δm and m_D respectively. Categories 1,2,3 and 4 are represented by blue, green, cyan and red respectively. Note that the red lines on the pull plot indicate a 2σ boundary.

Chapter 5

Background Treatment

This chapter outlines the treatment of the different types of background as they are outlined in section 4.1. All three categories of the background, including the secondary contamination are treated in a similar way - the ultimate goal is to subtract the number of background events in each CLEO bin i and each time bin j[a]. Because of this, a m_D- Δm fit is performed in each CLEO bin separately. This gives a good estimate of how yields of different categories vary across the CLEO bins. At the same time, the time-binned $Ln(\chi^2_{IP})$ fit (see section 4.6) is used to extract the time-dependence of the yields of individual categories.

5.1 m_D– Δm fit Results

The results of the individual fits to the 2D spectrum of m_D and Δm in each phase-space bin can be seen in Tables 5.1 for $D^0 \to K_S\pi^+\pi^-$ and 5.2 for $\bar{D}^0 \to K_S\pi^+\pi^-$ with the plots of individual fits shown in appendix F. It's obvious that the background contamination is not independent of the position within Dalitz plot. In the tables, the combinatorial background (category 4) and the reflected background (category 3) are grouped together because they behave similarly in the mass spectrum and thus the time evolution fits extract the combination of these rather than each separately. Due to the low yields of reflected background, any biases due to this simplified treatment can be safely neglected.

The misreconstructed π_s background (category 2) should be compared to signal because this component consists of real D^0 mesons and thus should behave

[a]Each CLEO bin i has a different time binning scheme, see section 6.3

very similarly to the signal in the time distribution, or at the very least, the proportion of misreconstructed π_s events to signal events should not vary in time. This proportion can be extracted from the 2D m_D- Δm fit in each phase-space bin and applied in each time bin separately.

Phase-space (CLEO) bin	Signal	Misreconstructed π_s	Background
1	16231.4	677.9	339.4
2	6315.6	264.0	118.3
3	4528.8	221.8	92.0
4	2006.5	98.0	44.7
5	5988.9	315.9	145.5
6	5576.5	226.1	89.6
7	13380.3	510.5	138.8
8	12693.3	497.7	173.6
-1	8638.1	707.6	255.3
-2	1825.4	213.0	83.0
-3	2093.5	160.7	64.6
-4	1712.7	100.5	35.1
-5	4312.3	245.7	119.4
-6	1389.5	181.7	53.9
-7	1481.6	351.5	72.9
-8	3163.1	395.9	106.1

Table 5.1: The extracted yields of $D^0 \to K_S\pi^+\pi^-$ within signal windows in individual phase-space bins. The Background column contains both the combinatorial yield and the yields of the reflected background (category 3 and 4).

Phase-space (CLEO) bin	Signal	Misreconstructed π_s	Background
1	16606.1	757.2	375.6
2	6374.2	261.7	127.9
3	4590.5	259.6	104.8
4	1976.7	127.3	57.3
5	6086.7	285.4	147.4
6	5582.0	234.4	121.0
7	13313.3	485.1	151.1
8	12995.5	430.6	169.1
-1	8975.8	609.1	269.7
-2	1906.7	197.1	66.1
-3	2010.6	184.8	85.0
-4	1777.4	80.5	46.4
-5	4231.6	257.6	141.9
-6	1410.0	177.6	43.7
-7	1549.8	302.7	60.7
-8	3147.6	412.6	104.8

Table 5.2: The extracted yields of $\bar{D}^0 \to K_S\pi^+\pi^-$ within signal windows in individual phase-space bins. The Background column contains both the combinatorial yield and the yields of the reflected background (category 3 and 4).

5.2 $Ln(\chi^2_{IP})$ Results and Fitted Model

In general, the yields of the different categories of events will depend on time. In particular the purity of the data decreases with increasing decay time. The yields of the secondary subcategories of signal and misreconstructed π_s components as well as the time depedence of the combinatorial background can be estimated using the $Ln(\chi^2_{IP})$ distribution. The method of fitting to this distribution is described in section 4.5.

The time-dependence of the combinatoric background is already fixed in the $Ln(\chi^2_{IP})$ fit and the same information can be used assuming that the form of the time-dependence doesn't depend on the position in the Dalitz plot[b]. In this case we extract a function of decay time shown in eq. 5.1, chosen empirically to obtain a good fit. The extracted function is normalised to the time-integrated yield

[b]The position in the Dalitz plot depends entirely on the steradian opening angle of the D^0 decay. The decay time of the D^0 meson depends mostly on the flight distance (and momentum) of the meson from the PV. The probability of a combinatoric event being accepted depends mostly on the possible combination space which mostly depends on the flight distance (more possible particles the closer the decay vertex is to PV). The dependence of the yield of the combinatoric events on the decay time should not change with different D^0 daughter opening angles.

of combinatorial and reflected background.

$$\frac{n_{3+4}(t)}{n_{3+4}} = Ae^{(\frac{t-B}{C})^2} + Dt^3 + Et^2 + Ft + G \tag{5.1}$$

The resulting fit is then normalized in each phase-space bin to the estimated total yield of combinatorial and reflected background and integrated in each time-bin during the final fit to get an estimate of these two components for each time bin.

The secondary contamination of both signal and misreconstructed π_s background is similarly dependent on D^0 decay time. The combined yield of secondary subcategories of both components normalised to the total number of events is extracted from the results of the $Ln(\chi^2_{IP})$ fit and its time dependence is parametrised with equation 5.2, chosen empirically for a good fit. The fit does not describe the distribution well past 2 ps in decay time, but the decay time domain in the fit does not extend beyond that point.

$$\frac{n_{1b+2b}}{n}(t) = Ax^2 + Bx + C \tag{5.2}$$

This normalised fraction is used directly in the final fit to determine the proportion of the secondary contamination of the signal component bin by bin. It's assumed here that signal and misreconstructed π_s have the same proportions of secondary contamination as prompt signal and that this holds for all decay times since they both represent real D^0 mesons.

The results of the fits to both functions can be seen in Figure 5.1.

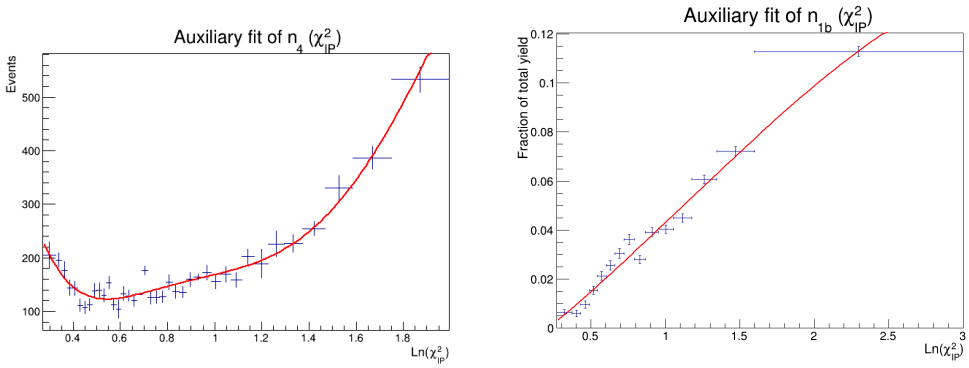

Figure 5.1: Auxiliary fits of time evolution of combinatorial yield (left) and secondary yield (right). The combinatorial yield is normalised globally to the time-integrated combinatorial yield. The data points used in the fit are taken in 2D m_D-Δm sidebands by fitting the combinatorial yields in bins of time, the identical data points used in the $Ln(\chi^2_{IP})$ fit for combinatorial component (see section 5.2). The secondary yield is normalised to the total yield in each time bin.

5.3 Extracted Background Yields

The procedure to extract yields of contaminants in each CLEO bin and in each time bin involves several steps. The time binning j in each CLEO bin i is performed as outlined in section 6.3. The population of each CLEO bin is fitted with a 2D m_D- Δm fit to get the total yields of different categories.

The yield of category 3 and category 4 is together set as the total integral of the extracted time-development function for these categories (eq. 5.1) - the time evolution of category 3 and 4 is treated in the same way. The integral of this function between the start and the end of a given time bin then gives the expected number of combinatoric and reflected background in the time bin.

Category 2 is easiest to estimate as it's expected that category 2 events behave like signal due to the fact they are real D^0 mesons. As such, one can calculate the ratio of category 2 to sum of categories 1 and 2 η_{π_s}

$$\eta_{\pi_s} = \frac{N_{i,2}}{N_{i,1} + N_{i,2}}, \tag{5.3}$$

where $N_{i,k}$ is the yield of category k in CLEO bin i. The estimate of category 2 events is simply the remaining yield of the events (after removing categories 3 and 4) in a given time bin multiplied by this ratio.

The integral of the function describing the time evolution of subcategories

1b and 2b (eq 5.2) cancels in the final PDF (this can be seen in ratio 6.21). This is due to the fact that the ratio of the secondary events to prompt events does not depend on the position in the Dalitz plot and furthermore, the time-dependence of this ratio doesn't depend on the position in the Dalitz plot. However it's still important to determine the level of the contamination of such that a systematic uncertainty can be determined due to the Poisson fluctuation of the secondary yield in each bin (see section 7.4).

After determining the estimated yield of each category of background in each time bin these are simply subtracted from the total yield to obtain the signal yield in each time bin which is used in the fit.

5.4 Correlation between Decay Tree Fitter and $Ln(\chi^2_{IP})$

The use of `DecayTreeFitter` (DTF) necessitates additional convergence requirements in the selection to ensure data quality. The convergence can be defined as

$$\chi^2_{DTF}/\mathrm{DoF}_{\mathrm{DTF}} < 10 \tag{5.4}$$

and[c]

$$\mathrm{DoF}_{\mathrm{DTF}} > 0. \tag{5.5}$$

The $\chi^2_{DTF}/\mathrm{DoF}_{\mathrm{DTF}}$ variable is also referred to as the "DTF quality" in the text (note that low values represent high "DTF quality" and vice versa). These criteria are applied for both the π_s constraint and the m_D constraint separately.

Relaxing the π_s constraint convergence criteria leads to destabilisation of the fit to the Δm spectrum due to the DTF extracted Δm values being unreliable as can be seen in Figure 5.2.

There exists a strong correlation between the π_s DTF quality distribution and the $Ln(\chi^2_{IP})$ distribution, as can be seen in Figure 5.3. Events with high $Ln(\chi^2_{IP})$ are more likely to fail the DTF quality criteria than events with low $Ln(\chi^2_{IP})$. This is because the events with high $Ln(\chi^2_{IP})$ are much more likely to be secondary and therefore constraining their origin to PV is much more likely to fail. It's also the case that the selection cut of $Ln(\chi^2_{IP}) < 3.2$ removes almost all events which fail the DTF quality criterion.

Given that this cut was removed from selection, a different way of stabilising the Δm spectrum fit had to be found. Using the DTF quality as a rectangular

[c]Requiring more than 0 degrees of freedom is a technical constraint to ensure the refit actually converged.

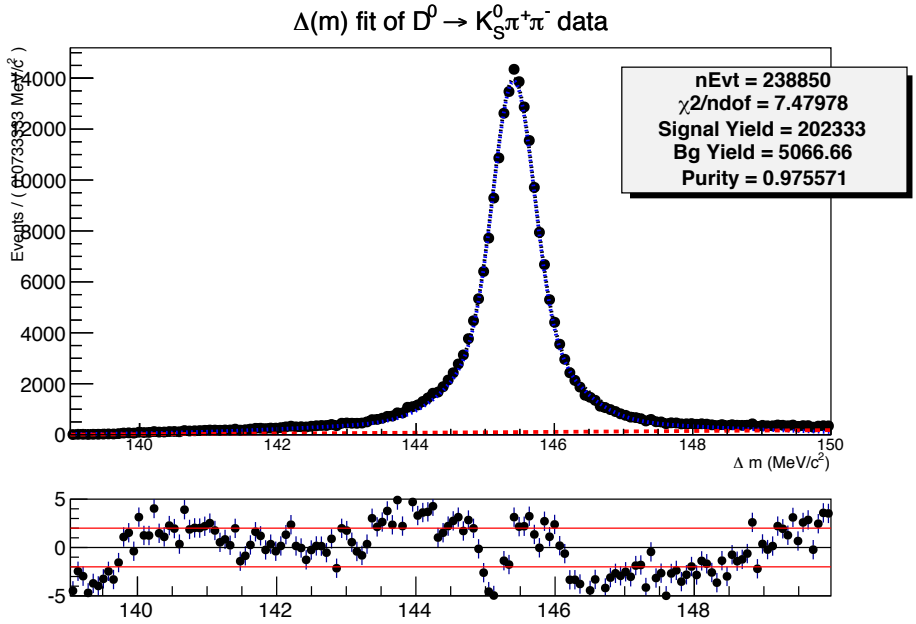

Figure 5.2: Fit to Δm distribution with DTF quality cuts disabled. The pull clearly demonstrates the deterioriation of the fit quality.

cut is undesirable due to previously shown correlation. After some consideration, it seems that performing a 2D m_D-Δm fit instead yields satisfactory results even without DTF quality criteria, see section 4.5.

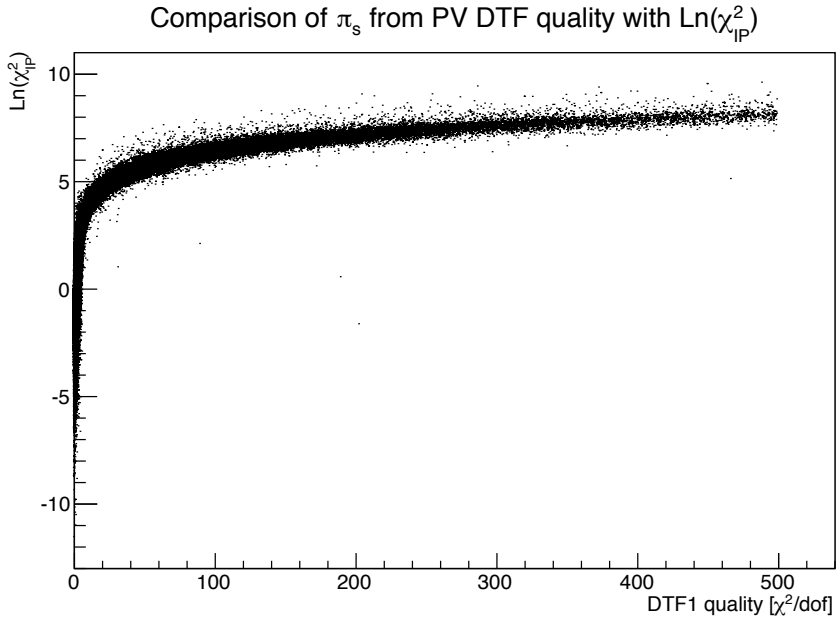

Figure 5.3: Comparison of π_s DTF constraint refit quality ($\chi^2_{DTF}/\mathrm{DoF}_{\mathrm{DTF}}$) with $Ln(\chi^2_{IP})$ of the D^0 meson. Clear correlation is indicated for high $Ln(\chi^2_{IP})$ and events failing the DTF quality criteria.

Chapter 6

Model Independent Formalism and Fit Strategy

The approach to extracting the mixing parameters from the $D^0 \to K_S\pi^+\pi^-$ channel discussed in this thesis is independent of the choice of the amplitude model. The principal motivation behind this is to eliminate the systematic error due to choice of the model and, instead of this, accruing the systematic uncertainty due to the error on the measurement of the integrated phase difference between D^0 and $\bar{D}^0$ amplitudes. At the same time the analysis technique is greatly simplified compared to a full amplitude fit.

6.1 Decay PDF Formalism

The choice of sign convention for x and y is shown in 6.1 so that the notation is consistent with the CLEO research. The mixing parameters under this convention become (as shown in section 1.2)

$$x_D \equiv \frac{M_2 - M_1}{\Gamma} \quad y_D \equiv \frac{\Gamma_2 - \Gamma_1}{2\Gamma} \quad r_{CP}e^{i\alpha_{CP}} \equiv \frac{q}{p} \tag{6.1}$$

The decay amplitude of $D^0 \to K_s\pi^+\pi^-$ can be expressed as

$$\mathcal{A}_{D^0}(m_+^2, m_-^2) \equiv a_{(m_+^2,m_-^2)}e^{\delta_{(m_+^2,m_-^2)}} \ , \ \ \mathcal{A}_{\bar{D}^0}(m_+^2, m_-^2) \equiv \bar{a}_{(m_+^2,m_-^2)}e^{\bar{\delta}_{(m_+^2,m_-^2)}}, \tag{6.2}$$

where m_+^2 and m_-^2 denote the invariant mass squared $m^2_{K_s\pi^+}, m^2_{K_s\pi^-}$ of the $K_s\pi^+$ and $K_s\pi^-$ daughter combinations respectively, and $\delta_{(m_+^2,m_-^2)}$ is the strong phase at

a given point in phasespace. Assuming no direct CP violation and due to the fact that the final state is self-conjugate[a]

$$\bar{a}_{(m_+^2,m_-^2)}e^{\bar{\delta}_{(m_+^2,m_-^2)}} = a_{(m_-^2,m_+^2)}e^{\delta_{(m_-^2,m_+^2)}} \tag{6.3}$$

Then one can write the time-dependent PDF [6][b] as

$$\begin{aligned}\mathcal{P}_{D^0}(m_+^2,m_-^2,t) =&\Gamma\left|g_+(t)\mathcal{A}_{D^0}(m_+^2,m_-^2)+\frac{q}{p}g_-(t)\mathcal{A}_{\bar{D}^0}(m_+^2,m_-^2)\right|^2\\ =&\Gamma|g_+(t)|^2a^2_{(m_+^2,m_-^2)}+\Gamma\left|\frac{q}{p}\right||g_-(t)|^2a^2_{(m_-^2,m_+^2)}\\ &+\Gamma\Re\left[\frac{q}{p}g_+^*(t)g_-(t)a_{(m_+^2,m_-^2)}a_{(m_-^2,m_+^2)}e^{i[-\delta_{(m_+^2,m_-^2)}+\delta_{(m_-^2,m_+^2)}]}\right]\\ &+\Gamma\Re\left[\left(\frac{q}{p}\right)^*g_+(t)g_-^*(t)a_{(m_+^2,m_-^2)}a_{(m_-^2,m_+^2)}e^{i[\delta_{(m_+^2,m_-^2)}-\delta_{(m_-^2,m_+^2)}]}\right]\end{aligned}$$

where we factorised the time-dependent part into $g_\pm(t) \equiv \frac{1}{2}(e^{-iz_1t} \pm e^{-iz_2t})$ with $z_{1,2} \equiv \frac{M_{1,2}-i\Gamma_{1,2}}{2}$ and $\Gamma = \frac{1}{2}(\Gamma_1+\Gamma_2)$. This follows from section 1.2. Expanding the PDF and ignoring terms of $\mathcal{O}(x_D^2), \mathcal{O}(y_D^2), \mathcal{O}(x_D \cdot y_D)$ and higher, we can rewrite the PDF as

$$\begin{aligned}\mathcal{P}_{D^0}(m_+^2,m_-^2,t) = \Gamma e^{-\Gamma t}\Big[&a^2_{(m_+^2,m_-^2)}+r_{CP}a_{(m_+^2,m_-^2)}a_{(m_-^2,m_+^2)}\Gamma t\\ &\times\Big\{y_D\cos[\delta_{(m_+^2,m_-^2)}-\delta_{(m_-^2,m_+^2)}-\alpha_{CP}]\\ &+\ x_D\sin[\delta_{(m_+^2,m_-^2)}-\delta_{(m_-^2,m_+^2)}-\alpha_{CP}]\Big\}\Big]\end{aligned} \tag{6.4}$$

We can apply binning to the Dalitz plot and integrate the PDF within a given Dalitz plot bin i

$$\begin{aligned}\int_i\mathcal{P}_{D^0} =&\Gamma e^{-\Gamma t}\left[\int_i a^2_{(m_+^2,m_-^2)}dm_+^2dm_-^2+r_{CP}\Gamma t\right.\\ &\times\left\{y_D\int_i a_{(m_+^2,m_-^2)}a_{(m_-^2,m_+^2)}\cos[\delta_{(m_+^2,m_-^2)}-\delta_{(m_-^2,m_+^2)}-\alpha_{CP}]dm_+^2dm_-^2\right.\\ &\left.\left.+\ x_D\int_i a_{(m_+^2,m_-^2)}a_{(m_-^2,m_+^2)}\sin[\delta_{(m_+^2,m_-^2)}-\delta_{(m_-^2,m_+^2)}-\alpha_{CP}]dm_+^2dm_-^2\right\}\right]\end{aligned} \tag{6.5}$$

[a] This means that, assuming no CP violation, if we overlay D^0 Dalitz plot and $\bar{D}^0$ Dalitz plot, the result will be entirely symmetric. In other words there is no way to distinguish between D^0 and $\bar{D}^0$ based on the decay products.

[b] Strictly speaking, this is not a PDF due to the missing normalization constant, and due to a missing factor of 2 coming from combining D^0 and $\bar{D}^0$ data. However, the method fits a ratio as is explained later in section 6.3 and the normalization cancels.

And we can define integrals of amplitude-weighted cosine and sine of phase difference c_i and s_i respectively

$$\begin{aligned} c_i \equiv & \frac{1}{\sqrt{T_i T_{-i}}} \int_i a_{(m_+^2,m_-^2)} a_{(m_-^2,m_+^2)} \cos(\delta_{(m_+^2,m_-^2)} - \delta_{(m_-^2,m_+^2)}) dm_+^2 dm_-^2 \\ s_i \equiv & \frac{1}{\sqrt{T_i T_{-i}}} \int_i a_{(m_+^2,m_-^2)} a_{(m_-^2,m_+^2)} \sin(\delta_{(m_+^2,m_-^2)} - \delta_{(m_-^2,m_+^2)}) dm_+^2 dm_-^2 \end{aligned} \tag{6.6}$$

with the integrals of amplitude T_i and T_{-i} defined as

$$\begin{aligned} T_i \equiv & \int_i a^2_{(m_+^2,m_-^2)} dm_+^2 dm_-^2 \\ T_{-i} \equiv & \int_i a^2_{(m_-^2,m_+^2)} dm_+^2 dm_-^2 \end{aligned} \tag{6.7}$$

Substituting these into eq. 6.4 we get

$$\begin{aligned} \mathcal{P}_{i,D^0}(t) = \Gamma e^{-\Gamma t} \Big[T_i + r_{CP} \Gamma t \sqrt{T_i T_{-i}} \times \{ & y_D \left[s_i \sin(\alpha_{CP}) + c_i \cos(\alpha_{CP}) \right] \\ & + x_D \left[s_i \cos(\alpha_{CP}) - c_i \sin(\alpha_{CP}) \right] \} \Big] \end{aligned} \tag{6.8}$$

This would be the formalism used to investigate both mixing and indirect CP violation parametrised by x_D, y_D and r_{CP}, α_{CP} respectively. Assuming no indirect CP violation (that is $r_{CP} = 1$ and $\alpha_{CP} = 0$) we can reduce this PDF to the final form

$$\begin{aligned} \mathcal{P}_{i,D^0}(t) &= \Gamma e^{-\Gamma t} \left[T_i + \Gamma t \sqrt{T_i T_{-i}} (y_D c_i + x_D s_i) \right] \\ \mathcal{P}_{i,\bar{D}^0}(t) &= \Gamma e^{-\Gamma t} \left[T_{-i} + \Gamma t \sqrt{T_i T_{-i}} (y_D c_i - x_D s_i) \right] \end{aligned} \tag{6.9}$$

These are analogous to the two body case of $D^0 \to K\pi$ [2] except that the mixing ratio R_D now becomes $R_i = T_{-i}/T_i$, and $\cos\delta_{K\pi}$ and $\sin\delta_{K\pi}$ become c_i and s_i respectively, dependent on the phase-space (see section 6.3).

6.2 CLEO Strong-Phase Information

The integrated strong phase information can be obtained using previous analyses performed by the CLEO-c collaboration[c]. The production of $\Psi(3770)$ and the decay into a quantum correlated $D^0\ \bar{D}^0$ pair allows the opposite side tagging of the CP content of one of the daughters [65]. Such analysis can provide information about the strong phase-difference $\Delta\delta_{K_s\pi^+\pi^-}$ between D^0 and $\bar{D}^0$ decaying into

[c]BES-III showed preliminary results of their analysis of the same channel at a conference [64] with 40% improved statistical precision. These are not used in this analysis.

$K_S\pi^+\pi^-$.

Originally, the model independent method discussed in this thesis was developed for extracting the angle γ of the Unitarity triangle in a $B \to DK, \quad D^0 \to K_S\pi^+\pi^-$ channel [66]. Later, it was shown that choosing a Dalitz plot binning such that the variation of the strong phase is minimised in the area of each bin improves the sensitivity of the method[d]. It was also shown that this method can be used to extract mixing information in the $D^0 \to K_S\pi^+\pi^-$ channel [67]. Lastly, it was shown that binning optimized for sensitivity to γ also has good sensitivity to charm mixing and the sensitivity of the method was evaluated using toy studies. It was determined that the current knowledge of the c_i and s_i parameters are sufficient to enable a measurement competitive with the full amplitude fit using the 2011 LHCb dataset. For larger datasets, the improvement of the measurement of c_i and s_i by next-generation charm factories would be necessary [68].

6.2.1 CLEO binning

Several non-uniform binning options were investigated for the purporse of integrating out the strong phase information. The salient criterion for the choice of binning is that it should provide good sensitivity to s_i. With this in mind, bins were chosen such that the range of $\Delta\delta_{K_s\pi^+\pi^-}$ in each bin would be equal and the variation in each bin minimal. This is equal-$\Delta\delta$ binning constructed using the BaBar 2008 model [67] and can be seen in figure 6.1.

The binning is symmetric in $m_+^2 = m_-^2$ axis with bins $-(N) \leq i \leq (N)$ and no null bin. For bin i and $-i$ the following hold

$$c_i = c_{-i}, \quad s_i = -s_{-i} \tag{6.10}$$

The limits on $\Delta\delta_{K_s\pi^+\pi^-}$ in each bin are given by

$$2\pi(i - 1/2)/\mathcal{N} < \Delta\delta_{K_s\pi^+\pi^-}(m_+^2, m_-^2) < 2\pi(i + 1/2)/\mathcal{N} \tag{6.11}$$

where $\mathcal{N}$ is the chosen number of CLEO bins. The asymmetric bin shape is implemented by the use of a map of square microbins of size $0.0054 \times 0.0054\ GeV^2/c^4$. Each microbin has an associated CLEO bin.

[d]While the binning is chosen according to model predictions, this does not introduce a model systematic error but rather reduces the statistical power of the sample [65].

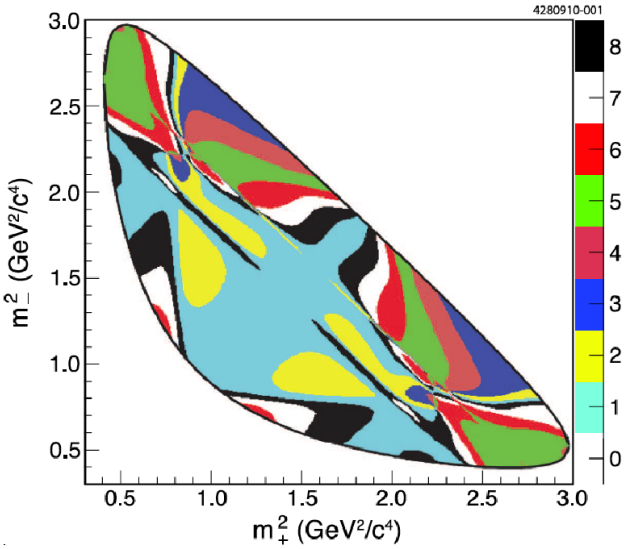

Figure 6.1: Equal-$\Delta\delta$ binning scheme designed to improve sensitivity to $\Delta\delta_{K_s\pi^+\pi^-}$ extraction [67]. The colours denote the bin number in the binning scheme.

6.2.2 Measuring CLEO parameters

The c_i and s_i parameters used in this analysis were obtained by an analysis of CLEO data performed by the CLEO collaboration [65]. Since the coefficients are crucial for this measurement, the analysis is summarised here. The CLEO analysis is based on the quantum correlated decays of $\Psi(3770) \to D^0\bar{D}^0$, $D^0 \to K_S\pi^+\pi^-$. Given that $CP(\Psi(3770)) = -1$, if one reconstructs the companion D^0 in a CP eigenstate, one gets immediate information about the CP content of the signal $\bar{D}^0$ candidate. With a CP tag and assuming no direct CP violation, the decay amplitude of $\bar{D}^0 \to K_S\pi^+\pi^-$ is given by

$$a^{CP\pm}_{(m^2_+,m^2_-)} = \frac{1}{\sqrt{2}}\left(a_{(m^2_+,m^2_-)} \pm a_{(m^2_-,m^2_+)}\right) \tag{6.12}$$

for the CP-even (+) and CP-odd (-) states of $\bar{D}^0 \to K_S\pi^+\pi^-$ decay. The number of events in the bin i of a CP-tagged Dalitz plot is then

$$M^{\pm}_i = h^{\pm}_{CP}(T_i \pm 2c_i\sqrt{T_iT_{-i}} + T_{-i}) \tag{6.13}$$

where $h^{\pm}_{CP} = S^{\pm}/2S_f$ is a normalization factor with S_f being the number of flavour tagged signal decays and $S^{\pm}$ is the number of D^0 mesons decaying into a CP eigen-

state irrespective of the other D meson (corrected for efficiencies). Alternatively, one can use the branching fractions of D^0 to a flavour tag ($\mathcal{B}_f$) and to a CP eigenstate ($\mathcal{B}^{\pm}$) to get the normalization factor $h^{\pm}_{CP} = \mathcal{B}^{\pm}/2\mathcal{B}_f$. This makes the sample single-tagged. This way, one can gain access to c_i by measuring the number of events $M\pm_i$ in a CP-tagged Dalitz plot and the number of events T_i in a flavour-tagged Dalitz plot.

The extraction of s_i is enabled by looking at both D^0 & $\bar{D}^0 \to K_S\pi^+\pi^-$ in $\Psi(3770) \to D^0\bar{D}^0$ events (double decays). In this case the amplitude becomes

$$a^{CP\pm}_{(m^2_+,m^2_-,m'^2_+,m'^2_-)} = \frac{a_{(m^2_+,m^2_-)}a_{(m'^2_-,m'^2_+)} - a_{(m'^2_+,m'^2_-)}a_{(m^2_-,m^2_+)}}{\sqrt{2}} \tag{6.14}$$

where the primed and unprimed coordinates correspond to the first and the second $\bar{D}^0 \to K_S\pi^+\pi^-$ respectively. Defining M_{ij} to be the number of events in bin i of first Dalitz plot and bin j of the second Dalitz plot respectively

$$M_{ij} = h_{corr}(T_iT_{-j} + T_{-i}T_j - 2\sqrt{T_iT_{-j}T_{-i}T_j}(c_ic_j + s_is_j)) \tag{6.15}$$

with the normalization factor $h_{corr} = N_{D\bar{D}}/2S_f^2 = N_{D\bar{D}}/8\mathcal{B}_f^2$, $N_{D\bar{D}}$ being the number of $D\bar{D}$ pairs and S_f being the number of signal flavour-tagged events as before. The sign of s_i can be obtained using weak model assumptions.

The values for R_i, c_i, and s_i measured by CLEO and used in this analysis can be seen in appendix H. The fit of the c_i and s_i parameters, as well as the 2008 BaBar model prediction can be seen in figure 6.2 where the unit circle $c_i^2 + s_i^2 = 1$ is also indicated.

6.2.3 Comparison of CLEO model with 2010 BaBar model

The study that developed the binning used the BaBar 2008 model [60] to predict the bin boundaries based on the phase difference content. Since then, an improved model became available, denoted the BaBar 2010 model [59].

An analysis of the statistical power of the binning under the BaBar 2010 model shows minimal degradation compared to the 2008 model [65] suggesting negligible impact on the mixing parameter extraction.

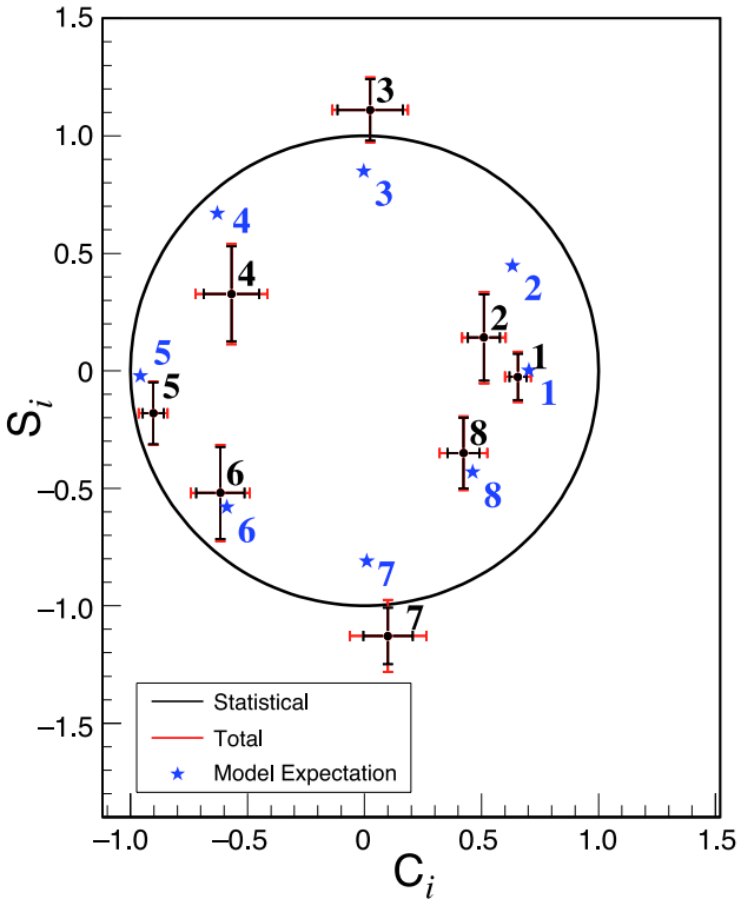

Figure 6.2: The fit of c_i and s_i parameters performed in the CLEO analysis [65]. The BaBar 2008 model predictions are indicated by blue stars. The unit circle $c_i^2 + s_i^2 = 1$ is also shown. Adopted from [65].

6.3 Fit Strategy

The fitting strategy uses a χ^2 minimization fit of a modified[e] time-binned ratio of numbers of events in bin i and bin $-i$. The fitted variable is

$$R(t) = \frac{N_{-i,sig}(t)}{N_{i,sig}(t)} \tag{6.16}$$

where R is binned in D^0 decay time and $N_{i,sig}$ is the background-subtracted number of events in bin i.

[e]The method tries to fit a ratio of time-dependent PDFs describing the signal yields in bin i and $-i$. The ratio is simplified by the use of Taylor expansion with higher order terms dropped. It's fitted to the measured ratio of background subtracted yields.

This approach requires the binning of the R distribution to be sufficiently fine so that the integration of $\mathcal{P}_i$ is not necessary in the fit bin. This analysis uses adaptive binning with the condition that $N_{i,j} + N_{-i,j} > 350$ in each CLEO bin i and decay time bin j. This means that each bin i will have a different decay time binning scheme j.

The choice of the fitted ratio is motivated by the predicted shape of the ratios of the dataset and due to simplification in algebra

$$R(t) = \frac{T_{-i} + \sqrt{T_i T_{-i}}\Gamma t(c_i y_D - s_i x_D)}{T_i + \sqrt{T_i T_{-i}}\Gamma t(c_i y_D + s_i x_D))} \tag{6.17}$$

or, substituting $R_i \equiv T_{-i}/T_i$ (values for R_i can be seen in appendix H)

$$R(t) = \frac{R_i + \sqrt{R_i}\Gamma t(c_i y_D - s_i x_D)}{1 + \sqrt{R_i}\Gamma t(c_i y_D + s_i x_D)} \tag{6.18}$$

This reduces the number of CLEO parameters by 8 and improves the fit stability. One can also use Taylor Expansion which simplifies the fitted formulation to

$$R = R_i + \sqrt{R_i}\Gamma t[(c_i y_D - s_i x_D) - R_i(c_i y_D + s_i x_D)] + R_i\Gamma^2 t^2(c_i^2 y_D^2 - s_i^2 x_D^2) + \dots \tag{6.19}$$

in regions of parameter space where the following holds, assuming $x_D \sim y_D \sim \mathcal{O}(0.01)$ and $c_i \sim s_i \sim \mathcal{O}(1)$ and $0 \leq \Gamma t \leq 15$

$$\begin{aligned} \sqrt{R_i}\Gamma t(c_i y_D + s_i x_D) &\ll 1 \\ \sqrt{R_i} &\ll \frac{50}{\Gamma t} \\ \sqrt{R_i} &\ll 3.34 \end{aligned} \tag{6.20}$$

This requires R_i to be reasonably small, but it's expected that the $T_{-i} \leq T_i, \;\; R_i \leq 1$ due to the Cabibbo suppression (see section 1.2.1). We can then neglect the $\mathcal{O}(x^2), \mathcal{O}(y^2)$ terms to get the final form

$$\begin{aligned} R &= R_i + \sqrt{R_i}\Gamma t[(c_i y_D - s_i x_D) - R_i(c_i y_D + s_i x_D)] \\ R &= R_i + \sqrt{R_i}\Gamma t[(1 - R_i)c_i y_D - (1 + R_i)s_i x_D] \end{aligned} \tag{6.21}$$

The final form of the fitted function is linear as can be seen from eq. 6.21. Also, given that $R_i \sim 0.5$ on average, the fitted pdf indicates that this method will be more sensitive to x_D than y_D by a factor of approximately 3[f].

The fit is performed simultaneously in all CLEO bins and decay time bins, with R_i being specific CLEO bin i, c_i and s_i fixed, and all other parameters being global. The interdependence of c_i and s_i is included transparently in the systematic effect due to the their uncertainty.

6.3.1 CLEO penalty term

There are two approaches that can be used to constrain the c_i, s_i and R_i parameters used as input to the fit. One can simply fix the values obtained using the CLEO analysis. The advantage of this is a much more stable fit while the disadvantage is that the uncertainty due to limited knowledge these parameters is not propagated automatically through to the final fit and has to be obtained in a different way.

The second possibility is to use a multi-dimensional Gaussian constraint evaluated using the covariance matrix and add this as the penalty term to the minimized χ^2. The advantage is that the associated systematic uncertainty is automatically propagated through to the final fit, however the fit stability suffers.

The covariant constraint term χ^2_{CLEO} can be formulated as

$$\chi^2_{c_i,s_i} \equiv \sum_{ij}^{16} (p_i - \bar{p}_i)\Sigma_{ij}(p_j - \bar{p}_j), \tag{6.22}$$

where i, j run from 1 to 16, p_i represents c_i for $i < 8$ and s_{i-8} for $i > 8$, Σ_{ij} is the covariance matrix for c_i and s_i as measured originally by CLEO, and $\bar{p}_i$ is the value of p_i measured by CLEO. The penalty term for R_i parameters are calculated using a Gaussian constraint

$$\chi^2_{R_i} \equiv \sum_{i}^{8} \frac{(R_i - \bar{R}_i)^2}{\sigma^2_{R_i}}, \tag{6.23}$$

where the variance of ratio $\sigma^2_{R_i}$ is calculated using simple propagation of errors for ratios

$$\sigma^2_{R_i} = R_i^2 \left(\frac{\sigma^2_{T_i}}{T_i^2} + \frac{\sigma^2_{T_{-i}}}{T_{-i}^2} \right). \tag{6.24}$$

[f]The ratio of R_i is generally constrained in $(0, 1)$. The final PDF depends on $(1 - R_i)c_i y_D - (1 + R_i)s_i x_D$. Doing a naive calculation, assuming $c_i = s_i, R_i \sim 0.5$ on average, we're left with the PDF depending on $0.5y_D - 1.5x_D$ which suggests better sensitivity to x_D rather than y_D

Then the complete penalty term is

$$\chi^2_{\rm CLEO} \equiv \chi^2_{c_i,s_i} + \chi^2_{R_i} \tag{6.25}$$

After careful testing, the fit staility was considered more important and therefore the method presented uses fixed CLEO parameters and evaluates the systematic uncertainty associated with the input parameters using a data driven method in chapter 8.

6.3.2 Minimization function

The minimization function is a simple χ^2 binned in Dalitz space (index i) and D^0 decay time (index j)

$$\chi^2_{\rm data} \equiv \sum_i \sum_j \frac{[R_i(\bar{t}_{i,j}) - \frac{N_{i,j}}{N_{-i,j}}]^2}{\sigma^2_{i,j}} \tag{6.26}$$

where $N_{i,j}$ is the number of signal events in time bin j in a Dalitz bin [g] i, $\bar{t}_{i,j}$ is the mean D^0 lifetime in bin i,j and $\sigma_{i,j}$ is the combined Poisson error in bin i,j

$$\sigma_{i,j} = R_{i,j}\sqrt{\frac{1}{N_{i,j}} + \frac{1}{N_{-i,j}}}. \tag{6.27}$$

The full function that is minimized by varying x_D and y_D (and other input parameters varied within their contraints) is then simply the sum

$$\chi^2 \equiv \chi^2_{\rm CLEO} + \chi^2_{\rm data}. \tag{6.28}$$

The fit performed on a toy MC sample with the same yield as the dataset used in this analysis can be seen in Figures 6.3, 6.4, 6.5 and 6.6.

6.3.3 Treatment of Data Contamination

The purity of the dataset is very good (see section 4.7) and the residual contamination can be simply subtracted on a bin by bin basis from the total number of events in the bin to get $N_{i,j,sig}$. Integrating the functional forms for $n_{cat}(t)$ obtained in chapter 4, one gets the expected yield of background events in each bin $N_{i,j,bg}$ which is simply subtracted from the total number of events in bin i,j.

[g] Recall that each bin i has its own time-binning scheme j

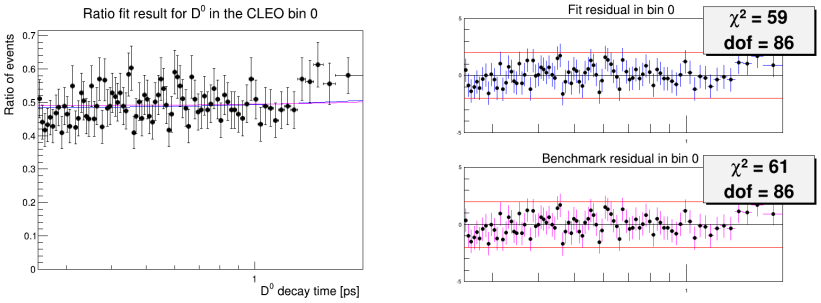

(a) CLEO bin 1 fit to $R(t)$

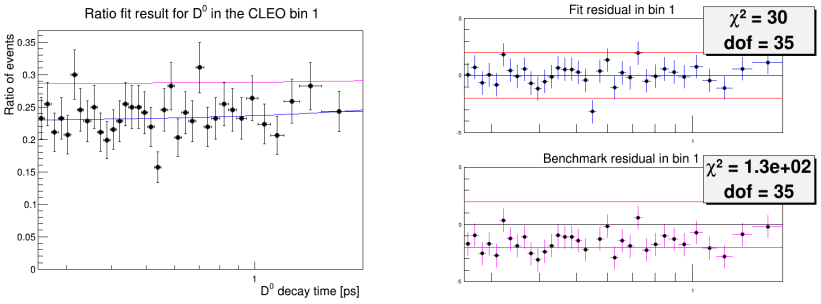

(b) CLEO bin 2 fit to $R(t)$

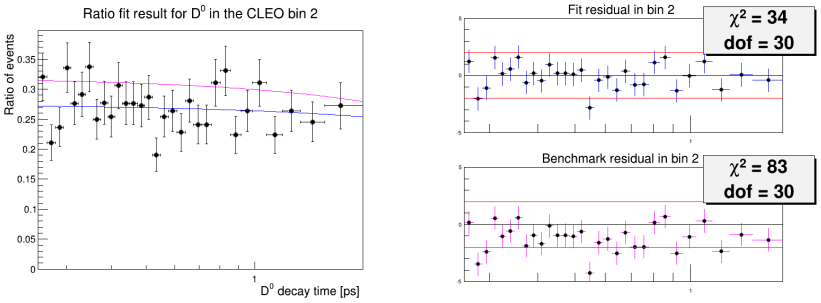

(c) CLEO bin 3 fit to $R(t)$

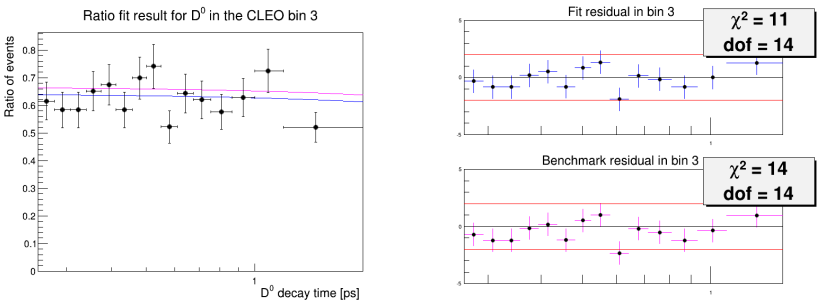

(d) CLEO bin 4 fit to $R(t)$

Figure 6.3: Simultaneous fit to $R(t)$ on a toy MC sample with yield of 166k events in CLEO bins 1-4 for $D^0 \to K_S\pi^+\pi^-$ events. The decay time on the x-axis is in logarithmic scale. Fit result is blue, reference fit with $x_D = y_D = 1\%$ is in magenta. Pulls are shown on the right for both fits.

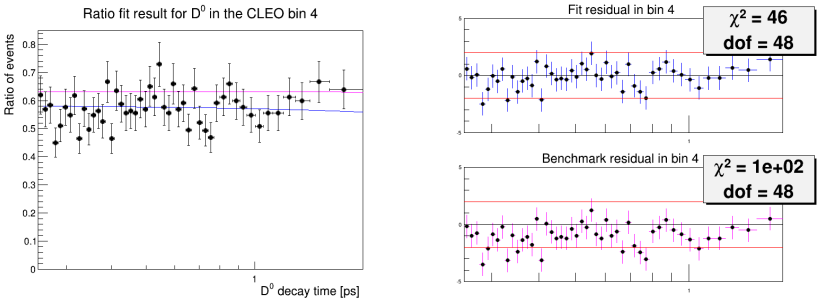

(a) CLEO bin 5 fit to $R(t)$

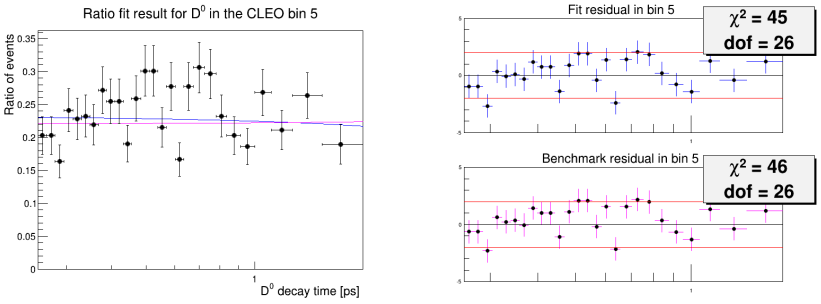

(b) CLEO bin 6 fit to $R(t)$

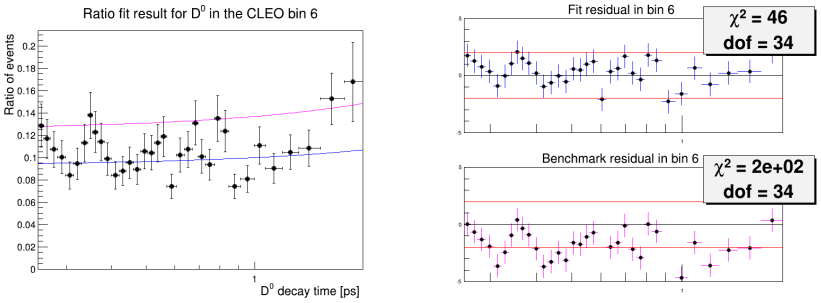

(c) CLEO bin 7 fit to $R(t)$

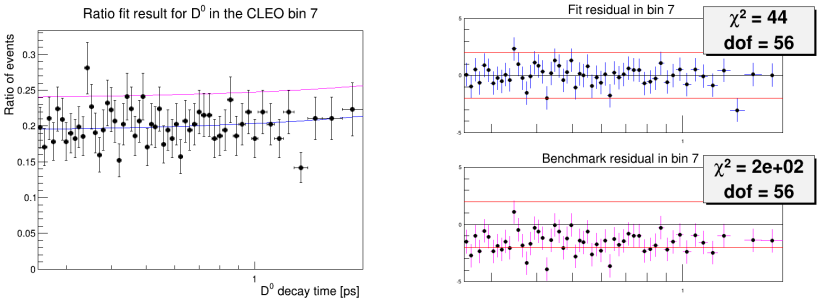

(d) CLEO bin 8 fit to $R(t)$

Figure 6.4: Simultaneous fit to $R(t)$ on a toy MC sample with yield of 166k events in CLEO bins 5-8 for $D^0 \to K_S\pi^+\pi^-$ events. The decay time on the x-axis is in logarithmic scale. Fit result is blue, reference fit with $x_D = y_D = 1\%$ is in magenta. Pulls are shown on the right for both fits.

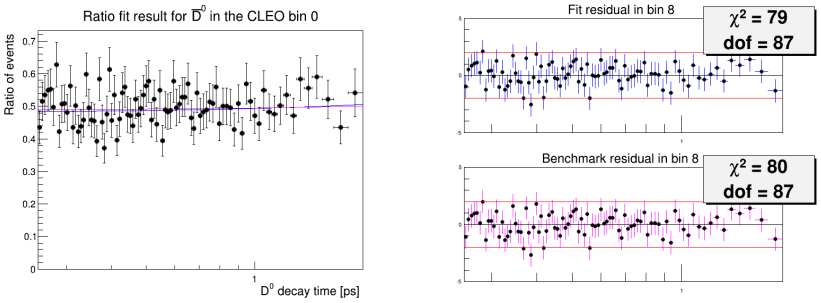

(a) CLEO bin 1 fit to $R(t)$

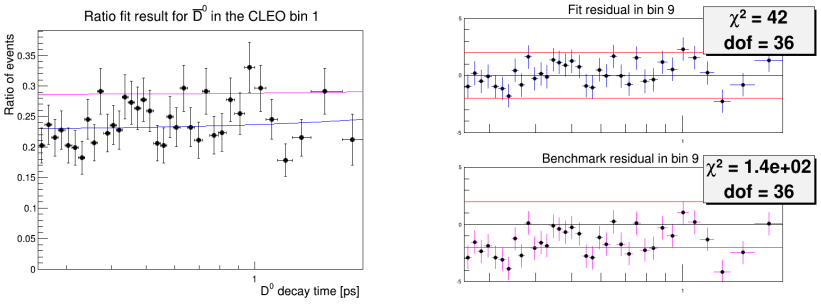

(b) CLEO bin 2 fit to $R(t)$

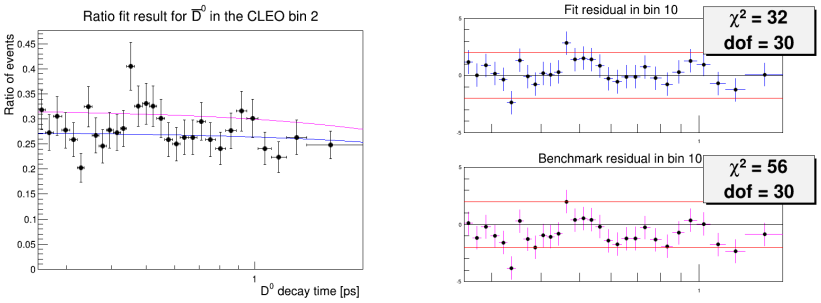

(c) CLEO bin 3 fit to $R(t)$

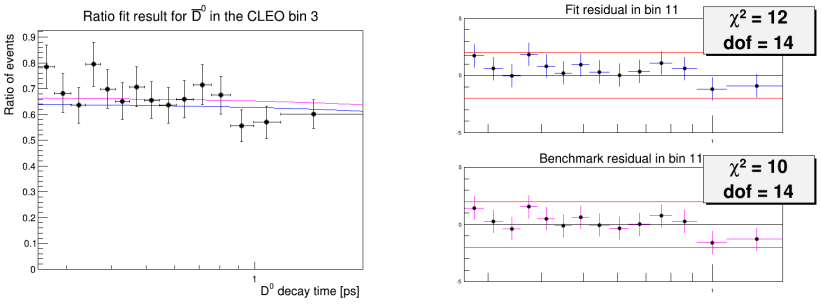

(d) CLEO bin 4 fit to $R(t)$

Figure 6.5: Simultaneous fit to $R(t)$ on a toy MC sample with yield of 166k events in CLEO bins 1-4 for $\bar{D}^0 \to K_S\pi^+\pi^-$ events. The decay time on the x-axis is in logarithmic scale. Fit result is blue, reference fit with $x_D = y_D = 1\%$ is in magenta. Pulls are shown on the right for both fits.

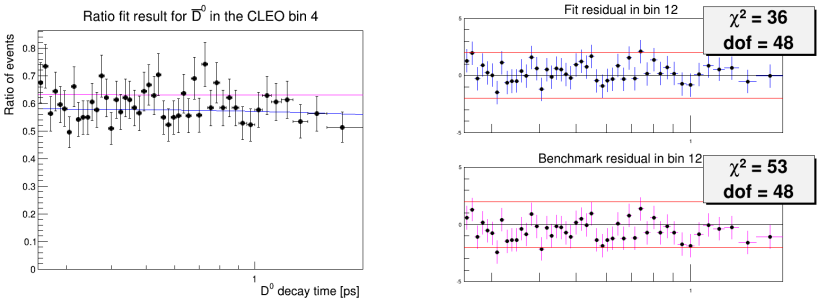

(a) CLEO bin 5 fit to $R(t)$

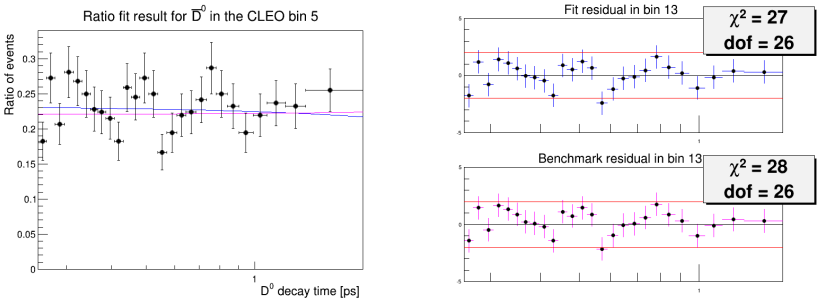

(b) CLEO bin 6 fit to $R(t)$

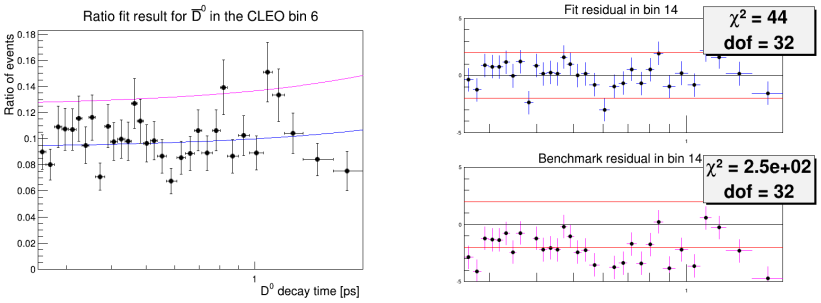

(c) CLEO bin 7 fit to $R(t)$

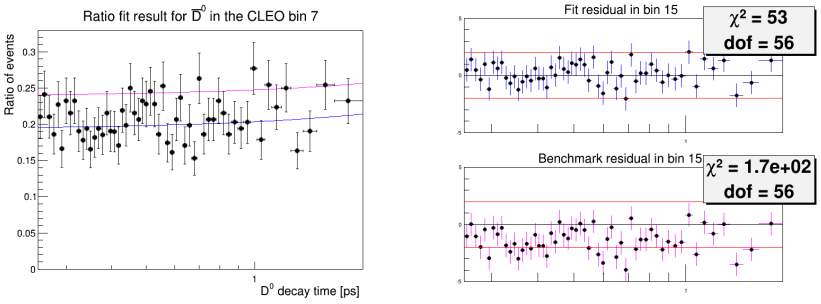

(d) CLEO bin 8 fit to $R(t)$

Figure 6.6: Simultaneous fit to $R(t)$ on a toy MC sample with yield of 166k events in CLEO bins 5-8 for $\bar{D}^0 \to K_S\pi^+\pi^-$ events. The decay time on the x-axis is in logarithmic scale. Fit result is blue, reference fit with $x_D = y_D = 1\%$ is in magenta. Pulls are shown on the right for both fits.

6.4 Fit Robustness

The fit was evaluated for stability using different versions of toy Monte Carlo (for MC samples used and the method of generation see section 3.2). First, the fit was evaluated on 500 different samples generated using the PDF described by equation 6.9[h] using an accept-reject method (up to a Poisson fluctuated yield) to get a decay time distribution of events in each CLEO bin. These samples were then binned using the adaptive binning and treated in the same way as real data. The fit results (absolute values of x_D, y_D and their respecive pulls) can be seen in Figure 6.7. Ideally, the pull plots should be centered at zero with unit width. The biases indicated by the means of the Gaussians fitted to the pull distributions are small enough to be safely neglected. The width of the pull gaussians indicates that the fitter overestimates the statistical error on the mixing parameters by a factor of ~ 1.8. This is not well understood but presumably is due to the method of generation used to produce the toy MC sample.

The fit was then validated using a second sample of Monte Carlo, produced using the BaBar 2010 full amplitude model. The fit results (absolute values and pulls of x_D and y_D) can be seen in Figure 6.8. The pulls are reasonably well centered on the origin, with the pulls introducing a small bias into the measurement at 13% of σ_{y_D} and 9% of σ_{x_D} which, when added in quadrature, can be neglected. This pull is most likely caused by the fact that the toys were generated by the BaBar 2010 model but were fitted with the CLEO values for the CLEO parameters. Similarly, the width of the pull of the x_D parameter suggests the fit overestimates the error on this parameter. This is not properly understood but is associated with the method of production for the MC sample.[i]

Additionally the χ^2 profile based on full amplitude MC can be seen in the Figure 6.9. The profile shows a single minimum, indicating the fit is stable. The χ^2 profile also shows that the method is more sensitive to x_D than y_D by a factor of ~ 3 as seen in section 6.3.

[h] In these, the x and y were set to 1% and the decay time was fixed to the world average [6]

[i] This effect was investigated at length and amongts the potential causes were excluded: choice of CLEO parameter values, CLEO parameter uncertainties, CLEO parameter correlations, approximations in the PDF formulation, interdependence of CLEO bins, decay time uncertainty, choice of amplitude model. Given that the fitter overestimates errors rather than underestimates them it is not considered a serious problem but an avenue of exploration for further analyses.

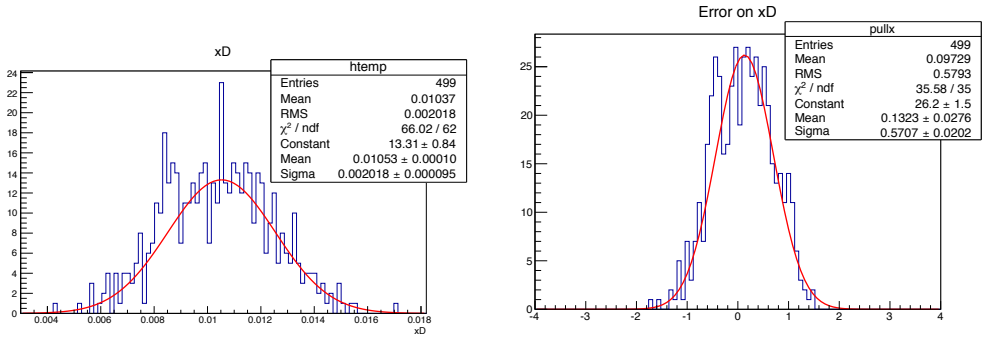

(a) Absolute value of x_D.

(b) Pull of x_D.

(c) Absolute value of y_D.

(d) Pull of y_D.

Figure 6.7: Absolute values and pulls of 500 fits to simple toy MC.

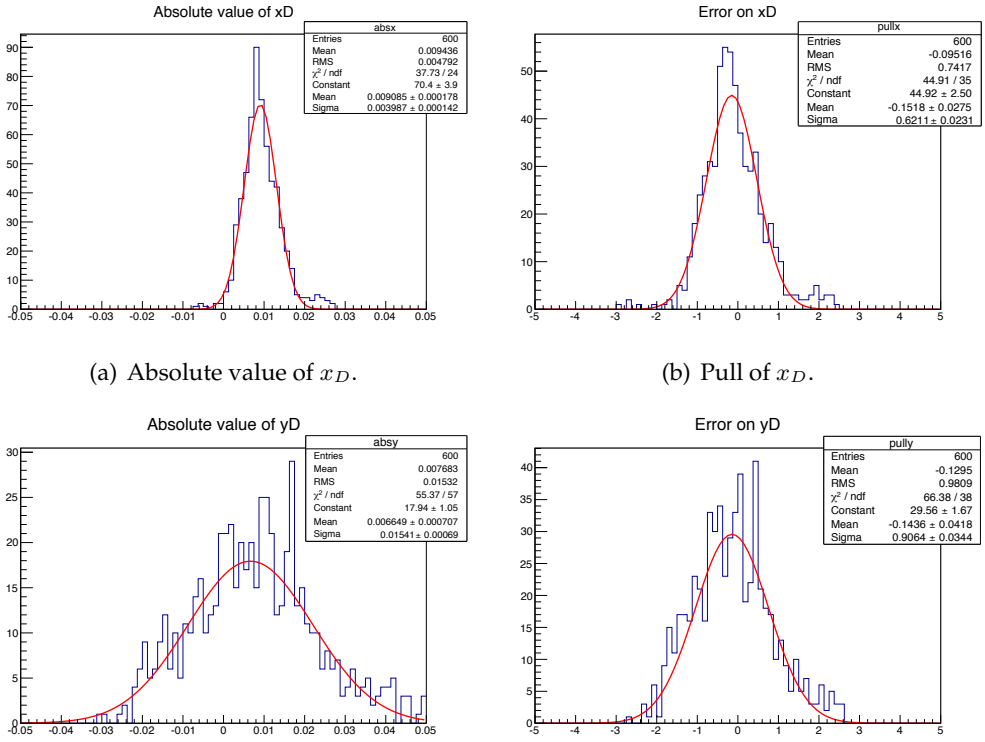

(a) Absolute value of x_D.

(b) Pull of x_D.

(c) Absolute value of y_D.

(d) Pull of y_D.

Figure 6.8: Absolute values and pulls of 600 fits to full amplitude toy MC.

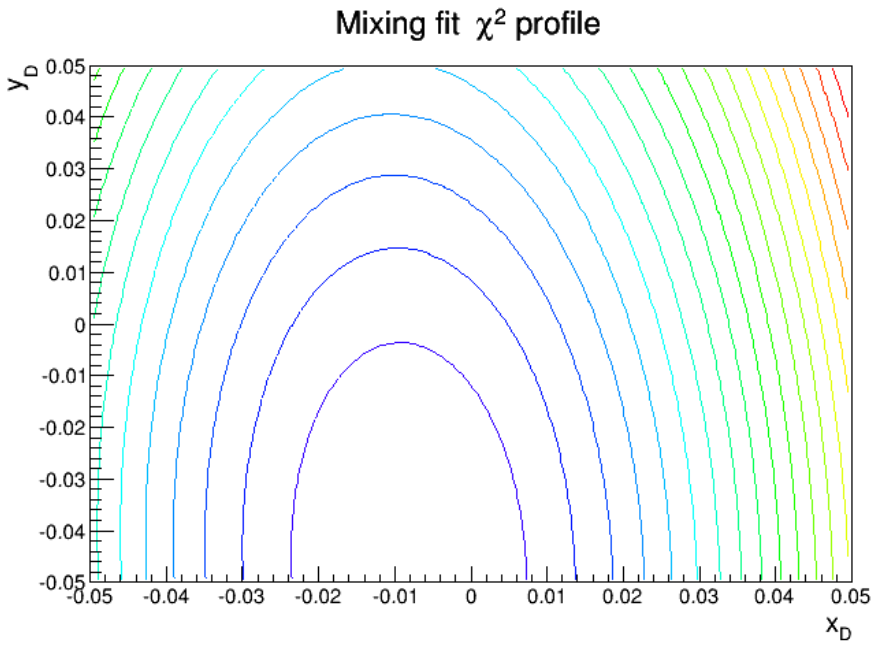

Figure 6.9: The χ^2 profile of a fit to a full amplitude MC sample. The profile shows a single minimum. The contours do not correspond to any scale and simply illustrate the well behaved range of the fit.

6.5 Efficiency variation across the Dalitz plot

Due to the binning described in section 6.2.1 the strong phase δ_D information is integrated over an area in the Dalitz plot. The binning was chosen to minimise the δ_D variation within each bin. If the reconstruction efficiency depends on the Dalitz coordinates of the event, this could enhance variation of δ_D across each bin in non-trivial way, potentially biasing the final fit. For this purpose, the estimation of the phase-space dependent efficiency $\epsilon(m^2_{12}, m^2_{13})$ is necessary. The actual estimation of the systematic effect of the selection on the measurement is shown in section 7.3. This section describes the way the efficiency model was obtained.

The efficiency is extracted using Monte Carlo generated with a flat phase-space model that is subsequently passed through trigger and selection. The curvature of the shape of the phase-space after reconstruction in Figure 6.10 indicates the efficiency due to position in the Dalitz plot.

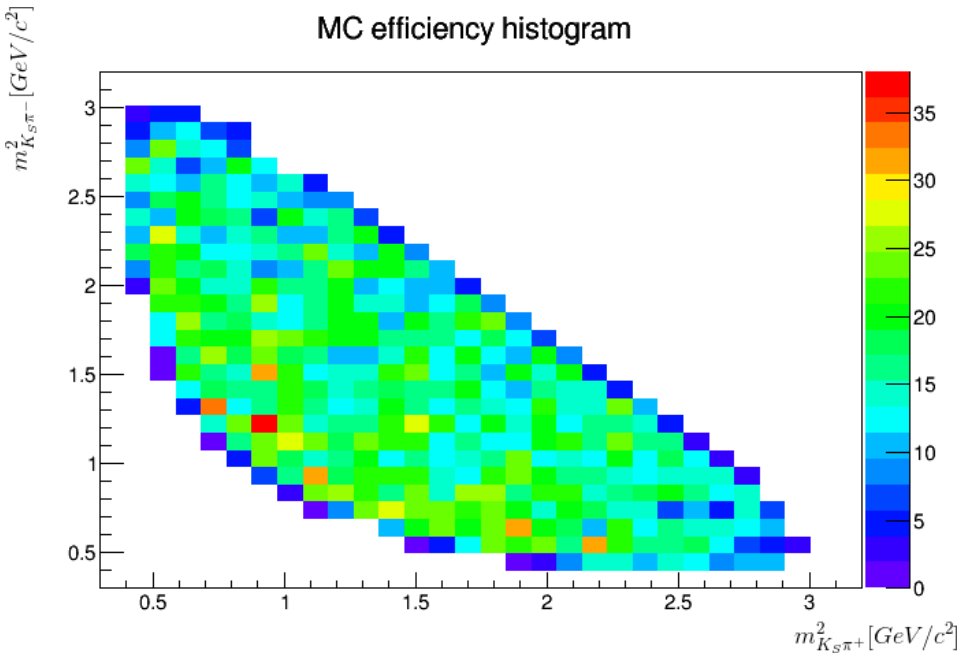

Figure 6.10: The flat phase-space Monte Carlo after reconstruction shows non-flat distribution due to the reconstruction and selection efficiency. The colour scale denotes the number of events in the sqaure phase-space bin.

The model to parametrize the efficiency

$$\begin{aligned}\epsilon(m_+^2, m_-^2) =& au^3 + bu^2 + cu^2v + du + euv + fv + gv^2 + hv^3 \\ u =& (m_+^2 + m_-^2),\ v = |m_+^2 - m_-^2|\end{aligned} \tag{6.29}$$

was chosen from several candidate polynomials of different orders by comparing the χ^2 per degree of freedom. Note that this model is symmetric under the $m_+^2 \leftrightarrow m_-^2$ transformation by construction.

The illustration of the model and the pull of the fit are shown in Figures 6.11 and 6.12. The bins with pull over 3σ are edge bins with low statistics where Poisson approximation of standard deviation breaks down.

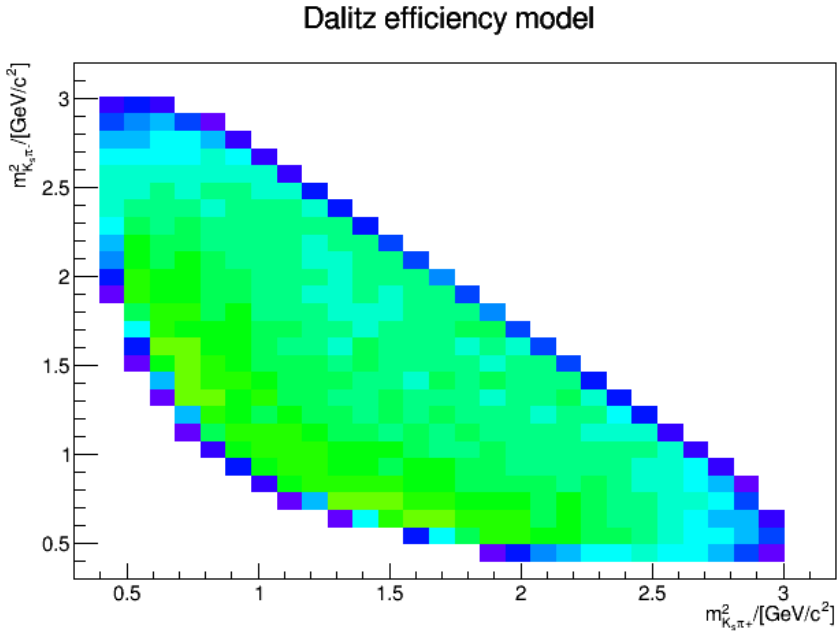

Figure 6.11: The efficiency model fitted to the Monte Carlo.

Due to the slow variation of the efficiency across the phase-space, it is not expected that it will have a large impact on the systematic error of the final measurement. This is evaluated in more detail in chapter 7.

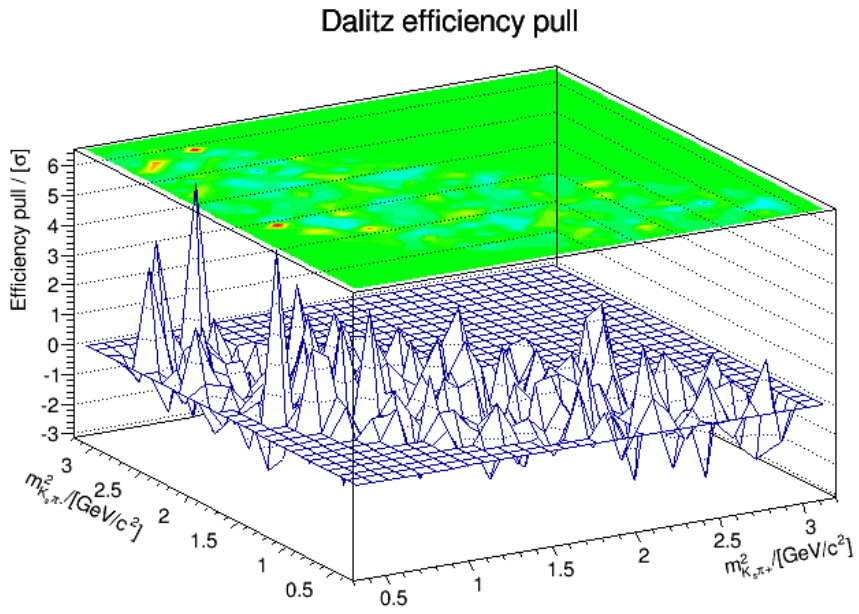

Figure 6.12: The pull of the efficiency model fit to the Monte Carlo. Bins with large pulls are low-statistics boundary bins.

Chapter 7

Sources of Systematic Uncertainty

This chapter discusses the sources of systematic uncertainty for the measurement, and how the magnitudes of the systematic uncertainties are determined. A summary of the systematic uncertainties can be seen in Table 7.1.

Source of uncertainty	$x_D(\%)$	$y_D(\%)$
Fitter bias	0.09	0.34
Decay time bias	0.07	0.71
Sel. Efficiency asymmetry	0.05	0.09
Sel. Efficiency model	0.02	0.01
Efficiency effect on binning	0.08	0.07
PID MC-data discrepancy	Negl.	Negl.
Combinatoric background	0.14	0.80
Misreconstructed π_s	0.03	0.08
Secondary contamination	0.04	0.07
Total systematic uncertainty	0.21	1.13

Table 7.1: Summary of all absolute systematic uncertainties estimated in this analysis.

7.1 Fitter bias

The stability of the fitter that minimizes the function described in section 6.3.2 was investigated in section 6.4 and was found to be stable. Based on toy MC studies, a small bias on the extracted mixing parameters was found and the absolute magnitude of this bias is applied as an associated systematic uncertainty on the extraction of the mixing parameters.

While the bias in theory could be corrected for, based on estimates, the fit bias is not a dominant systematic uncertainty and thus can be left uncorrected.

7.2 CLEO Strong-Phase Information

A significant source of the systematic uncertainty is the limited knowledge of the strong phase difference as determined by CLEO [65]. The magnitude of the uncertainty can be determined by performing parallel fits with toy MC as shown in section 6.4 with constrained CLEO parameters. The uncertainty determined is the combination of the statistical uncertainty and the systematic uncertainty due to CLEO parameter constraint. One can remove the statistical uncertainty in quadrature (to get the statistical uncertainty, the same set of fits is performed with the CLEO parameters fixed to their central values) yielding purely the systematic uncertainty due to the CLEO parameter constraint.

Alternatively, one can perform repeated fit to data with CLEO parameters fluctuated using a multi-dimensional Gaussian constraint. The extracted values of mixing parameters can be plotted and fitted with a Gaussian distribution. The width of the distribution represents the systematic uncertainty due to limited knowledge of the CLEO parameters. This is shown in chapter 8.

The toy MC fits with CLEO parameters fixed and fluctuated within constraint can be seen in Figure 7.1 and the corresponding uncertainties are shown in Table 7.2.

Uncertainty	$x_D(\%)$	$y_D(\%)$
Combined	0.38	1.49
Statistical	0.38	1.36
Systematic	0.05	0.60

Table 7.2: Table of absolute uncertainties due to knowledge of CLEO parameters.

There is no significant bias when fitting with the CLEO parameters fixed. The systematic uncertainty coming from the CLEO parameters is however also evaluated on data and is found to be significantly different from the result from toy MC. This is attributed to the fact that the toys are generated with different values of CLEO parameters compared to those extracted by the CLEO analysis and that the degree of fluctuation of the CLEO parameters in toys is difficult to replicate. Therefore this analysis uses the data-driven method to assign the systematic uncertainty as shown in chapter 8.

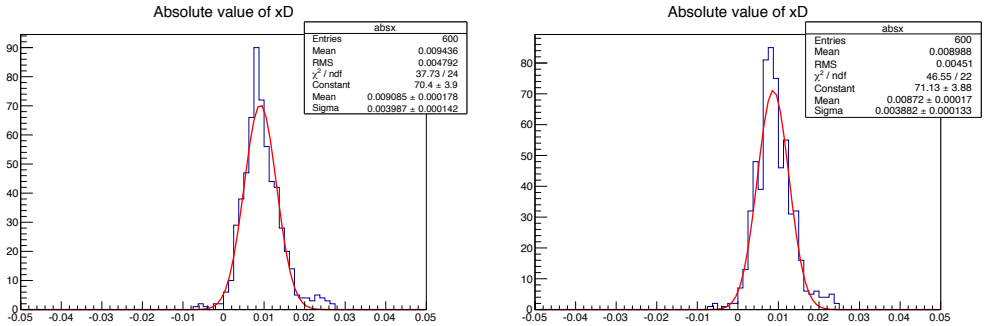

(a) Absolute value of x_D. Fluctuated CLEO parameters

(b) Absolute value of x_D. Fixed CLEO parameters.

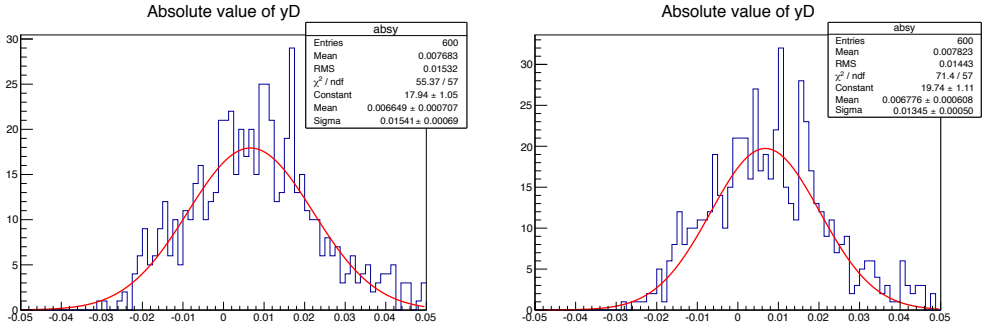

(c) Absolute value of y_D. Fluctuated CLEO parameters

(d) Absolute value of y_D. Fixed CLEO parameters.

Figure 7.1: Absolute values of 600 fits to full amplitude toy MC with fluctuated CLEO parameters (left) and fixed CLEO parameters (right).

For the analysis of the combined dataset at LHCb from 2011 and 2012, the systematic error due to the knowledge of CLEO parameters will most likely be the dominant uncertainty [68]. The analysis of quantum correlated $\Psi(3770)$ decays at BES-III should provide better precision on the measurement of the c_i and s_i parameters in the future.

7.3 Selection

The selection used to purify the dataset is described in chapter 3. The application of the selection can in general bias the resulting Dalitz plot distribution which would in turn introduce a bias into the measurement.

The measurement is performed by fitting the time dependent ratio of yields in CLEO bin i and bin $-i$, thus a Dalitz plot bias that is asymmetric in the $m^2_+ = m^2_-$

reflection axis is a source of systematic uncertainty. This potential bias was already investigated in section 6.5 where a symmetric model was fitted to the Dalitz plot of a MC sample after performing the selection.

The systematic uncertainty arising due to this asymmetry can be evaluated by applying the efficiency model (normalised such that the maximum of the efficiency is unity) as a correction on the signal yield in each CLEO bin and time bin[a] and performing the measurement on suchly modified simulated data. This can be safely performed on a toy MC sample that is used to validate the fitter, this has the benefit of being able to repeat the fit 600 times and obtain a much clearer picture of the bias. The change in the distribution of the measurements compared to the original set of measurements performed for fit stability will reveal potential bias due to selection efficiency.

The selection also contains particle identification cuts (see sections 2.4 and 3.4). While these are in theory included in the previous estimates as a part of the selection, there is a systematic uncertainty coming from the fact that the LHCb Monte Carlo is not perfect at describing the PID performance of the detector. This can cause a systematic bias if the PID performance is not symmetric in the $m^2_+ = m^2_-$ reflection axis in the Dalitz plot as before. Given the nature of the cuts, this is equivalent to PID efficiency being different for π^+ and π^-. To determine the magnitude of this effect, one can plot the PID performance for the data (as a function of p and p_T of the particle), reduce the inefficiency by the PID inefficiency determined from MC (to correct for the systematic uncertainty already accounted for previously), use this map to weigh the symmetric efficiency model due to position in Dalitz plot and use the resulting map as an efficiency correction in toy MC fits. The resulting bias is the systematic effect due to the discrepancy between the PID performance in MC and in data.

The efficiency due to the selection is not constant across the CLEO bin and therefore a systematic effect can arise if the population of a given CLEO bin is depleted in a non-uniform way. To quantify this effect, each CLEO bin is subdivided into three partitions with equal area (see Figure 7.2 for illustration), the fit ratio is evaluated in each sub-bin and a population weighed average is used instead of full population ratio. The modified ratio is then used in the standard fit with an asymmetric efficiency model and the pull is compared to the pull on normal binning result. The difference is assigned as the systematic uncertainty due to the Dalitz plot binning.

[a] Alternatively it can be used as a per event weight (especially if the fitting approach requires more information than simple yields.

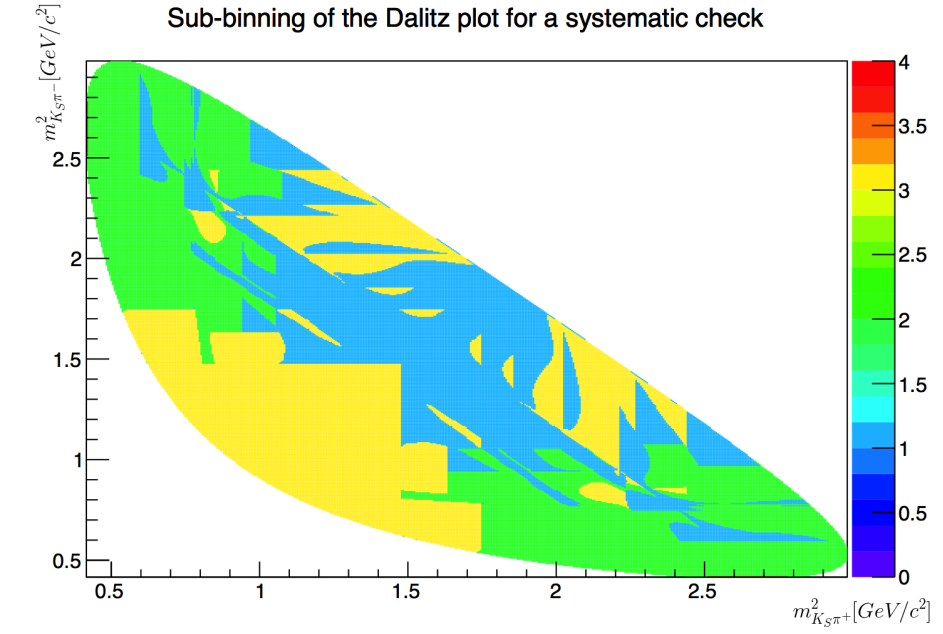

Figure 7.2: Illustration of the sub-binning across the Dalitz plot. The CLEO binning is not visible, but the boundaries between different sub-bins are indicated by the change of colour, otherwise the colour scale is immaterial. The areas of the three sub-bins are equal.

The estimated systematic uncertainties on the measurement due to the selection process are shown in Table 7.3. They are well under the sensitivity limit of the methods to obtain them and therefore can be safely neglected.

Source of syst. uncertainty	$x_D(\%)$	$y_D(\%)$
Efficiency asymmetry	0.05	0.09
Efficiency model	0.02	0.01
PID MC-data discrepancy	Negl.	Negl.
Efficiency effect on binning	0.08	0.07

Table 7.3: The absolute systematic uncertainties on the measurement of the mixing parameters due to the selection.

7.4 Background contamination

A significant source of systematic uncertainty is due to the contamination of the signal with background events. To reduce this effect, the background is removed from the dataset by the use of selection (chapter 3) and yield estimation and

subtraction (chapter 5). Nevertheless the function estimating the background is not perfect, some contamination remains and a systematic bias has to be evaluated.

The combinatorial background is removed in each time bin and CLEO bin separately, the time-evolution of the combinatorial background (the choice of model and goodness of fit) as well as the uncertainty on the total yield will propagate as a systematic error on the measurement. To estimate the magnitude of the effect one can propagate the uncertainty onto the yields of signal events in each bin and fit the dataset. The increase in uncertainty can be removed in quadrature to get the effect due to the combinatorial background estimation technique.

The systematic effect due to misreconstructed π_s can be estimated by propagating the error on the fraction of the misreconstructed π_s component through to the yields on each bin and removing the statistical error in quadrature.

The systematic error due to the secondary background is more tricky to determine. The fit to data assumes that the secondary events behave like signal. This is an incorrect assumption, but it sets an upper bound on the decay times of the true secondary component. One can determine the lower bound on the decay time by assuming that secondaries do not mix [2]. To achieve such a dataset, one can add toy MC with standard mixing and toy MC with no mixing in the time dependent proportion determined by the fit to the $Ln(\chi^2_{IP})$ distribution (see section 4.5). The difference in the bias of toy fits to both datasets is the systematic uncertainty due to the secondary contamination.

The systematic uncertainties on the measurement of the mixing parameters due to the background estimation and contamination can be seen collected in Table 7.4.

Source of syst. uncertainty	x_D	y_D
Combinatoric background	0.14	0.80
Misreconstructed π_s	0.03	0.08
Secondary contamination	0.04	0.07

Table 7.4: Absolute systematic uncertainties on the measurement of the mixing parameters due to the background estimation and contamination.

7.5 Tag efficiency

The efficiency of the tag does not cause a systematic uncertainty since the events with a wrong tag are contained entirely in the Category 2 dataset component

(Misreconstructed π_s). Since the fraction of Category 2 events is determined using real data independently in each CLEO bin, this covers any potential asymmetry in the tagging mechanism. See the previous subsection for a systematic uncertainty associated with the contamination due to Category 2 events.

7.6 Decay time bias

Potential bias on the decay time of the D^0 candidate can cause a systematic effect if this bias is not symmetric on the opposite sides of the Dalitz plot. This is is assumed to be true for the signal candidates but would be difficult to determine for combinatorial background and secondary contamination. A systematic uncertainty is assigned due to this issue by extracting per-event weights using the swimming technique (see appendix B) in the form of top-hat functions that determine the part of the decay time domain where the event would be accepted. An accept-reject MC algorithm chooses a random top-hat from this distribution for each event and checks whether the decay time of the candidate lies within the top hat. The event is rejected if it does not. A toy study accounting for the acceptance in this way shows a minor bias which is used as a systematic uncertainty. Interestingly, it's mostly the measurement of y_D that is affected by the bias rather than the measurement of x_D which is unbiased. This could be consistent with the fact that y_D is the difference in decay widths of the two flavour eigenstates while x_D is the difference in mass.

7.7 Systematic uncertainty cross-checks

The effects listed in table 7.5 were investigated and were found to have no effect on the final measurement and therefore do not contribute a systematic uncertainty to the final measurement.

Source of syst. uncertainty	Cross-check method
m_D model	Add bifurcated Gaussian to the model.
Δm model	Add bifurcated Gaussian to the model.
$Ln(\chi^2_{IP})$ binning	Modify the bin size for the adaptive binning
$Ln(\chi^2_{IP})$ model	Add a Gaussian to each category
Taylor expansion in fit PDF	Fit without the Taylor expansion
Wrong PV association	Randomly associate events with a different PV
Domain size	Validated with MC with x & y sampled from a large domain

Table 7.5: Table of effects that were found to not contribute a systematic effect to the final measurement. Each potential source of uncertainty has an associated method of cross-cheking that was performed and no effect on the final fit was observed.

Chapter 8

Results

The final fit to the data is illustrated in Figure 8.3, 8.4, 8.5 and 8.6. The collected uncertainties are shown in Table 8.1. The systematic uncertainty due to the CLEO parameters is determined by repeated fits to the dataset with the CLEO parameters fluctuated using an accept-reject MC method with the covariant multi-dimensional Gaussian constraint as the distribution. Fitting a Gaussian PDF to the resulting distribution of results yields the systematic uncertainty due to CLEO parameters as the width of the Gaussian PDF. This is shown in figure 8.1 and the respective values are shown in Table 8.1.

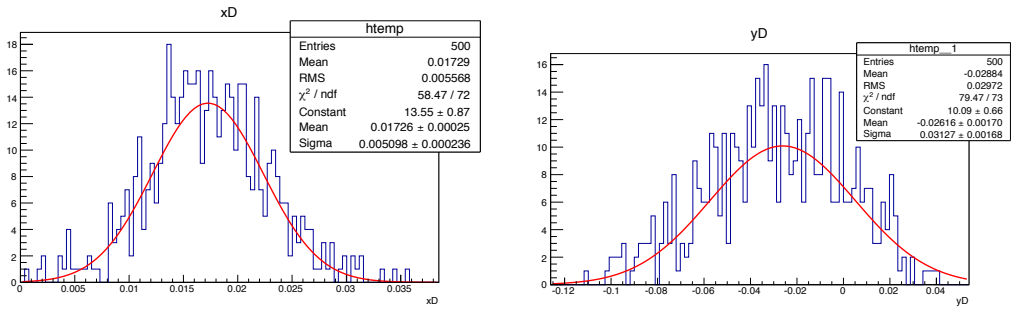

(a) x_D (b) y_D

Figure 8.1: Fit of a Gaussian PDF to the distribution of 600 results with perturbed CLEO input parameters. The rest of the fit is identical to the final fit. Fit results of the Gaussian PDF are indicated.

Source of uncertainty	$x_D(\%)$	$y_D(\%)$
Uncertainty due to CLEO parameters	0.51	3.12
Statistical	0.43	1.36
Other Systematic	0.21	1.13
Total	0.70	3.59

Table 8.1: Table of absolute uncertainties on the measurement of the mixing parameters in data.

The measured values of the mixing parameters along with their uncertainties are shown in Table 8.2

Parameters	value $\pm$ (stat.) $\pm$ (CLEO) $\pm$ (syst.)
x_D	$1.89 \pm 0.43 \pm 0.51 \pm 0.21$
y_D	$-2.59 \pm 1.36 \pm 3.12 \pm 1.13$

Table 8.2: Mixing parameters measured in this analysis. Uncertainties are the statistical uncertainty, uncertainty due to the CLEO input parameters and the systematic uncertainty respectively.

The contours of the fit showing standard deviations due to statistical uncertainty can be seen in Figure 8.2. The statistical uncertainties of x_D and y_D are clearly uncorrelated.

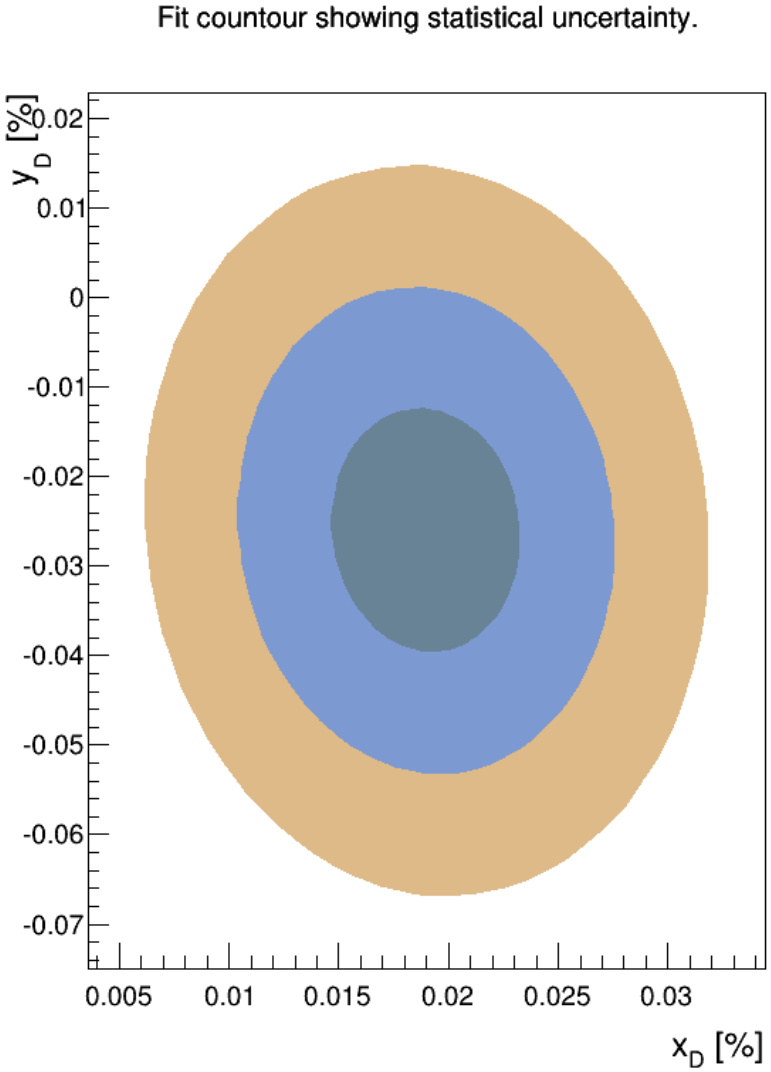

Figure 8.2: The fit countours showing the 1, 2, and 3 σ levels of the statistical uncertainty obtained from the final fit to the data. The statistical uncertainties of x_D and y_D are not correlated. The $\Delta\chi^2$ definition for the contours is n^2 where n is the number of statistical deviations from the result.

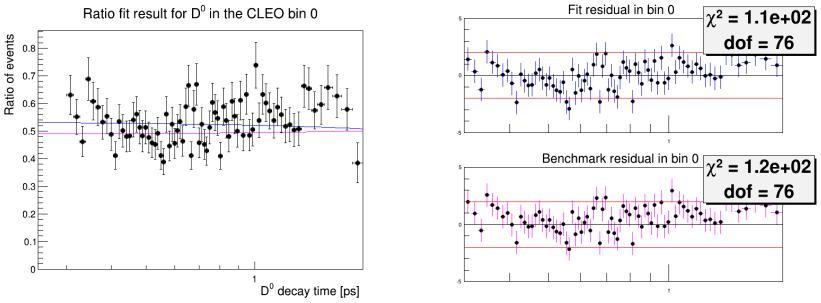

(a) CLEO bin 1 fit to $R(t)$

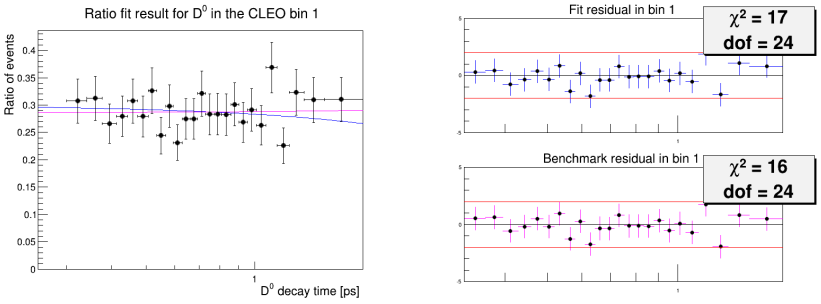

(b) CLEO bin 2 fit to $R(t)$

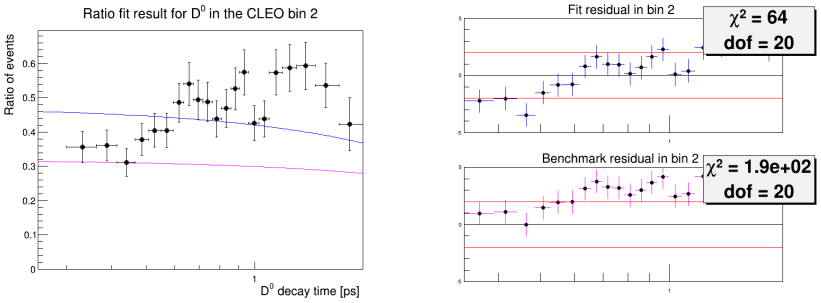

(c) CLEO bin 3 fit to $R(t)$

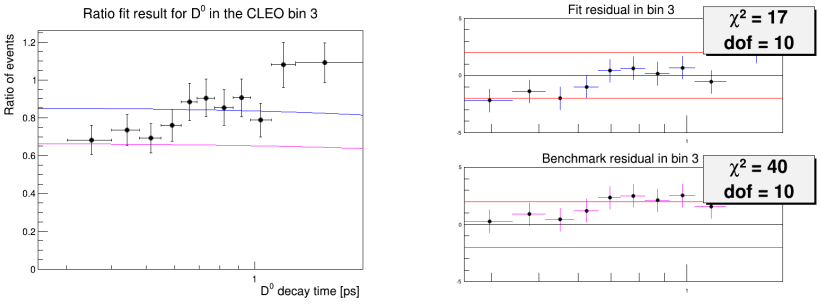

(d) CLEO bin 4 fit to $R(t)$

Figure 8.3: Simultaneous fit to $R(t)$ on the full dataset. CLEO bins 1-4 for $D^0 \to K_S\pi^+\pi^-$ events. The decay time on the x-axis is in logarithmic scale. Fit result is blue, reference fit with $x_D = y_D = 1\%$ is in magenta. Pulls are shown on the right for both fits.

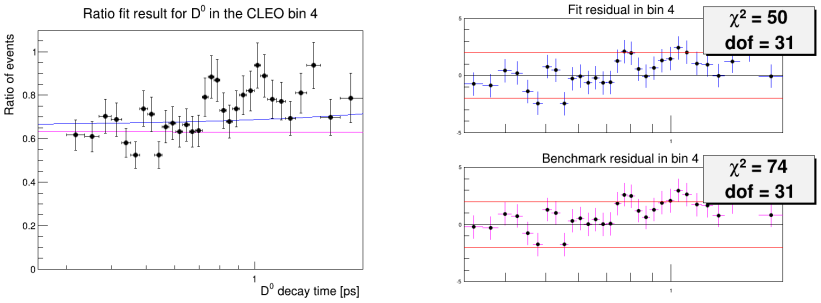

(a) CLEO bin 5 fit to $R(t)$

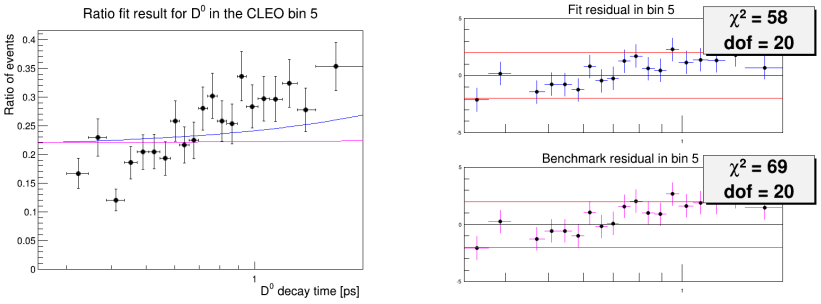

(b) CLEO bin 6 fit to $R(t)$

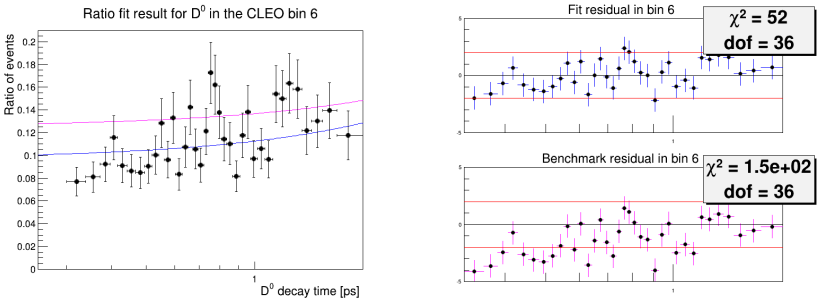

(c) CLEO bin 7 fit to $R(t)$

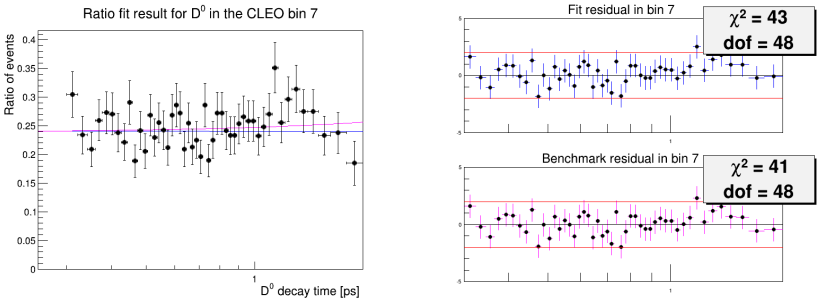

(d) CLEO bin 8 fit to $R(t)$

Figure 8.4: Simultaneous fit to $R(t)$ on the full dataset in CLEO bins 5-8 for $D^0 \to K_S\pi^+\pi^-$ events. The decay time on the x-axis is in logarithmic scale. Fit result is blue, reference fit with $x_D = y_D = 1\%$ is in magenta. Pulls are shown on the right for both fits.

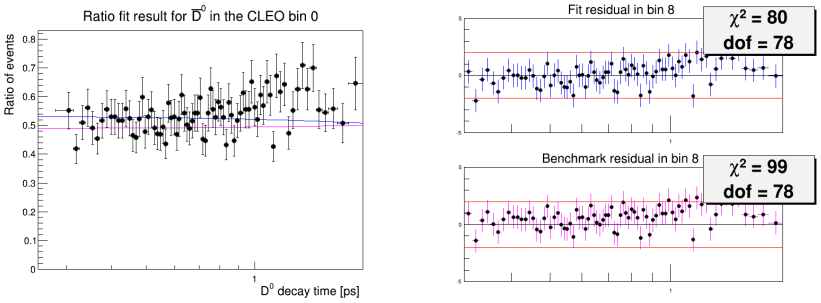

(a) CLEO bin 1 fit to $R(t)$

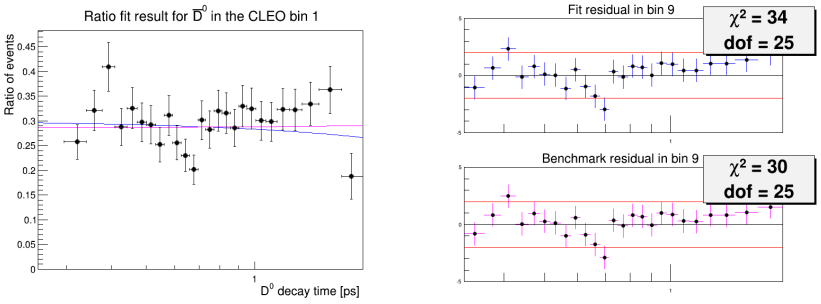

(b) CLEO bin 2 fit to $R(t)$

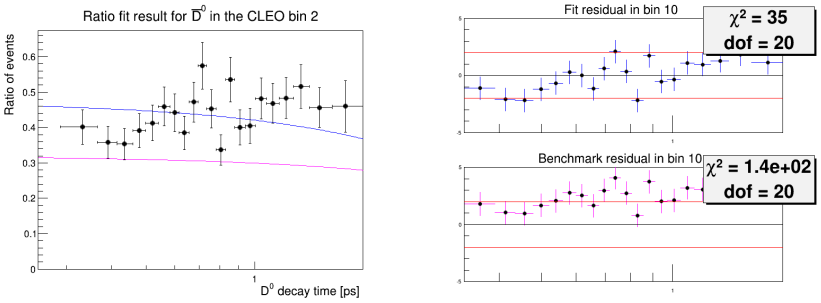

(c) CLEO bin 3 fit to $R(t)$

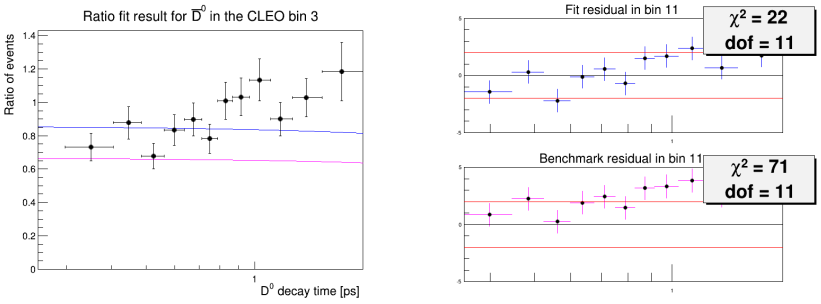

(d) CLEO bin 4 fit to $R(t)$

Figure 8.5: Simultaneous fit to $R(t)$ on the full dataset in CLEO bins 1-4 for $\bar{D}^0 \to K_S\pi^+\pi^-$ events. The decay time on the x-axis is in logarithmic scale. Fit result is blue, reference fit with $x_D = y_D = 1\%$ is in magenta. Pulls are shown on the right for both fits.

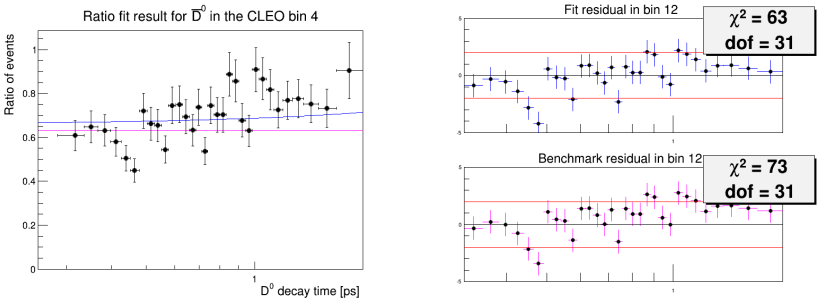

(a) CLEO bin 5 fit to $R(t)$

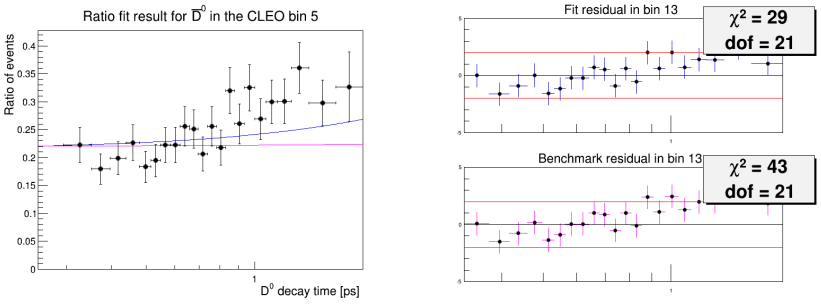

(b) CLEO bin 6 fit to $R(t)$

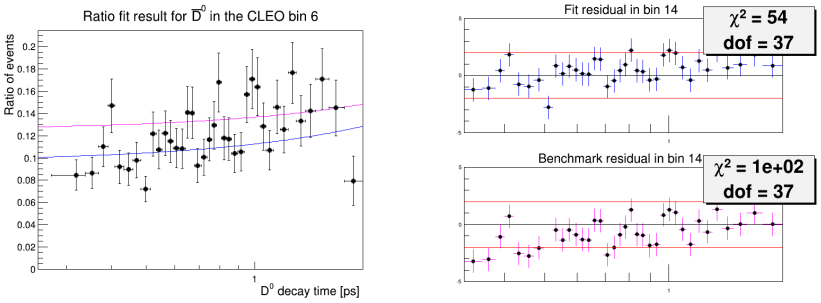

(c) CLEO bin 7 fit to $R(t)$

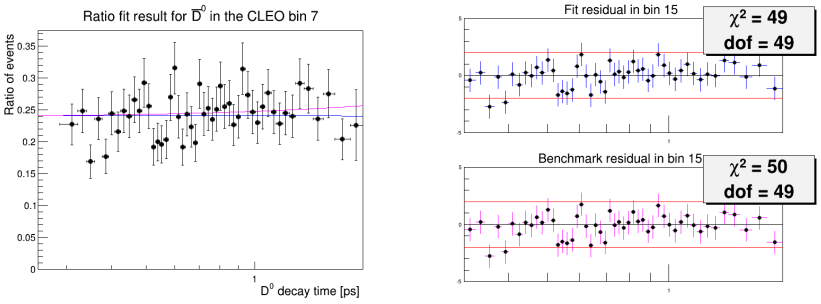

(d) CLEO bin 8 fit to $R(t)$

Figure 8.6: Simultaneous fit to $R(t)$ on the full dataset in CLEO bins 5-8 for $\bar{D}^0 \to K_S\pi^+\pi^-$ events. The decay time on the x-axis is in logarithmic scale. Fit result is blue, reference fit with $x_D = y_D = 1\%$ is in magenta. Pulls are shown on the right for both fits.

Chapter 9

Discussion

The analysis discussed in this thesis presents a model independent approach to extracting the charm mixing parameters in a three-body decay. It eliminates the systematic uncertainty due to the model assumptions which is in general difficult to assess and difficult to quantify the degree to which it can be suppressed. On the other hand this method accrues a systematic uncertainty due to the limited knowledge of the integrated amplitude-weighed strong phase difference parameters. The knowledge of these will however be improved in the future by the BES-III experiment and the relationship between the knowledge on the strong-phase difference parameters and the mixing parameters is much more readily understood.

The results presented in this thesis are consistent with the current world averages of measurements as determined by the HFAG within two standard deviations, see Table **??**. While the results obtained here do not improve the knowledge of the mixing parameters significantly, the method presented is a valuable tool in determining mixing parameters in a model-independent way. In particular, the sensistivity to the mixing parameter x_D makes this approach interesting for analyses with larger datasets which should be able to improve the measurement of x_D and potentially perform searches for CP violation in charm mixing.

Parameter	$x_D(\%)$	$y_D(\%)$
Result of the analysis	$1.89 \pm 0.43 \pm 0.51 \pm 0.21$	$-2.59 \pm 1.36 \pm 3.12 \pm 1.13$
World Average	0.419 ± 0.211	$(0.456 \pm 0.186$

Table 9.1: Comparison of the obtained results with the world averages as presented by the Heavy Flavour World Averaging Group [3].

An interesting observation is the way in which a non-flat efficiency affects the sensitivity to the mixing parameters in a non-uniform way. A feasibility study

should be performed to determine if the development of a trigger and stripping lines with a phase-space flat efficiency would overall improve the sensitivity to the desired parameter.

It should also be noted that this analysis includes two more approaches which, when finished, will be cross-checked to compare the extracted values, precision and potential systematics. Notably, while the method described in this thesis is not sensitive enough to float both the strong-phase difference parameters (constrained by the available CLEO-c information) and the mixing parameters in the same fit, the other approaches used in the analysis should allow for floating all parameters using a global set of constraints.

The input parameters obtained using CLEO analyses contribute a significant uncertainty to the measurement, more than predicted by previous studies [68]. It is unclear why this is the case but a comparison with the other methods used in the analysis should determine if it's an effect associated with the presented method of mixing extraction.

This analysis was performed with the 2011 LHCb dataset. It can be extended to the combined 2011 and 2012 dataset which would guarantee an order of magnitude increase in yields thanks to exteded data-taking and improvements in trigger and stripping lines.

Bibliography

[1] A. D. Sakharov, *Violation of CP in variance, C asymmetry, and baryon asymmetry of the universe*, Soviet Physics Uspekhi **34** (1991) 392.

[2] LHCb Collaboration, R. Aaij *et al.*, *Measurement of D^0-$\bar{D}^0$ mixing parameters and search for CP violation using $D^0 \to K^+\pi^-$ decays*, Phys. Rev. Lett. **111** (2013) 251801 CERN-PH-EP-2013-176, LHCB-PAPER-2013-053, arXiv:1309.6534.

[3] Heavy Flavor Averaging Group, Y. Amhis *et al.*, *Averages of B-Hadron, C-Hadron, and tau-lepton properties as of early 2012*, arXiv:1207.1158 SLAC-R-1002, FERMILAB-PUB-12-871-PPD, arXiv:1207.1158.

[4] Belle Collaboration, T. Peng *et al.*, *Measurement of D^0-$\overline{D}^0$ Mixing and Search for Indirect CP Violation Using $D^0 \to K^0_S\pi^+\pi^-$ Decays*, arXiv:1404.2412.

[5] J. F. Donoghue, E. Golowich, and B. R. Holstein, *Dynamics of the standard model*, vol. 2, Cambridge university press, 1994.

[6] Particle Data Group, J. Beringer *et al.*, *Review of particle physics*, Phys. Rev. D **86** (2012) 010001.

[7] J. Secrest, *Lectures in astrophysics*, http://chemphys.armstrong.edu/secrest/Astro/astro_1.html.

[8] K. G. Wilson, *Confinement of quarks*, Phys. Rev. D **10** (1974) 2445.

[9] M. Gell-Mann and Y. Ne'eman, *The eightfold way [a review, with a collection of reprints]*, Frontiers in physics, W.A. Benjamin, New York, 1964.

[10] V. E. Barnes *et al.*, *Observation of a hyperon with strangeness minus three*, Phys. Rev. Lett. **12** (1964) 204.

[11] ATLAS Collaboration, G. Aad *et al.*, *Search for $t\bar{t}$ resonances in the lepton plus jets final state with ATLAS using 4.7 fb^{-1} of pp collisions at $\sqrt{s} = 7$ TeV*, Phys. Rev. **D88** (2013), no. 1 012004 CERN-PH-EP-2013-032, arXiv:1305.2756.

[12] CMS Collaboration, P. Turner, *Search for $t\bar{t}$ resonances in semileptonic final states in pp collisions at $\sqrt{s}$ = 8 TeV*, arXiv:1310.7859 CMS-CR-2013-281, arXiv:1310.7859.

[13] P. W. Higgs, *Broken Symmetries and the Masses of Gauge Bosons*, Phys. Rev. Lett. **13** (1964) 508.

[14] J. Goldstone, *Field theories with superconductor solutions*, Il Nuovo Cimento **19** (1961) 154.

[15] L. Alvarez-Gaume and J. Ellis, *Eyes on a prize particle*, Nat Phys **7** (2011) 2.

[16] M. Kobayashi and T. Maskawa, *CP-Violation in the Renormalizable Theory of Weak Interaction*, Progress of Theoretical Physics **49** (1973) 652.

[17] M. Battaglia *et al.*, *The CKM matrix and the unitarity triangle. Workshop, CERN, Geneva, Switzerland, 13-16 Feb 2002: Proceedings*, arXiv:hep-ph/0304132 CERN-2003-002, FERMILAB-CONF-02-422, arXiv:hep-ph/0304132.

[18] R. Barbieri and G. F. Giudice, *Upper bounds on supersymmetric particle masses*, Nuclear Physics B **306** (1988) 63.

[19] A. F. Falk *et al.*, *The D^0 - $\bar{D}^0$ mass difference from a dispersion relation*, Phys. Rev. **D69** (2004) 114021 SLAC-PUB-10342, LBNL-54319, WIS-05-04-DPP, WSU-HEP-0401, arXiv:hep-ph/0402204.

[20] G. Luders, *On the Equivalence of Invariance under Time Reversal and under Particle-Antiparticle Conjugation for Relativistic Field Theories*, Kong. Dan. Vid. Sel. Mat. Fys. Med. **28N5** (1954) 1.

[21] CPLEAR Collaboration, A. Angelopoulos *et al.*, *Measurement of the $K_L - K_S$ mass difference using semileptonic decays of tagged neutral kaons*, Phys. Lett. **B444** (1998) 38 CERN-EP-98-152.

[22] Belle Collaboration, K. Hara *et al.*, *Measurement of the $B^0 - \bar{B}^0$ mixing parameter $\Delta m(D)$ using semileptonic B^0 decays*, Phys. Rev. Lett. **89** (2002) 251803 KEK-PREPRINT-2002-69, BELLE-PREPRINT-2002-23, arXiv:hep-ex/0207045.

[23] T. D. Lee and C. N. Yang, *Question of parity conservation in weak interactions*, Phys. Rev. **104** (1956) 254.

[24] M. Fukugita and T. Yanagida, *Barygenesis without grand unification*, Physics Letters B **174** (1986) 45.

[25] D. E. Morrissey and M. J. Ramsey-Musolf, *Electroweak baryogenesis*, New J. Phys. **14** (2012) 125003 NPAC-12-08, arXiv:1206.2942.

[26] E. W. Kolb, A. D. Linde, and A. Riotto, *GUT baryogenesis after preheating*, Phys. Rev. Lett. **77** (1996) 4290 FERMILAB-PUB-96-133-A, SU-ITP-96-22, arXiv:hep-ph/9606260.

[27] C. A. Baker *et al.*, *Improved Experimental Limit on the Electric Dipole Moment of the Neutron*, Phys. Rev. Lett. **97** (2006) 131801, arXiv:hep-ex/0602020.

[28] R. D. Peccei and H. R. Quinn, *CP conservation in the presence of pseudoparticles*, Phys. Rev. Lett. **38** (1977) 1440.

[29] M. Gell-Mann and A. Pais, *Behavior of neutral particles under charge conjugation*, Phys. Rev. **97** (1955) 1387.

[30] ARGUS Collaboration, H. Albrecht *et al.*, *Observation of $B^0 - \bar{B}^0$ Mixing*, Phys. Lett. **B192** (1987) 245 DESY-87-029.

[31] CDF Collaboration, A. Abulencia *et al.*, *Observation of $B_s^0 - \bar{B}_s^0$ Oscillations*, Phys. Rev. Lett. **97** (2006) 242003 FERMILAB-PUB-06-344-E, arXiv:hep-ex/0609040.

[32] LHCb Collaboration, R. Aaij *et al.*, *Measurement of the CP-violating phase ϕ_s in the decay $B_s^0 \to J/\psi\phi$*, Phys. Rev. Lett. **108** (2012) 101803 CERN-PH-EP-2011-214, LHCB-PAPER-2011-021, arXiv:1112.3183.

[33] J. Christenson, J. Cronin, V. Fitch, and R. Turlay, *Evidence for the 2 π Decay of the k_2^0 Meson*, Phys. Rev. Lett. **13** (1964) 138.

[34] V. Fanti and S. Palestini, *A new measurement of direct CP violation in two pion decays of the neutral kaon*, Physics Letters B **465** (1999) 335, arXiv:hep-ex/9909022.

[35] BaBar Collaboration, B. Aubert *et al.*, *Observation of CP violation in the B^0 meson system*, Phys. Rev. Lett. **87** (2001) 091801 SLAC-PUB-8904, BABAR-PUB-01-18, arXiv:hep-ex/0107013.

[36] CERN, *LHC Performance and Statistics*, https://lhc-statistics.web.cern.ch/LHC-Statistics/#.

[37] O. S. Brüning *et al.*, *LHC Design Report*, CERN, Geneva, 2004.

[38] J. Haffner, *The CERN accelerator complex. Complexe des accélérateurs du CERN*, , General Photo.

[39] LHCB Collaboration, *Lhcb operations plots*, http://lhcb-operationsplots.web.cern.ch/lhcb-operationsplots/index.htm.

[40] LHCb Collaboration, S. Amato *et al.*, *LHCb technical proposal*, no. CERN-LHCC-98-04, CERN-LHCC-P-4, 1998.

[41] CERN, *Op vistar webtools*, op-webtools/vistar/vistars.php?usr=LHCLUMINOSITY.

[42] LHCb Collaboration, *Speaker's bureau press material*, http://lhcb.web.cern.ch/lhcb/speakersbureau/html/bb_ProductionAngles.html.

[43] LHCb Collaboration, *The LHCb Detector at the LHC*, Journal of Instrumentation **3** (2008), no. 08 S08005.

[44] R. Aaij *et al.*, *Performance of the LHCb Vertex Locator*, arXiv:1405.7808 CERN-LHCB-DP-2014-001, arXiv:1405.7808.

[45] LHCb VELO Group, *VELO Conference Approved Plots*, https://lbtwiki.cern.ch/bin/view/VELO/VELOConferencePlots.

[46] R. Aaij *et al.*, *The LHCb Trigger and its Performance in 2011*, JINST **8** (2013) P04022, arXiv:1211.3055.

[47] T. Sjostrand, S. Mrenna, and P. Z. Skands, *A Brief Introduction to PYTHIA 8.1*, Comput. Phys. Commun. **178** (2008) 852 CERN-LCGAPP-2007-04, LU-TP-07-28, FERMILAB-PUB-07-512-CD-T, arXiv:0710.3820.

[48] Pythia Development Team, *PYTHIA Project Website*, http://home.thep.lu.se/~torbjorn/Pythia.html.

[49] A. Ryd *et al.*, *EvtGen: A Monte Carlo Generator for B-Physics*, EVTGEN-V00-11-07.

[50] LHCb Collaboration, Gauss Development Team, *Gauss Project Website*, http://lhcb-release-area.web.cern.ch/LHCb-release-area/DOC/gauss/.

[51] LHCb Collaboration, I. Belyaev *et al.*, *Handling of the generation of primary events in Gauss, the LHCb simulation framework*, J. Phys. Conf. Ser. **331** (2011) 032047.

[52] M. Asai, *Geant4-a simulation toolkit*, Trans. Amer. Nucl. Soc. **95** (2006) 757 SLAC-REPRINT-2006-223.

[53] M. M. Reid, *Multiple scattering and em physics*, http://indico.cern.ch/getFile.py/access?contribId=6&sessionId=0&resId=0&materialId=slides&confId=144956, October, 2011. LHC detector simulations: status, needs and prospects.

[54] LHCb Collaboration, Boole Development Team, *Boole Project Website*, http://lhcb-release-area.web.cern.ch/LHCb-release-area/DOC/boole/.

[55] LHCb Collaboration, Moore Development Team, *Moore Project Website*, http://lhcb-release-area.web.cern.ch/LHCb-release-area/DOC/moore/.

[56] LHCb Collaboration, Brunel Development Team, *Brunel Project Website*, http://lhcb-release-area.web.cern.ch/LHCb-release-area/DOC/brunel/.

[57] LHCb Collaboration, DaVinci Development Team, *DaVinci Project Website*, http://lhcb-release-area.web.cern.ch/LHCb-release-area/DOC/davinci/.

[58] LHCb Collaboration, R. Aaij *et al.*, *Prompt charm production in pp collisions at* $\sqrt{s} = 7\ TeV$, Nuclear Physics B **871** (2013), no. 1 1 .

[59] BABAR Collaboration, P. del Amo Sanchez *et al.*, *Measurement of* $D^0 - \bar{D}^0$ *Mixing Parameters Using* $D^0 \to K^0_S\pi^+\pi^-$ *and* $D^0 \to K^0_S K^+ K^-$ *Decays*, Phys. Rev. Lett. **105** (2010) 081803.

[60] BaBar Collaboration, B. Aubert *et al.*, *Improved measurement of the CKM angle* γ *in* $B^\mp \to D^{(*)}K^{(*\mp)}$ *decays with a Dalitz plot analysis of D decays to* $K^0_S\pi^+\pi^-$ *and* $K^0_S K^+ K^-$, Phys. Rev. **D78** (2008) 034023 SLAC-PUB-13209, BABAR-PUB-08-006, arXiv:0804.2089.

[61] M. Pivk and F. R. Le Diberder, *SPlot: A Statistical tool to unfold data distributions*, Nucl. Instrum. Meth. **A555** (2005) 356 LAL-04-07, arXiv:physics/0402083.

[62] W. D. Hulsbergen, *Decay chain fitting with a Kalman filter*, Nucl. Instrum. Meth. **A552** (2005) 566, arXiv:physics/0503191.

[63] LHCb collaboration, R. Aaij *et al.*, *Measurements of indirect CP asymmetries in $D^0 \to K^-K^+$ and $D^0 \to \pi^-\pi^+$ decays*, Phys. Rev. Lett. **112** (2014) 041801 LHCB-PAPER-2013-054, CERN-PH-EP-2013-180, arXiv:1310.7201.

[64] BES-III Collaboration, D. Ambrose, H. Muramatsu, and E. Thorndike, *Measurement of the relative strong-phase difference between D^0 and $\bar{D}^0 \to K^0_S\pi^+\pi^-$*, http://meetings.aps.org/Meeting/APR14/Session/Y12, April, 2014.

[65] CLEO Collaboration, J. Libby *et al.*, *Model-independent determination of the strong-phase difference between D^0 and $\bar{D}^0 \to K^0_{S,L}h^+h^-$ ($h = \pi, K$) and its impact on the measurement of the CKM angle γ/ϕ_3*, Phys. Rev. **D82** (2010) 112006 CLNS-10-2070, CLEO-10-07, arXiv:1010.2817.

[66] A. Giri, Y. Grossman, A. Soffer, and J. Zupan, *Determining gamma using $B^\mp \to DK^\mp$ with multibody D decays*, Phys. Rev. **D68** (2003) 054018, arXiv:hep-ph/0303187.

[67] A. Bondar and A. Poluektov, *The Use of quantum-correlated D^0 decays for ϕ_3 measurement*, Eur. Phys. J. **C55** (2008) 51, arXiv:0801.0840.

[68] C. Thomas and G. Wilkinson, *Model-independent $D^0 - \bar{D}^0$ mixing and CP violation studies with $D^0 \to K^0_S\pi^+\pi^-$ and $D^0 \to K^0_S K^+K^-$*, JHEP **1210** (2012) 185, arXiv:1209.0172.

Appendix A

Three-body decay kinematics and Dalitz Plot Formalism

This appendix briefly discusses the kinematics of a three-body decay of a particle and the formalism of Dalitz plots. A much deeper discussion can be found in [1]. Note that we assume natural unit system with $\hbar = c = 1$.

A.1 Basic kinematics

A particle with energy E, 3-momentum $\mathbf{p}$ and mass m has a 4-vector momentum $p_\mu = (E, \mathbf{p})$. The square of a 4-vector is the Minkowski inner product $p^2 = p_\mu \eta^\mu_\nu p^\nu = E^2 - |\mathbf{p}|^2 = m^2$ where

$$\eta^\nu_\mu = \begin{pmatrix} 1 & 0 & 0 & 0 \\ 0 & -1 & 0 & 0 \\ 0 & 0 & -1 & 0 \\ 0 & 0 & 0 & -1 \end{pmatrix} \tag{A.1}$$

is the Minkowski metric. Suppose the particle is viewed from a frame moving with a velocity $\beta_x = p_x/E$ in the x-axis direction. The apparent momentum and energy $(E', \mathbf{p}')$ of the particle would be

$$\begin{pmatrix} E' \\ p'_x \end{pmatrix} = \begin{pmatrix} \gamma_x & -\gamma_x\beta_x \\ -\gamma_x\beta_x & \gamma_x \end{pmatrix} \begin{pmatrix} E \\ p_x \end{pmatrix}, \quad p'_y = p_y, \quad p'_z = p_z \tag{A.2}$$

where $\gamma_x = 1/\sqrt{1-\beta_x^2}$. Other 4-vectors follow the same transformations. The Minkowski inner products of 4-vectors are invariant under Lorentz transforma-

tions.

For a collision of two particles we can express the total energy in a Lorentz invariant form, in the Center of Mass (CoM) frame

$$\begin{aligned} E_{tot} &= \sqrt{(E_1 + E_2)^2 - (\mathbf{p}_1 + \mathbf{p}_2)^2} \\ &= \sqrt{m_1^2 + m_2^2 + 2E_1E_2(1 - \beta_1\beta_2\cos\theta)}, \end{aligned} \tag{A.3}$$

where θ is the angle between the particles or in the rest frame of particle 1 (Lab)

$$E_{tot} = \sqrt{m_1^2 + m_2^2 + 2E_{2,lab}m_1^2}. \tag{A.4}$$

Given that these two are expressions of a Lorentz invariant quantity, they have to be equal.

If a particle decays into n daughters in it's rest frame, the decay rate is given by

$$d\Gamma = \frac{16\pi^4}{2M}|\mathcal{M}|^2 d\mathbf{\Phi}n(P; p_1, ..., p_n), \tag{A.5}$$

where $|\mathcal{M}|^2$ is the square of the Lorentz invariant amplitude $-i\mathcal{M}$ and $d\mathbf{\Phi}n$ is the infinitesimal element of the n-dimensional phase-space given by

$$d\mathbf{\Phi}n(P; p_1, ..., p_n) = \delta^4(P - \sum_{i=1}^{n} p_i)) \prod_{i=1}^{n} \frac{d^3p_i}{(2\pi)^3 2E_i}. \tag{A.6}$$

A.2 Dalitz plot

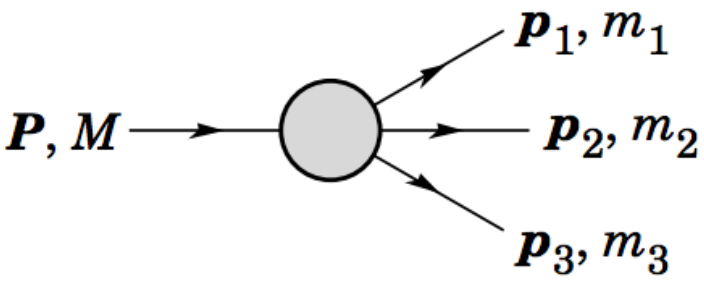

Figure A.1: Illustration of a three body decay of a mother particle. Adopted from [1].

Suppose a particle decays into three daughters in the rest frame of the

mother particle such as in Figure A.1. We can define the 4-vector sum $p_{ij} = p_i + p_j$ and the Lorentz invariant mass square combination $m_{ij}^2 = p_{ij}^2$. Then $m_{12}^2 + m_{13}^2 + m_{23}^2 = M^2 + m_1^2 + m_2^2 + m_3^2$ and $m_{12}^2 = (P - p_3)^2 = M^2 + m_3^2 - 2ME_3$ with E_3 being the energy of daughter 3 in the rest frame of the mother particle. In this frame the 3-momenta of the daughters lie in a plane and the system can be specified using three Euler angles. The decay rate becomes

$$d\Gamma = \frac{1}{16M(2\pi)^5}|\mathcal{M}|^2 dE_1 dE_2 d\alpha d(\cos\beta) d\gamma \tag{A.7}$$

or

$$d\Gamma = \frac{1}{16M(2\pi)^5}|\mathcal{M}|^2 |\mathbf{p}_1^*||\mathbf{p}_3| dm_{12} d\Omega_1^* d\Omega_3 \tag{A.8}$$

where $(\mathbf{p}_1^*, \Omega_1^*)$ is the momentum of the particle 1 in the rest frame of the combination of particles 1 and 2 and Ω_3 is the angle of the particle 3 in the rest frame of the mother particle. The variables $|\mathbf{p}_1^*|$ and $|\mathbf{p}_3|$ are given by

$$\begin{aligned} |\mathbf{p}_1^*| &= \frac{\sqrt{(m_{12}^2 - (m_1 + m_2)^2)(m_{12}^2 - (m_1 - m_2)^2)}}{2m_{12}}, \\ |\mathbf{p}_3| &= \frac{\sqrt{(M^2 - (m_{12} + m_3)^2)(M^2 - (m_{12} - m_3)^2)}}{2M}. \end{aligned} \tag{A.9}$$

After averaging over spins (or if the mother is a scalar particle) and integrating over the three of the angles, the decay rate becomes

$$d\Gamma = \frac{1}{(2\pi)^3 32M^3}|\bar{\mathcal{M}}|^2 dm_{12}^2 dm_{13}^2 \tag{A.10}$$

which has two degrees of freedom and can be projected onto a two dimensional scatter-plot with axes being m_{12}^2 and m_{13}^2. If $|\mathcal{M}|^2$ is constant, the scatter-plot will be uniformly populated (flat). Therefore any structure observed in the scatter-plot offers information about the complex amplitude of the process, generally in the form of bands with constant m_{ij} that indicate resonances. This scatter-plot is called the Dalitz plot[a].

The minimum and maximum of m_{12}^2 is given by the kinematic constraints

[a] Named after Richard Dalitz who invented this formalism to examine $K \to 3\pi$ decays [2].

of the decay

$$
\begin{aligned}
{}_{\max}m_{12}^2 &= (E_2^* + E_3^*)^2 - \left(\sqrt{E_2^{*2} - m_2^2} - \sqrt{E_3^{*2} - m_3^2}\right)^2 \\
{}_{\min}m_{12}^2 &= (E_2^* + E_3^*)^2 - \left(\sqrt{E_2^{*2} - m_2^2} + \sqrt{E_3^{*2} - m_3^2}\right)^2
\end{aligned}
\tag{A.11}
$$

where $E_2^* = (m_{12}^2 - m_1^2 + m_2^2)/2m_{12}$ and $E_3^* = (M^2 - m_{12}^2 - m_3^2)/2m_{12}$ are the energies of particle 2 and 3 in the m_{12} rest frame. The illustration of a Dalitz plot with kinematic boundaries indicated is shown in Figure A.2.

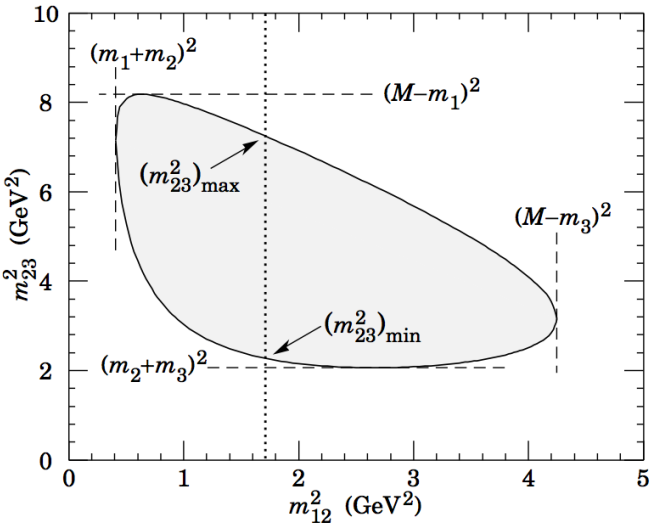

Figure A.2: Illustration of a Dalitz plot with the kinematic boundaries indicated. Adopted from [1].

Appendix B

Swimming Formalism

Swimming is a data-driven mechanism developed to correct the decay time bias of reconstructed particles cause by the trigger. It has been originally developed at DELPHI [3] and CDF [4] and the LHCb experiment is well suited to exploit this mechanism thanks to modular trigger that can be rerun entirely offline and due to the nature of typical trigger requirements for events analysed [5]. The technique can be extended for the correction of decay time bias introduced by stripping and selection as well.

The main body of the algorithm lies in scanning the decay time domain of each event by simulating the PV moving along the flight path of the candidate and sampling the trigger (stripping or selection) decision along the entire domain (see Figure B.1). A step function indicating where in the decay time domain the candidate would be and wouldn't be accepted is obtained. The step function is then used as a per-event weight when performing the decay time fit with an overall Bayesian normalisation applied to normalize the weights. In general it's sufficient to only consider the first (and longest) "top-hat" in the step function which consists of only two relevant points - TP_1 which is the point where the step function starts (i.e. the acceptance begins) and TP_{diff} which is the length of the acceptance interval.

Suppose that a candidates have a decay time distribution

$$P(t) = \frac{1}{\tau} e^{-t/\tau} \tag{B.1}$$

and a decay acceptance from t_{min} to t_{max} as illustrated in Figure B.2. The probabil-

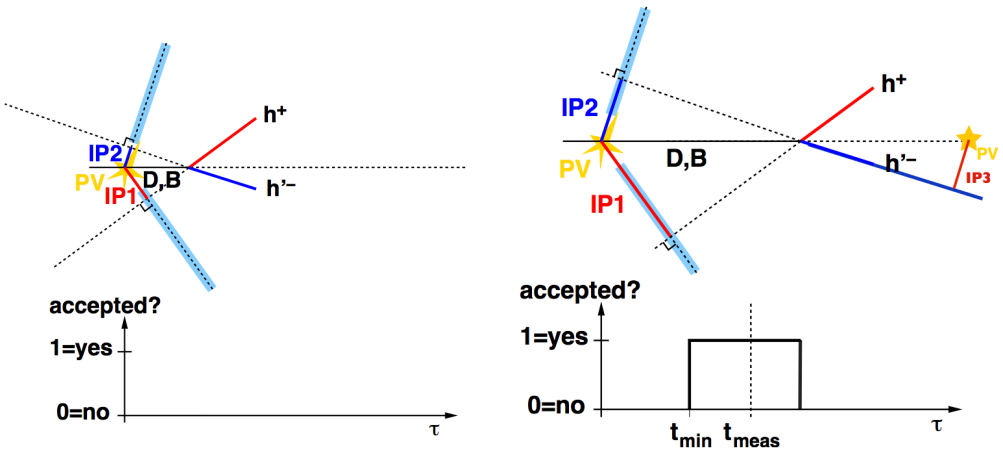

Figure B.1: Illustration of the determination of a top-hat acceptance function for an event.

ity of an event lying within an acceptance range can be written as

$$\begin{aligned} P(t, t_{min}, t_{max}) &= P(t_i | t_i \in [t_{min}, t_{max}]) \cdot \mathcal{A}_i \\ &= \frac{\frac{1}{\tau} e^{\frac{-t_i}{\tau}}}{\int_{t_{min,i}}^{t_{max,i}} e^{\frac{-t'_i}{\tau}} dt'} \cdot \mathcal{A}_i \\ &= \frac{\frac{1}{\tau} e^{\frac{-t_i}{\tau}}}{e^{\frac{-t'_{min,i}}{\tau}} - e^{\frac{-t'_{max,i}}{\tau}}} \cdot \mathcal{A}_i \end{aligned} \tag{B.2}$$

where $\mathcal{A}_i$ is the acceptance function for event i and we assume that there is only one "top-hat" in the acceptance function.

This weighing is performed on a per-event basis and normalized againts the sum of all weights.

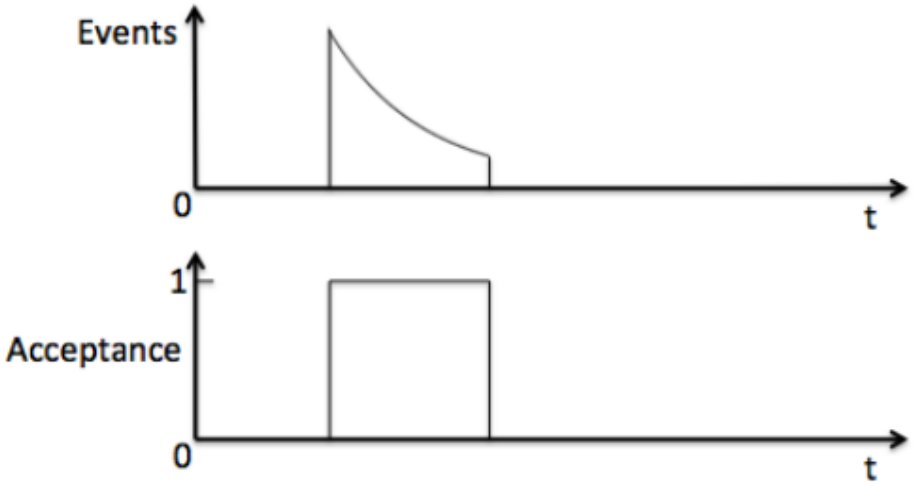

Figure B.2: Time acceptance for a sample event.

Appendix C

EvtGen MC Generator

EVTGEN is a heavy flavour physics generator developed originally by Anders Ryd and David Lange [6] for the BaBar and CLEO Collaborations. Since then it has been used at CERN, Fermilab, KEK and many other locations. The current development team for the EvtGen MC generator is located at the University of Warwick [7]. A very good in-depth overview of MC generators used in particle physics is given in [1].

Several advantages that EVTGEN offers are:

Modularity — Decay models are modular classes that can be added or modified without changing the EVTGEN core.

Decay Amplitudes — The generator uses decay amplitudes rather than probabilities at every node of a decay tree, including all angular correlations.

Decay tables — The decays of individual particles are specified using decay tables listing possible decays of the mother particle along with associated branching fractions and decay models. These are user friendly and can be specified without changing the EVTGEN code.

CP violation and neutral meson oscillations — These effects are correctly implemented for K,D, and B sectors.

In general there are two ways to implement a MC generation algorithm at the highest level of abstraction. One can calculate the total amplitude for all parameter space, square to get the probability and use an accept-reject mechanism to generate an event. This has serious drawbacks because one needs to know the maximum probability of the decay chain which is logistically difficult for B decays with

hundreds of decay modes. A second drawback is that accept-reject at top level is inefficient for large parameter spaces as the whole decay chain has to be regenerated on reject and the accept probability is small. For these reasons, EVTGEN generates the decay tree as a sequence of sub-decays.

At the LHC experiment, the process starts by using the PYTHIA generator to get the initial pp collision and hadronization. The generation proceeds from signal mother particle to a single decay mode selected from a decay table based on branching fractions used as probabilities. Having chosen the mode, the generator uses the associated decay model to generate kinematics, including angular correlations, mixing, CP violation and any associated effects. The PHOTOS [8] generator is used for initial state and final state radiation corrections where applicable. For decays of the tau lepton, the external TAUOLA [9] generator is called. Parts of the decay tables are incomplete and some hadrons have a chance of being passed back to PYTHIA for further hadronization. This whole step is repeated for every particle in the signal tree until only long-lived particles remain (particles with no decays defined in the EVTGEN decay table). If one uses the models that preserve the angular correlations for individual sub-decays, the whole decay tree preserves the correlations.

This versatility of this process is limited by two factors: the complexity of the decay models and the completeness of the decay tables. The decay models are encapsulated in C++ classes that are loaded into the EVTGEN base as modules and currently there are three base classes: models that calculate decay amplitude, models that calculate decay probability and models that create unpolarized daughters (see Figure C.1). This allows dynamic creation of more intelligent models by the users whenever required. The decay tables fall into two categories: the master decay table encapsulated in a single file called DECAY.DEC and user decay tables that override a small, selected part of the master decay table to force a decay into a single desired decay tree (or a cocktail of decay trees, or an entirely inclusive selection).

The master decay table contains every single mother particle to be decayed and every single mode the mother decays into, including models and branching fractions. A decay table for a sample particle looks like this:

```
Decay D*+
0.67 D0 pi+ VSS;
0.33 D+ pi0 VSS;
Enddecay
```

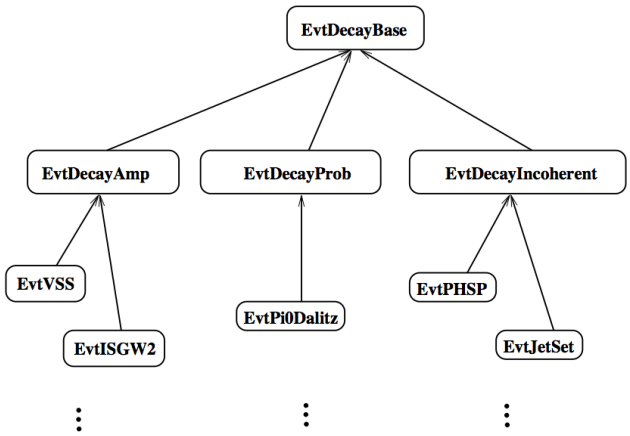

Figure C.1: Illustration of the templated virtual base classes that are extended into decay models in EVTGEN. The three classes derive into models that use decay amplitude, decay probability or return unpolarized daughters. Adopted from [6].

which uses the `VSS` model to decay the D^{*+} mother into either $D^0\pi^+$ or $D^+\pi^0$. The `VSS` model requires a vector mother to decay into two scalar or pseudoscalar particles. Since the master decay table determines all the possible decays and their branching fractions, it has to be regularly updated with the newest branching fractions as averaged by the Particle Data Group [1]. This effort is generally undertaken every two years and as the part of my studies I have developed an automated tool that should reduce the time requirements for any future updates.

Appendix D

MC Filtering

Monte Carlo filtering is a technique employed to increase the statistical significance of the MC sample without using more storage space by performing a selection while the sample is being generated and only saving events which pass the selection process. Given the modular nature of the MC production at LHCb (see section 2.10.1) there are two natural places where the filtering can be applied, at the generator-level or at the reconstruction-level.

Only a small number of event properties are available at the generation stage and thus the full selection cannot be performed [a]. The advantage is that CPU time can be saved on not digitizing and reconstructing events that are not passing through generator-level selection. These cuts are introduced into Gauss in two ways, either by adding a C++ module into the Gauss package which is then referenced in the user written DecFile or by using LoKi::GenCutTool and adding the code directly into the DecFile itself. The former method is marginally more powerful and better documented, but requires the central release of a new version of the Gauss package while the latter only requires the release of a new version of DecFiles package. This analysis uses the cuts shown in Table D.1

Using the LoKi::GenCutTool the cuts can be encoded as follows

```
gen = Generation()
gen.SignalPlain.addTool ( LoKi__GenCutTool , 'TightCut' )
tightCut = gen.SignalPlain.TightCut
tightCut.Decay     = '^[ D*(2010)+ -> ^( D0 => ^( KS0 => ^pi+ ^pi- ) ^pi+ ^pi- ) ^pi+]CC'
tightCut.Preambulo += [
  'GVZ = LoKi.GenVertices.PositionZ() ' ,
  'from GaudiKernel.SystemOfUnits import millimeter ',
  'inAcc     = in_range ( 0.005 , GTHETA , 0.400 ) ',
```

[a] For example the K_S decay time is determined during digitization when the material interactions are taken into account and therefore it's impossible to use generator-level filtering to remove candidates where the K_S decays outside of VELO (i.e. a "downstream" K_S).

Property	Cut
All $\pi^{\pm}$ azimuthal angle	$0.005 < \theta < 0.4$
$D^0 p_T$	> 2 GeV
$D^0 \tau$	> 0.25 ps
D^0 end vertex z-position	< 8 m
D^0 and K_S daughter p	> 1.5 GeV
D^0 and K_S daughter PID	$\pi^{\pm}$
N. of hard $\pi^{\pm}$ with $p > 2.2$ GeV and $p_T > 1.4$ GeV	> 0.5
2D $D^{*+} p_T$ vs. $D^{*+} p$ cut	$(7/300)p + 7/3$ MeV$> p_T > 0.3p$

Table D.1: List of cuts applied for generator level filtering.

```
    'goodD0     = ( GPT > 2000 * MeV) & (GTIME > 0.075 * millimeter)
                  & (GFAEVX( abs( GVZ ) , 0 ) < 8000.0 * millimeter ) ',
    'pioncuts   = ( GNINTREE( (''pi+'' == GABSID ) & (GP > 1500 * MeV) , 4) > 3.5 )',
    'goodKS     = ( GFAEVX( abs( GVZ ) , 0 ) < 800.0 * millimeter ) ',
    'goodDst    = ( (GPT > 1500 * MeV) & (GPT < (3 * GP / 10)) & (GPT > (7*GP/300 - 7/3)) ) ',
    'trigger    = ( GNINTREE( (''pi+'' == GABSID) & (GPT > 1400 * MeV )
                  & (GP > 2700 * MeV) , 4) > 0.5) ',
                    ]
tightCut.Cuts      =  {
    '[pi+]cc'   : 'inAcc',
    '[D0]cc'    : 'goodD0 & pioncuts & trigger',
    '[D*(2010)+]cc' : 'goodDst',
    'KS0'       : 'goodKS',
}
```

The reconstruction-level filtering allows the application of the entire selection after the reconstruction of an event has been performed to determine if the event should be kept[b]. This method applies the entire stripping and selection at the final step of the production and therefore saves no CPU time but does save disk space. It should be noted that even this method of production is not perfectly efficient and the number of truth matched candidates in the final MC sample is smaller than the total yield of the sample. This method is performed by passing a python filtering script to the DA VINCI framework during the reconstruction.

Utilized together, these methods can be used to save both CPU time and disk space when producing MC and, given that those are the practical limitations during the production, it can increase the statistical power of the sample produced.

[b] Alternatively, the stripping is performed in pass-through, meaning that the events that fail are not removed but only flagged.

Appendix E

Results of the simultaneous fit to $Ln(\chi^2_{IP})$ distribution

The results of the simultaneous fit to the $Ln(\chi^2_{IP})$ distribution in each decay time bin are shown in this appendix. Each plot includes a legend with the decay time interval (units of ps are implied) that the events in the fit lie within as well as the yields of the relevant components in the signal window of the $Ln(\chi^2_{IP})$ distribution. Each plot also shows a distribution of pulls with lines indicating $\pm 2\sigma$ interval from the fit.

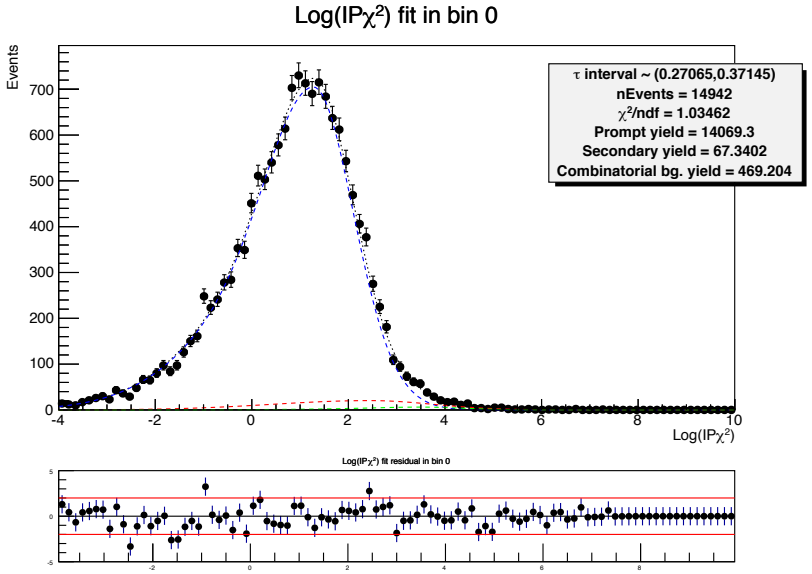

(a) Decay time bin 1

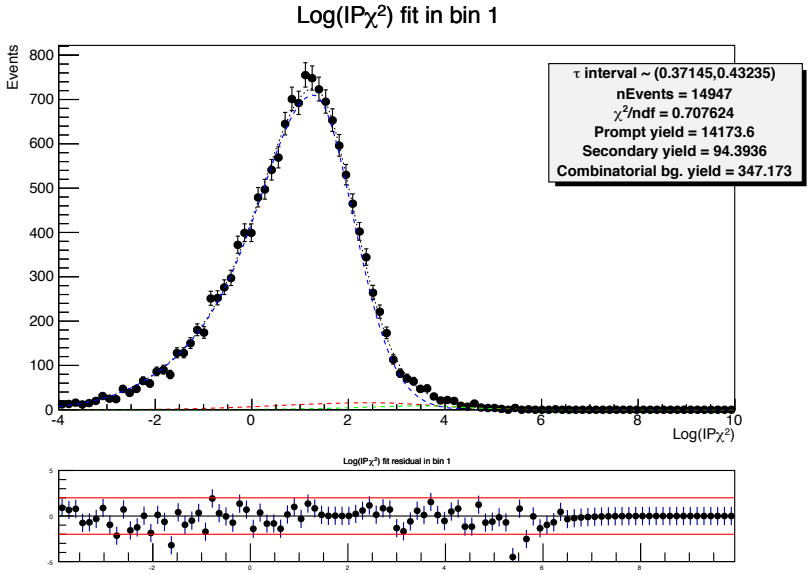

(b) Decay time bin 2

Figure E.1: Fit projections of the simultaneous fit to the $Ln(\chi^2_{IP})$ distribution in decay time bins 1-2. The decay time intervals of the time bins and the yields of components within the signal window are shown in the plots.

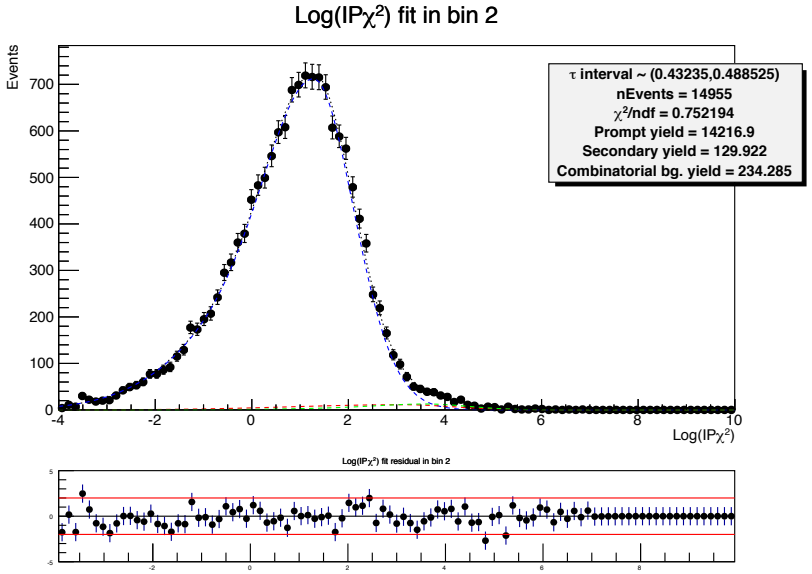

(a) Decay time bin 3

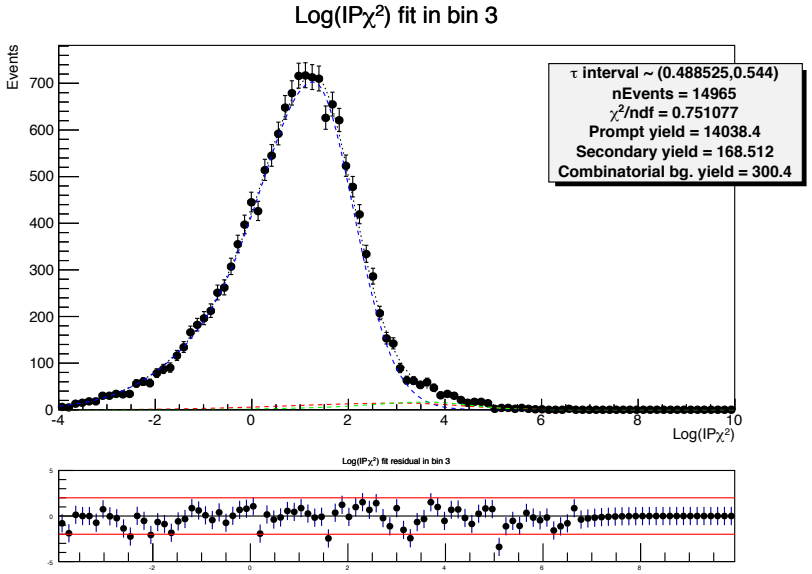

(b) Decay time bin 4

Figure E.2: Fit projections of the simultaneous fit to the $Ln(\chi^2_{IP})$ distribution in decay time bins 3-4. The decay time intervals of the time bins and the yields of components within the signal window are shown in the plots.

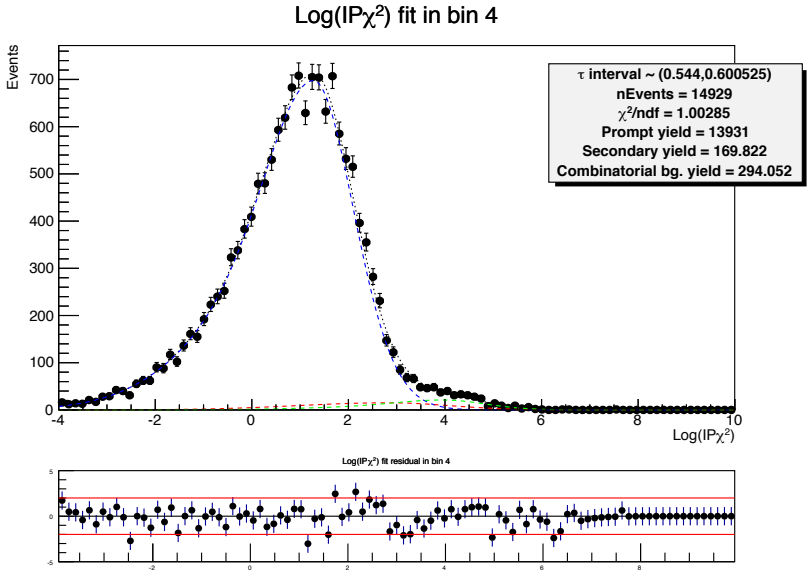

(a) Decay time bin 5

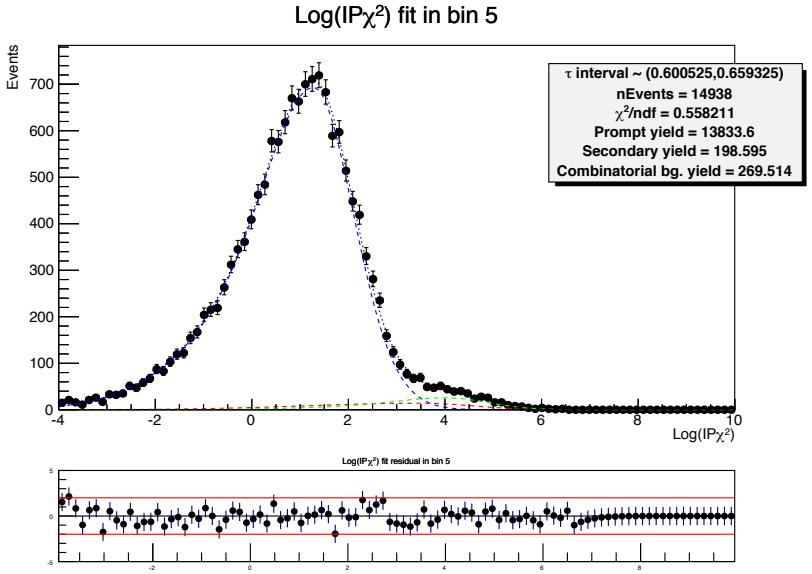

(b) Decay time bin 6

Figure E.3: Fit projections of the simultaneous fit to the $Ln(\chi^2_{IP})$ distribution in decay time bins 5-6. The decay time intervals of the time bins and the yields of components within the signal window are shown in the plots.

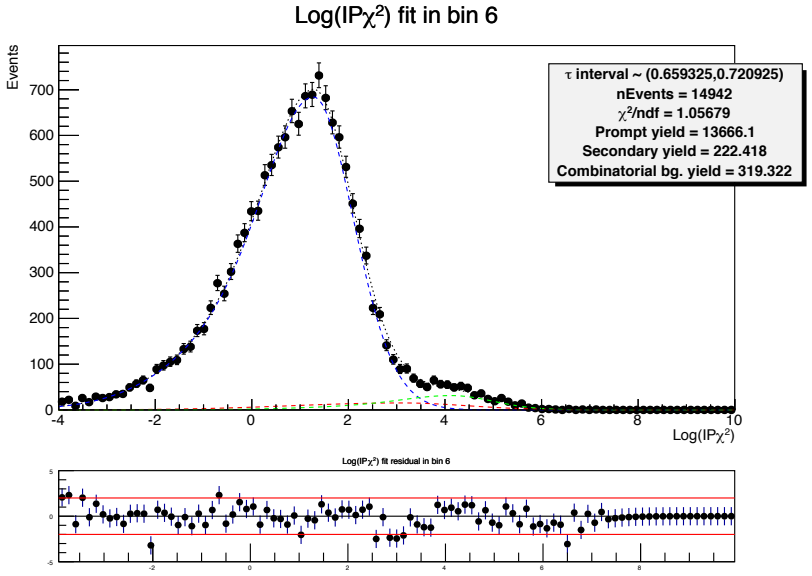

(a) Decay time bin 7

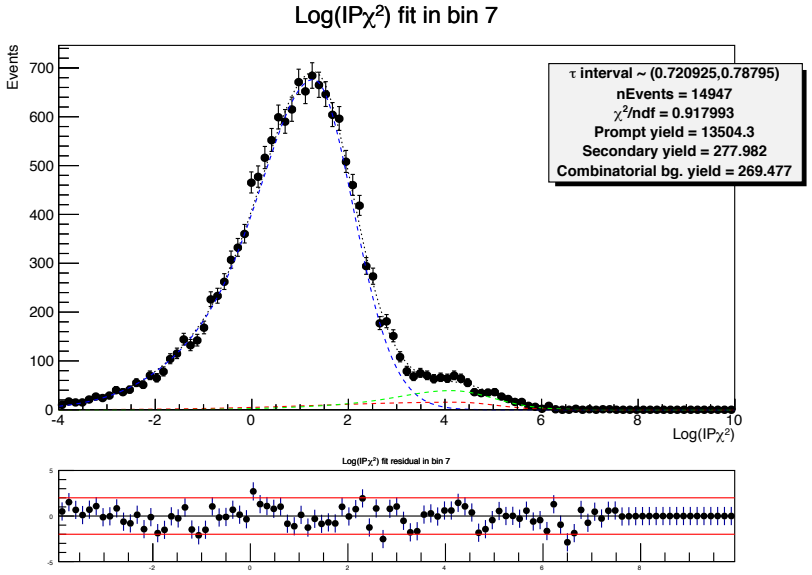

(b) Decay time bin 8

Figure E.4: Fit projections of the simultaneous fit to the $Ln(\chi^2_{IP})$ distribution in decay time bins 7-8. The decay time intervals of the time bins and the yields of components within the signal window are shown in the plots.

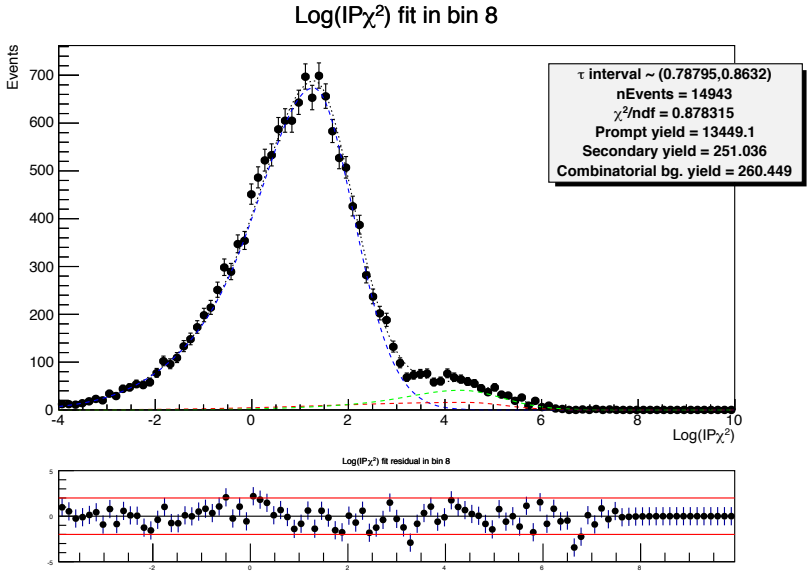

(a) Decay time bin 9

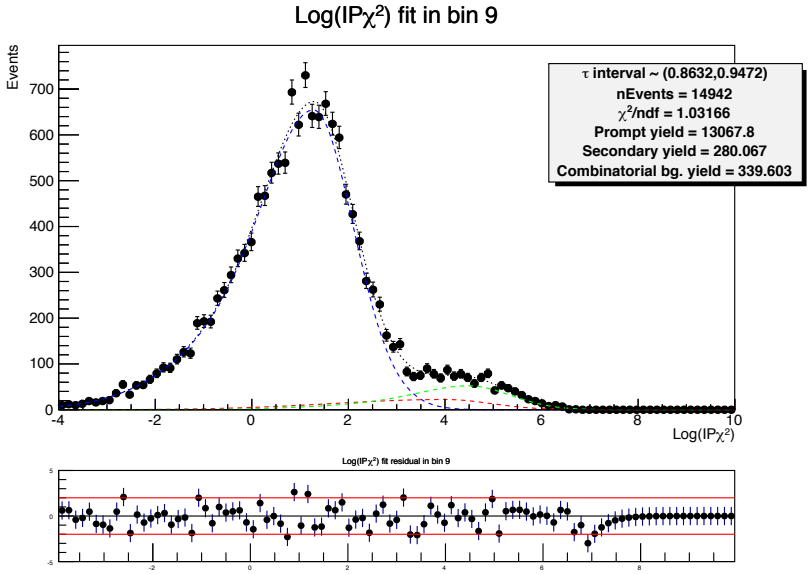

(b) Decay time bin 10

Figure E.5: Fit projections of the simultaneous fit to the $Ln(\chi^2_{IP})$ distribution in decay time bins 9-10. The decay time intervals of the time bins and the yields of components within the signal window are shown in the plots.

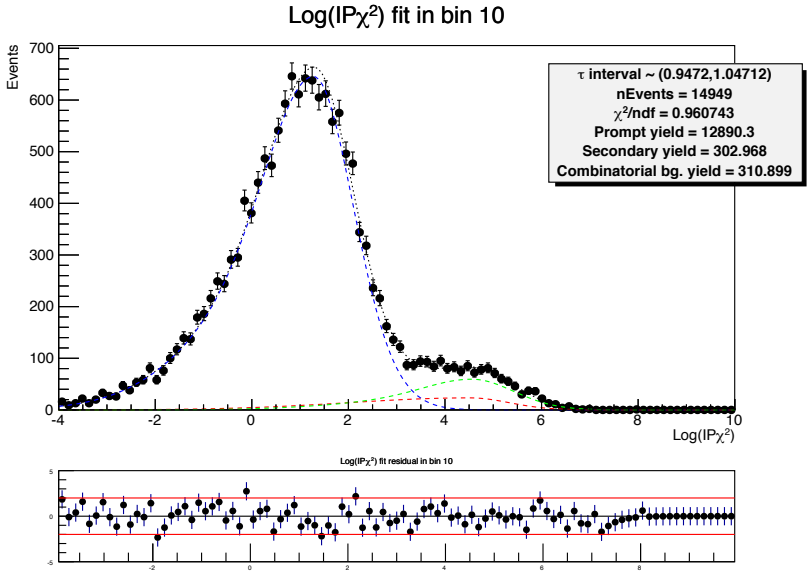

(a) Decay time bin 11

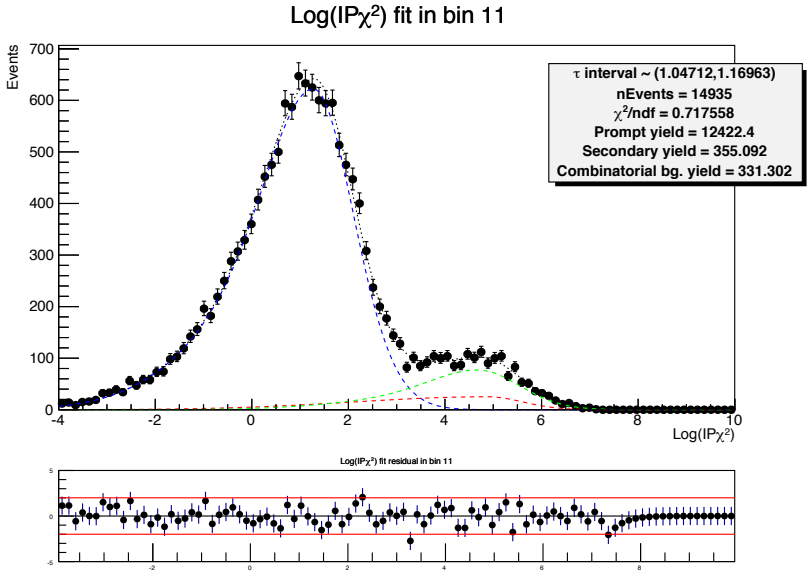

(b) Decay time bin 12

Figure E.6: Fit projections of the simultaneous fit to the $Ln(\chi^2_{IP})$ distribution in decay time bins 11-12. The decay time intervals of the time bins and the yields of components within the signal window are shown in the plots.

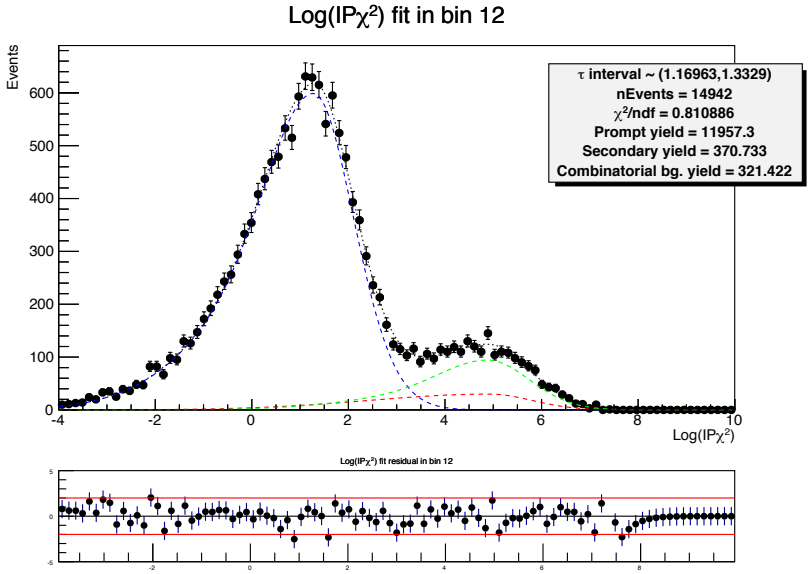

(a) Decay time bin 13

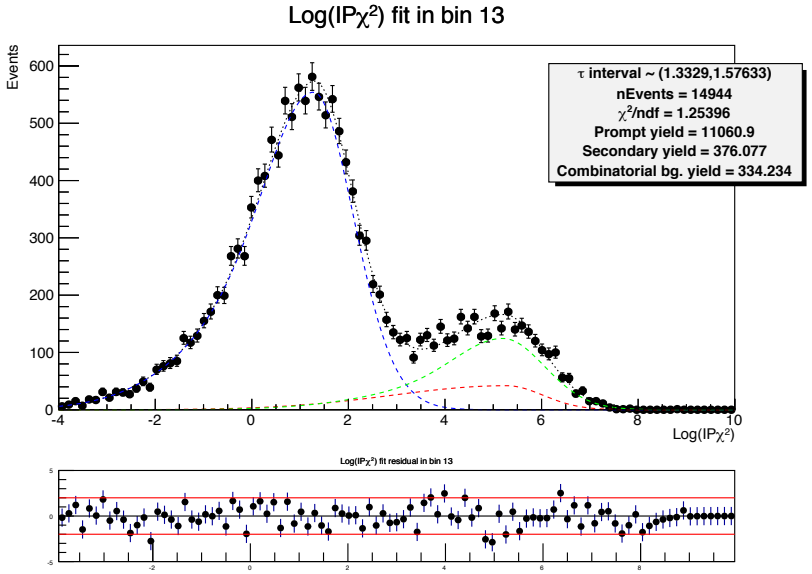

(b) Decay time bin 14

Figure E.7: Fit projections of the simultaneous fit to the $Ln(\chi^2_{IP})$ distribution in decay time bins 13-14. The decay time intervals of the time bins and the yields of components within the signal window are shown in the plots.

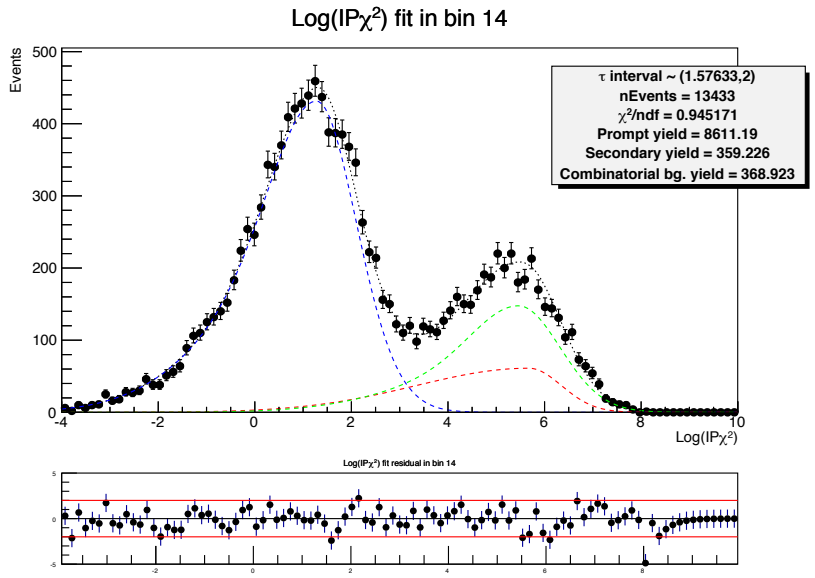

(a) Decay time bin 15

Figure E.8: Fit projections of the simultaneous fit to the $Ln(\chi^2_{IP})$ distribution in decay time bin 15. The decay time intervals of the time bin and the yields of components within the signal window are shown in the plot.

Appendix F

Results of the 2D m_D- Δm fits in individual bins of phase-space.

The plots of m_D and Δm projections of the 2D m_D- Δm fit to all CLEO bins i are shown here. The plots shown in Figure F.1 through F.8 are the $D^0 \to K_S\pi^+\pi^-$ data in individual phase-space bins while the Figure F.9 through F.16 show the $\bar{D}^0 \to K_S\pi^+\pi^-$ data in phase-space bins.

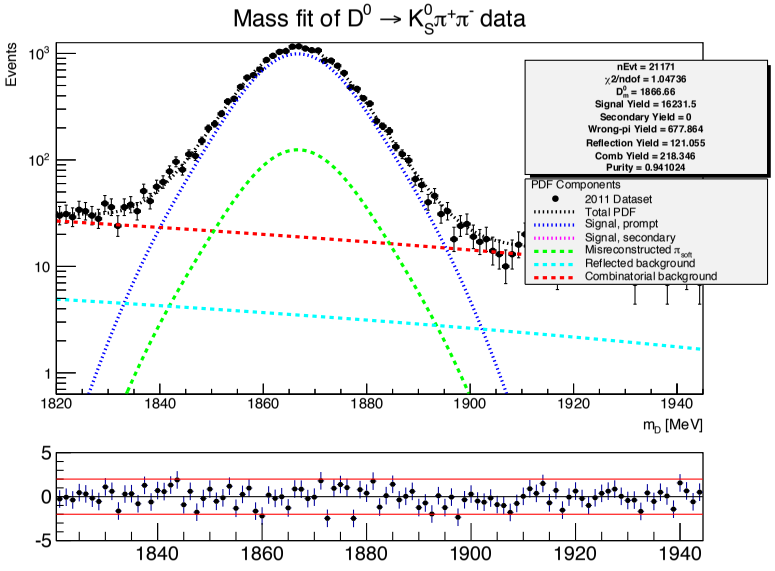

(a) Cleo bin 1 m_D

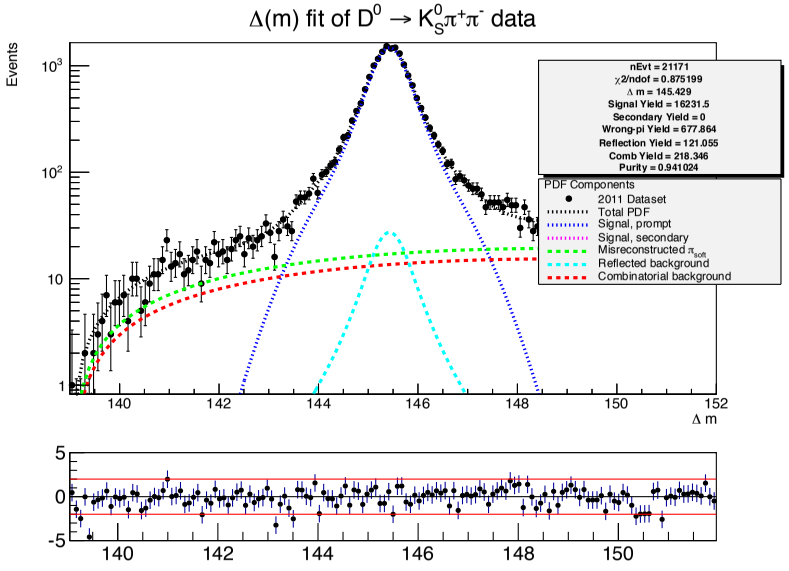

(b) Cleo bin 1 Δm

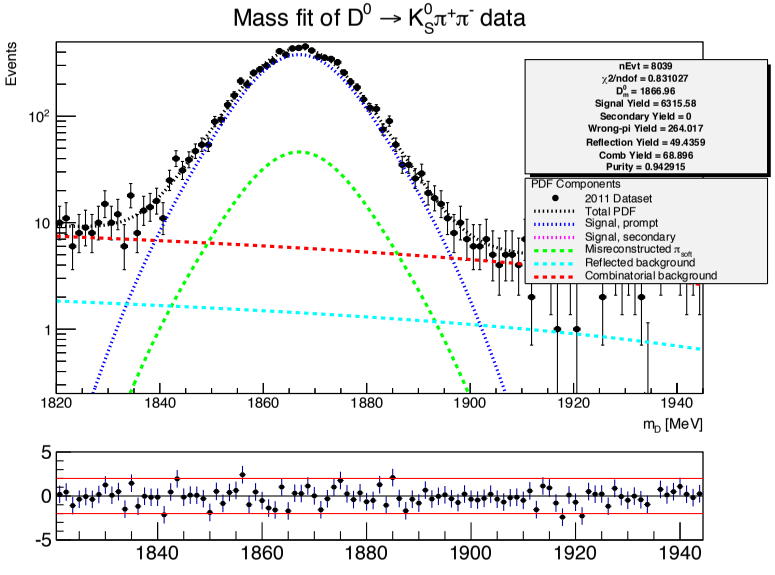

(c) Cleo bin 2 m_D

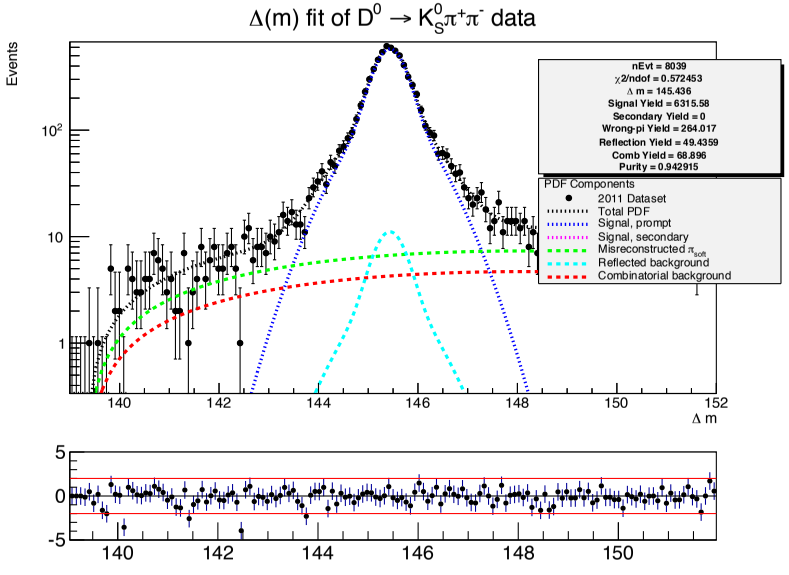

(d) Cleo bin 2 Δm

Figure F.1: Fit projections for the 2D m_D- Δm fit in CLEO bins 1 and 2 of the $D^0 \to K_S\pi^+\pi^-$ data.

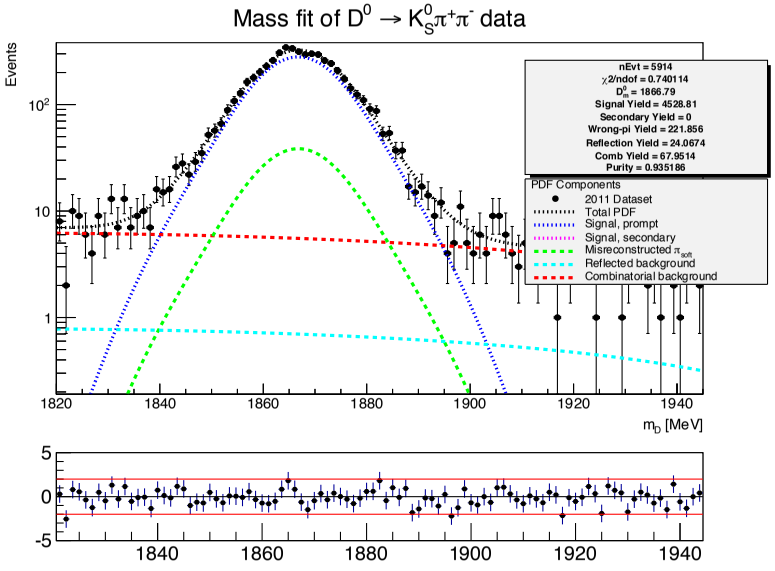

(a) Cleo bin 3 m_D

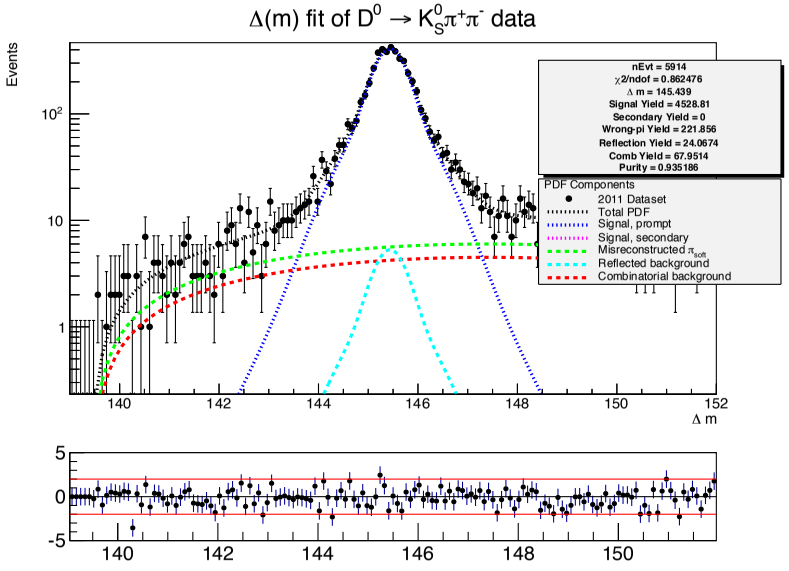

(b) Cleo bin 3 Δm

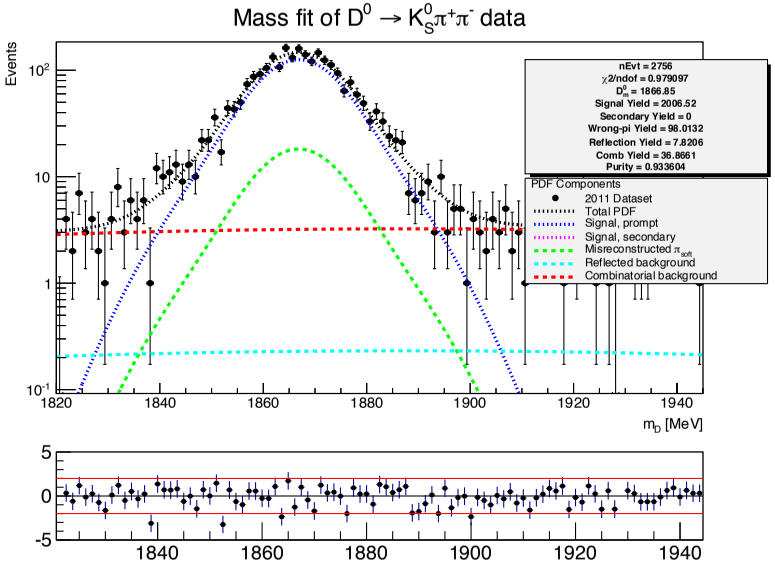

(c) Cleo bin 4 m_D

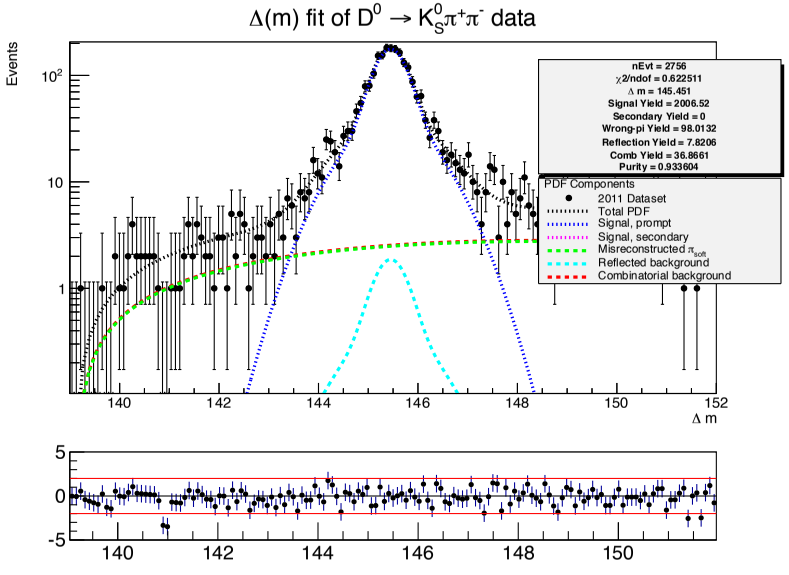

(d) Cleo bin 4 Δm

Figure F.2: Fit projections for the 2D m_D- Δm fit in CLEO bins 3 and 4 of the $D^0 \to K_S\pi^+\pi^-$ data.

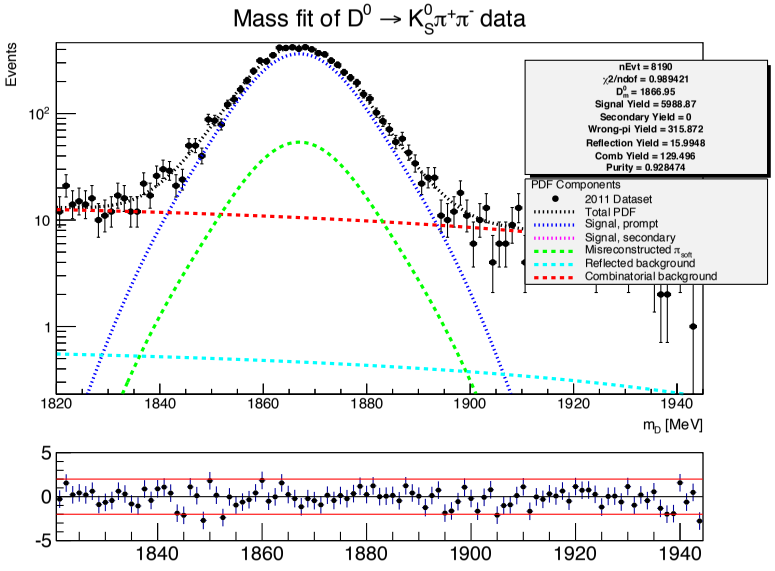

(a) Cleo bin 5 m_D

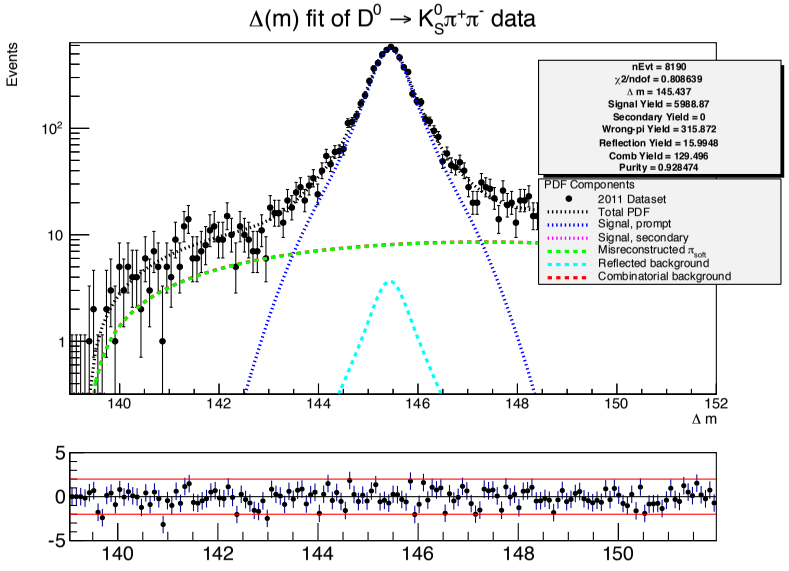

(b) Cleo bin 5 Δm

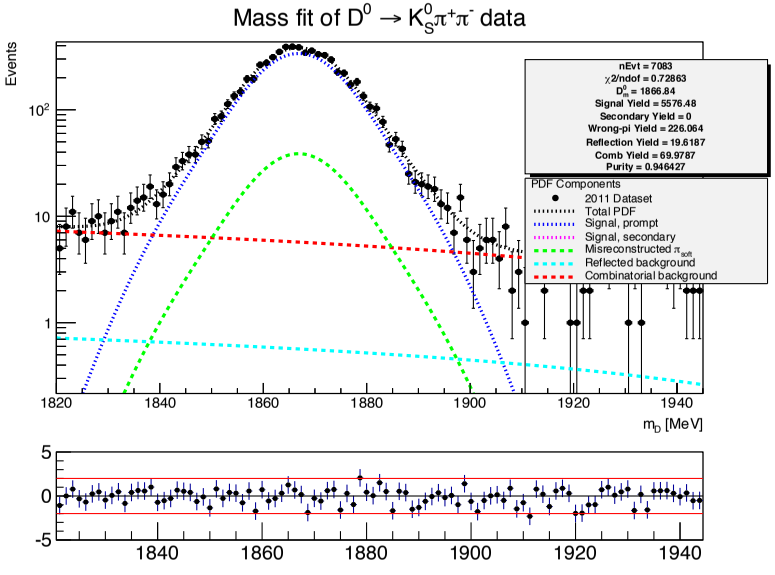

(c) Cleo bin 6 m_D

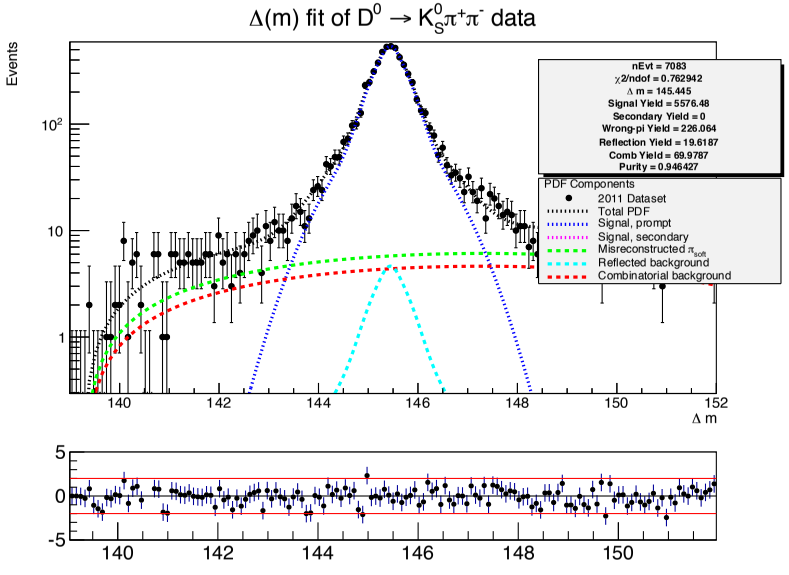

(d) Cleo bin 6 Δm

Figure F.3: Fit projections for the 2D m_D- Δm fit in CLEO bins 5 and 6 of the $D^0 \to K_S\pi^+\pi^-$ data.

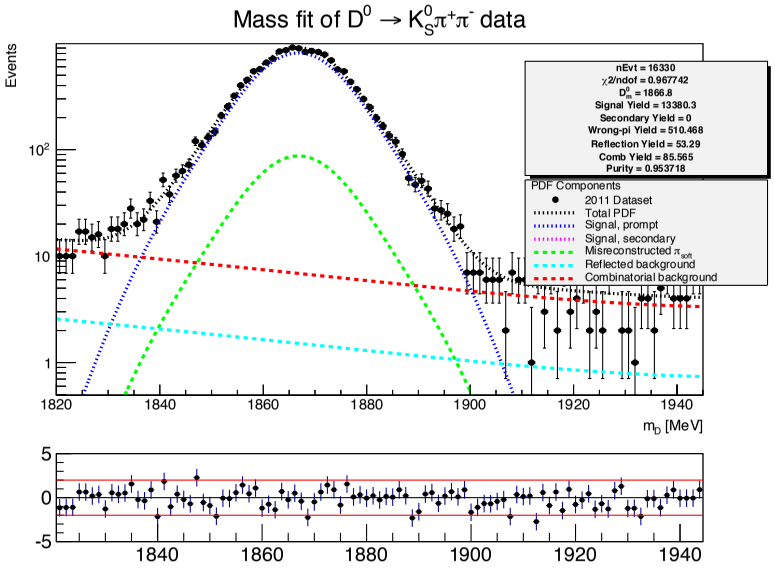

(a) Cleo bin 7 m_D

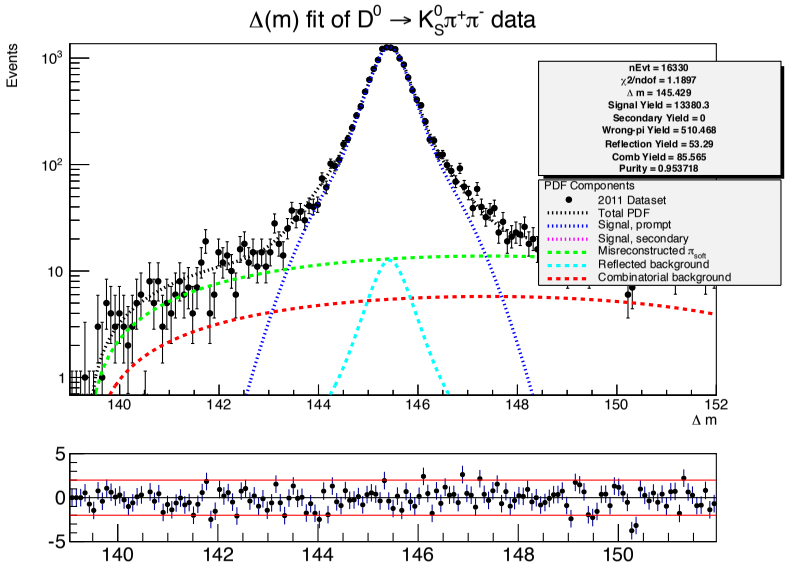

(b) Cleo bin 7 Δm

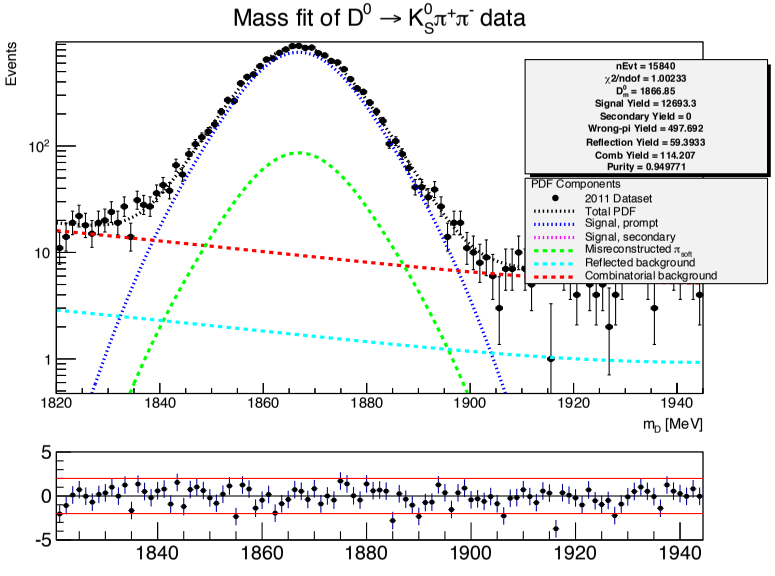

(c) Cleo bin 8 m_D

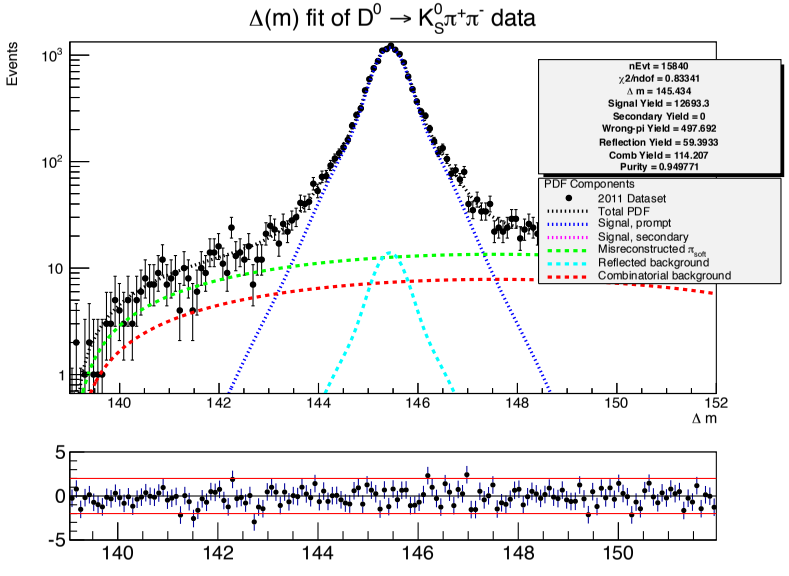

(d) Cleo bin 8 Δm

Figure F.4: Fit projections for the 2D m_D- Δm fit in CLEO bins 7 and 8 of the $D^0 \to K_S\pi^+\pi^-$ data.

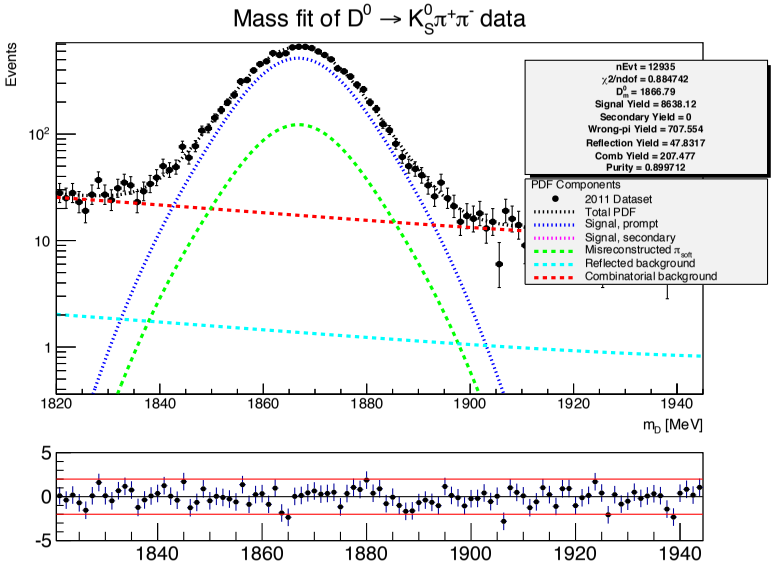

(a) Cleo bin -1 m_D

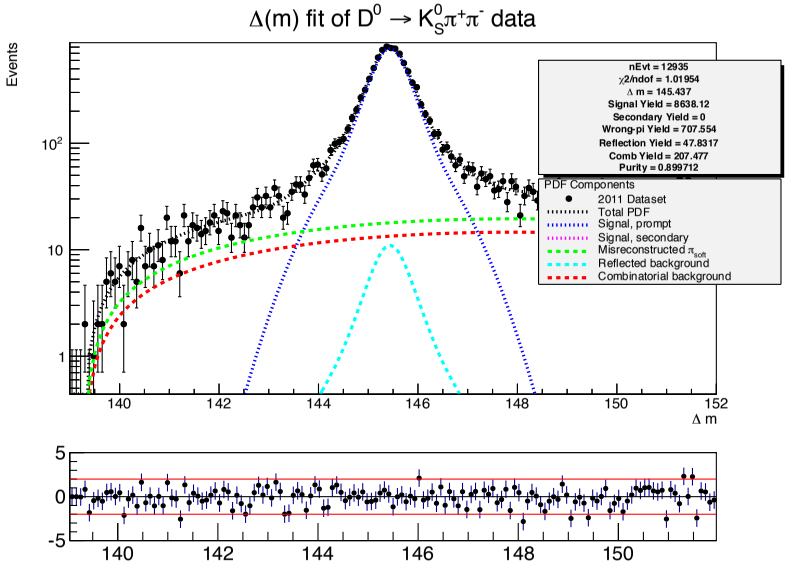

(b) Cleo bin -1 Δm

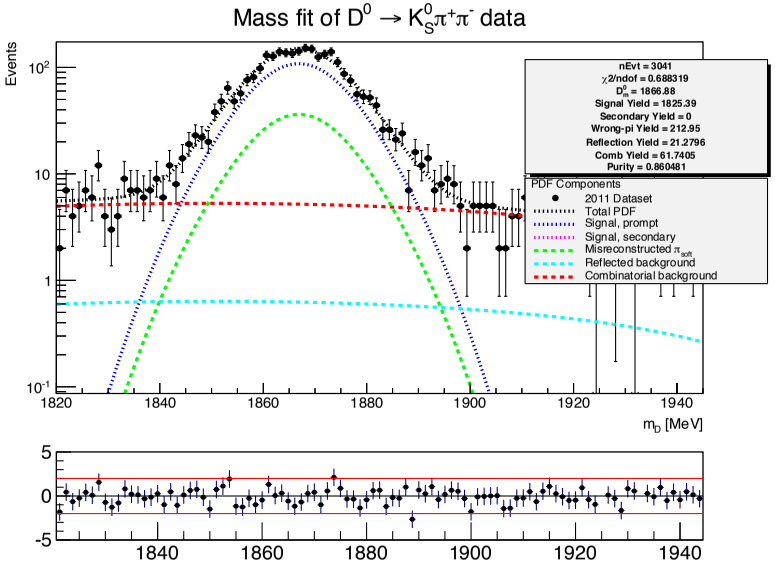

(c) Cleo bin -2 m_D

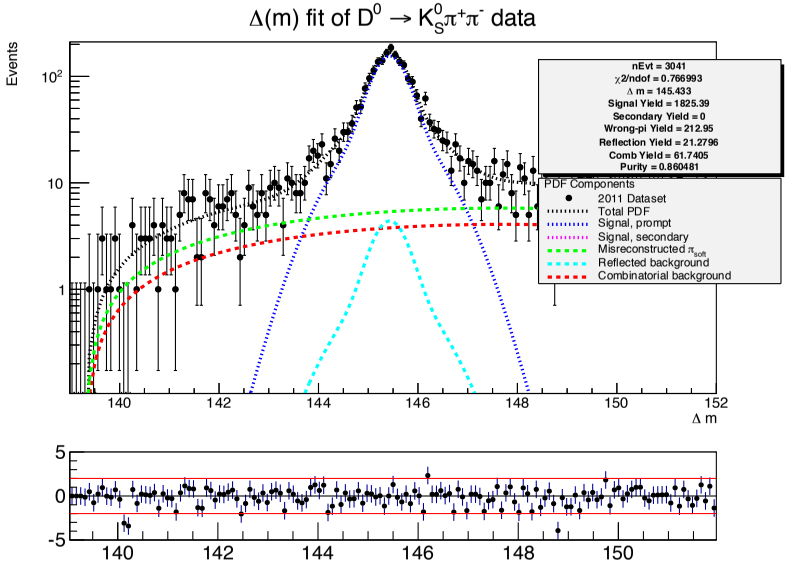

(d) Cleo bin -2 Δm

Figure F.5: Fit projections for the 2D m_D- Δm fit in CLEO bins -1 and -2 of the $D^0 \to K_S\pi^+\pi^-$ data.

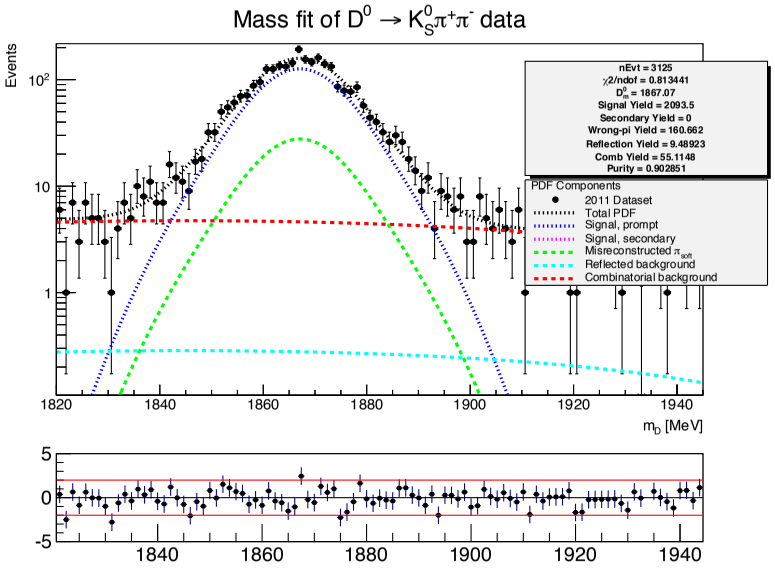

(a) Cleo bin -3 m_D

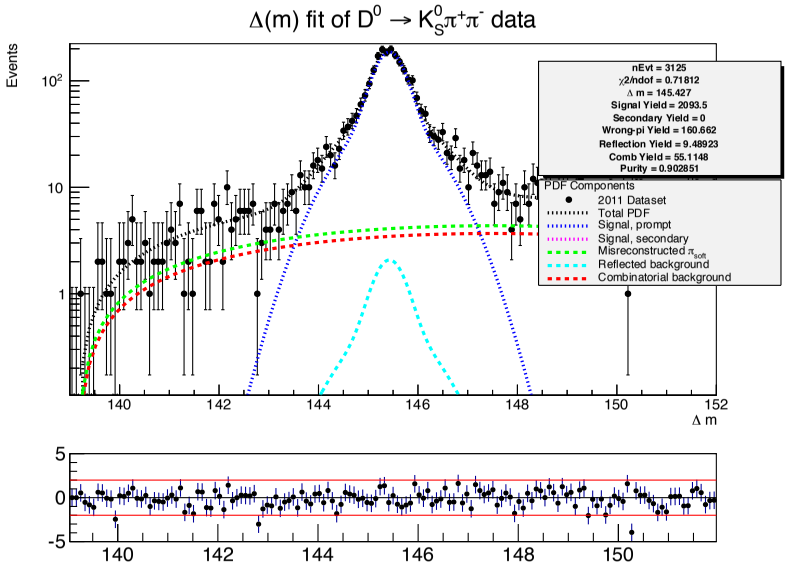

(b) Cleo bin -3 Δm

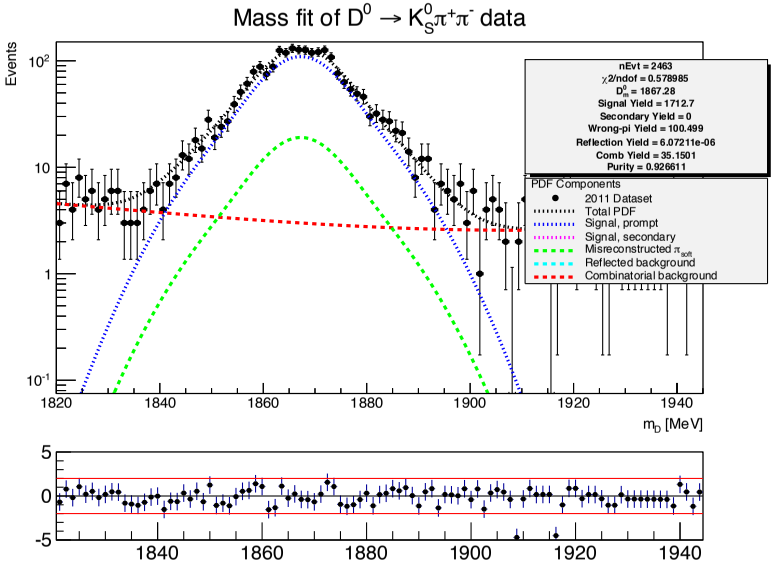

(c) Cleo bin -4 m_D

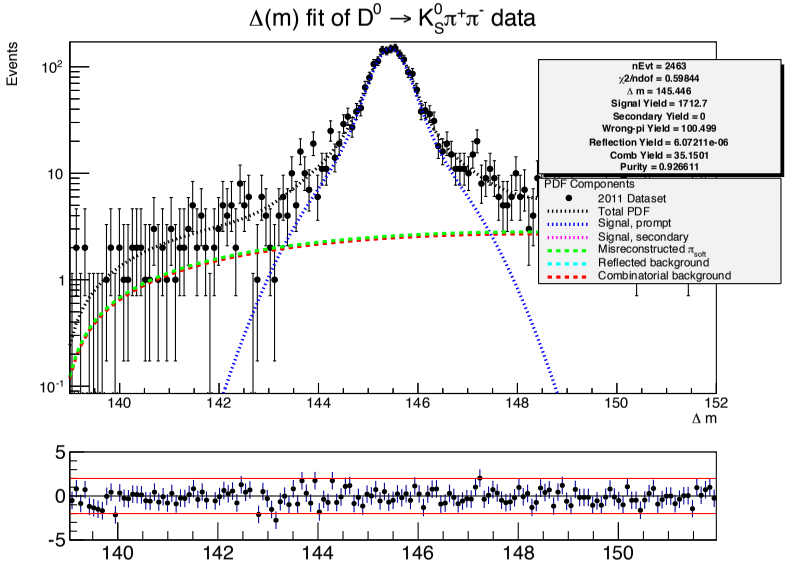

(d) Cleo bin -4 Δm

Figure F.6: Fit projections for the 2D m_D- Δm fit in CLEO bins -3 and -4 of the $D^0 \to K_S\pi^+\pi^-$ data.

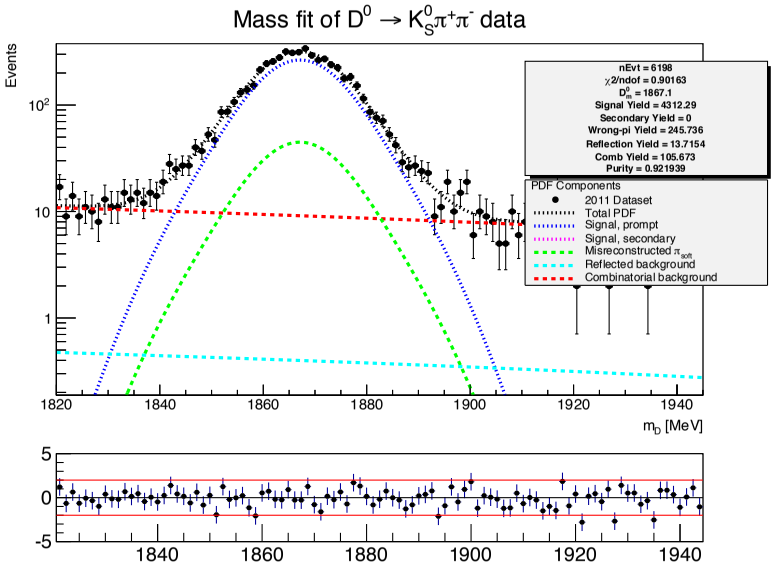

(a) Cleo bin -5 m_D

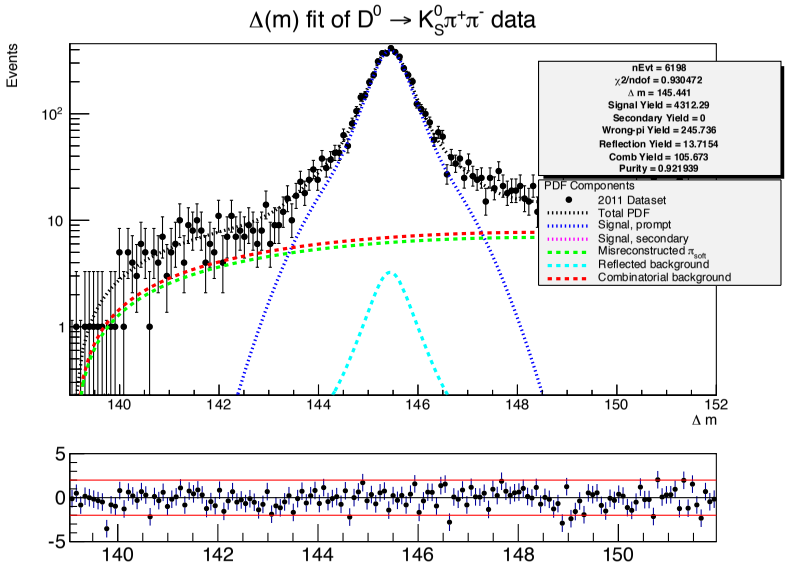

(b) Cleo bin -5 Δm

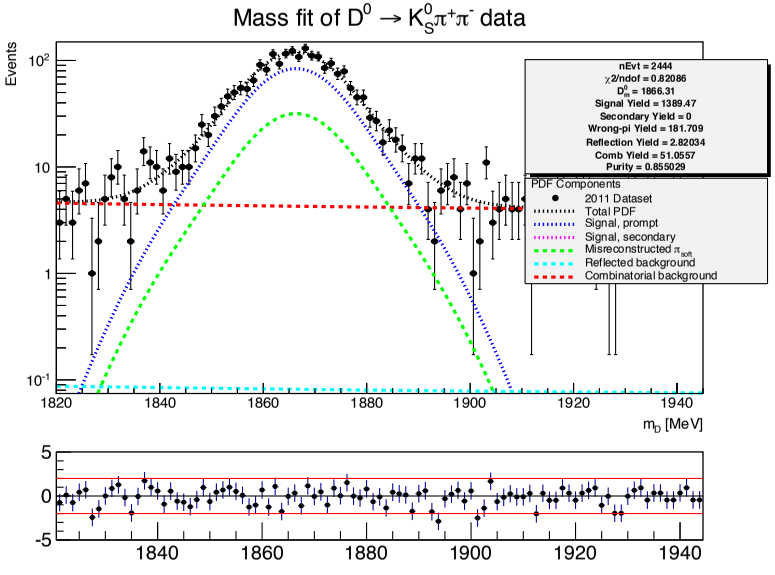

(c) Cleo bin -6 m_D

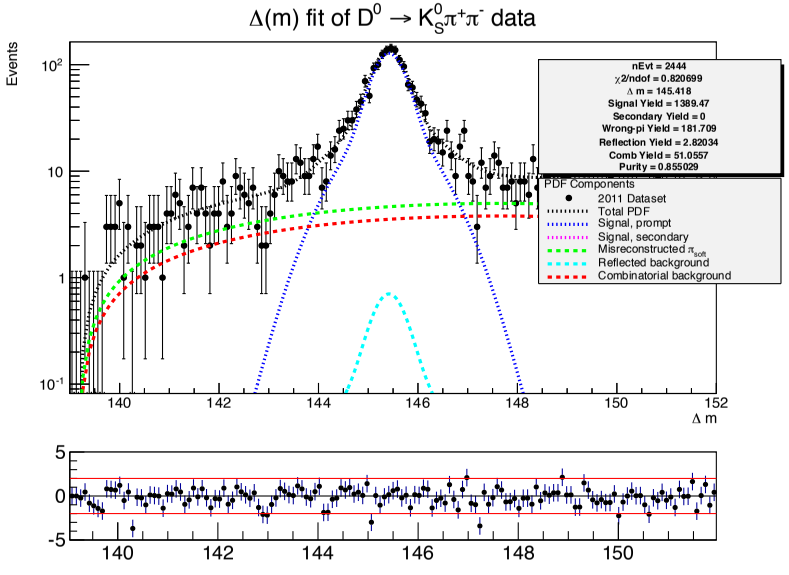

(d) Cleo bin -6 Δm

Figure F.7: Fit projections for the 2D m_D- Δm fit in CLEO bins -5 and -6 of the $D^0 \to K_S\pi^+\pi^-$ data.

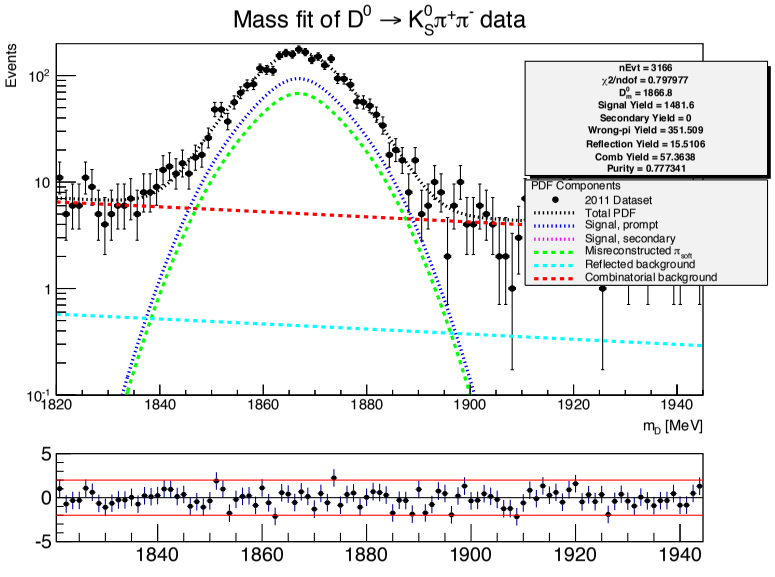

(a) Cleo bin -7 m_D

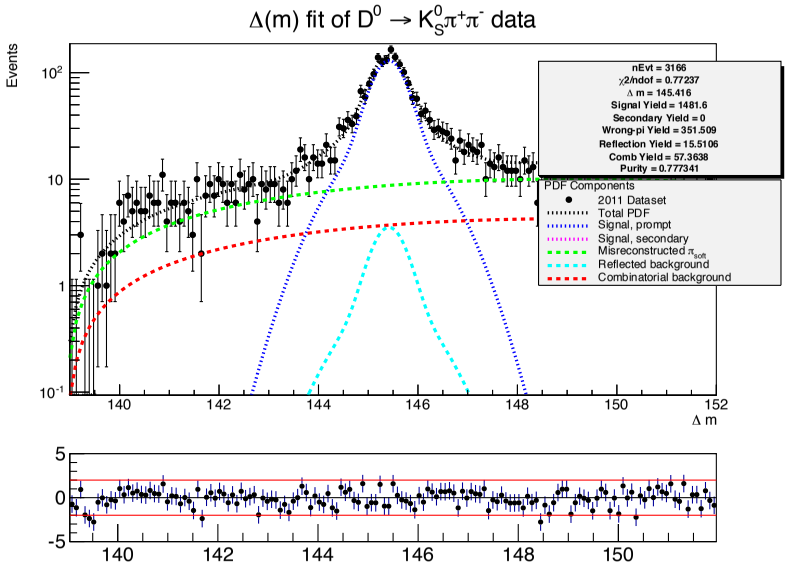

(b) Cleo bin -7 Δm

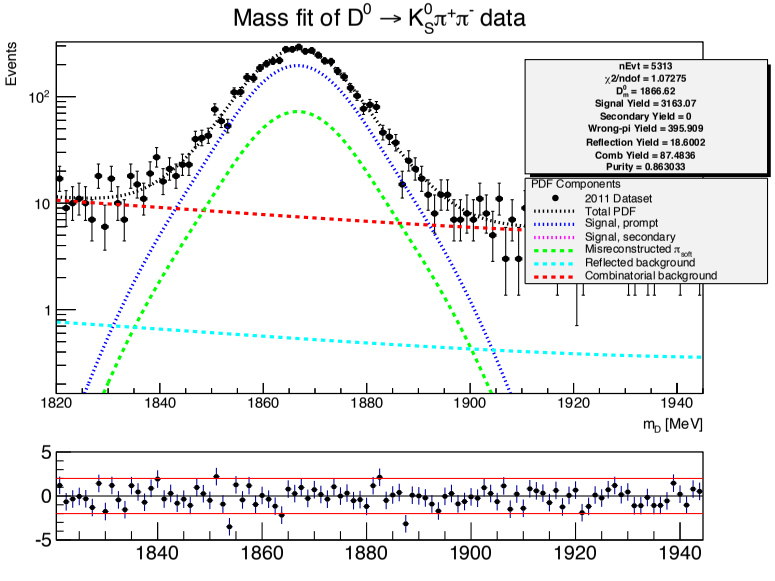

(c) Cleo bin -8 m_D

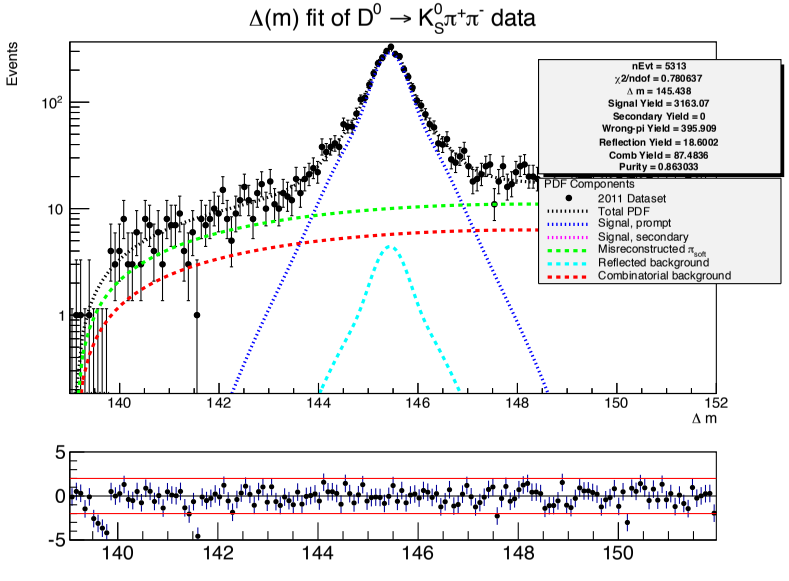

(d) Cleo bin -8 Δm

Figure F.8: Fit projections for the 2D m_D- Δm fit in CLEO bins -7 and -8 of the $D^0 \to K_S\pi^+\pi^-$ data.

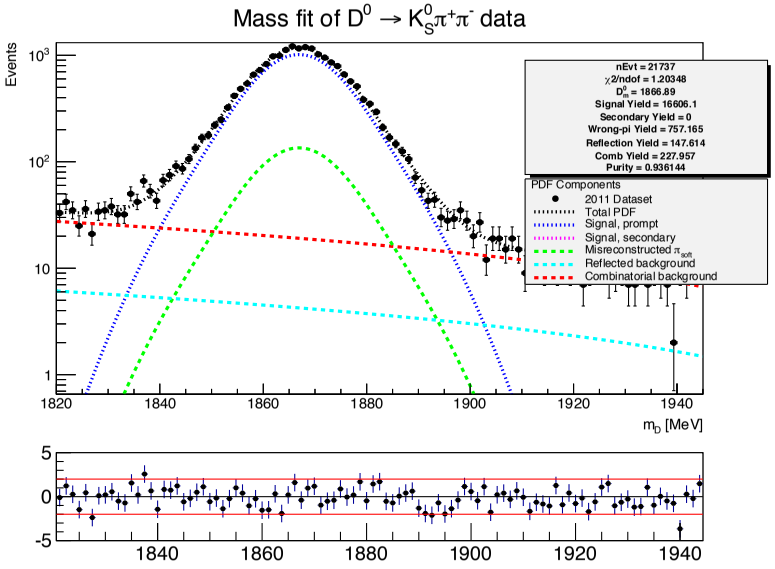

(a) Cleo bin 1 m_D

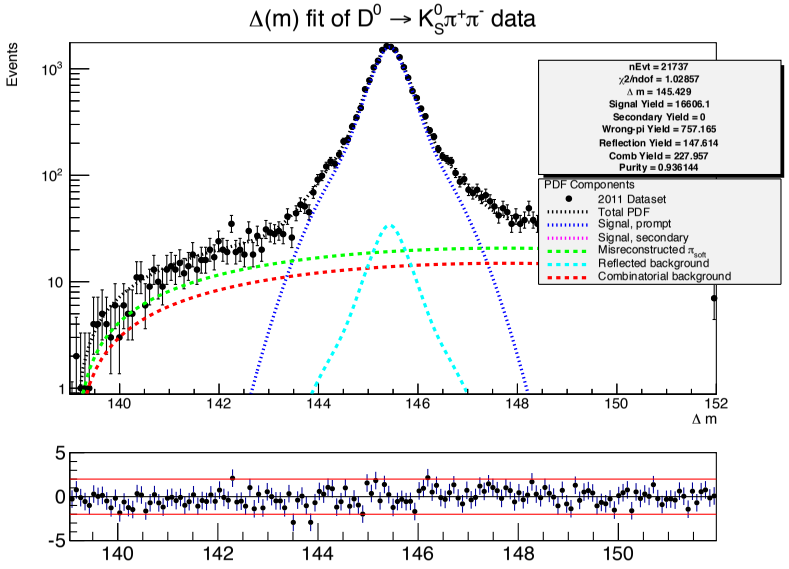

(b) Cleo bin 1 Δm

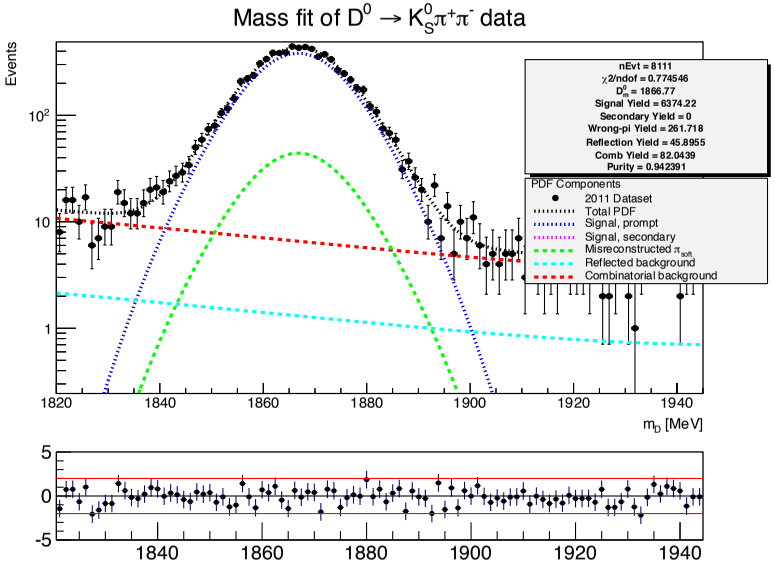

(c) Cleo bin 2 m_D

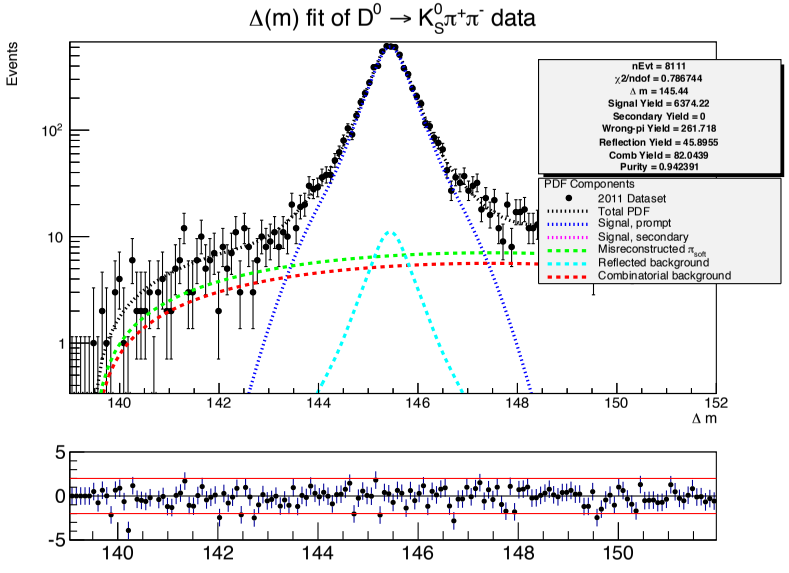

(d) Cleo bin 2 Δm

Figure F.9: Fit projections for the 2D m_D- Δm fit in CLEO bins 1 and 2 of the $\bar{D}^0 \to K_S\pi^+\pi^-$ data.

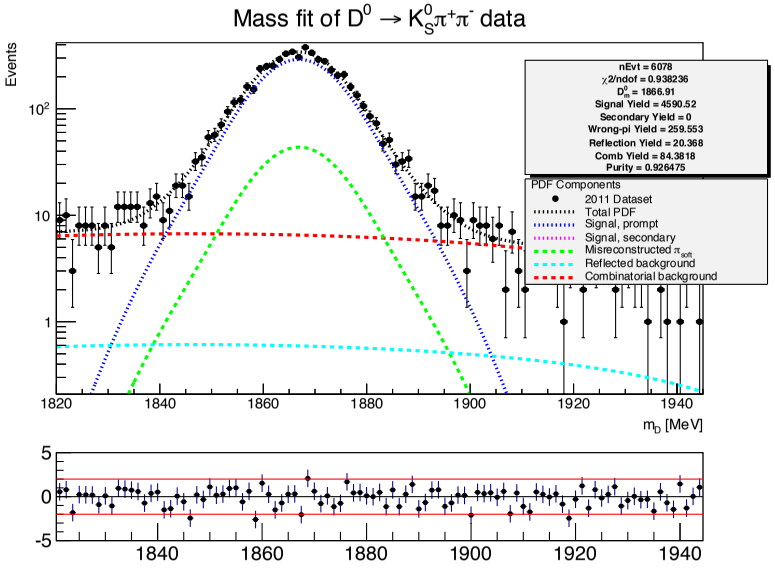

(a) Cleo bin 3 m_D

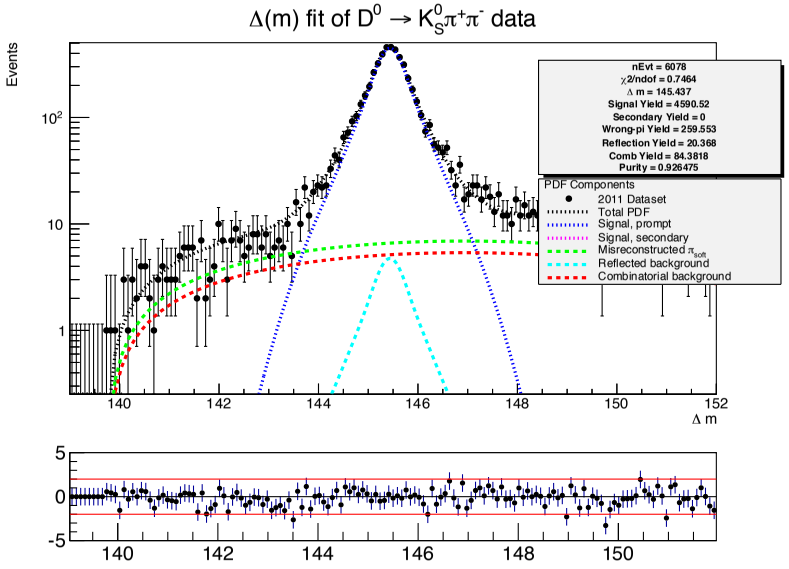

(b) Cleo bin 3 Δm

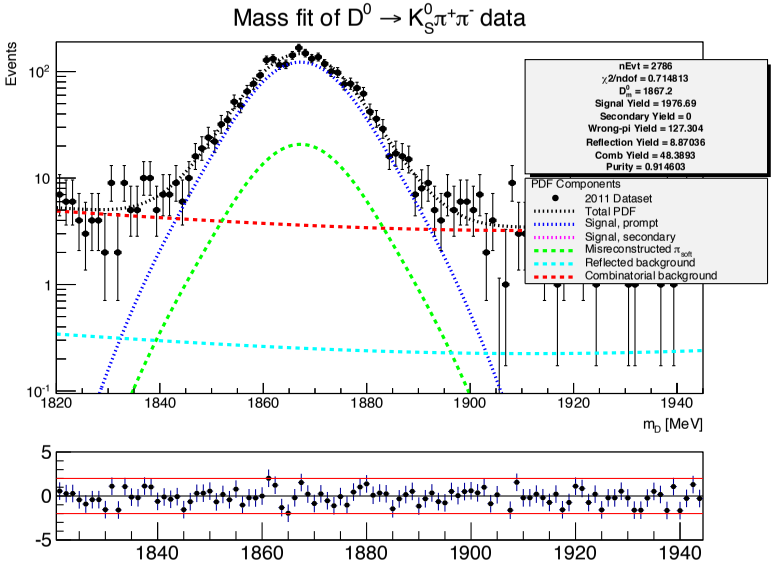

(c) Cleo bin 4 m_D

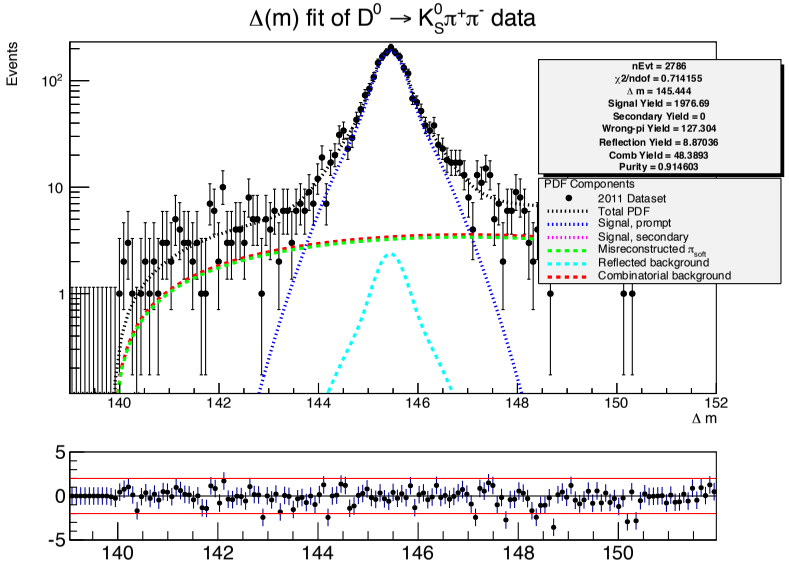

(d) Cleo bin 4 Δm

Figure F.10: Fit projections for the 2D m_D- Δm fit in CLEO bins 3 and 4 of the $\bar{D}^0 \to K_S\pi^+\pi^-$ data.

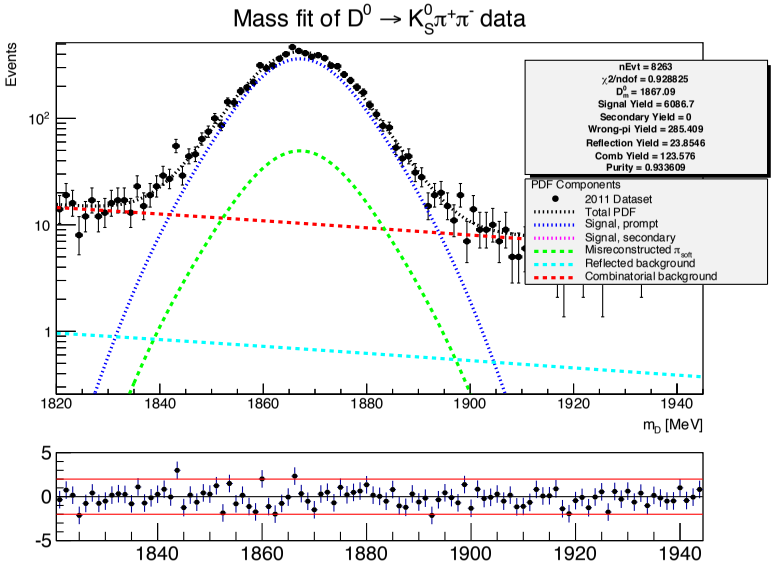

(a) Cleo bin 5 m_D

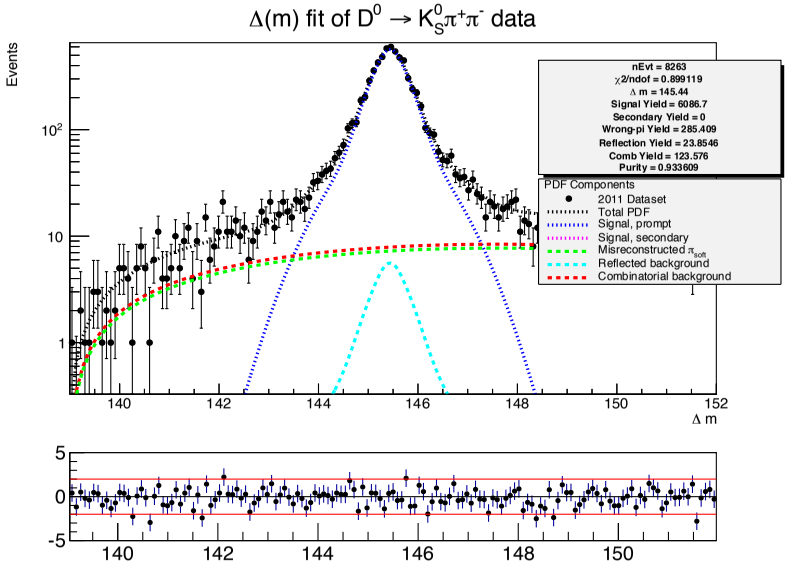

(b) Cleo bin 5 Δm

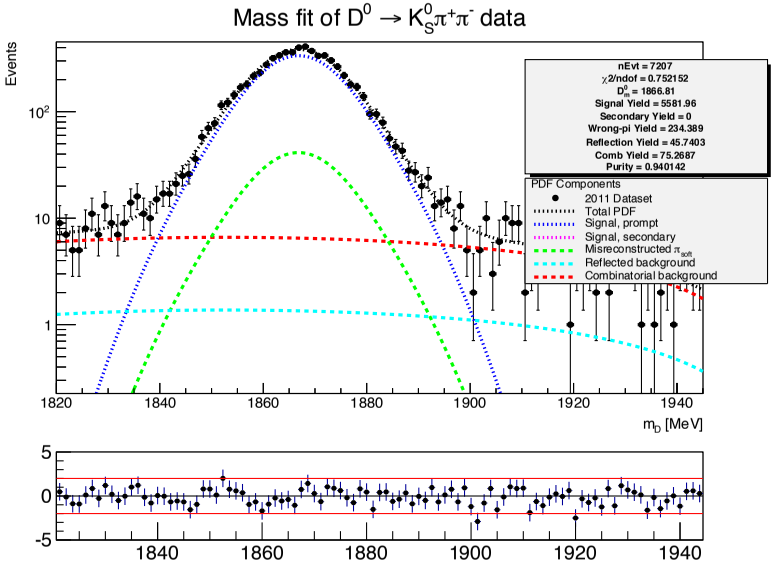

(c) Cleo bin 6 m_D

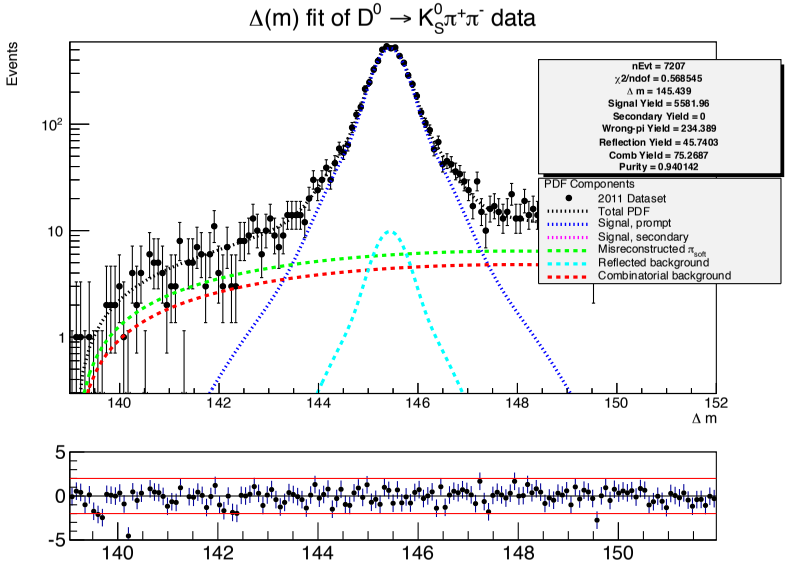

(d) Cleo bin 6 Δm

Figure F.11: Fit projections for the 2D m_D- Δm fit in CLEO bins 5 and 6 of the $\bar{D}^0 \to K_S\pi^+\pi^-$ data.

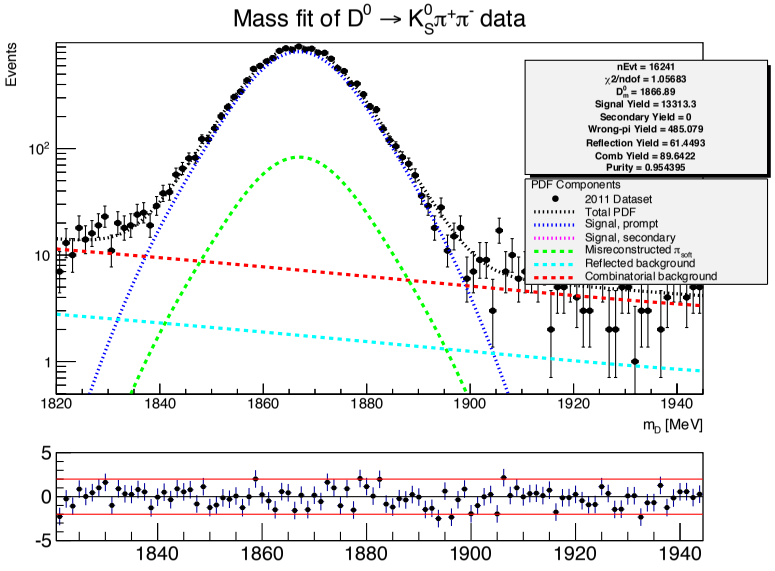

(a) Cleo bin 7 m_D

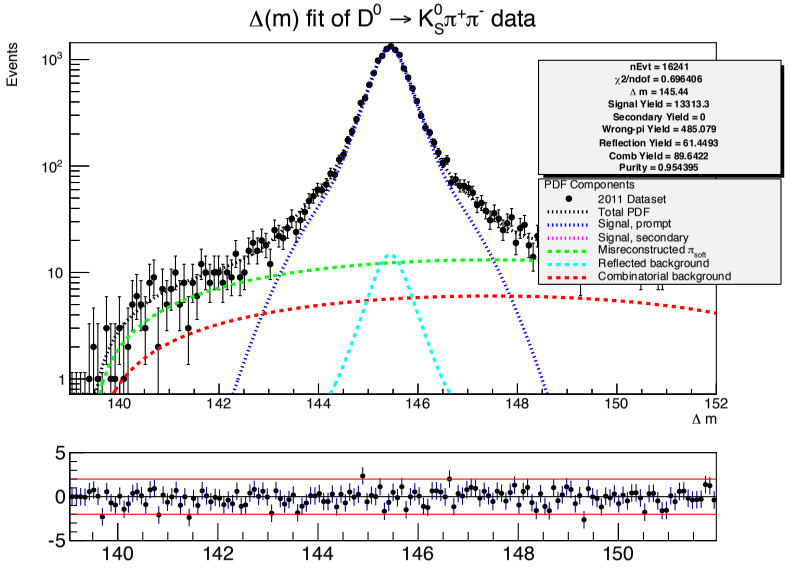

(b) Cleo bin 7 Δm

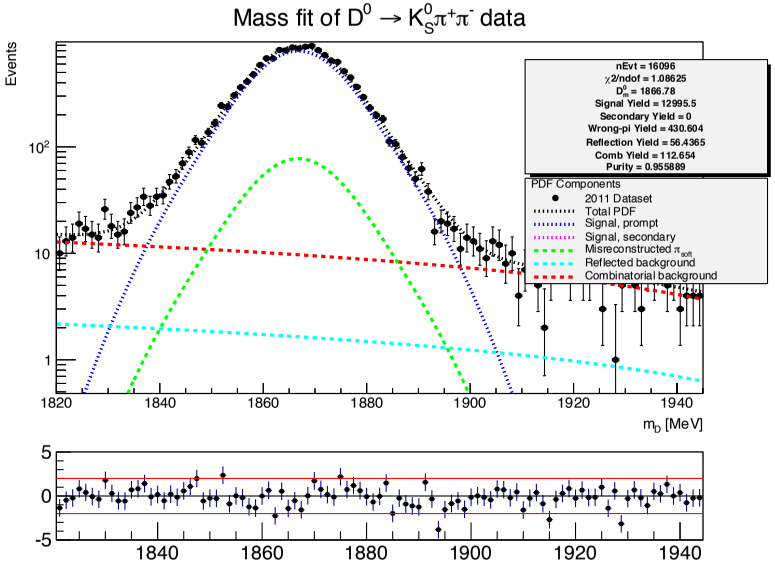

(c) Cleo bin 8 m_D

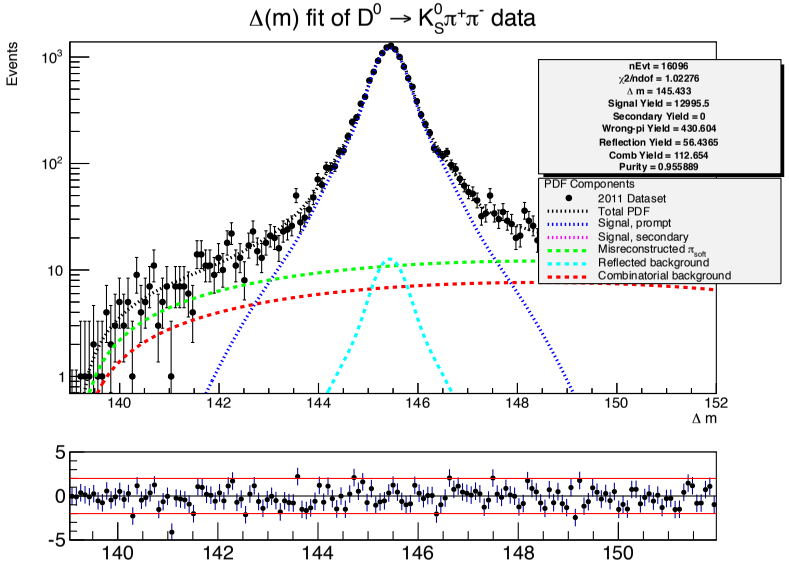

(d) Cleo bin 8 Δm

Figure F.12: Fit projections for the 2D m_D- Δm fit in CLEO bins 7 and 8 of the $\bar{D}^0 \to K_S\pi^+\pi^-$ data.

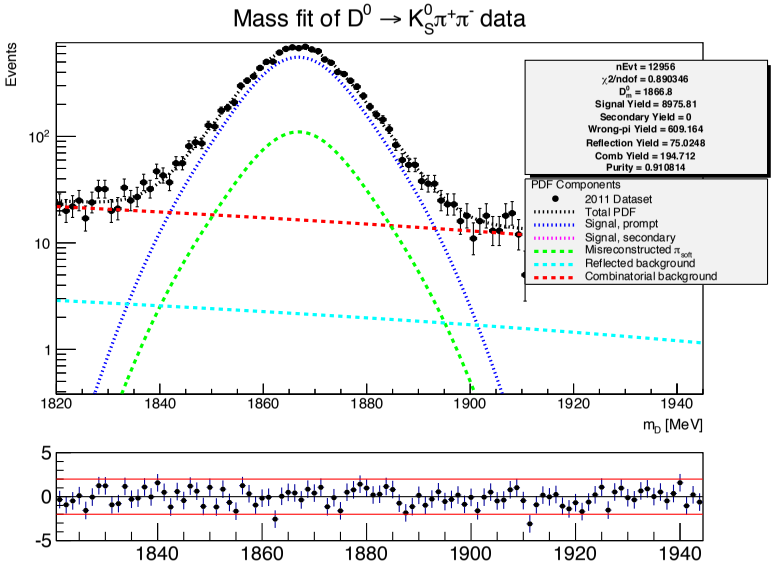

(a) Cleo bin -1 m_D

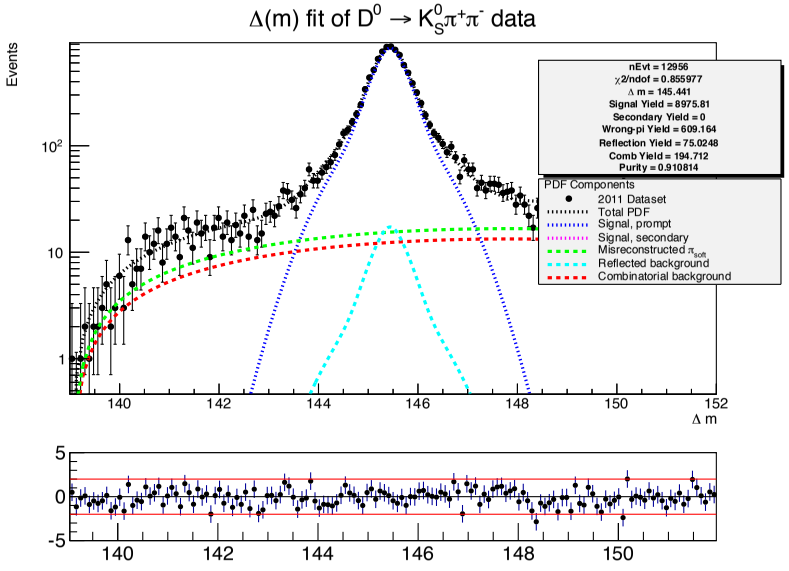

(b) Cleo bin -1 Δm

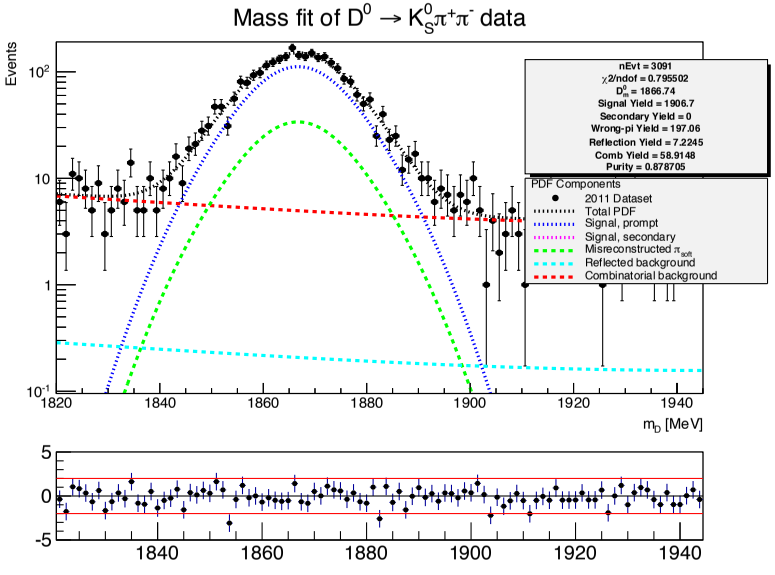

(c) Cleo bin -2 m_D

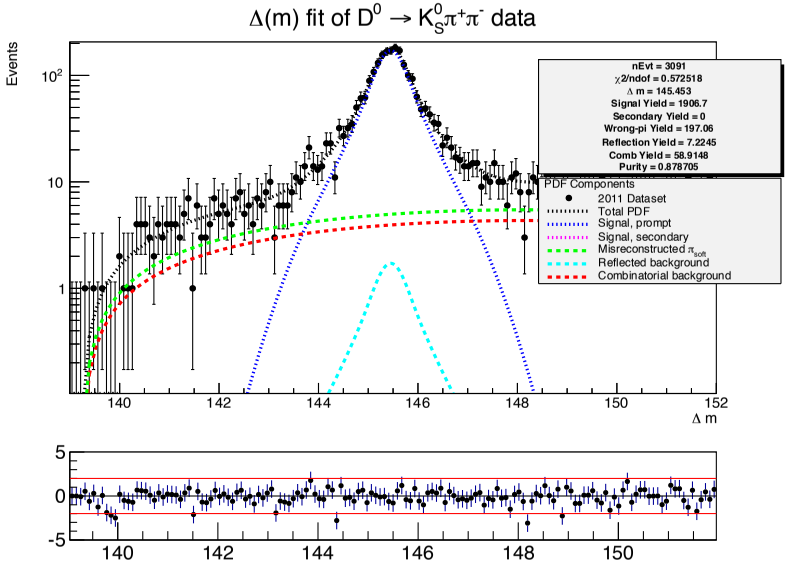

(d) Cleo bin -2 Δm

Figure F.13: Fit projections for the 2D m_D- Δm fit in CLEO bins -1 and -2 of the $\bar{D}^0 \to K_S\pi^+\pi^-$ data.

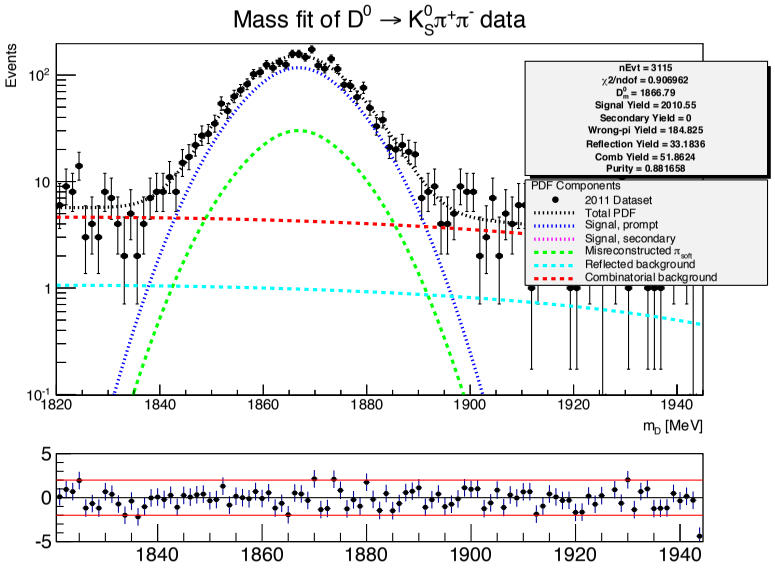

(a) Cleo bin -3 m_D

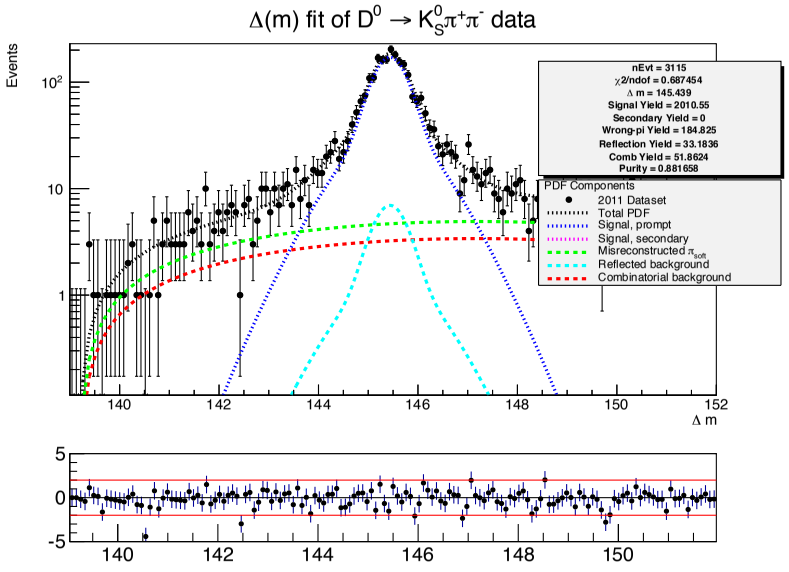

(b) Cleo bin -3 Δm

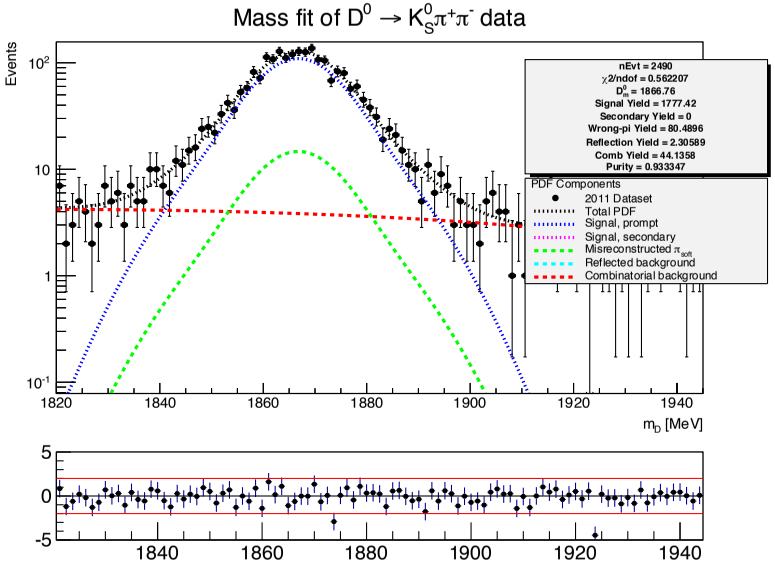

(c) Cleo bin -4 m_D

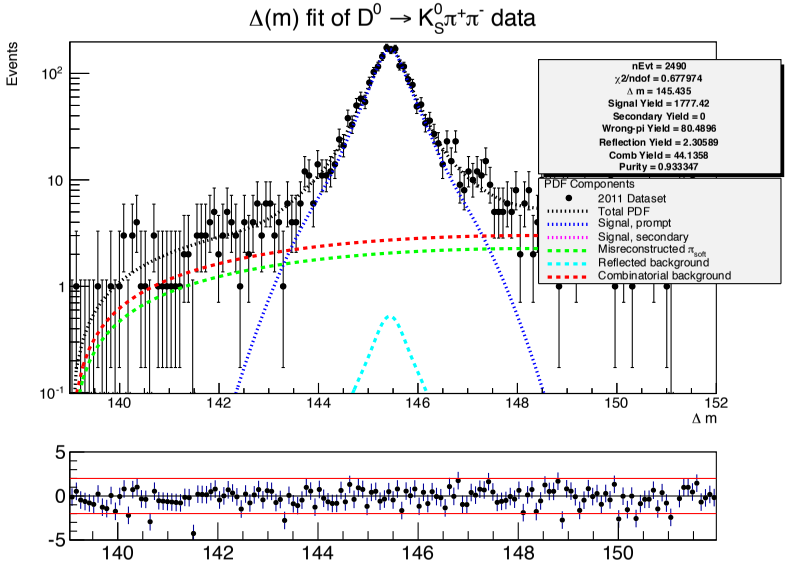

(d) Cleo bin -4 Δm

Figure F.14: Fit projections for the 2D m_D- Δm fit in CLEO bins -3 and -4 of the $\bar{D}^0 \to K_S\pi^+\pi^-$ data.

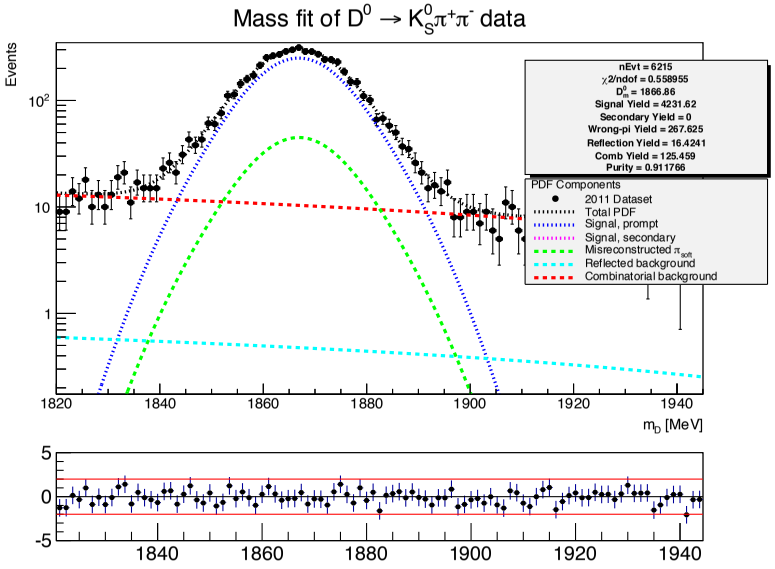

(a) Cleo bin -5 m_D

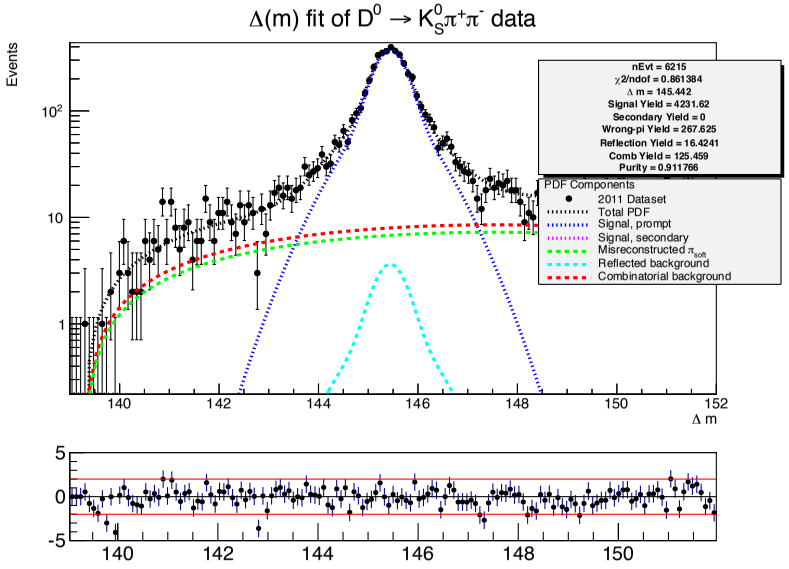

(b) Cleo bin -5 Δm

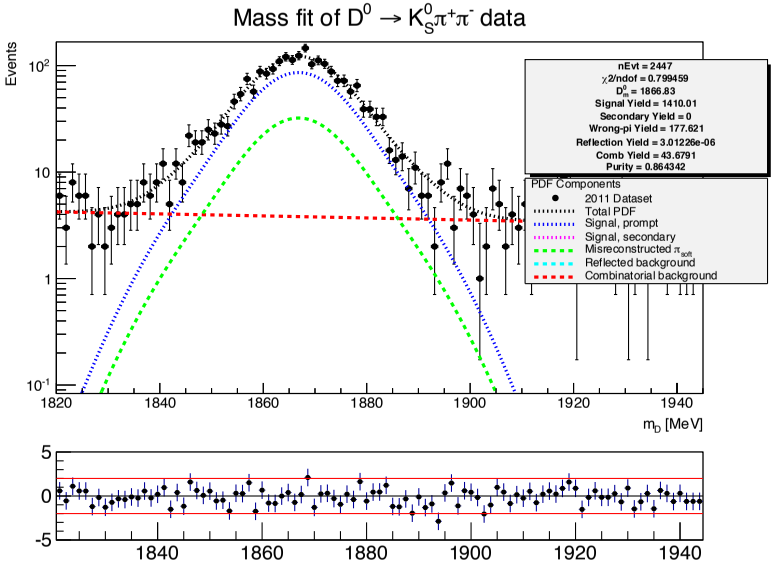

(c) Cleo bin -6 m_D

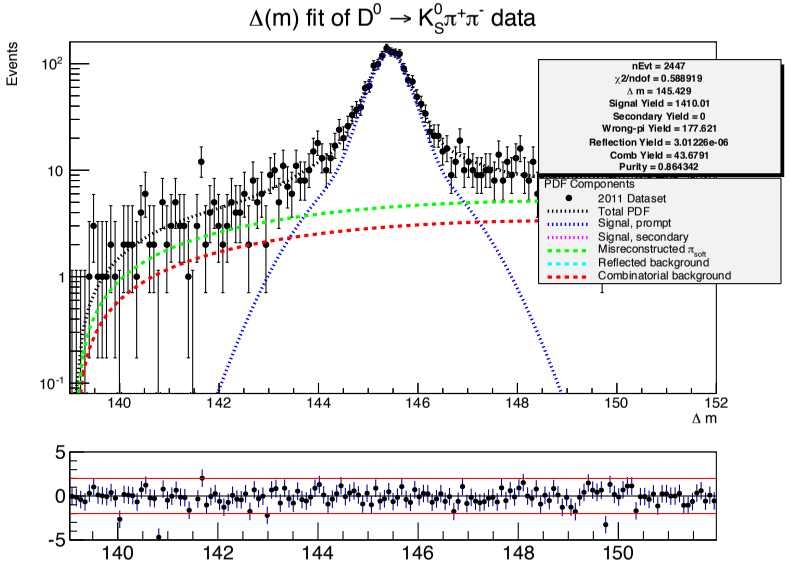

(d) Cleo bin -6 Δm

Figure F.15: Fit projections for the 2D m_D- Δm fit in CLEO bins -5 and -6 of the $\bar{D}^0 \to K_S\pi^+\pi^-$ data.

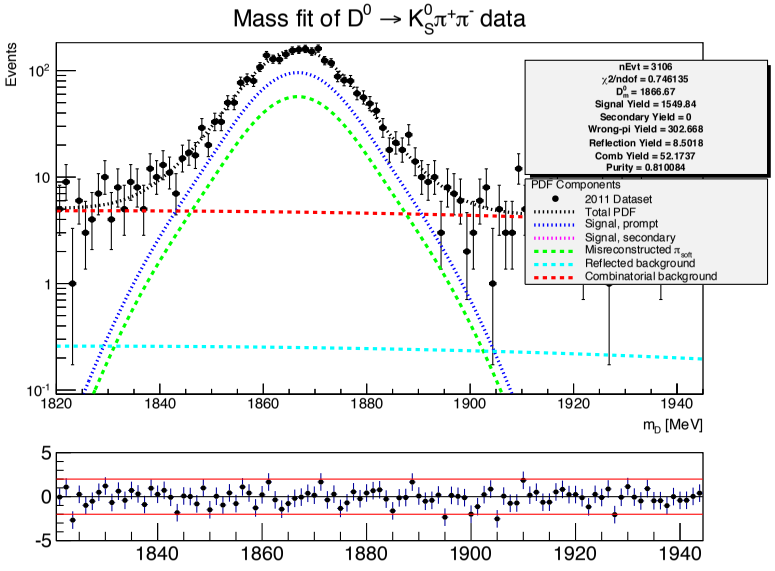

(a) Cleo bin -7 m_D

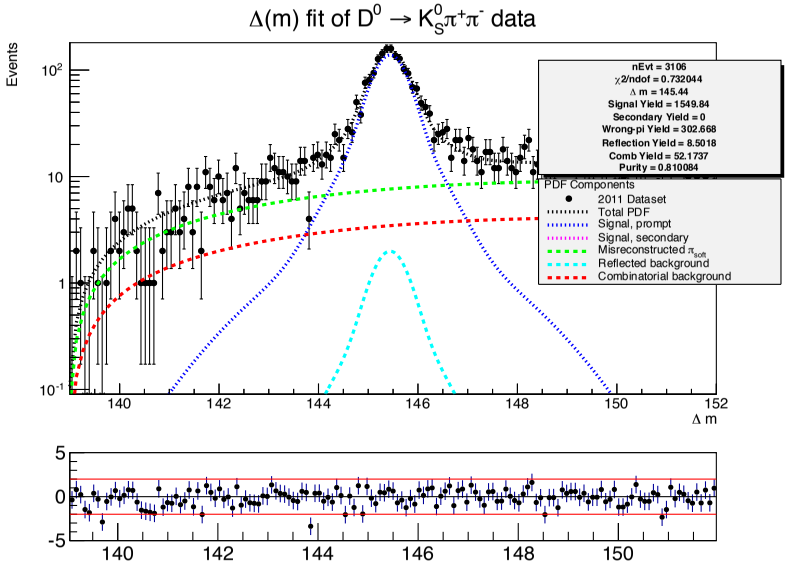

(b) Cleo bin -7 Δm

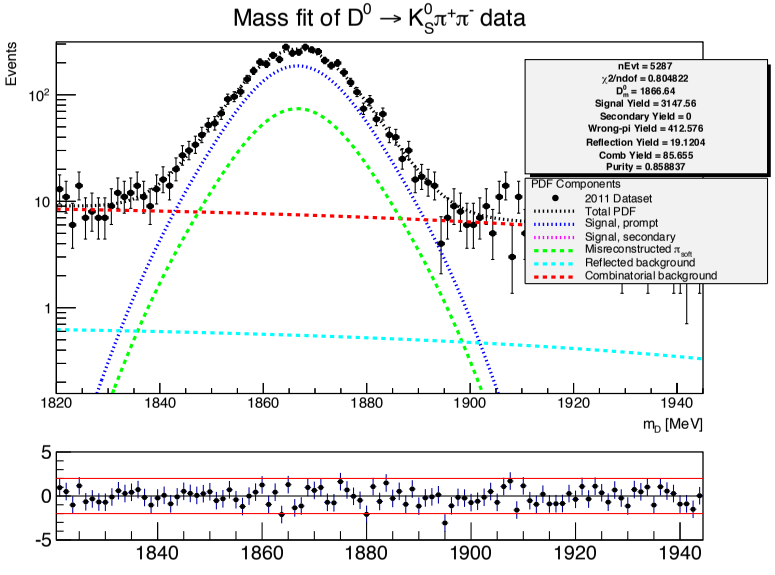

(c) Cleo bin -8 m_D

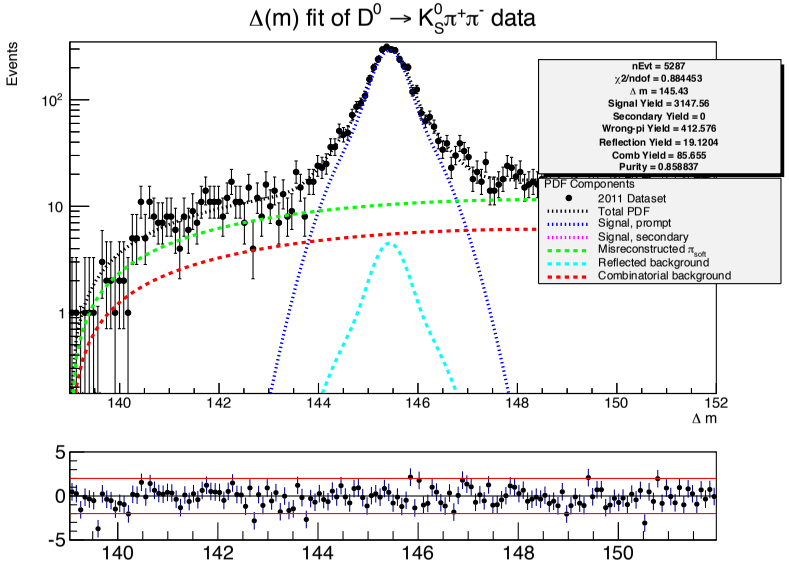

(d) Cleo bin -8 Δm

Figure F.16: Fit projections for the 2D m_D- Δm fit in CLEO bins -7 and -8 of the $\bar{D}^0 \to K_S\pi^+\pi^-$ data.

Appendix G

Alternative choice of fit ratio

There are several issues with formulation of the fit variable that is used in chapter 6.3. It's possible to not know which of the numerator or denominator is vanishing if one doesn't have good prior information about the phase-space of the decay model of D^0 meson, the choice of R to be T_i/T_{-i} or T_{-i}/T_i changes the subsequent algebra enough to be inconvenient. Thus one can choose a symmetric ratio such as

$$\tilde{R}_i \equiv \frac{\mathcal{P}_i \mathcal{P}_{-i}}{\mathcal{P}_i^2 + \mathcal{P}_{-i}^2} = \frac{N_{i,sig} N_{-i,sig}}{N_{i,sig}^2 + N_{-i,sig}^2} \tag{G.1}$$

which has the following benefits

$$\begin{aligned} \lim_{T_i \ll T_{-i}} \tilde{R} &= T_i/T_{-i} \\ \lim_{T_{-i} \ll T_i} \tilde{R} &= T_{-i}/T_i. \end{aligned} \tag{G.2}$$

The numerator and denominator of the expression for $\tilde{R}$ then evaluates into

$$\begin{aligned} N_{i,sig} N_{-i,sig} &= e^{-2\Gamma t} \Big\{ T_i T_{-i} + \sqrt{T_i T_{-i}} \Gamma t \left[T_i (c_i y_D - s_i x_D) + T_{-i} (c_i y_D + s_i x_D) \right] \\ &\quad + T_i T_{-i} \Gamma^2 t^2 (c_i^2 y_D^2 - s_i^2 y_D^2) \Big\} \\ N_{i,sig}^2 + N_{-i,sig}^2 &= e^{-2\Gamma t} \Big\{ T_i^2 + T_{-i}^2 + 2\sqrt{T_i T_{-i}} \Gamma t \left[T_i (c_i y_D + s_i x_D) + T_{-i} (c_i y_D - s_i x_D) \right] \\ &\quad + 2 T_i T_{-i} \Gamma^2 t^2 (c_i^2 y_D^2 + s_i^2 y_D^2) \Big\} . \end{aligned} \tag{G.3}$$

Neglecting the terms $\mathcal{O}(x^2), \mathcal{O}(y^2)$, the expression reduces to

$$\tilde{R}_i = \frac{T_i T_{-i} + \sqrt{T_i T_{-i}} \Gamma t \left[T_i (c_i y_D - s_i x_D) + T_{-i} (c_i y_D + s_i x_D) \right]}{T_i^2 + T_{-i}^2 + 2\sqrt{T_i T_{-i}} \Gamma t \left[T_i (c_i y_D + s_i x_D) + T_{-i} (c_i y_D - s_i x_D) \right]} \tag{G.4}$$

Which can be approximated using Taylor series to leading order as

$$\begin{aligned}\tilde{R}_i = \frac{T_i T_{-i}}{T_i^2 + T_{-i}^2} \left\{ 1 + \frac{\Gamma t}{\sqrt{T_i T_{-i}}} \left[T_i (c_i y_D - s_i x_D) + T_{-i} (c_i y_D + s_i x_D) \right] \right\} \cdot \\ \cdot \left\{ 1 - 2\sqrt{T_i T_{-i}} \Gamma t \frac{T_i (c_i y_D + s_i x_D) + T_{-i} (c_i y_D - s_i x_D)}{T_i^2 + T_{-i}^2} \right\}\end{aligned} \tag{G.5}$$

if the following assumption holds

$$\frac{T_i^2 + T_{-i}^2}{\sqrt{T_i T_{-i}}} \gg T_i (c_i y_D + s_i x_D) + T_{-i} (c_i y_D - s_i x_D) \tag{G.6}$$

One can check that this assumption holds if $T_i \ll T_{-i}$ or $T_{-i} \ll T_i$ and when $T_i \approx T_{-i}$ we have

$$\begin{aligned} 2 T_i c_i y_D &\ll \frac{2 T_i^2}{T_i} \\ c_i y_d &\ll 1 \end{aligned} \tag{G.7}$$

which holds given that $c_i \leq 1$ and $y_D \sim 0.01$. This lets us use equation G.5 and neglect $\mathcal{O}(x^2), \mathcal{O}(y^2)$ terms again to get

$$\begin{aligned}\tilde{R}_i = \frac{T_i T_{-i}}{T_i^2 + T_{-i}^2} \left\{ 1 + \frac{\Gamma t}{\sqrt{T_i T_{-i}}} \left[T_i (c_i y_D - s_i x_D) + T_{-i} (c_i y_D + s_i x_D) \right] - \right. \\ \left. - 2 \frac{T_i T_{-i} \Gamma t}{T_i^2 + T_{-i}^2} \left[T_i (c_i y_D + s_i x_D) + T_{-i} (c_i y_D - s_i x_D) \right] \right\}\end{aligned} \tag{G.8}$$

or, substituting $R_i \equiv T_{-i}/T_i$

$$\begin{aligned}\tilde{R}_i = \frac{R_i}{1 + R_i^2} \left\{ 1 + \frac{\Gamma t}{\sqrt{R_i}} \left[R_i (c_i y_D + s_i x_D) + (c_i y_D - s_i x_D) \right. \right. \\ \left. \left. - \frac{2 R_i}{1 + R_i^2} \left[(c_i y_D + s_i x_D) + R_i (c_i y_D - s_i x_D) \right] \right] \right\}\end{aligned} \tag{G.9}$$

The final form of the fitted function is linear as can be seen from eq. G.9.

The propagated Poisson error for $\tilde{R}$ can be calculated using the leading or-

der multivariate Taylor expansion for independent variables

$$\begin{aligned}
\tilde{\sigma}^2_{i,j} &\equiv \left(\frac{\partial \tilde{R}_{i,j}}{\partial N_{i,j}}\right)^2 N_{i,j} + \left(\frac{\partial \tilde{R}_{i,j}}{\partial N_{-i,j}}\right)^2 N_{-i,j} \\
\tilde{\sigma}^2_{i,j} &\equiv \left[\frac{N_{-i,j}(N^2_{i,j} + N^2_{-i,j}) - 2N^2_{i,j}N_{-i,j}}{(N^2_{i,j} + N^2_{-i,j})^2}\right]^2 N_{i,j} \\
&+ \left[\frac{N_{i,j}(N^2_{i,j} + N^2_{-i,j}) - 2N_{i,j}N^2_{-i,j}}{(N^2_{i,j} + N^2_{-i,j})^2}\right]^2 N_{-i,j}
\end{aligned} \tag{G.10}$$

This approach has a major drawback in that the following limit

$$\lim_{T_i \to T_{-i}} \tilde{R} \to \frac{1}{2} \tag{G.11}$$

maximizes the function, and more importantly, at maximum the simple propagated error for $\tilde{R}$ vanishes

$$\lim_{T_i \to T_{-i}} \tilde{\sigma} = 0 \tag{G.12}$$

as seen from equation G.10. A different way to obtain the propagated error for the $\tilde{R}$ fit function is to use a Monte Carlo efficiency estimation or a Bayesian error estimation in a similar way to propagating errors for efficiencies [10]. However since the fit described in chapter 6 is stable and unbiased, this approach was not pursued further.

Appendix H

Values of the CLEO parameters used in this analysis

The parameters extracted in the quantum correlated $\Psi(3770)$ CLEO analysis [11] for the equal-$\Delta\delta_{K_S\pi^+\pi^-}$ BaBar 2008 binning can be seen in tables H.1 and H.2 and the statistical and systematic correlation matrices for c_i and s_i can be seen in tables H.3 and H.4.

CLEO bin	$c_i \pm$ (stat.) $\pm$ (syst.)	$s_i \pm$ (stat.) $\pm$ (syst.)
1	$0.655 \pm 0.036 \pm 0.042$	$-0.025 \pm 0.098 \pm 0.043$
2	$0.511 \pm 0.067 \pm 0.063$	$0.141 \pm 0.183 \pm 0.066$
3	$0.024 \pm 0.140 \pm 0.080$	$1.111 \pm 0.131 \pm 0.044$
4	$-0.569 \pm 0.118 \pm 0.098$	$0.328 \pm 0.202 \pm 0.072$
5	$-0.903 \pm 0.045 \pm 0.042$	$-0.181 \pm 0.131 \pm 0.026$
6	$-0.616 \pm 0.103 \pm 0.072$	$-0.520 \pm 0.196 \pm 0.059$
7	$0.100 \pm 0.106 \pm 0.124$	$-1.129 \pm 0.120 \pm 0.096$
8	$0.422 \pm 0.069 \pm 0.075$	$-0.350 \pm 0.151 \pm 0.045$

Table H.1: The values of integrated amplitude weighed phase difference c_i and s_i extracted in the CLEO analysis [11] used in the model independent fit in this thesis. The uncertainties are statistical and systematic respectively.

CLEO bin	$T_i \pm$ (stat.) [%]	$T_{-i} \pm$ (stat.) [%]	$R_i \pm$ (stat.)
1	9.0 ± 0.4	2.6 ± 0.2	0.485 ± 0.028
2	14.4 ± 0.5	0.5 ± 0.1	0.238 ± 0.027
3	14.7 ± 0.5	0.3 ± 0.1	0.279 ± 0.032
4	9.9 ± 0.4	5.9 ± 0.3	0.671 ± 0.094
5	5.7 ± 0.3	3.3 ± 0.2	0.597 ± 0.044
6	7.5 ± 0.4	0.5 ± 0.1	0.235 ± 0.034
7	10.9 ± 0.4	5.5 ± 0.3	0.096 ± 0.015
8	2.2 ± 0.2	6.9 ± 0.3	0.193 ± 0.017

Table H.2: The values of integrated amplitude extracted in the CLEO analysis [11] used in the model independent fit in this thesis. The T_i and T_{-i} parameters are multiplied by normalization constant to get the number of events in the corresponding bin. The value of R_i is absolute as the normalization constant cancels. The errors are statistical only.

CLEO bin	c_2	c_3	c_4	c_5	c_6	c_7	c_8	s_1	s_2	s_3	s_4	s_5	s_6	s_7	s_8
c_1	1	-1	1	0	-1	0	-2	0	2	0	2	2	1	-1	-5
c_2		2	12	2	0	0	-3	0	2	2	-8	0	1	0	-3
c_3			4	0	0	0	-1	0	11	6	4	-1	12	2	-5
c_4				0	5	8	0	0	3	0	3	0	2	0	-2
c_5					3	0	-1	0	-6	-6	-8	1	-3	4	4
c_6						0	0	0	-8	-12	9	-4	7	0	1
c_7							-7	0	0	0	0	0	0	-2	-1
c_8								0	0	-1	1	0	-1	-3	-3
s_1									-8	8	-2	6	10	7	18
s_2										15	15	10	25	2	-5
s_3											1	8	57	18	15
s_4												-5	17	-9	-7
s_5													-4	2	20
s_6														20	8
s_7															24

Table H.3: Statistical correlations (in %) between parameters c_i and s_i for $D^0 \to K_S\pi^+\pi^-$ as obtained in [11] using equal-$\Delta\delta_{K_S\pi^+\pi^-}$ BaBar 2008 binning scheme.

CLEO bin	c_2	c_3	c_4	c_5	c_6	c_7	c_8	s_1	s_2	s_3	s_4	s_5	s_6	s_7	s_8
c_1	79	87	69	91	89	79	88	−13	27	−20	30	−4	43	0	−46
c_2		76	68	82	82	66	71	0	5	−16	10	−6	27	1	−24
c_3			78	91	89	76	79	−14	4	−26	23	−16	27	−10	−31
c_4				83	76	72	58	−6	−4	−22	7	−16	20	−6	−16
c_5					92	80	81	−9	6	−22	16	−13	29	−6	−30
c_6						75	82	−6	8	−22	14	−10	31	−3	−32
c_7							74	−15	20	−20	24	−7	34	−8	−41
c_8								−10	21	−20	27	−3	36	−3	−44
s_1									−15	23	−26	16	6	31	32
s_2										26	56	34	75	25	−70
s_3											13	34	47	28	6
s_4												13	57	0	−52
s_5													28	10	−7
s_6														28	−49
s_7															4

Table H.4: Systematic correlations (in %) between parameters c_i and s_i for $D^0 \to K_S\pi^+\pi^-$ as obtained in [11] using equal-$\Delta\delta_{K_S\pi^+\pi^-}$ BaBar 2008 binning scheme.

Bibliography

[1] Particle Data Group, J. Beringer *et al.*, *Review of particle physics*, Phys. Rev. D **86** (2012) 010001.

[2] R. Dalitz, *On the analysis of τ-meson data and the nature of the τ-meson*, Philosophical Magazine Series 7 **44** (1953), no. 357 1068.

[3] DELPHI Collaboration, W. Adam *et al.*, *Lifetimes of charged and neutral B hadrons using event topology*, Z. Phys. **C68** (1995) 363 CERN-PPE-95-059, CERN-PPE-95-59.

[4] CDF Collaboration, T. Aaltonen *et al.*, *Measurement of the B^- lifetime using a simulation free approach for trigger bias correction*, Phys. Rev. **D83** (2011) 032008 FERMILAB-PUB-10-095-E, arXiv:1004.4855.

[5] V. V. Gligorov, G. Wilkinson, and J. Rademacker, *Measurement of the CKM angle gamma and B meson lifetimes at the LHCb detector*, PhD thesis, Oxford U., Oxford, UK, 2008, Presented on 28 May 2008.

[6] A. Ryd *et al.*, *EvtGen: A Monte Carlo Generator for B-Physics*, EVTGEN-V00-11-07.

[7] EvtGen Development Team, *EvtGen Project Website*, http://evtgen.warwick.ac.uk.

[8] N. Davidson, T. Przedzinski, and Z. Was, *PHOTOS Interface in C++: Technical and Physics Documentation*, arXiv:1011.0937 CERN-PH-TH-2010-261, IFJPAN-IV-2010-6, arXiv:1011.0937.

[9] S. Jadach, J. H. Kuhn, and Z. Was, *TAUOLA: A Library of Monte Carlo programs to simulate decays of polarized tau leptons*, Comput. Phys. Commun. **64** (1990) 275 CERN-TH-5856-90.

[10] D. Casadei, *Estimating the selection efficiency*, JINST **7** (2012) P08021, arXiv:0908.0130.

[11] CLEO Collaboration, J. Libby *et al.*, *Model-independent determination of the strong-phase difference between D^0 and $\bar{D}^0 \to K^0_{S,L} h^+ h^-$ ($h = \pi, K$) and its impact on the measurement of the CKM angle γ/ϕ_3*, Phys. Rev. **D82** (2010) 112006 CLNS-10-2070, CLEO-10-07, arXiv:1010.2817.